CRYSTALLIZATION AND MELTING BEHAVIOR OF AN AROMATIC SEMICRYSTALLINE POLYIMIDE, LaRC CPI–2

by

Donald Keith Brandom

Dissertation submitted to the Faculty of the
Virginia Polytechnic Institute and State University
in partial fulfillment of the requirements for the degree of

DOCTOR OF PHILOSOPHY

in

MATERIALS ENGINEERING SCIENCE

APPROVED:

Garth L. Wilkes, Chairman

Richey M. Davis

Ronald G. Kander

Herve Marand

James E. McGrath

June, 1996
Blacksburg, Virginia

Key Words: LaRC Polyimide, Crystallization, Melting, Synthesis, Processing

CRYSTALLIZATION AND MELTING BEHAVIOR OF AN AROMATIC SEMICRYSTALLINE POLYIMIDE, LaRC CPI–2

by

Donald Keith Brandom

Garth L. Wilkes, Chairman

MATERIALS ENGINEERING SCIENCE

(ABSTRACT)

Research is presented on the crystallization and melting behavior of an aromatic semicrystalline polyimide known as LaRC CPI–2 (Langley Research Center Crystalline Polyimide - second generation). This aromatic polyimide, a structural variant of the well known LaRC CPI, is synthesized from 1,4-bis(4-aminophenoxy-4'-benzoyl)benzene (1,4-BABB) and 4,4'-oxydiphthalic dianhydride (ODPA).

The multiple melting behavior at ca. 334°C and 364°C, characteristic of this polymer, is analyzed and explained. Transmission electron microscopy (TEM), wide angle X-ray diffraction (WAXD), and small angle X-ray scattering (SAXS) studies, in conjunction with differential scanning calorimetry (DSC) analysis, show that the high melting transition results from the melting of lamellae which were melt recrystallized during heating in a DSC.

The effects of synthesis and process variables upon the crystallization and melting properties of this polyimide were also studied. The DSC response of LaRC CPI–2 films and powders of varying molecular weight are compared and

contrasted. Powders generally melt at a higher temperature than films of the same molecular weight. The glass transition temperature, T_g, of both the powders and films are found to be dependent upon molecular weight. An interpolated value of T_g for the infinite molecular weight LaRC CPI−2 is ca. 234°C. In a study of the development of crystallinity in films during standard thermal imidization, crystallinity was found to initiate off the glass surface very early in the process leaving an amorphous layer at the air surface after the full thermal treatment.

LaRC CPI−2 powder 'types' synthesized in different solvents, dimethylacetamide (DMAc) and *m*-cresol present with dramatically different melting, melt stability and crystallization properties. Though the chemical architecture and crystal lattice structure are the same, the powders synthesized in DMAc display dual melting transitions at ca. 334°C and 364°C, while the powders from *m*-cresol melt singularly at ca. 409°C. Rheological analysis, along with annealing data, revealed a higher temperature melt stability in the powders from *m*-cresol. It is postulated that the differences in the properties of the two powders are the result of differing initial molecular weights and a suppression of a cross-linking ketimine reaction in the polymer produced in *m*-cresol.

In memoriam,

Helen Maxine Brandom

(1931 - 1979)

ACKNOWLEDGEMENTS

Foremost, I am extremely grateful for the unceasing support of my daughters Shevaun and Jessica Brandom, and my soul-mate and partner in life, Jeri Brandom. They have been exceptionally understanding and supportive throughout my graduate school career. The camaraderie I have with my family is unparalleled in my experience. I cannot adequately express in words my gratitude. It is to them that I am devoted.

To my father, Brandy Brandom, I am also greatly indebted. From across the waters and continents of the world, he has always 'been there' for me. In the fulfillment of a final promise to my mother, he has been nothing short of extraordinary. A. Vati, thank you.

I wish to thank my advisor, Prof. Garth L. Wilkes. His expert guidance and uncommon patience throughout my doctoral work has been invaluable. Furthermore, he is the exemplar of integrity and honor. He has earned my deepest respect.

Thanks to Profs. R. Davis, R. Kander, J. McGrath and H. Marand for serving as members of my committee. Their input during my tenure has been greatly appreciated. I also wish to thank Prof. J. Riffle for standing in for Prof. R. Kander during my dissertation defense.

I wish to acknowledge the financial support of this research by the National Aeronautics and Space Administration under contract number NGT-51117.

I have been fortunate to have received guidance and sound advice regarding the synthesis of polyimides, from Paul Hergenrother, Dr. Steven Havens and Dr. Heather Brink.

Special thanks are due to Dr. Don Loveday for acquiring synchrotron SAXS data and to Dr. Ben Hsiao of DuPont for facilitating the use of this instrument and, along with Dr. Ravi Verma, for helpful discussions regarding SAXS analysis. I am also indebted to Slade Gardner for his expert guidance and help in setting up the Bohlin rheometer to perform crystallization kinetics analysis.

I have gained much from the discussions with Dr. Pamela Percha and Dr. Srivatsan Srinivas. I value their knowledge and insight.

NMR analysis by Tom Glass, Mass Spectrometry analysis by Kim Herrick and TEM work performed by Steve McCartney were sincerely appreciated. I found the technical advice from these experts to be invaluable.

A final special thanks to Sandy Simpkins. She provided me with invaluable guidance and assistance while navigating through grad school. Furthermore, (indeed) Sandy always had her finger on the pulse Prof. Wilkes' schedule and many many times went out of her way to help me 'make contact'.

CONTENTS

LIST OF FIGURES

LIST OF TABLES

CHAPTER 1

INTRODUCTION

The research presented in this dissertation focuses on the crystallization and melting behavior of an aromatic semicrystalline polyimide known as LaRC CPI-2. After a literature review of the relevant topics in Chapter 2, and explanation of experimental procedures in Chapter 3, the research work is divided into three main chapters, each of which has its own focus upon different aspects of crystallization and melting of LaRC CPI-2.

Chapter 4 provides a necessary introduction into the somewhat unusual characteristic of multiple melting in this polymer. This chapter presents results of an investigation into the morphological origins of this multiple melting phenomenon. Transmission electron microscopy (TEM), wide angle X-ray diffraction (WAXD), and small angle X-ray scattering (SAXS) studies, in conjunction with differential scanning calorimetry (DSC) analysis, show that the high melting transition results from the melting of lamellae which were melt recrystallized during heating in a DSC. DSC heating rate studies reveal that the rate of transformation from thin to thick lamellae is dependent upon molecular weight and is very rapid for low molecular weight films. Synchrotron SAXS analysis confirms that the melt recrystallization process is very rapid.

In chapter 5 the effect of synthesis and process variables on the

crystallization and melting properties of LaRC CPI-2 is presented. Within this chapter three main areas are presented. First the DSC response of LaRC CPI-2 films and powders, particularly differences in glass and melting transitions, are compared and contrasted. Next, a study of the changes in LaRC CPI-2 films during thermal imidization is presented. Here the development of crystallinity was followed during the imidization process. Lastly this chapter presents the unusually strong dependence of melting temperature of LaRC CPI-2 powders upon processing conditions. Specifically, the synthesis of powders in DMAc and *m*-cresol is discussed and the greatly differing melting behavior is presented. The results of several analytical techniques used in an attempt to explain the differences in melting behavior are also presented.

Chapter 6 presents a detailed analysis of powders synthesized from the two solvents, DMAc and *m*-cresol. In particular, the response of these materials to various conditions of melt time and melt temperature are investigated, including their unusual ability to 'anneal' at temperatures above their observed melt transition. Though thermodynamic melting temperatures are not determined, lower limits are presented. Crystallization kinetics information for both powders, as determined through rheological analysis, is also presented. Lastly, a comparison of the two powders is presented with postulated reasons for their divergent melting and crystallization behavior.

Recommendations for future work is presented in chapter 7.

CHAPTER 2

LITERATURE REVIEW

2.1 Introduction.

This literature review presents background information in two primary areas: Polyimides and polymer crystallization. The review is specifically designed to provide in-depth information in areas that have direct relevance to the work presented in this dissertation. In the polyimides section of this chapter much discussion focuses on the synthesis of poly(amic acid)s and their subsequent imidization. Particular attention is given to reaction mechanisms and solvent effects that help to provide answers to questions posed in this dissertation. The latter portion of this chapter describes some important features of polymer crystallization theory as they relate to work presented in this dissertation. Included in this section is some discussion of the multiple melting behavior found in some polymers, a characteristic feature of LaRC CPI-2 polyimides.

2.2 Polyimides

Aromatic polyimides may be synthesized through a variety of different methods, some of which are presented in the following sections. Polyimides offer a diverse array of attractive properties which can be engineered for specific applications. Through the proper choice of monomers from a vast array of

starting materials, properties such as glass transition temperature (T_g), melting temperature (T_m), modulus, solubility, melt viscosity, dielectric constant etc..., may be tailor-made into the finished product. Polyimides have applications in a variety of areas including coatings, films, separation membranes, resin matrices for composites, fibers, foams and adhesives. Several books and reviews dedicated to polyimides are available [1 - 8].

2.2.1 Synthesis of Polyimides

Polyimides are a class of polymers containing an imide structural unit present as a linear or heterocyclic unit along the main chain of the polymer backbone. Aromatic heterocyclic polyimides display excellent mechanical properties along with outstanding thermal and oxidative stability. As a result these materials are often used for high performance applications in the electrical, electronics, automotive, aerospace, and packaging industries [1 - 7].

The most widely used method for the preparation of linear aromatic polyimides involves the formation of a poly(amic acid) intermediate, produced from the reaction of a carboxylic acid dianhydride and a primary diamine, followed by cyclodehydration to form the polyimide [7]. This two-step procedure will be the primary focus of this review of polyimide synthesis. An overview of other synthetic methods are presented, as well.

2.2.1.1 Poly(amic acid) Synthesis

The reaction of carboxylic acid dianhydrides with a primary diamines at ambient temperatures in a polar aprotic solvent produces a soluble poly(amic acid), less commonly referred to as a poly(amide acid) or poly(amido) acid. The corresponding polyimide is formed via a cyclodehydration of the amic acid group via thermal or chemical means. A general schematic of this process is shown in Fig. 2.1. Typically the solution is allowed to stir overnight at room temperature in order to ensure full solvation and reaction of the monomers.

The mechanism for the formation of the poly(amic acid) is thought to begin with the development of a charge transfer complex between amine and anhydride functionalities as shown in Fig. 2.2 [9]. The formation of the poly(amic acid) is reversible [10, 11]. Since the anhydride moiety is cyclic, the carboxyl reaction 'by-product', carboxylic acid group, remains attached to the product of the reaction. Thus, it cannot be removed in order to drive the reaction forward. This is overcome by employing the use of polar aprotic solvents which form hydrogen bond complexes with the carboxyl group. These complexes act to inhibit the reverse reaction by lowering the energy of the poly(amic acid). For example, the equilibrium constants for the acylation reaction (attachment of the —COR group to the amine, a result of the 'amidization' reaction) have been shown to be on the order of 10^5 l/mole for many anhydride amine pairs in dimethylacetamide (DMAc), dimethylsulfoxide (DMSO) and tetrahydrofuran (THF) at 40°C [10, 11].

It is important to note also that the greater the basicity of the amine and/or electrophilicity of the anhydride, the more favored the forward reaction [10 - 12]. The specific effect of the solvent basicity was shown clearly in a study where the same monomer reactions were compared in THF versus DMAc [11]. The equilibrium constant increased an order of magnitude from $1.7X10^4$ l/mole in THF to $>10^5$ l/mole in DMAc. Clearly, the aprotic amine forms a stronger complex with the carboxyl group. Indeed, many studies have focused on the tenacity of the complexes formed between DMAc and NMP with poly(amic acid)s [13 - 16]. It should be noted that the exothermic character of the forward reaction, as seen in Fig. 2.2, will favor the reverse reaction with increasing polymerization temperature. The equilibrium in basic aprotic solvents is so high, however, that the effect of temperature is negligible [9]. Thus, from a thermodynamic perspective, it can be generally stated that the poly(amic acid) is favored under typical reaction conditions of polar aprotic basic solvents at room temperature.

It has also been established that the kinetics of the poly(amic acid) formation are affected by the solvent medium [17, 18]. In particular the reaction rate increases with increasing polarity and basicity of the solvent medium. In general terms, Vygodskii et al. found that the rate increased on changing from the less polar dioxane solvent to NMP when studying the reaction between diamines and dianhydrides [17]. Due to the excessively large equilibrium constants favoring

the formation of the poly(amic acid), these researchers assumed *non*-reversible second order reaction kinetics. In a detailed study of the acylation reaction between a mono-anhydride and mono-amine, phthalic anhydride (PA) and *para*-aminodiphenylether (p-ADPO), Solomin et al. clearly quantified rate constants in a series of solvents: THF, acetonitrile (ACN), DMAc and *m*-cresol [18]. The researchers were careful to include an equilibrium term in the second order reaction kinetics analysis as seen in the Eqn. 2−1 below, where K_p is the equilibrium constant. It should be noted that the in all solvents, K_p was found to be very large (10^3 to $>10^5$l/mole), so the effect of the equilibrium term is negligible.

$$\frac{d[P]}{dt} = (k_1[A][B] + k_2[A][B][P])\left(1 - \frac{[P]}{K_p[A][B]}\right) \qquad (2-1)$$

Here, $[A]$, $[B]$ and $[P]$ are the anhydride, diamine and product (amic acid) concentrations, respectively. The authors determined two separate rate constants for the formation of the amic acid. The first rate constant, k_1, is concerned with the standard bimolecular reaction between the amine and anhydride. The second rate constant, k_2, is the *catalyzed* rate constant for reaction between the amine and anhydride. As can be seen in Eqn. 2−1, the catalyst is the product of the reaction, i.e., k_2 is an *auto*-catalyzed rate constant: The authors determined that the acid functionality in the amic acid product acts to catalyze the reaction.

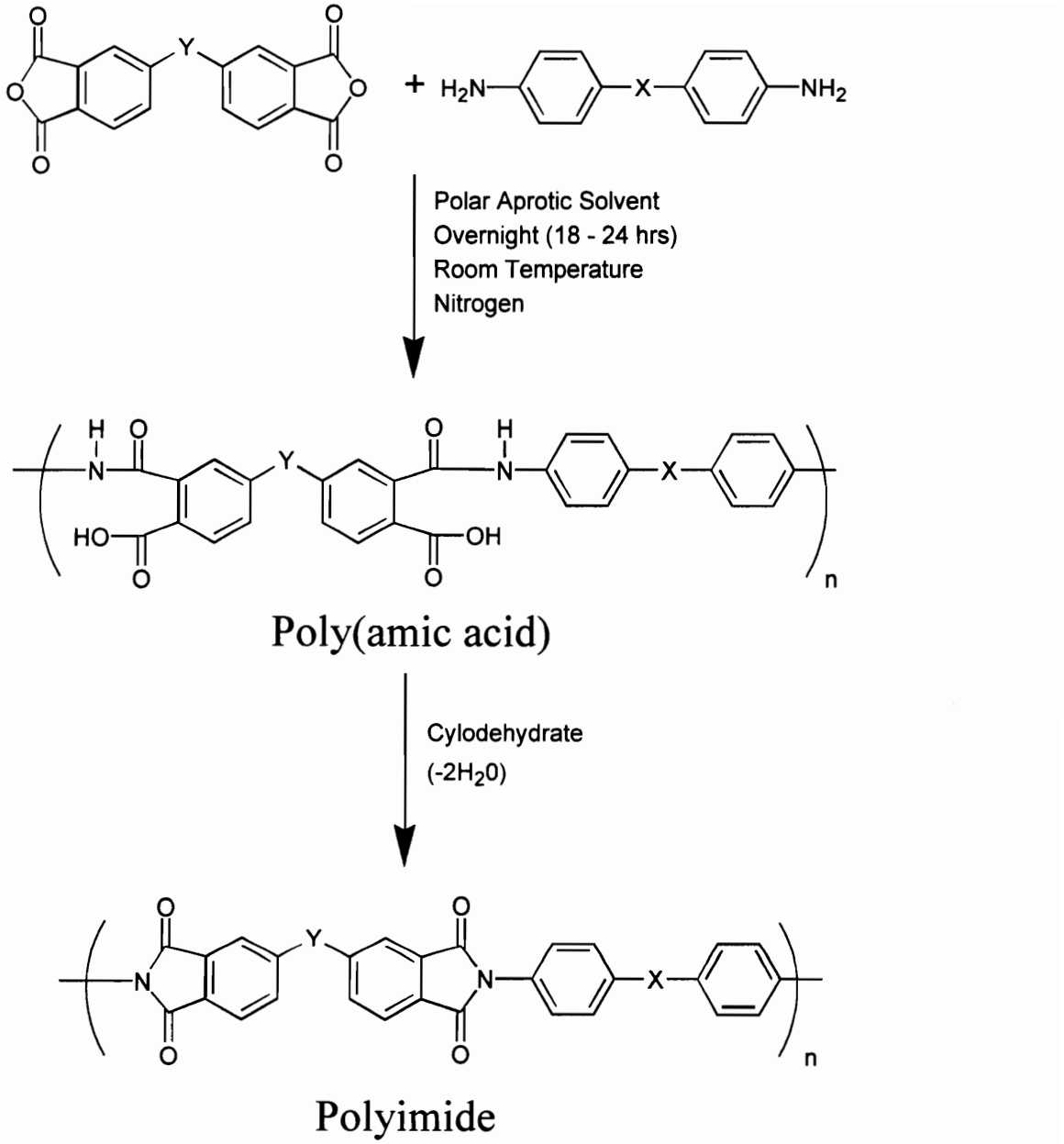

Figure 2.1 A schematic of the reaction between a diamine and dianhydride with subsequent cyclodehydration to form a polyimide.

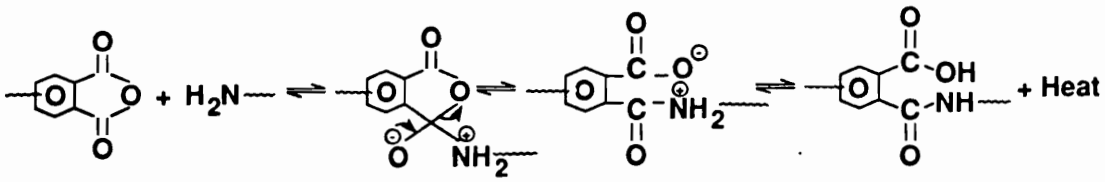

Figure 2.2 Proposed mechanism for the formation of the poly(amic acid) [9].

The importance of separating the two rate constants becomes clear when comparing reaction rates in different solvents. In particular the reaction in THF, ACN and *m*-cresol were auto-catalyzed while this was not the case in DMAc. This was explained in terms of DMAc deactivating the amide-acid group. This was illustrated by measuring the effect of the addition of external acids. Adding an equimolar amount of benzoic acid, much more acidic than the amide-acid, nearly doubled the reaction rate. However, addition of an external acid of nearly the same acidity as the amide-acid group hardly effected the rate. Thus, the relatively weak amide-acid is neutralized by the basic DMAc solvent. The other solvents (THF, ACN and *m*-cresol) do not bind with the acid group thereby allowing it to catalyze further reactions.

Other researchers have also found that the addition of external acids accelerated the reaction rate [12, 17]. It was also found that the addition of water accelerated the reaction between a dianhydride and diamine [17]. However, this was most likely the result of hydrolysis by the anhydride with subsequent catalysis from the resulting diacid. Too much of a strong acid will interfere with the completion of the reaction, however. Addition of 20% (w/w) of acetic acid, in the system studied by Solomin et al., sharply increased the reaction rate but terminated the conversion at 80% due to partial neutralization of the amine. Looking at the uncatalyzed rate constant in the Solomin system, k_1, one finds a dramatic solvent effect. The rate increases in order of solvent THF<ACN

<DMAc<*m*-cresol as 1 : 2.5 : 200 : 1,800. It is interesting to note this trend with the dielectric constants in mind: 7.4, 37.4, 36.7 and 11.8 for THF, ACN, DMAc and *m*-cresol, respectively [19]. The more than doubling of the rate in ACN over THF could be related to the increase in polarity of the solvent. The increase of an order of magnitude in the rate in DMAc does not follow a polarity trend, however. The authors do not offer any explanation of the rate differences observed between THF, ACN and DMAc. One might speculate that the DMAc is more efficient at lowering the energy of the intermediate charge-transfer complex shown in Fig. 2.2. The authors attribute the exceptionally high rate in *m*-cresol to the inherent acidic nature of the phenolic group which acts to catalyze the reaction. The exact mechanism for the acid catalysis was not offered. Presumably the acidic group complexes with the oxygen to activate (make more positive) the carboxyl carbon for nucleophilic attack by the amine.

Some researchers have argued that there is no catalytic effect offered by carboxylic acids in the formation of poly(amic acid)s [20]. However, these authors based their conclusion on a single data point measuring inherent viscosity taken after two hours of polymerization at 60°C. It is entirely plausible that any differences in the rate of poly(amic acid) formation are noticeable only at much shorter times.

An interesting view of the effect of the *m*-cresol on the reaction between amines and anhydrides is provided by a study by Dror and Levy [21]. These

researchers studied the reaction of 1,5-cyclooctadiene-1,2,5,6-tetracarboxylic dianhydride (CODA) with various diamines. Because of the tremendous ring strain, poly(amic acid) intermediates could not be isolated. The reaction proceeded immediately from monomers to polyimide. Of particular interest is the fact that polymers could not be produced in the standard polar aprotic solvents DMAc, N,N-dimethyl formamide (DMF) nor DMSO. However, the reaction proceeded well in *m*-cresol. Applying the knowledge discussed thus far, one could postulate that the thermodynamically stabilizing effects offered by the polar aprotic solvents is of no value in this system since the poly(amic acid) 'intermediate' is simply a high energy meta-state. Also, the kinetic enhancing effects of the polar aprotic solvents were not of sufficient magnitude to drive this system to completion. Significantly, the reaction occurred well in *m*-cresol. Thus, one might speculate that the overwhelming catalytic effect of the acidic *m*-cresol was sufficient to allow the reaction to proceed through the high energy poly(amic acid) meta-state. It should be noted that the authors stated that the reaction was possible in tetrachloroethane, as well. No experimental evidence nor procedures were offered, however. It should also be noted that an equimolar amount of quinoline (a cyclic aromatic amine) was introduced into the *m*-cresol reaction mixture. No reason was given for the use of this additive. Other researchers have also used quinoline as an additive when synthesizing polyimides in *m*-cresol [22]. Likewise, no reason was provided for the addition of this substance.

As with any step-growth polymerization, certain criteria must be met in order to achieve a high molecular weight polymer: a very high monomer and solvent purity (~99.9%), 1:1 stoichiometric ratio of the difunctional monomers, very high conversion (>99%) with minimal side reactions and end group accessibility. With regard to poly(amic acid) synthesis, impurities lead to two important side reactions: 1) Water can react with the dianhydride before polymerization forming carboxylic acids [23 - 25]. This results in an upset in the stoichiometric ratio with consequent lowering of the product molecular weight. 2) Monofunctional amines, often present in amide solvents, will compete with the difunctional amine monomer resulting in the presence of unreactive chain ends and, thus, a lower molecular weight product [9, 26].

Like any step-growth polymer, control of the molecular weight of the poly(amic acid) is affected through the stoichiometric offset of the monomers as described in the Carothers relationship [27]. As described in standard polymer textbooks [28 - 30], the number average degree of polymerization, $<X_n>$, in step-growth polymers is calculated by

$$<X_n> = \frac{1 + r}{1 - r} \qquad (2-2)$$

where r is the stoichiometric offset [ratio] of the quantity of monomers N_A to N_B:

$$r = \frac{N_A}{N_B} \qquad (2-3)$$

Monomer **A** is taken as the limiting reagent so that the stoichiometric offset is always equal to, or less than 1. It should be noted that the calculation of $<X_n>$ in this manner assumes full functional group conversion of the monomers. This reinforces the importance of accurately weighed pure monomers in an non-contaminated reaction medium. As written, Eqn. (**2–2**) is accurate only for **A–B** monomer systems, where **A** and **B** are reactive ends of a monomer which react with their opposite only. In order to account for an **A–A** + **B–B** system, as in the case of the dianhydride + diamine reaction, one must take half of the quantity calculated in Eqn. (**2–2**). Since polyimides with free amine or anhydride endgroups can undergo chain extension or branching/cross-linking during processing at elevated temperatures, endgroup control is important. Reactive chain ends in stoichiometric offset polyimides are capped by adding stoichiometric quantities of monomeric species, such as aniline or phthalic anhydride, to the reaction mixture. McGrath et al. have shown that endgroup control techniques can be employed to overcome the problems associated with residual reactive endgroups without sacrificing the desirable characteristics of aromatic polyimides [31 - 35].

Early researchers found that the sequence of the monomer addition during poly(amic acid) synthesis has an effect on the achieved molecular weight. Higher molecular weight poly(amic acid)s were obtained when dianhydrides were added to solutions of diamines [36, 23]. In a more recent study researchers found that

the addition sequence did not have an effect [37]. The latter authors suggested that the differences were the result of rigorous exclusion of moisture from the system. From a practical standpoint it is entirely conceivable that moisture could become introduced into a solution of [probably stirring] dianhydride while the chemist weighs and prepares the diamine for addition to the reaction flask.

Poly(amic acid) solutions have been shown to be quite unstable. After initial polymerization of the monomers to reach high molecular weight, solutions of poly(amic acid) display a considerable drop in molecular weight with time [23 - 25, 36]. A rapid early drop in molecular weight has been shown to be the result of hydrolysis of adventitious water [24]. Further decreases in molecular weight is the result of hydrolysis of the amide links from the water produced by cyclization/imidization of amic acid groups. Since the carboxylic acid 'by-product' remains attached to the reaction product to form the poly(amic acid), the reverse reaction is unimolecular, while the forward reaction is bimolecular. Thus, the loss in molecular weight over time is much more severe in dilute than in concentrated solutions [25]. This effect is dramatically shown in Fig. 2.3. Here the inherent viscosity of a 10% and 0.5% solution, held at 23°C, is plotted as a function of time to ca. 30 days. The exponential decay in inherent viscosity of the dilute solution is sharply contrasted with the modest lowering of molecular weight in the more concentrated solution.

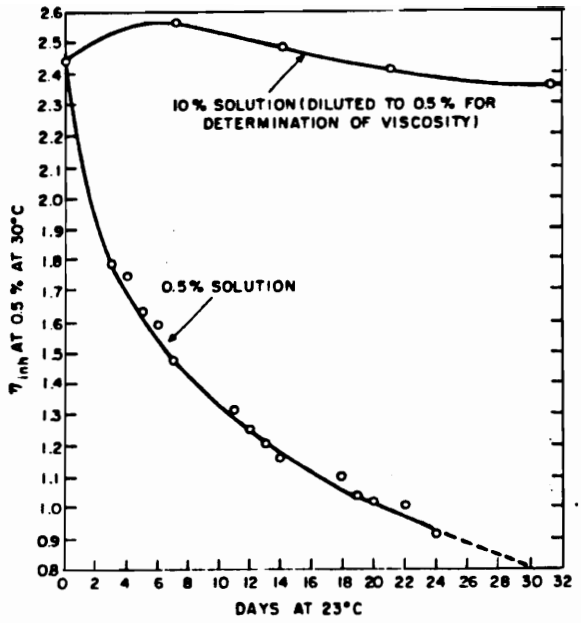

Figure 2.3 The inherent viscosity of a 10% and 0.5% poly(amic acid) solution held at 23°C as a function of time [25].

A wide variety of dianhydride and diamine monomers are used in the formation of poly(amic acid)s. The ultimate properties of the material are strongly dependent upon the structural features of these monomer units. A discussion of structure-property relationships is presented in section **2.2.2**. A listing of the wide variety of common diamine and dianhydride monomers used in poly(amic acid)/polyimide synthesis, along with common solvents, can be found in the many books and reviews on polyimides [1 - 8]. The conversion of the poly(amic acid) to the polyimide can be accomplished via a thermal bulk or solution process, or chemically. Each case will be discussed individually.

2.2.1.2 Thermal [bulk] Imidization

Bulk thermal imidization is the most common method for converting the poly(amic acid) to the polyimide. When making films, spun fibers and coatings they are cast from the poly(amic acid) solution with subsequent solvent removal via moderate temperature drying or by extraction under vacuum. The poly(amic acid) is then heated through stages to about 300°C to complete imidization. In systems employing amide solvents the "dried" poly(amic acid) still contains quite a high proportion of solvent firmly retained in the polymer. This is a result of the tightly bound hydrogen-bonded associations with the carboxyl groups which have been well catalogued [13 - 16, 23, 38 - 40]. In fact, the kinetics of the cyclization reaction (imidization) are profoundly affected by the strength of the hydrogen-

bonded complexes [16, 40, 41]. In order to allow for easier solvent removal during thermal imidization, one group of researchers purposely sought a non-amide solvent system [42]. These researchers used a THF/methanol mixture which was easily removed from the films during imidization. The effect was a 'drier' film which was not plasticized during final processing. Feger et al. [13 - 15] showed that the complex formed between a poly(amic acid) and an NMP solvent medium interfered with imidization until decomplexation occurred at higher temperatures (ca 350°C), at which point the newly freed NMP acts as a plasticizer and facilitates imidization.

During the thermal imidization treatment several transformation reactions are possible. The *o*-carboxycarboxamide group may cyclize to form the imide or isoimide structure as shown in Fig. 2.4. The presence of isoimide moieties is barely detectable in thermally imidized polyimides. It is thought that isoimides are formed in this process but are rapidly rearranged to imides at elevated temperatures [9]. As seen in Fig. 2.4 the *o*-carboxycarboxamide group may also cyclize *intra*molecularly to regenerate the anhydride. This, of course, is a de-polymerization reaction which lowers the molecular weight of the polymer. This can be followed via Fourier Transform Infrared (FTIR) spectroscopy by monitoring the presence of an anhydride peak at ca. 1850 to 1860 cm^{-1}. This peak first appears in the 50°C to 100°C range and reaches a maximum in the 175°C to 225°C range. The anhydride band decreases and disappears in the 250°C

to 300°C range [39, 43, 44]. This can be seen graphically in Fig. 2.5 [43]. Here the height of the anhydride peak is plotted as a function of temperature for two poly(amic acid)s: $PISO_2$ [poly(amic acid) from BTDA and 3,3'-diaminodiphenylsulphone] and PMDA-ODA (pyromellitic dianhydride-oxydianiline). The amount of the anhydride formed during thermal imidization is a function of the molecular architecture of the poly(amic acid). It has been reported that in stiff chain polymers degradation may be as high as 10% whereas more flexible polymers degrade to only about 2% [39]. As would be expected, the emergence and eventual disappearance of the anhydride band in FTIR correlates well with observed molecular weight changes during imidization. In a model study of a soluble polyimide Young et al. documented changes in molecular weight during thermal imidization [44]. As seen in Fig. 2.6, both M_n and M_w drop dramatically in the 50°C to 125°C range and then increase near the end of the thermal treatment at temperatures exceeding 250°C.

Early qualitative physical observations of the flexibility in polyimide films by Dine-Hart and Wright provided useful insight into the effect of changes in molecular weight on mechanical properties during thermal imidization [36]. They determined that the magnitude of the changes in film flexibility was very much dependent upon the initial molecular weight of the poly(amic acid) as seen in Fig. 2.7. Films prepared from low molecular weight poly(amic acid)s (inherent viscosities less than 0.2) were brittle throughout the thermal treatment. Films

prepared from high molecular weight poly(amic acid)s (inherent viscosities greater than 1.0) became creasable at the intermediate stage of ca. 100°C and remained so throughout the thermal treatment. Interestingly, intermediate molecular weight poly(amic acid)s (inherent viscosities in the 0.2 to 1.0 range) provided films which underwent dramatic changes in mechanical properties during thermal imidization. Flexibility increased to become creasable at intermediate stage of ca. 100°C and then dropped precipitously to become brittle in the 150°C to 200°C range. Thereafter the flexibility increased until it became creasable in the final stages of thermal treatment.

In another study measuring the effects of imidization temperature on the mechanical properties of polyimide film, researchers found that a full thermal treatment to 350°C was necessary to maximize tensile strength and elongation properties [45]. They found, qualitatively through FTIR analysis, that the imidization process reached a maximum at 200°C with very little change afterwards. However, the mechanical properties continue to improve as the imidization temperature is increased to 350°C. The authors argue that solvent loss and efficient molecular packing are the key factors affecting the mechanical properties. One might argue that, without a clear accounting of the exact level of imidization, it is difficult to identify precisely the relationship between imidization temperature and mechanical properties in their particular system.

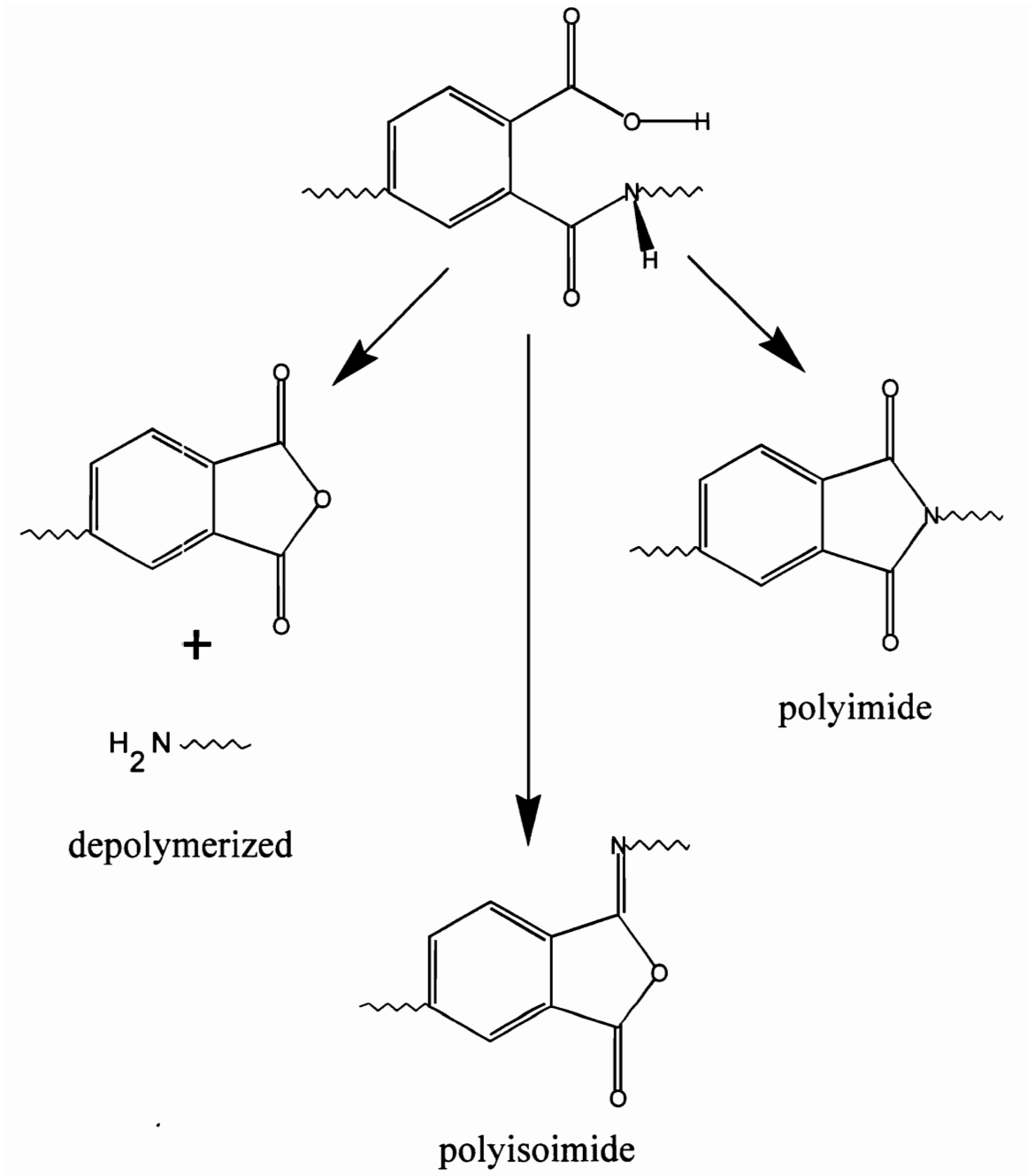

Figure 2.4 The *o*-carboxycarboxamide group may cyclize to form the imide or isoimide structure.

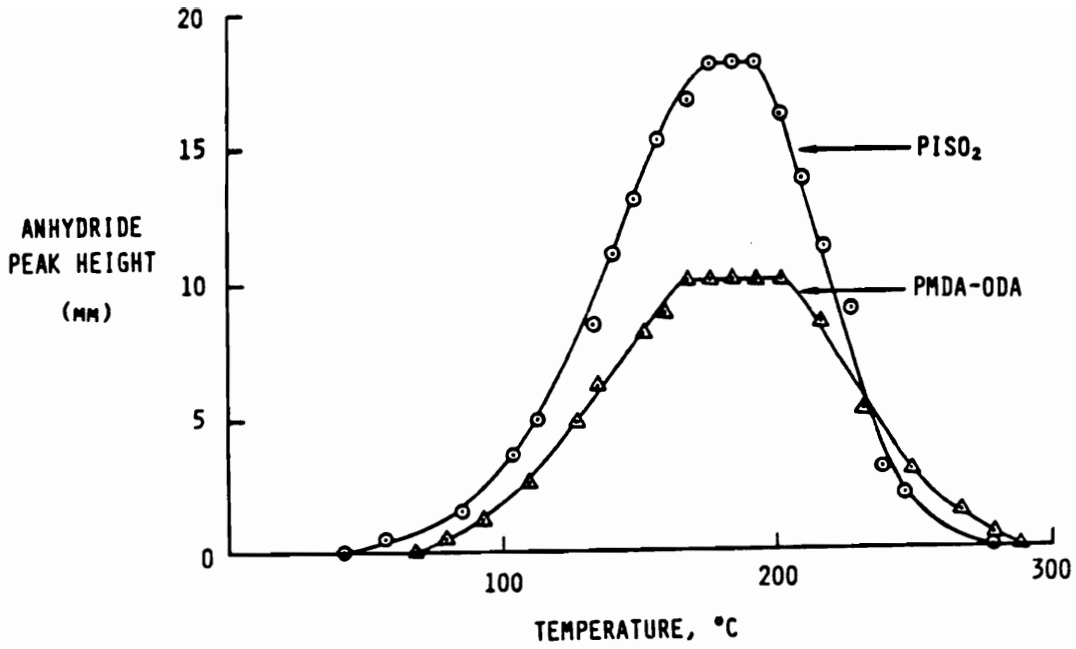

Figure 2.5 Anhydride peak height from FTIR spectroscopy plotted as a function of temperature for two poly(amic acid)s: $PISO_2$ [poly(amic acid] from BTDA and 3,3'-diaminodiphenylsulphone] and PMDA-ODA (pyromellitic dianhydride-oxydianiline) [43].

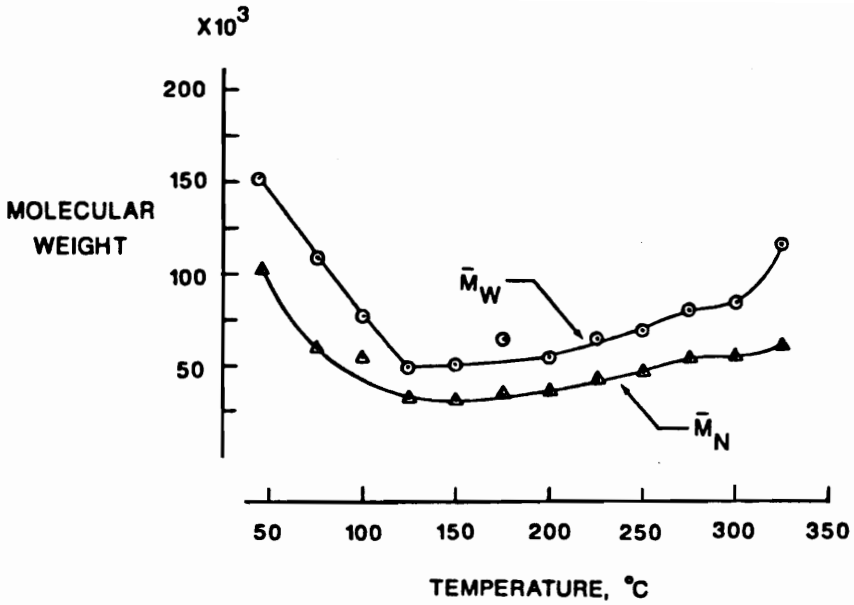

Figure 2.6 Molecular weight, M_n and M_w, of thermally staged films [44].

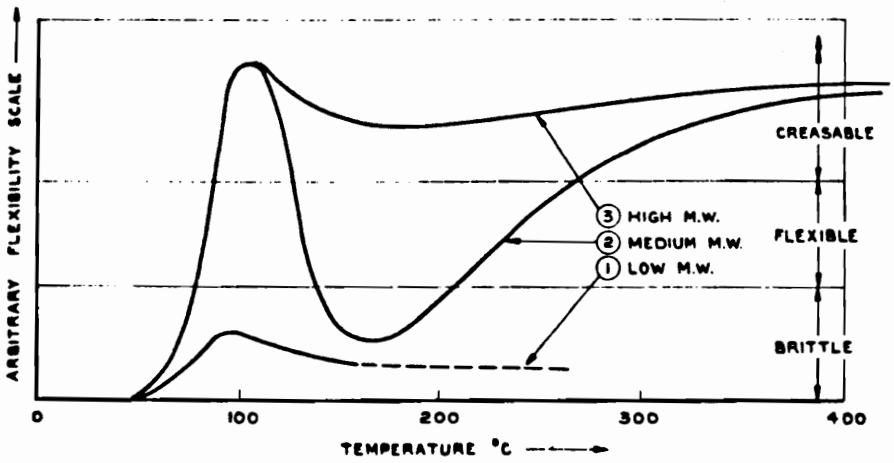

Figure 2.7 Effect of molecular weight on film flexibility as a function of process temperature [36].

A typical thermal treatment cycle for the imidization of a poly(amic acid) is a stepwise heating for 1 hour each at 100°C, 200°C and 300°C. This stepwise thermal imidization cycle was originally developed by researchers at NASA [46]. Though the exact reasoning for this particular process has never been established, it has been adopted by many others in the production of a variety of polyimide films [47 - 51].

In general, the early stages of imidization are characterized by a molecular weight decreases as a result of hydrolysis with a subsequent increase in molecular weight as amine and anhydride end groups recombine with further heating. However, steric effects may prevent the full reaction of all the hydrolyzed end groups. This results in a net loss in molecular weight. The rate of cyclization is thought to be a function of molecular mobility. Under isothermal conditions the cyclization rate is thought to proceed in two stages [7, 9, 39, 52]. Initially, the reaction temperature is above the glass transition temperature, T_g, of the polymer. This facilitates the arrangement of the reactive species into favorable conformations for cyclization. With time the increasing 'stiffness' of polyimide/poly(amic acid) structure will result in the T_g increasing to the reaction temperature. At this point the decreased chain mobility slows the reaction dramatically as the system vitrifies. Any solvent present during cyclization will act to plasticize the system resulting in a greater degree of imidization. For example, in a study employing stepwise heating for 1 hour each at 100°C, 200°C and 300°C,

found that thin films were only imidized to 85% [53]. However, rapid heating of the films to 230°C to 250°C resulted in over 99% imidization. This was attributed to the plasticizing effect of a higher level of solvent retained in the rapidly heated films. Similarly, thicker films have been reported to imidize more rapidly due to solvent retention [54]. Initially, thin films (4.6μm) reached much higher levels of imidization than thicker ones (12.2μm and 17.3μm). However, with sufficient time (40 minutes) the imidization level converged for all films as seen in Fig. 2.8. The more rapid imidization in the thick films was attributed to increased solvent retention and, consequently, enhanced chain mobility.

Bessonov et. al. [7] argue that chain mobility alone does not account for the dramatic drop in reaction rate witnessed experimentally. They propose that there exists a kinetic non-equivalence in the amic acid moieties as a result of the long chains attached to them: Some of the units are always in favorable conformations for chemical interaction of the amide and acid groups, while the rest are not. Once the fragments with favorable conformations have been used up, the cyclization rate will decrease since profound rearrangements in the structure of the rest of the fragments are necessary for the functional groups to draw together. Experimental support is provided by their experiment in which poly(amic acid)s of varying molecular weights (monomer, oligomers, & polymer) were imidized at temperatures ranging form 140° to 180°C in a glassy polyimide matrix with a T_g of 200°C. The samples were prepared from mixed solutions of

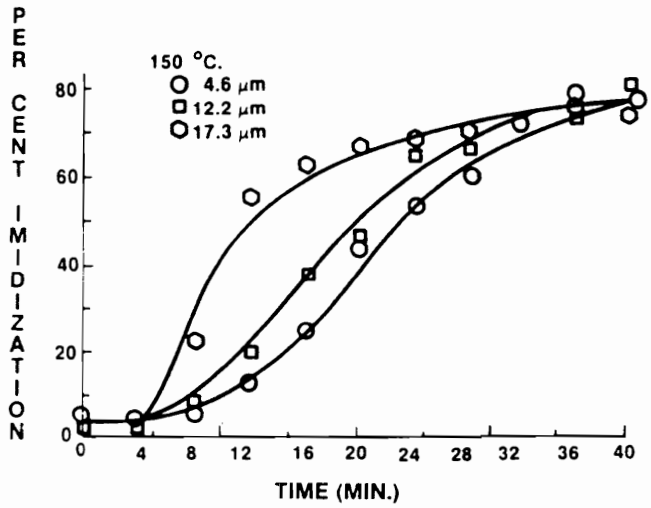

Figure 2.8 Percent imidization as a function of time for films of differing thicknesses [54].

these polymers in DMF. In each case, excepting the monomeric amic-acid, the cyclization reaction shows a distinct cessation of reaction, paralleling closely a standard condition imidization process. The monomeric species showed no change in cyclization rate. The concept here is that even though the long chain structures are held in a glassy state they were still able to react to the same point that they would have in the normal bulk process. This indicates that the change in rate is not solely a vitrification-like phenomena. As further evidence, Bessonov et. al., imidized a film to the point where the cyclization rate slowed down, then solvated it in DMF and recast the film. Though all the conditions were the same, degree of cyclization (confirmed via FTIR), solvent content in the film and temperature (molecular mobility), the cyclization rate increased sharply. As will be discussed in section **2.2.1.3**, more recent research has shown that the apparent two-stage imidization process is actually a manifestation of the true second order (auto-acid-catalyzed) reaction kinetics [55].

2.2.1.3 Solution Imidization

The solution imidization technique is designed for the production of soluble polyimides [31, 32, 34, 55 - 58]. The factors associated with cessation of imidization in the bulk process, such as vitrification, are not present if the poly(amic acid) is in solution. Thus, quantitative imidization in solution is possible at lower temperatures. Full imidization can be achieved in the

temperature range of 150°C to 180°C. This process employs the use of an azeotrope, such as o-dichlorobenzene or N-cyclohexyl pyrrolidone, to remove water from the system as imidization proceeds. An example of this process is the imidization of poly(imide siloxane) segmented copolymers utilizing a solvent/azeotroping system of N-methylpyrrolidinone (NMP) and cyclohexylpyrrolidinone (CHP) at ca. 165°C. CHP serves as the azeotrope for the water condensate [31, 56 - 58]. Polymers produced in this manner have been shown to be more soluble and processable than those produced via the traditional bulk thermal process. The reasons for this most probably involve the lack of side reactions in this process as seen in bulk thermal imidization.

It is also possible to perform the polymerization and imidization process via a one-step method [21, 22, 59, 60]. Here the dianhydride-diamine monomer/solvent mixture is immediately heated to temperatures in excess of 180°C. In 1970 Vinogradova et al. [59] showed that this process could be successfully employed for a variety of solvents including nitrobenzene, NMP and tricresol (a mixture of cresols in which *m*-cresol is the primary component). More recently Takekoshi et al. [60] produced forty-six different polyetherimides via the one-step method in *m*-cresol using toluene as an azeotrope. As discussed in section **2.2.1.1**, Dror and Levy synthesized the CODA dianhydride based polyimide in *m*-cresol [21]. Here the researchers used the much lower temperature of 110°C and no azeotrope was used. As noted before they also used

quinoline as an additive without explanation. Likewise the one-step method for polyimides synthesized in *m*-cresol as described by Feld, Ramalingham and Harris uses isoquinoline as an additive without explanation [22]. These researchers used toluene as an azeotrope at a 175°C reaction temperature.

In a recent study of the solution imidization process by Kim et al. it was clearly shown that imidization follows a second-order auto-catalyzed rate law [55]. Of particular significance was that the data that deviated from first-order kinetics at high conversions was well fit by a second order auto catalyzed rate law. As discussed in section **2.2.1.2**, previous researchers have attributed the two-step kinetic features noted in the solid-state (films) imidization process to decreased molecular mobility [52], kinetic non-equivalence [7] and solvent effects [13, 38, 54]. Similar to the case for the formation of the amic acid, the auto-catalysis here is attributed to the acid functionality present in the amic acid group. These researchers have proposed a mechanism for the auto-catalytic effect, as seen in Fig. 2.9. Notably, these researchers also found that the addition of *p*-toluenesulfonic acid catalyzed the imidization.

2.2.1.4 Chemical Imidization

Chemical imidization of poly(amic acid) employs the use of a tertiary amine and an aliphatic dianhydride, typically triethylamine and acetic anhydride, respectively. Essentially, the OH group on the carboxylic acid is replaced with an

acetate group, forming an anhydride. The acetate functionality, being a much better leaving group, facilitates nucleophilic attack of the anhydride carbonyl carbon by either the amide amine or oxygen to form the imide or isoimide, respectively. It is important to note that the mechanism involves the formation of the carboxylic acid salt. This prevents the reverse reaction and subsequent lowering of molecular weight as seen in bulk thermal imidization. This process is used industrially in the preparation of molding powders. The process is not used extensively however, because of the reagents involved [7, 9].

2.2.1.5 Ester-Acid Route to Polyimides

Polyimides may also be synthesized via an ester-acid route [61]. Here diester-diacid derivatives of aromatic tetracarboxylic dianhydrides are reacted with aromatic diamines in solution. High molecular weight polyimides are achieved within 8 to 10 hours at 180°C. One particularly important feature of this route is the insensitivity of the diacid-diester monomers to moisture, in contrast to their dianhydride counterparts.

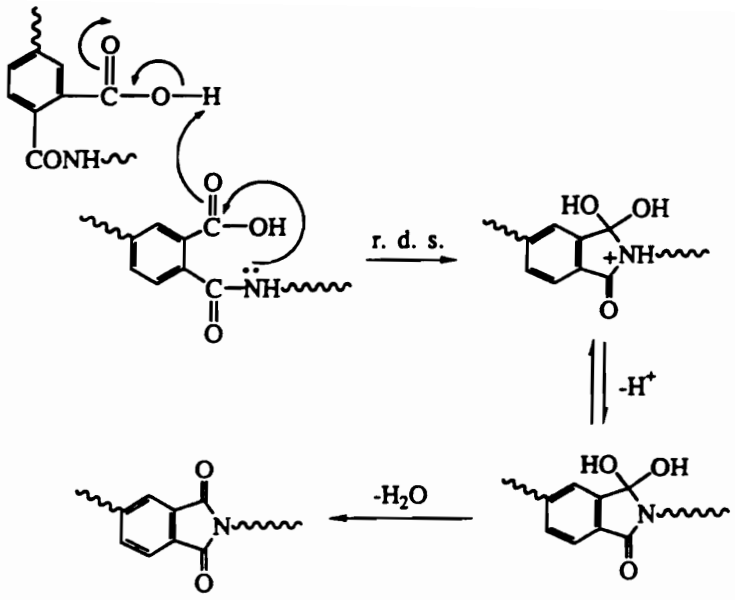

Figure 2.9 Proposed mechanism for the auto-acid-catalysis during imidization of poly(amic acid)s [55].

2.2.1.6 Transimidization Route

This method involves reacting a nucleophilic diamine, such as ODA, with a di-imide wherein the imide nitrogen is attached to an electron withdrawing group, e.g., N,N'-Bis(ethoxycarbonyl)pyromellitimide [62, 63]. The exchange reaction occurs over several days and it is necessary to heat the system to 240°C to complete the reaction. The carbamide by-product is removed under vacuum.

2.2.1.7 Aromatic Nucleophilic Displacement Polymerization

Soviet researchers discovered that the introduction of flexible linkages into the backbone of polyimides reduced the glass transition temperature without sacrificing thermal stability [5]. Practical synthesis of these materials was first achieved by researchers at General Electric via an aromatic nitro-displacement reaction [1, 5]. This introduced the polyetherimide class of materials, of which Ultem from General Electric is the most important commercial example. The synthesis of this class of polyimides is based on the condensation polymerization of the salts of bisphenols and dinitrobisimides. The reaction occurs via a nucleophilic aromatic substitution forming an aromatic ether linkage. High molecular weight is reached in these polymers without the need for a catalyst. The dinitrobisimides are very sensitive to hydrolysis and will form nitroamic salts which are unreactive toward nucleophilic aromatic substitution.

2.2.1.8 Addition Polyimides

As the title implies, addition polyimides are produced via an addition polymerization process. Though many variations are possible the most important subclass of this imides are the bismaleimides. The imide monomers are prepared by the condensation reaction between an aromatic diamine and maleic anhydride [64]. The resulting bifunctional addition monomer can then be reacted to form a cross-linked network. These polymers are intermediate between epoxies and standard aromatic polyimides in their use-temperature range. The primary attraction to these polymers is that they process under epoxy-like conditions without the evolution of gaseous by-products.

2.2.2 Structure-Property Relationships

As with most polymers, the glass transition temperature is very dependent upon the microstructure of the polyimide chain. Similarly, it can be generally stated that introducing flexible linkages into the backbone act to lower the T_g by allowing greater degrees of freedom. However, there are other factors involved with polyimides that are not immediately obvious. It has been found that the introduction of flexible linkages into the dianhydride portion of the polyimide is more effective at reducing T_g than introducing the same group into the diamine portion of the polymer. This is explained in terms of interchain charge transfer complexes (CTC). These CTCs are the result of the high electron affinities of the

dianhydride functionalities [65 - 67]. Pyromellitic dianhydride (PMDA) has the highest electron affinity, E_A, of all the dianhydride monomers at 1.9ev. Fryd states that the introduction of a flexible linkage 'into' this monomer with any substituent, regardless of its electron donating or withdrawing properties, will separate the strongly electron withdrawing anhydride moieties and thereby lower the E_A of the anhydride group [65]. For example, 'introduction' of the electron withdrawing carbonyl group results in a lowering of the E_A to 1.55ev in BTDA. Gathering T_g data from another source [66] one can see that the effect on T_g seems to mirror the lowering of the E_A as implied by Fryd-- see Table 2–1. In each case the BTDA-based polyimide has a lower T_g.

In general the T_g decreases as the substitution becomes more *meta* from *para* in aromatic polyimides. It is argued that this is the result of an increase in backbone flexibility [66]. However, as can be seen in Fig. 2.10, this 'trend' is not continued in the case of *ortho* substituted diamine. The *ortho* linkages in the DABP lead to strong dipolar unit as the imide and carbonyl groups are in close proximity [66]. Presumably, this has a similar effect on T_g as argued by Fryd [65].

Highly polar bridging groups in the diamine monomer act to increase the T_g, as well. In a series of polyimides where the bridging group was varied the trend can be seen that the T_g increases in order of increasing polarity of the bridging groups -- see Table 2–2 [66].

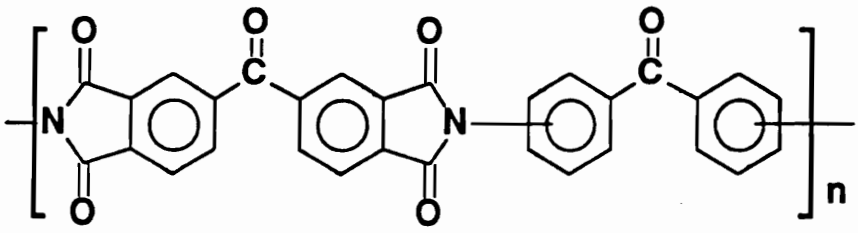

Amine attachment	T_g, °C*
2,2′	289
2,3′	259
2,4′	289
3,3′	264
3,4′	282
4,4′	293

Figure 2.10 Effect of isomeric attachment in diaminobenzophenone on the glass transition temperature [66].

Table 2.1. Comparison of glass transition temperatures between PMDA- and BTDA-based polyimides.

Diamine	PMDA-based T_g (°C)	BTDA-based T_g (°C)
APB	221	202
BDAF	305	249
$DDSO_2$	338	273

PMDA: Pyromellitic dianhydride [E_A = 1.9ev]
BTDA: 3,3',4,4'-benzophenone tetracarboxylic acid dianhydride [E_A = 1.55ev]
APB: 1,3-bis(3-aminophenoxy)benzene
BDAF: 2,2'-bis[(4-aminophenoxy)phenyl]hexafluoropropane
$DDSO_2$: 3,3'-diaminodiphenylsulfone

Table 2.2. Effect of bridging groups on glass transition temperature in BTDA-derived polyimides [66].

Diamine	Glass Transition Temperature, °C
3,3'-methylenedianiline	234
3,3'-oxydianiline	236
3,3'-diaminobenzophenone	255
3,3'-diaminodiphenylsulphone	273

The tendency for polyimides to be semicrystalline is also very much a function of the molecular architecture. For example, in aryl ether ketone containing polyimides, a greater proportion of ketone groups enhances the crystallizability of the polymer [49]. The polyimide from ODPA/1,3-BABB (oxydiphthalic dianhydride/1,3-bis(4-aminophenoxy-4'-benzoyl)benzene) is completely amorphous. However, the substitution of a ketone group for the ether in the dianhydride gives a BTDA/1,3-BABB (3,3',4,4'-benzophenone tetracarboxylic acid dianhydride/1,3-bis(4-aminophenoxy-4'-benzoyl)benzene) polyimide which is semicrystalline and has a melting transition of 350°C. The BTDA/1,3-BABB polyimide has many attractive properties and it is known as LaRC CPI. This polyimide has been thoroughly investigated for its solvent resistant, mechanical, adhesive and crystallization properties [49, 50, 68 - 75]. The presence of crystallinity in polyimides has been shown to provide better mechanical properties [50]. Adhesive specimens of LaRC CPI (T_g = 222°C; T_m = 350°C) annealed to possess a higher level of crystallinity (316°C for 100 hours) displayed much better mechanical properties than their non-annealed counterparts at a test temperature of 232°C. Tensile strength values increased from 4.8ksi to 8.4ksi and tensile shear values increased from 1,840psi to 3,670psi. In addition to mechanical properties it is also generally known that crystallinity enhances solvent resistance. For example, in a comparison of a series of aryl ether ketone polyimides, Hergenrother et al. found that amorphous films failed [solvated]

almost immediately upon exposure to methylene chloride or DMAc whereas semicrystalline films were unaffected [49].

Upon reviewing the literature it becomes apparent that a great many linear aromatic polyimides are insoluble, even in the most aggressive solvent systems such as *m*-cresol or *o*-chlorophenol at 150°C. The strong CTCs have been cited as the reason for poor solubility [65, 67]. As noted before, the presence of crystallinity imparts a great deal of solvent resistance and may be the cause of the insolubility in some polyimides. It has been proposed that the general insolubility of polyimides is due to cross-linking [76, 77]. Hergenrother et al. found that polyimides from ketone bearing dianhydrides formed gels during polymerization of the poly(amic acid)s [50]. The gels dissipated overnight with stirring. These authors speculated that an imine may have formed between the ketone and amine groups initially. As water was liberated from the cyclization of some of the amic acid groups it may have then hydrolyzed the imine groups. However, ^{13}C–NMR found no imine functional groups in the gel. A recent study by Kim et al. [55] clearly showed that imine links formed during solution imidization of BTDA-based polyimides. Through deductive reasoning they assigned ^{1}H NMR peaks at 6.8 and 7.1 ppm to the ketimine containing aromatic protons. The gels formed in solution were easily hydrolyzed by the addition of a small amount of aqueous hydrochloric acid. These authors made the logical prediction that all ketone containing polyimides based on condensation reactions with diamines are at risk

of forming the imine branches/cross-links.

The thermo-oxidative stability in polyimides is a function of the oxidation state of the functional groups along the backbone [66]. That is, the higher the oxidation state of the functional groups in the polyimide the higher the thermo-oxidative stability of the polyimide. Thus, in order of decreasing stability one should find for common diamines: biphenyl> benzophenone> *p*- or *m*-phenylene> diphenyl ether> diphenylmethane.

2.3 Polymer Crystallization

2.3.1 Thermodynamics of Crystal Nucleation and Growth

Crystallization of polymer chains from the molten state begins with the formation of a crystalline nucleus. If there are no foreign particles or pre-existing nuclei are involved, then the process proceeds via homogenous nucleation and is explainable in terms of fundamental thermodynamic quantities. Specifically, crystal growth occurs when the Gibbs free energy of formation, ΔG, is less than zero. The Gibbs free energy for a crystal is the sum of the crystal surface free energies and the bulk free energy. This is expressed in Eqn. **2–4**,

$$\Delta G = \Delta G_c + \sum A\gamma \qquad \textbf{(2–4)}$$

where ΔG_c is the bulk free energy change upon crystallization, γ is the surface free energy, and A is the corresponding surface area. The summation covers all

surfaces typically having a different specific surface free energy affiliated with them.

Since the surface energies of a crystal are positive there is an initial energy barrier that must be overcome in order to form a crystal structure. As seen in Fig. 2.11 [78], the free energy increases from the initial embryo state. Below the 'critical nucleus' size the surface energies are greater than the bulk free energy of change. At the size corresponding to the 'critical nucleus' the bulk free energy begins to dominate and further growth lowers the free energy of the system. In order to overcome the initial positive ΔG barrier local random fluctuations of order are required [78, 79]. This process of forming an initially unstable nucleus is known as primary nucleation.

The general expression for the steady-state nucleation rate, $\dot{N}$, of any substance, regardless of its geometry, was developed by Fisher and Turnbull in 1949 for small molecules [78 - 83]. This is given as Eqn. **2–5**:

$$\dot{N} = N_0 \exp\left(-\frac{E_D}{RT}\right) \exp\left(-\frac{\Delta G^*}{RT}\right) \qquad (2-5)$$

where E_D is the activation energy for molecular chain transport across the liquid-nucleus interface, ΔG^* is the critical free energy of formation of the nucleus of critical size, N_0 is a pre-exponential factor, R is the universal gas constant, and T is absolute temperature.

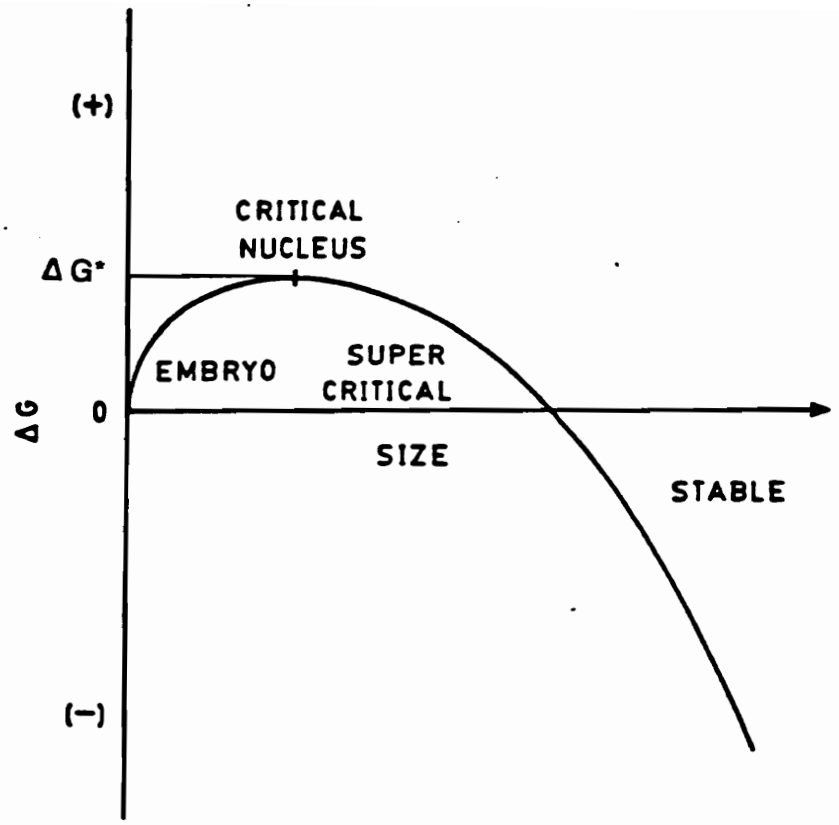

Figure 2.11 Schematic illustration the change in bulk free energy, ΔG, as a function of size for primary nucleation [78].

The earliest attempts to devise a model for polymeric crystal growth were based upon the work of Fisher and Turnbull. The general shape of the growth rate curve is shown schematically as a function of crystallization temperature in Fig. 2.12. The general equation for growth rate, G, at given temperature, T, is shown below in Eqn. **2–6**:

$$G = G_0 \exp\left(-\frac{E_D}{RT}\right)\exp\left(-\frac{\Delta G^*}{RT}\right) \qquad \textbf{(2–6)}$$

where G_0 is a pre-exponential factor and the other parameters are as defined earlier. As was the case for the nucleation rate equation, no specific growth geometry is assumed for the present equation. At low undercoolings, the overall growth process is controlled by nucleation while diffusion effects occur at high undercooling [84, 85].

In order to explain the melting behavior of polymers it is necessary to understand the thermodynamic relationship between the crystalline superstucture and the melting temperature. Figure 2.13 shows a schematic diagram of a single chain-folded lamellar crystal. The Gibbs free energy of formation for this crystalline superstructure is described by [83]:

$$\Delta G = 4x\ell\sigma + 2x^2\sigma_e - x^2\ell(\Delta f) \qquad \textbf{(2–7)}$$

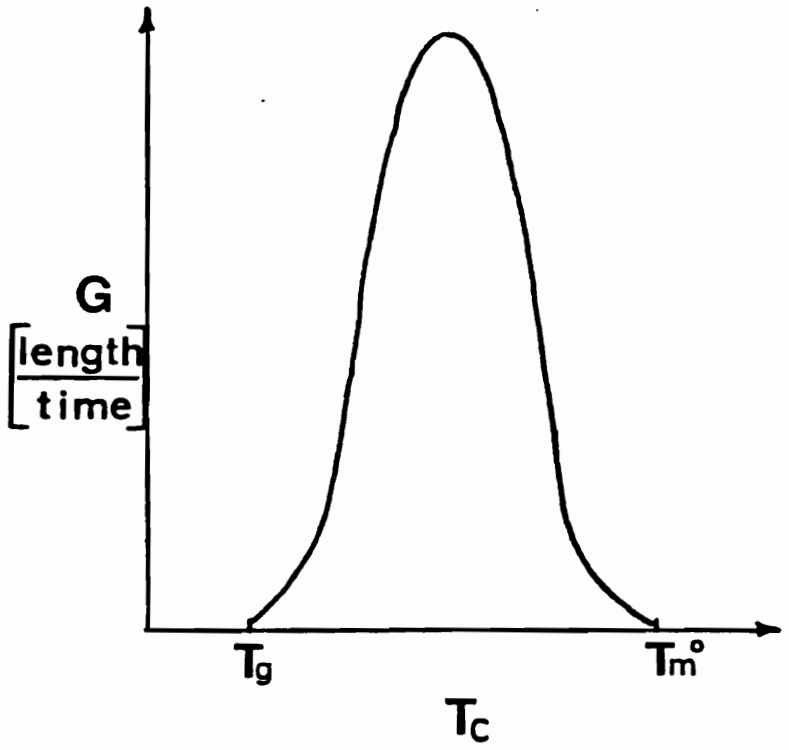

Figure 2.12 A general schematic of the growth rate, G, as a function of crystallization temperature.

where ΔG is the free energy of formation of the crystal, σ is the lateral surface free energy, σ_e is the fold surface free energy, x is the lateral dimension, ℓ is the thickness and Δf is the bulk free energy of fusion. Assuming that the heat of fusion is independent of temperature, (valid near the melting point), Δf becomes:

$$\Delta f = \Delta h_f \left(\frac{\Delta T}{T_m^0} \right) k \qquad \textbf{(2–8)}$$

where Δh_f is the heat of fusion per volume of crystal, ΔT equals supercooling defined as (T_m^o-T) , T_m^o equals the equilibrium melting point and k is a correction factor which accounts for the temperature dependence of Δf away from T_m^o [83, 86]. Substituting Eqn. 2–8 into Eqn. 2–7 and noting that at the melting point of a crystal ΔG = 0, an expression is revealed relating the observed melting point, T_m, to fundamental thermodynamic quantities:

$$T_m = T_m^o \left(1 - \frac{2\sigma_e}{(\Delta h_f)\ell} \right) \qquad \textbf{(2–9)}$$

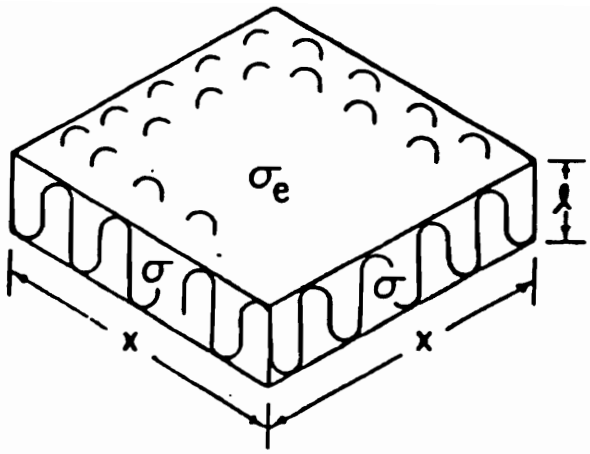

Figure 2.13 A schematic diagram of a single chain-folded lamellar crystal where σ is the lateral surface free energy, σ_e is the fold surface free energy, x is the lateral dimension and ℓ is the thickness [83].

A key approximation in the development of this relationship, known as the Gibbs-Thomson equation, is that the lateral dimension of a lamellar crystal is very much larger than the thickness dimension, which is indeed the case for polymer lamellar crystals [87]. It can be seen from this relationship that the observed melting point approaches the thermodynamic value as the thickness of the crystal increases. Of course, in the limit of infinite thickness $T_m = T_m^o$.

2.3.2 Avrami Isothermal Kinetics Analysis

The kinetics of an overall phase transformation such as isothermal crystallization was developed by Avrami [88 - 90]. Initially developed for metals, this work was one of the early efforts to describe the macroscopic development of crystallinity. The initial theory was developed based on the presence of pre-existing "germ" nuclei, which could either develop into active nucleation sites or be ingested by other active growing centers. It was assumed that growth occurred at an equal rate in all directions, and that a constant volume transformation took place. It was further assumed that growth ceases once impingement of growing entities occurs [88]. By relating the transformed volume to a related parameter known as the extended volume, and examining a series of limiting cases involving different probabilities of growth nuclei development and growth dimensionality, the following general equation was developed, now known as the Avrami equation:

$$X_c(t) = 1 - e^{-Kt^n} \qquad \textbf{(2-10)}$$

where X_c (t) is the transformed volume fraction, K is a parameter which is a function of temperature, t is time, and *n* is a constant. More specifically, K is a bulk rate constant consisting of both nucleation and growth terms as seen and *n*, known as the Avrami exponent, is associated with the dimensionality of growth. For the case of nucleation instantaneous in time or heterogeneous nucleation, *n* matches the growth dimension, while for sporadic (homogeneous) nucleation, *n* - 1 equals this value [78, 91, 92]. The Avrami exponent affiliated with different types of crystallization and modes of nucleation are shown in Table 2–3 [78]. The range in exponent values can be from less than 1 to greater than 6. Furthermore, the same value of the Avrami exponent can apply to different crystallization conditions. As a consequence, additional morphological and nucleation information is needed to interpret the exponent value. If the growth rate G is diffusion rather than nucleation limited, this leads to an additional exponential dependence of 0.5 which must be taken into account [78, 91].

Table 2.3. Avrami Exponents Affiliated with Different Types of Crystallization and Nucleation [78]

Type of crystallization	Nucleation	n	Remarks
A. Linear problem:			
Line	Athermal	1	Exact, analogous to Eq. (27B)
Line	Thermal	2	Exact, analogous to Eq. (27A)
B. Two-dimensional problem:			
Ribbon	Athermal	≤ 1	Limiting, analogous to Eq. (48)
Ribbon	Thermal	≤ 2	Limiting, analogous to Eq. (49)
Circular	Athermal	2	Exact, Eq. (27B)
Circular	Thermal	3	Exact, Eq. (27A)
Circular, diffusion control	Athermal	1	Exact, see tabulation p. 141
Circular, diffusion control	Thermal	2	Exact, see tabulation p. 141
Circular	Thermal, exhaustion	$3 \rightarrow 2$	Successive, p. 141
C. Three-Dimension Problem:			
Filbrillar	Athermal	≤ 1	Limiting, small v^c, Eq. (48)
Fibrillar	Thermal	≤ 2	Limiting, small v^c, Eq. (49)
Circular lamellar	Athermal	≤ 2	Limiting, small v^c, Eq. (50)
Circular lamellar	Thermal	≤ 3	Limiting, small v^c, Eq. (51)
Spherical	Athermal	3	Exact, Eq. (32A)
Spherical	Thermal	4	Exact, Eq. (32B)
Spherical, diffusion control	Athermal	3/2	Exact, see tabulation p. 141
Spherical, diffusion control	Thermal	5/2	Exact, see tabulation p. 141
Spherical	Thermal, exhaustion	$4 \rightarrow 3$	Successive, p. 141
Two-stage	Athermal/thermal	fractional	Limiting, Eq. (61)
Branching fibrillar	Athermal/thermal	$1, 2 \rightarrow$ large	Limiting, Eq. (55)
Solid sheaf	Athermal	≥ 5	Limiting, Eq. (56)
Solid sheaf	Thermal	≥ 6	Limiting, Eq. (57)
Truncated sphere	Athermal	2–3	Exact, Eqs. (35)–(39)
Truncated sphere	Thermal	3–4	Exact, Eqs. (35)–(39)
Volume decrease on cryst.	Athermal/thermal	fractional increase	See Eqs. (40)–(47)
Perfection after initial cryst.	Athermal/thermal	decrease	See Sect. 6.1.6.

The application of Avrami analysis to polymers typically involves the analysis of the crystallization exotherm via differential scanning calorimetry (DSC). Here the transformed crystal fraction, X_c (t), is determined by the analysis of the partial integral of the exotherm area at time t normalized for the entire exotherm process:

$$X_c(t) = \frac{\int_o^t \left(\frac{dH}{dt}\right) dt}{\int_o^\infty \left(\frac{dH}{dt}\right) dt} \qquad (2-11)$$

where dH/dt is the rate of heat evolution as a function of time. The Avrami equation shown in Eqn. 2−11 is arranged into a manageable linear form by taking the logarithm twice to yield:

$$\ln\{-\ln[1 - X_c(t)]\} = \ln(K) + n\ln(t) \qquad (2-12)$$

Thus, a plot of the double logarithm of the amorphous fraction as a function of logarithm time yields a linear relationship with a slope equal to the Avarami parameter, *n*, and an intercept equal to the logarithm of the rate constant.

It is important to note that some of the assumptions inherent in the Avrami treatment do not necessarily apply to polymer crystallization. Complications to the analysis when applied to polymers include the following [78]:

1) A constant volume transformation does not necessarily occur when crystallization takes place.

2) The linear growth rate G can vary with time under certain

circumstances, such as for crystallization governed by transport processes.

3) The number of nuclei in the system for nucleation sporadic in time can reach a limiting value as the nuclei are exhausted, rather than continue to increase with time.

4) The morphological structure of the crystal is not exactly spherical in three-dimensional case or circular in the two-dimensional case.

5) Branching frequently occurs within the developing superstructure causing non-linear growth.

6) Secondary crystallization can occur, which results in a two-stage process.

7) Crystal perfection following crystallization can occur.

Furthermore, it must be remembered that the Avrami exponent is applicable to more than one set of crystallization conditions. This, combined with the other complicating features of polymer crystallization, requires that the microscopic crystallization mechanism be determined independently before making conclusions based upon the Avrami analysis alone [78].

2.3.3 Influence of Thermal History on Crystallization

The nature and level of crystallinity in a polymer determines the resulting material morphology and material properties [93 - 100]. These properties can include, for example, fracture toughness, impact resistance, and yield strength [93]. Consequently, it is important to understand variables affecting crystallinity so that

the crystallinity can be controlled in a reproducible fashion [94].

Polymer crystallization is greatly dependent upon the thermal history imparted during processing [78, 93, 94, 96, 98, 99, 101, 102]. Both time and temperature in the melt affect the number of nucleation sites remaining in the material. As the temperature increases, more nuclei are destroyed [94, 96, 102, 103] while increasing the holding time in the melt can have a similar effect [94, 96, 98, 99]. With insufficient melting the residual nuclei promotes crystallization upon cooling [78]. The dependence of the number of surviving nuclei on time and temperature in the melt has been observed for semicrystalline thermoplastics such as PEEK, poly(ethylene terephthalate) (PET), nylon 6, and isotactic polypropylene [78, 94, 96, 98, 99, 102].

The nucleation density has a direct effect on the crystalline superstructure. For example, a low nucleation density leads to an overall lower bulk rate of crystallization allowing for the formation of larger spherulites [96, 99, 102]. The size of the crystalline superstructure has been shown to affect mechanical properties such as failure behavior and impact strength, where an increase in size results in a decrease in these properties [102]. Depending upon the crystalline growth rate relative to processing cooling rates, the level of crystallinity can also be altered as a function of the cooling rate. Different levels of crystallinity in, for example, PEEK and PPS have been reported as a function of cooling rate [98, 101, 104]. Of course, a slower cooling rate translates to a longer effective time in

the melt. Other reports described differing cooling conditions under which the final level of crystallinity was the same, however the crystal size and distribution were different [93, 99].

2.3.4 Multiple Melting Behavior

As will be seen in chapter 4 of this dissertation, LaRC CPI-2 polyimides characteristically display a multiple melting behavior. The purpose of this section of the literature review is simply to provide some background on this phenomenon noted in other polymer systems.

The presence of a dual endotherm response during DSC analysis has been noted in a number of other polymers. Keller and coworkers [105] found that by annealing polyethylene crystals at 128.5°C (from the melt) two distinct melting transitions developed at times between 2 and 100 minutes. The first transition temperature of 131°C remained constant with annealing time. However, the second transition ranged from 134°C to 136°C, the temperature being higher with longer crystallization times. The relative proportion of the overall crystallinity contributed by the higher melting transition increased with annealing time in a logarithmic fashion. For times less than 2 minutes only the 131°C peak was noted and for times longer than 100 minutes only the 136°C peak existed. Electron microscopy of a sample annealed so as to present a dual melt response revealed a dual population of lamellae: thick and thin. The authors' conclusion that the

dual melt response corresponded to the melting of thick and thin lamellae (produced through an isothermal lamellar thickening process) was thus, well supported. In a crystallization study of ultralong n-paraffins Ungar and coworkers [106] found a dual melt response develop as a result of once-folded lamellar crystals melting and reorganizing into extended chain (higher melting) crystals. In a study of low molecular weight poly(ethylene oxide) (PEO) crystals Cheng and coworkers [107] assigned multiple endothermic and exothermic events to consecutive melting and recrystallizations, respectively, which yielded successively higher melting, more extended chain crystals. Similarly, in studies of nylon-6,6, poly(ethylene terephthalate) [108, 109] it has been suggested that a melt reorganization/lamellar thickening process was occurring during heating to give rise to a second, higher melting, transition. In a crystallization study of an aromatic polyketone, Blundell, Liggat and Flory [110] found a coupled melting and recrystallization process occurring at about 260°C. The highest melting transition was attributed to the melting of melt recrystallized 'thicker' lamellae. As an explanation for the presence of the dual endothermic transition, the authors propose that there is a kinetic barrier to be overcome in order to form thicker lamellae. Specifically, the meta linkages at the ends of a repeat unit prohibits a continuous lamellar thickening process since the energy required for their incorporation requires that the thinner lamellae must first melt before reorganization can take place. Cheng and coworkers [27, 111] found that, in a

polyimide system based on oxydiphthalic dianhydride (ODPA) -- poly(ethylene oxide) (PEO) copolymer (n=3 ODPA, in refs. 110 & 111], high melting crystals formed initially with subsequent formation of lower melting crystals with time during isothermal crystallization. The lower endotherm in the ODPA-PEO polyimide was attributed to the melting of thinner branched or in-filled lamellar structures [27].

CHAPTER 3

EXPERIMENTAL

3.1 Materials

3.1.1 Solvents

3.1.1.1 Dimethylacetamide (DMAc)

Source: Aldrich Chemical Company

Boiling Point: 165°C

Purification: Ultra pure as received (>99.8%) in air sensitive reagent bottle. Solvent purity maintained via transfer under nitrogen blanket using standard air sensitive solvent handling procedures.

3.1.1.2 1-methyl-2-pyrrolidinone (NMP)

Source: Aldrich Chemical Company

Boiling Point: 205°C

Purification: Ultra pure as received (>99.8%) in air sensitive reagent bottle. Solvent purity maintained via transfer under nitrogen blanket using standard air sensitive solvent handling procedures.

3.1.1.3 *m*-cresol

Source:	Aldrich Chemical Company
Boiling Point:	191°C
Purification:	Ultra pure as received (>99%) in air sensitive reagent bottle. Solvent purity maintained via transfer under nitrogen blanket using standard air sensitive solvent handling procedures.

3.1.1.4 Toluene

Source:	Aldrich Chemical Company
Boiling Point:	110.6°C
Purification:	Ultra pure as received (>99%) in air sensitive reagent bottle. Solvent purity maintained via transfer under nitrogen blanket using standard air sensitive solvent handling procedures.

3.1.2 Monomers and Reagents

3.1.2.1 1,4-bis(4-aminophenoxy-4'-benzoyl)benzene (1,4-BABB)

Source:	Daychem Corporation
Molecular Weight:	500.55
Melting Point:	227°C
Purification:	Monomer grade as received. Monomer dried at 160°C

in a vacuum oven for 12 hours prior to use.

3.1.2.2 4,4'-Oxydiphthalic dianhydride (ODPA)

Source:	Occidental Chemical Corporation
Molecular Weight:	310.22
Melting Point:	228°C
Purification:	Monomer grade ODPA was obtained after drying at 160°C in a vacuum oven for 12 hours.

3.1.2.3 Phthalic anhydride (PA)

Source:	Aldrich Chemical Company
Molecular Weight:	148.12
Melting Point:	134°C
Purification:	PA was sublimed under ca. 10^{-4} torr vacuum at ca. 110°C (sublimator heated in an oil bath).

3.2 Polymer Synthesis and Processing

The synthetic processes used in this dissertation for the production of the LaRC CPI-2 polyimide films and powders were developed by researchers at NASA Langley. In particular, the procedures described in the following sections specifically follow the methods used by researchers at NASA Langley [112]. A

general schematic diagram for the synthesis of LaRC CPI-2 polyimide via the standard two-step method is shown in Fig. 3.1.

3.2.1 LaRC CPI-2 Films

3.2.1.1 Poly(amic acid) Synthesis

The poly(amic acid)s were produced in a round bottom 3-neck flask equipped with a nitrogen inlet, mechanical stirrer, Dean-Stark trap and condenser. The trap and condenser were only installed if the subsequent production of a powder was intended. All glassware was oven dried and the reaction apparatus was placed under nitrogen purge immediately after assembly. All monomers were weighed to an accuracy of 10^{-4} g in clean, oven dried glassware in a Mettler AE 160 balance. Transfer of the monomers to the reaction flask was affected using the reaction solvent as a wash to ensure quantitative transfer. The oxydiphthalic dianhydride (ODPA) monomer was added to a stirring solution of 1,4-bis(4-aminophenoxy-4'-benzoyl)benzene (1,4-BABB), followed by the addition of the phthalic anhydride (PA) endcapper. Of course, PA was not used in the 1:1 stoichiometric monomer ratio reactions. Molecular weight control was affected by employing stoichiometric offset of the monomers according to the Carothers relationship [27] as described in section **2.2.1.1**. The reactions proceeded under a nitrogen blanket, at room temperature with stirring, for approximately 18 hours. The solids concentration was 15% (w/w) in dimethyl acetamide (DMAc) or

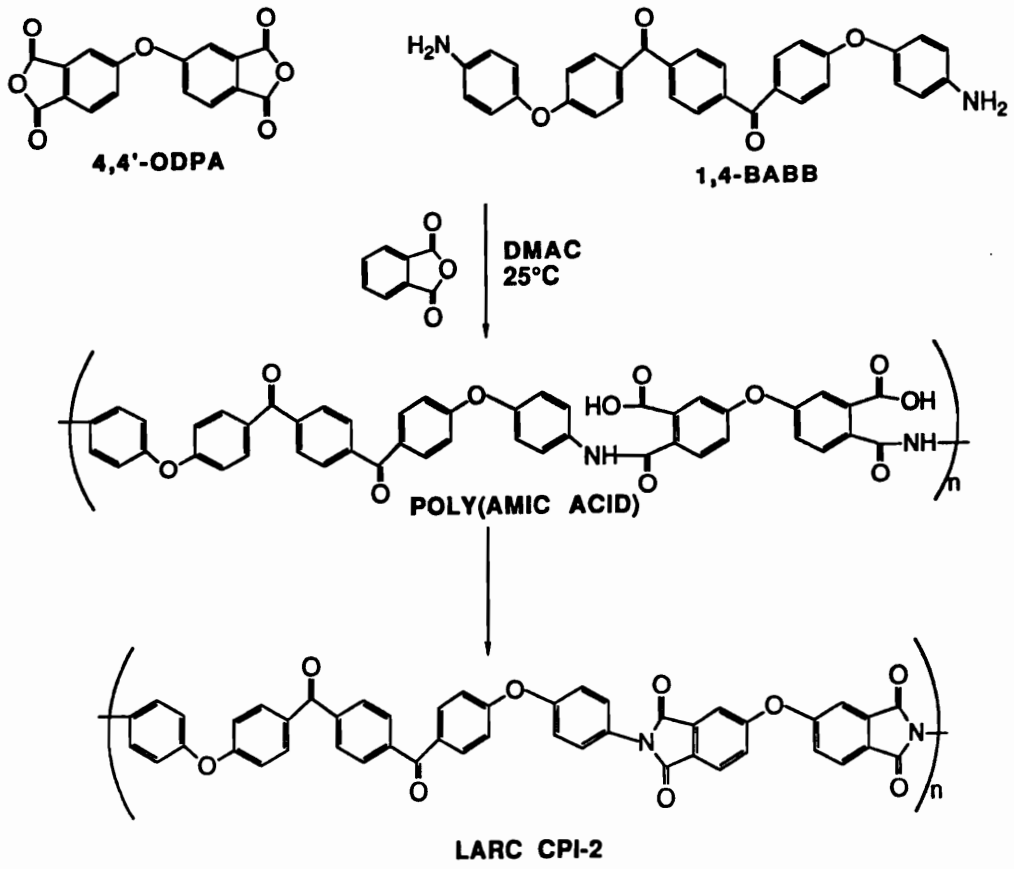

Figure 3.1 A general schematic diagram for the synthesis of LaRC CPI-2 polyimide via the standard two-step method.

1-methyl-2-pyrrolidinone (NMP).

3.2.1.2 Film Processing

After polymerization of the poly(amic acid), it was the removed and centrifuged for approximately 1 hour. The solution was then cast onto a clean, dry glass plate and spread out with a doctor blade set at a 30mil gap. The films were dried under forced dry air overnight for approximately 24 hours. Thermal imidization was achieved by placing the films in a Fisher IsoTemp programmable forced air oven for 1 hour each at 50°C, 100°C, 200°C and 300°C. The heating rate between isothermal hold temperatures was 5°C/minute. The oven was then allowed to cool slowly to room temperature. Films were removed from the glass by soaking in ca. 50°C water.

3.2.2 LaRC CPI-2 Powders

LaRC CPI-2 powders were produced via two separate methods. Powders synthesized in either NMP or DMAc were thermally imidized in solution after the standard polymerization of the poly(amic acid), as described above. Powders synthesized in *m*-cresol were produced in a manner analogous to the one-step method discussed in section **2.2.1.3**. In both cases it should be noted that the polyimide powders precipitated from solution during the thermal imidization 'in' solution. Thus, these methods cannot be considered true 'solution' imidization

procedures.

3.2.2.1 Powders from Dimethylacetamide and 1-methyl-2-pyrrolidinone

After polymerization of the poly(amic acid) the solution was brought to 10% (w/w) solids by the addition of the appropriate reaction solvent (NMP or DMAc). Toluene was then added at about 30%(v/v) so as to act as an azeotroping agent. The reaction temperature was maintained at 150°C to 155°C for about 18 hours. Azeotroped water was collected in a Dean-Stark trap which had been pre-filled with toluene. The precipitated polyimide powder was then washed in methanol stirring in a blender and filtered with multiple washings in methanol through a Büchner funnel. The isolated powder was allowed to air dry overnight. In order to maintain some degree of uniformity with regard to thermal imidization conditions between the powders and films, the dry powders were then subjected to the same thermal imidization cycle as for the films: 1 hour each at 100°C, 200°C and 300°C (see section **3.2.1.2**).

3.2.2.2 Powders from *m*-cresol

The production of powders from *m*-cresol follows the method used by Feld, Ramalingham and Harris [22]. Here the monomers and solvent were charged into the same glassware apparatus described in section **3.2.1.1** for the synthesis of poly(amic acid). The solution concentration here was 15% (w/w), as well.

Toluene (azeotrope) was then added at about 30%(v/v). Additionally, isoquinoline was added to the reaction mixture in a proportion of ca 0.5% (v/v). The reaction mixture was maintained at 180°C to 185°C for about 18 hours. The work-up and subsequent post reaction thermal staging of the precipitated powder was the same as for the powders from DMAc and NMP (see section **3.2.2.1**).

3.2.3 Nomenclature

Throughout this dissertation reference is made to various LaRC CPI-2 polymer 'types'. The variables between the polyimides are the stoichiometric offset, sample type and solvent/process used in their production. The nomenclature used to differentiate the types first indicates the stoichiometric offset followed by the polyimide type (f = film, p = powder) and lastly reveals the solvent in which it was made (n = NMP, d = DMAC and m = *m*-cresol). For example a 2.5% stoichiometric offset film synthesized in DMAc is designated: 2.5/f/d. A 7.5% offset powder synthesized in m-cresol is designated 7.5/p/m.

3.3 Characterization

3.3.1 Thermal Analysis

3.3.1.1 Differential Scanning Calorimetry (DSC)

Differential scanning calorimetry (DSC) was performed on either a Seiko DSC model 210 or model 220C under a nitrogen purge of 20ml/min at a heating

rate of 20°C/min, unless otherwise noted. The DSC was calibrated with indium, tin, and zinc standards. Samples were prepared by weighing them in aluminum pans using a Mettler AE 160 balance to an accuracy of 10^{-4} g. Sample sizes were typically ca. 7.5 mg.

As will be shown in this chapter 5, LaRC CPI-2 polymers have dramatically differing melting transitions depending upon the particular synthetic method employed. LaRC CPI-2 polymers, powders and films, synthesized in either NMP or DMAc have melting transitions on the range of 333°C to 364°C, while CPI-2 powders synthesized in m-cresol have melting transitions in the range of 408°C. Thus, each of these 'types' of polymer have their own specific DSC protocol. The standard protocol, for the polyimides produced in NMP and DMAc, and the modified protocol for the higher melting powders produced in m-cresol are shown below:

Standard protocol:

Used for:	CPI-2 synthesized in DMAc or NMP
Nitrogen Flow:	20cc/min
First heating:	150°C to 395°C @ 20°C/min
Isothermal Hold:	395°C for 1 minute
Cooling:	395°C to 150°C @ -10°C/min
Second heating:	150°C to 450°C @20°C/min

Modified protocol:

Used for:	CPI-2 synthesized in m-cresol
Nitrogen Flow:	20cc/min
First heating:	150°C to 435°C @ 20°C/min
Isothermal Hold:	435°C for 1 minute
Cooling:	435°C to 150°C @ -10°C/min
Second heating	150°C to 475°C @20°C/min

3.3.1.2 Thermogravimetric Analysis (TGA)

Thermogravimetric analysis (TGA) was performed using a Seiko Model 200 TGA. Sample sizes were generally ca. 5 mg-10 mg. Scans were conducted either in a nitrogen environment at a flow rate of 50 ml/min, or in static air. A heating rate of 10°C/min was typically used.

3.3.2 X-Ray Analysis

3.3.2.1 Wide Angle X-Ray Diffraction (WAXD)

Wide angle X-ray analysis was performed on a Nicolet model Stoe/V-2000 X-ray diffractometer using CuK_{α} radiation with a wavelength of 1.54Å. The operating conditions were 40 kV and 30 mA. The goniometer was calibrated with a silicon standard having characteristic peak maxima at 3.14 Å, 1.926 Å, and 1.64

Å. Two-theta values from 3° to 40° were scanned at 0.05° steps with a 10 second dwell.

3.3.2.2 Slit Smeared Small Angle X-Ray Scattering (SAXS)

Smeared small angle X-ray (SAXS) profiles were taken from a slit-collimated compact Kratky equipped with an M. Braun position sensitive detector. The X-ray source was a Philips PW-1729 generator providing Ni-filtered CuK_{α} radiation with a wavelength of 1.54Å. Operating conditions were 40 kV and 20 mA.

3.3.2.3 Pinhole Synchrotron Small Angle X-Ray Scattering (SAXS)

Real-time SAXS measurements were carried out at the SUNY X3A2 beamline at the National Synchrotron Light Source (NSLS) at the Brookhaven National Laboratory (λ=1.54Å). Data was collected using a linear position sensitive detector (EG&G, PARC, model 1453) in the angular range of 2θ = 0 to 1.5°. Pinhole SAXS data was collected using modified Kratky optics (sample to detector distance = 495mm and a beam size of 1.5 X 0.2mm). For the temperature jump experiment the sample were equilibrated in an external chamber at 300°C and then moved to the sample chamber set at 331°C by means of a pneumatic piston. The estimated equilibration time at the higher temperature is approximately 20 seconds.

3.3.3 Electron Microscopy

3.3.3.1 Scanning Electron Microscopy (SEM)

Samples were prepared for SEM by mounting them on aluminum stubs using silver paint. Following drying overnight in a vacuum oven, samples were sputter-coated with gold using a Biorad ES400 high resolution sputter-coater. Gold coating thicknesses ranged from ca. 70 Å - 140 Å.

Samples were analyzed using a Cambridge Instruments Stereoscan Model 200 SEM equipped with a secondary electron detector. Acceleration voltages of either 25 kV or 10 kV were generally used.

3.3.3.2 Transmission Electron Microscopy (TEM)

Bright-field TEM images were obtained from a Philips model 1L 420T STEM. No staining of the films was necessary since the lamellar textures were readily visible without a staining agent as reported earlier for the similar LaRC CPI-1 system [68]. In fact, attempts at staining these particular polyimides with osmium tetroxide or ruthenium tetroxide resulted in an obliteration of the otherwise visible lamellae [113]. Air and glass surfaces were distinguished by imbedding duplicate film specimens in epoxy with the air surfaces facing one another. The film samples were microtomed perpendicular to the film plane in the usual fashion on a Reichert-Jung Ultracut E43 equipped with a diamond knife.

3.3.4 Rheological Analysis

For both the melt viscosity and the isothermal crystallization measurements a Bohlin parallel plate dual-loop PID rheometer was used. Nitrogen was employed simultaneously as both the heating and inert gas. All samples were prepared from powdered LaRC CPI-2 polyimides by compressing samples in a machined steel cylinder of 1.5cm in diameter with removable plungers. Sample masses ranged from 0.250g to 0.260g and were compressed at approximately 2,000lbs force (ca. 7,300psi). The finished sample disks ranged from 1.2cm to 1.3cm in thickness. For both the melt viscosity and the isothermal crystallization measurements oscillation was 1Hz at 10% strain amplitude. Other conditions, which are specific to each measurement type, are presented in the following two sections.

3.3.4.1 Melt Viscosity

The melt viscosity analyses at both 375°C and 430°C were run with a 1.59g−cm torque bar. In each case the rheometer was stabilized at the test temperature before introduction of the sample and initiation of the run. The gap setting was zeroed at the analysis temperature for each run prior to the introduction of the sample.

3.3.4.2 Isothermal Crystallization Kinetics

All isothermal crystallization analyses were run with a 300g−cm torque bar. The conditions for the crystallization studies of the two polymer 'types', DMAc versus *m*-cresol powders, are different in their staging protocols. These were determined empirically and represent the best conditions for observing crystallization over a wide range in temperature. Each protocol is identified by the solvent from which the polyimide powder was made. The DMAc protocol holds the sample isothermally at 375°C before cooling and data collection begins. The *m*-cresol protocol holds the sample at 435°C for 5.0 minutes before cooling and data collection begins. The gap setting was zeroed at the analysis temperature for each run prior to elevation to the isothermal hold temperature. Under both conditions the time for the rheometer to reach thermal equilibrium was subtracted from the time to crystallization.

3.3.5 Fourier Transform Infrared (FTIR) Spectroscopy

Fourier Transform Infrared (FTIR) Spectroscopy analysis was performed on a Nicolet model 510 Fourier Transform Infrared Spectrometer in transmission. Powder samples were spread on potassium chloride plates with Nujol. The machine was set up to collect 32 scans each of the background and sample files.

3.3.6 Nuclear Magnetic Resonance Spectrometry

Carbon 13 nuclear magnetic resonance spectrometry (^{13}C n.m.r.) was run on a Varian Unity 400 MHz NMR.

CHAPTER 4

MULTIPLE MELTING BEHAVIOR OF LaRC CPI-2

4.1 Introduction

As an introduction to LaRC CPI-2 polymers it is necessary to focus on the singular property of melting, specifically the somewhat unusual characteristic of multiple melting. The ubiquitous nature of this multiple melting phenomenon in LaRC CPI-2 polymers makes it imperative to give an explanation for its presence before any other research is presented. Low molecular weight powders and films of this polymer display dual endothermic transitions in the range of 325°C to 365°C in differential scanning calorimetry (DSC) thermograms. An example is displayed in Fig. 4.1 for the 10.0/f/d film. This dual endothermic response is evident on both the first- and second-heat scan (followed by a -10°C/minute cooling to the glass), though the overall magnitude of both the transitions is reduced upon re-heating. (First- and second-heat thermograms for LaRC CPI-2 powders and films are presented in chapter 5). It should be noted that much of the material in this chapter has been published separately [114].

It is important to understand the origins of this dual endotherm response from the perspective that a higher melting polymer is more desirable due to its potential use in high temperature applications. This chapter presents results of an investigation into the morphological origins of this dual melt phenomenon.

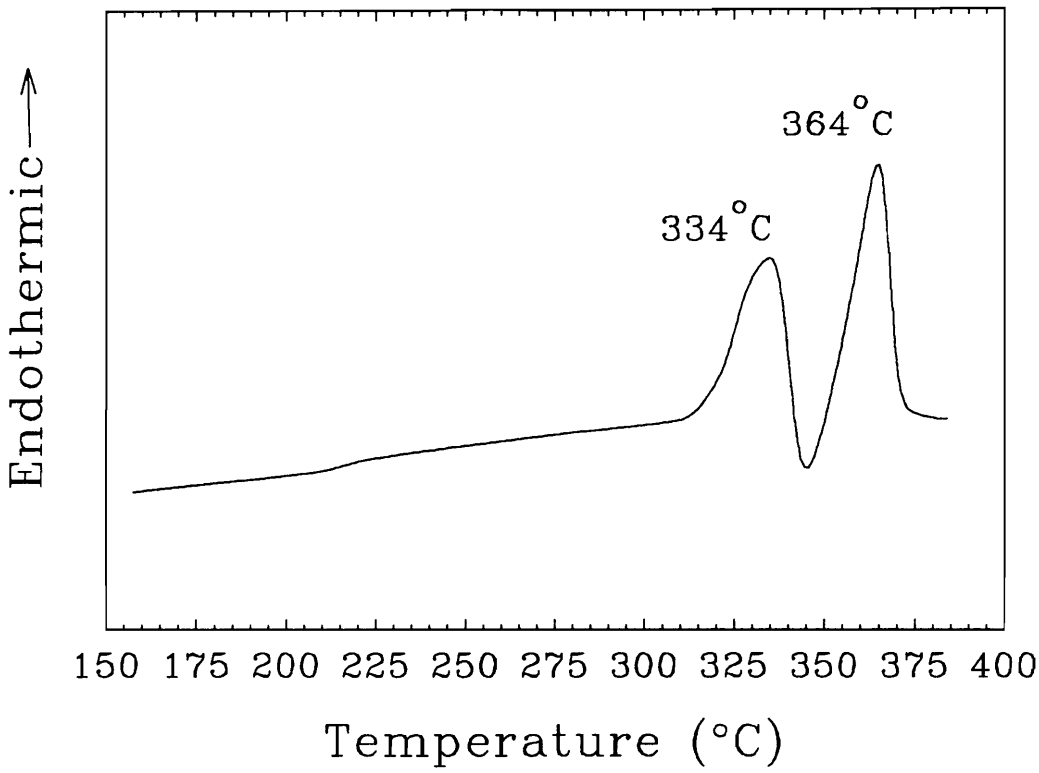

Figure 4.1 DSC scan of a low molecular weight LaRC CPI-2 film displaying a glass transition temperature of ca. 217°C and two endothermic transitions at 334°C and 364°C.

Transmission electron microscopy (TEM), wide angle X-ray diffraction (WAXD), and small angle X-ray scattering (SAXS) studies, in conjunction with differential scanning calorimetry (DSC) analysis, show that the high melting transition results from the melting of lamellae which were melt recrystallized during heating in a DSC. DSC heating rate studies reveal that the rate of transformation from thin to thick lamellae is dependent upon molecular weight and is very rapid for low molecular weight films. Synchrotron SAXS analysis confirms that the melt recrystallization process is very rapid.

4.2 Materials

A brief note is in order with regard to the materials used in this study. With the exception of the 7.5/p/n film, all films were synthesized in DMAc as seen in Table 4.1. At the time that the synchrotron SAXS equipment was available no 7.5/p/d film had yet been synthesized, hence the 7.5/p/n film was used so that the most comprehensive series of films could be studied. The 7.5/p/n film was obtained from Steven Havens at the NASA Langley research center (Film ref# SH-148-52-7). All films, however, were synthesized according to the processes parameters described in chapter 3.

4.3 Thermal Analysis of the Dual Melting Transition

Calorimetric analysis of the films listed in Table 4.1 reveals a distinct

Table 4.1. Calculated number averaged repeat unit and molecular weight values based on the Carothers relationship.

Film	<Xn>	<Mn>
0/p/d	∞	∞
2.5/p/d	79	30K
5.0/p/d	39	15K
7.5/p/n	26	9.8K
10.0/p/d	19	7.2K

dependence of the crystallinity upon molecular weight. This can be seen from the DSC scans in Fig. 4.2. The crystalline character of the films increases with increasing stoichiometric offset (lower M_n). Parallel to this effect, the glass transition temperature decreases from 229°C to 217°C. As discussed in more detail in chapter 5, this is consistent with the low calculated molecular weights of the films. Though crystallinity is apparent in the 2.5/f/d film, the dual endothermic transitions, in the range of 325°C to 365°C, exist in only the higher stoichiometric offset films (5%, 7.5% and 10.0%). The multiple transitions become successively more pronounced as the higher temperature transition overtakes the lower melting transition in magnitude with increasing stoichiometric offset. Coincident with these effects it can be seen that an exothermic peak develops between the two endotherms. Referring back to Fig. 4.1, it can be seen that the DSC trace for the 10% stoichiometric offset film has a very clear exothermic transition dipping below the baseline between the endothermic transitions. This provides the first evidence that a crystallization (exothermic) event is occurring after the first endothermic transition. As will be shown in the following sections of this chapter, this exothermic peak is a recrystallization event which immediately follows the first endothermic (melting) transition.

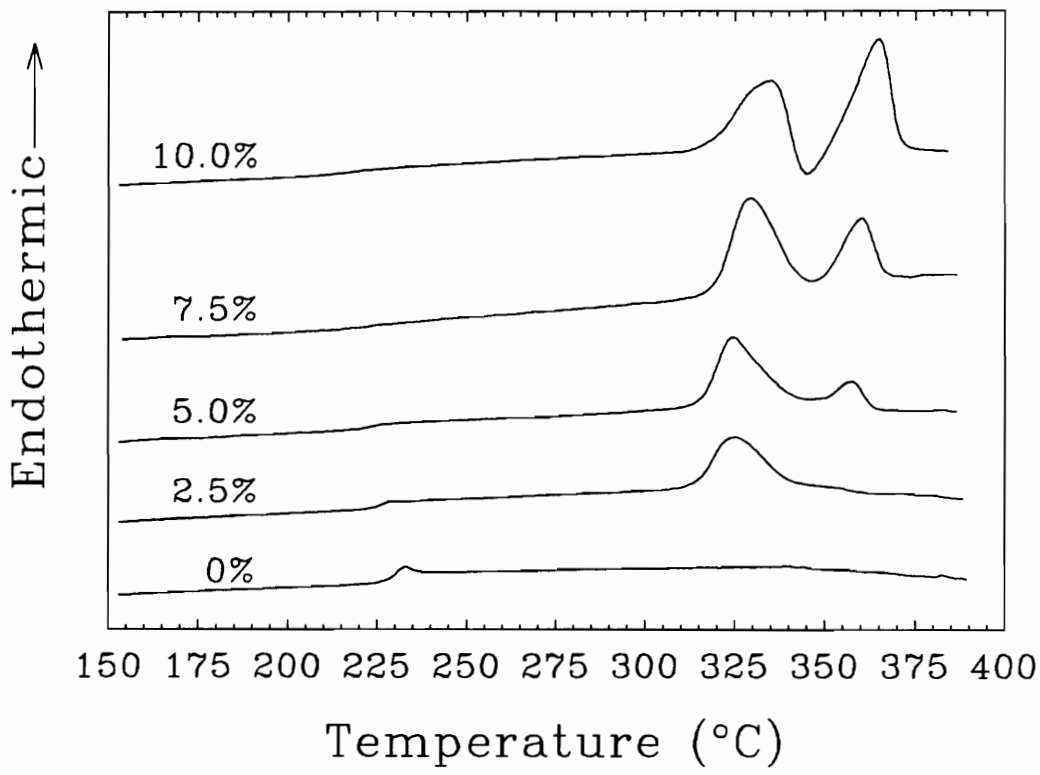

Figure 4.2 DSC thermograms of stoichiometric offset CPI-2 polyimide films showing the development of crystallinity with decreasing molecular weight.

4.4 Preparation of Thermally Treated Films

In order to determine the exact nature of the morphological structures responsible for the two endothermic transitions displayed in DSC analysis it was necessary to prepare special film specimens. The first objective was to produce a film which contained only the structures responsible for the higher endothermic transition. Secondly, it was necessary to enhance the morphological features responsible for the lower endothermic transition so that clear comparisons could be made. The comparison of WAXD, SAXS and TEM analysis of these thermally treated films provides critical insight into the nature of the crystalline structures attributable to the upper and lower melting transitions. Since the 10.0/f/d film displays the most dramatic dual endotherm response, it was chosen for thermal treatment. Sample identification along with the thermal treatments applied are listed below:

Film sample **A**: This film was treated so as to possess only the highest melting transition. This was achieved by holding the film at the temperature of 341°C (near the maximum exotherm between the two endotherms) for one hour in the DSC-- see Fig. 4.3. The 341°C annealed sample displayed a melting temperature, T_m, and heat of fusion value, ΔH_f, considerably higher than possessed by the second endotherm of an untreated sample: 371°C vs 364°C and 53 J/g vs ca 33 J/g, respectively.

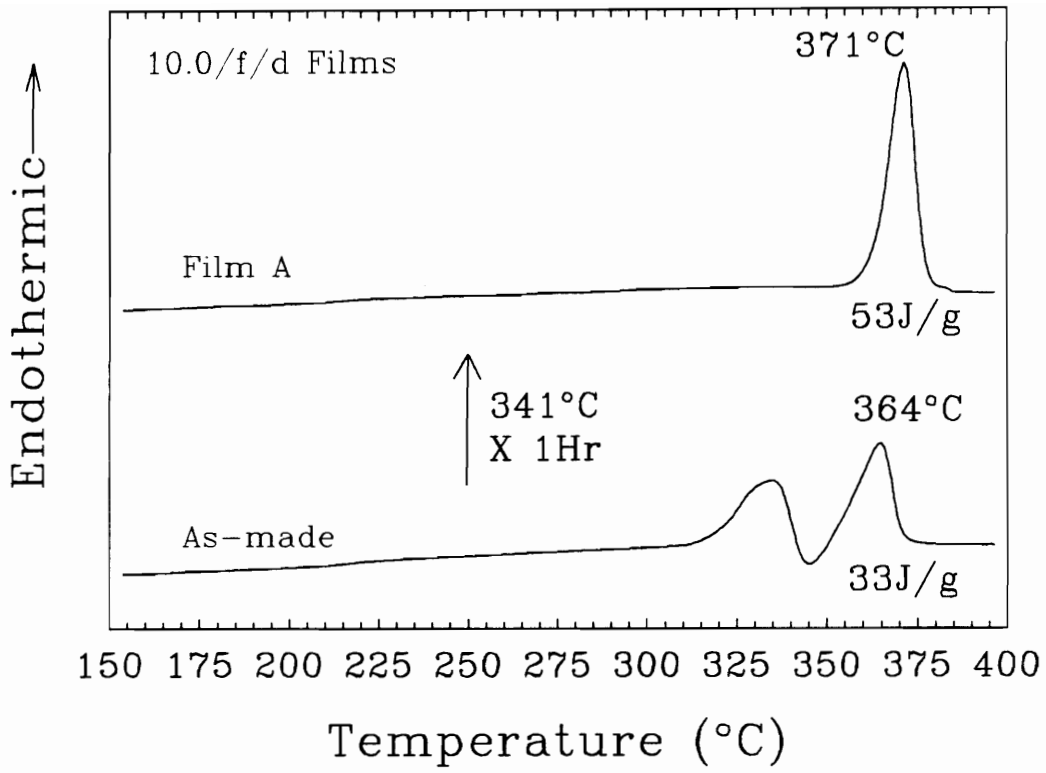

Figure 4.3 DSC trace of the as-made and the 341°C annealed (Film A) 10% offset CPI-2 film showing the increase in heat of fusion and melt temperature with annealing.

Film sample **B**: This film was thermally treated to increase the population/perfection of the crystalline structures responsible for the lower melting transition. Here the 10.0/f/d film sample was annealed at 275°C for approximately 50 hours under a nitrogen blanket in the block heating device described in chapter **3**. The result of this annealing was an increase in the magnitude of the lower melting endotherm with only a slight change in the melting profiles. Peak melting temperatures shifted only a small amount to 339°C and 361°C. This can be seen in Fig. 4.4.

Film sample **C**: This film sample was prepared exactly as sample **B** but for a longer period of annealing: 65 vs 50 hours. The reason for this extra film sample lies in the need for greater clarity from TEM analysis. Though sample **B** was sufficient for DSC, WAXD and SAXS analysis the crystalline lamellae visible in TEM micrographs were not of sufficient [photo-reproductive] quality to publish. This sample displayed dual melting transitions at slightly different temperatures, 335°C and 360°C, as seen Fig. 4.4. The first melting transition peak shape is slightly more narrow than in sample **B** and greater in magnitude relative to the second transition, though the magnitude of these both peaks is less than in sample **B**. Regardless of these differences in the thermograms, the end result was more visible lamellae under TEM analysis.

It should not go without notice that long anneal times at 275°C for films **B** and **C** (shown in Fig. 4.4) did not cause the first melting transition to increase

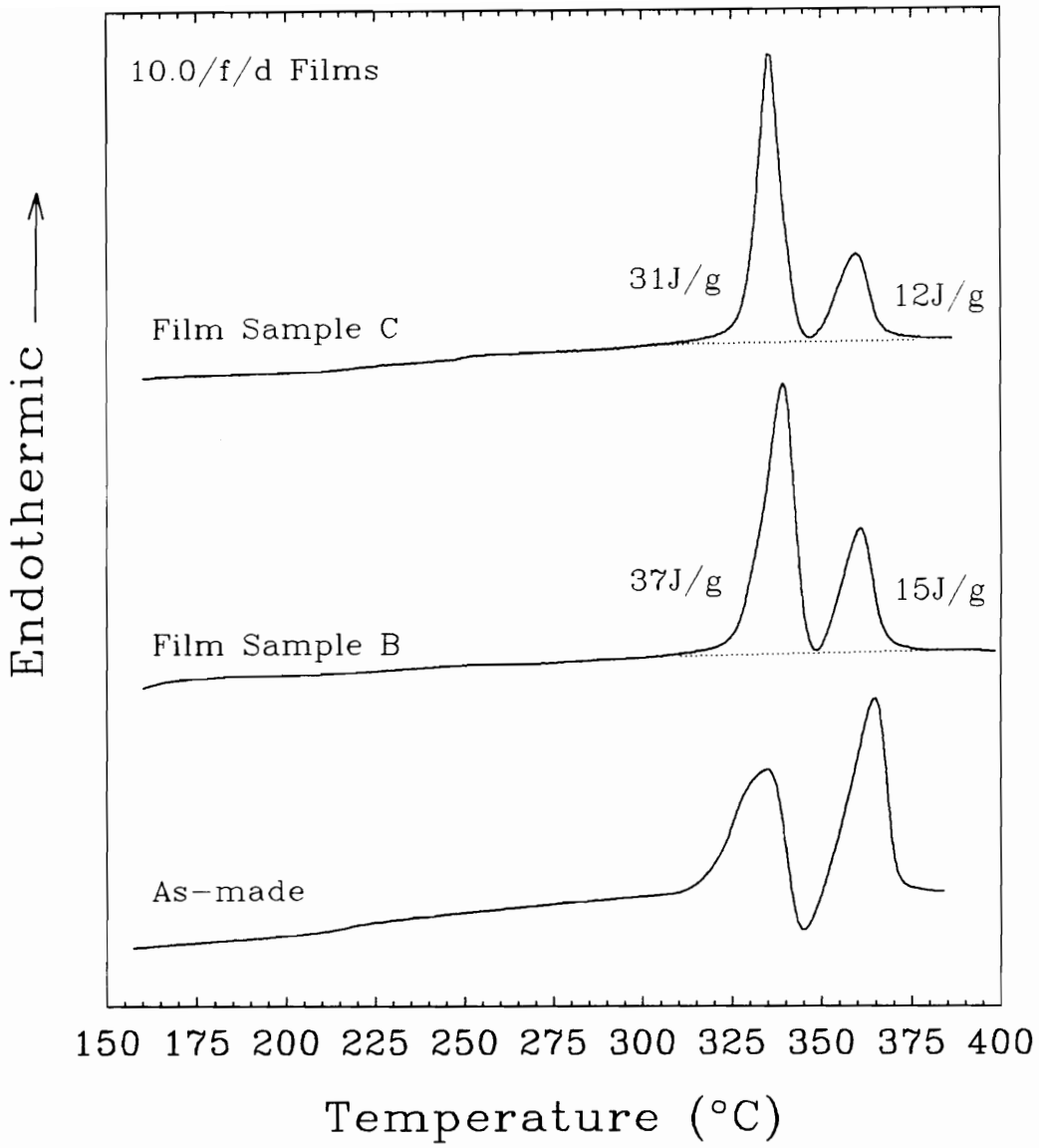

Figure 4.4 DSC thermograms of the as-made and 275°C annealed 10.0/f/d films (**B** and **C**).

dramatically in temperature. Meanwhile the magnitude of the first endotherm did increase relative to the second. From this observation it would appear that there was some barrier to thickening that required more energy to overcome than was provided at 275°C. It is possible that there is some conformational energy barrier akin to the meta-linkages in the aromatic polyketone studied by Blundell et al [115] as discussed in chapter 2. It is also possible that an energy barrier exists in terms of quantized/integral chain folding as was shown by Cheng and coworkers [110, 111], also discussed in chapter 2.

4.5 WAXD Analysis

Wide angle X-ray diffraction (WAXD) analysis was performed on portions of film **A** and film **B**. As can be seen in Fig. 4.5, there was no change in the crystal lattice structure as a result of the annealing process to form the high melting structure: The diffraction profiles for both samples are identical with regard to the location of the diffraction peaks. The better peak resolution seen in the 341°C annealed film indicates a greater degree of crystalline order and/or crystallite size. Thus, the crystal lattice structure is the same for both the upper and lower melting transitions.

4.6 Smeared SAXS Analysis

Figure 4.6 shows small angle X-ray scattering (SAXS) profiles of films **A**

and **B** plotted as the smeared intensity as a function of **s**, where $\mathbf{s} = 2/\lambda \sin(\Theta/2)$, λ is the wavelength and Θ is the radial scattering angle. Here it can be seen that the smeared 'long spacing' increases from 180Å sample **B** to 230Å in sample **A**. This increased long spacing for the film possessing the higher melting transition shows that the scattering centers are further apart. It is possible that this is due to thicker lamellae, but it is not proven by this data alone. TEM analysis presented below provides a visual perspective on the changes in crystalline superstructure. It should be noted here that desmearing and the Lorentz correction were not employed since only general trends in long spacing were sought and the resolution of the each peak was sufficient for this purpose.

4.7 TEM Analysis

Transmission electron microscopy (TEM) was employed to detect differences in lamellar texture between the dual melting (**C**) and the single high-melting (**A**) films. The micrograph of the film possessing both melt transitions, film **C**, reveals the presence of some faint, wisp-like lamellae-- see Fig. 4.7. In the single, higher melting film (**A**), thicker and more clearly defined lamellae are readily seen throughout the sample-- see Fig. 4.8. Rough approximations of lamellar thicknesses estimated from the micrographs are 70Å and 130Å for the low and high temperature annealed films, respectively. Thus, TEM analysis confirms that the increased long spacing in SAXS is due to thicker lamellae.

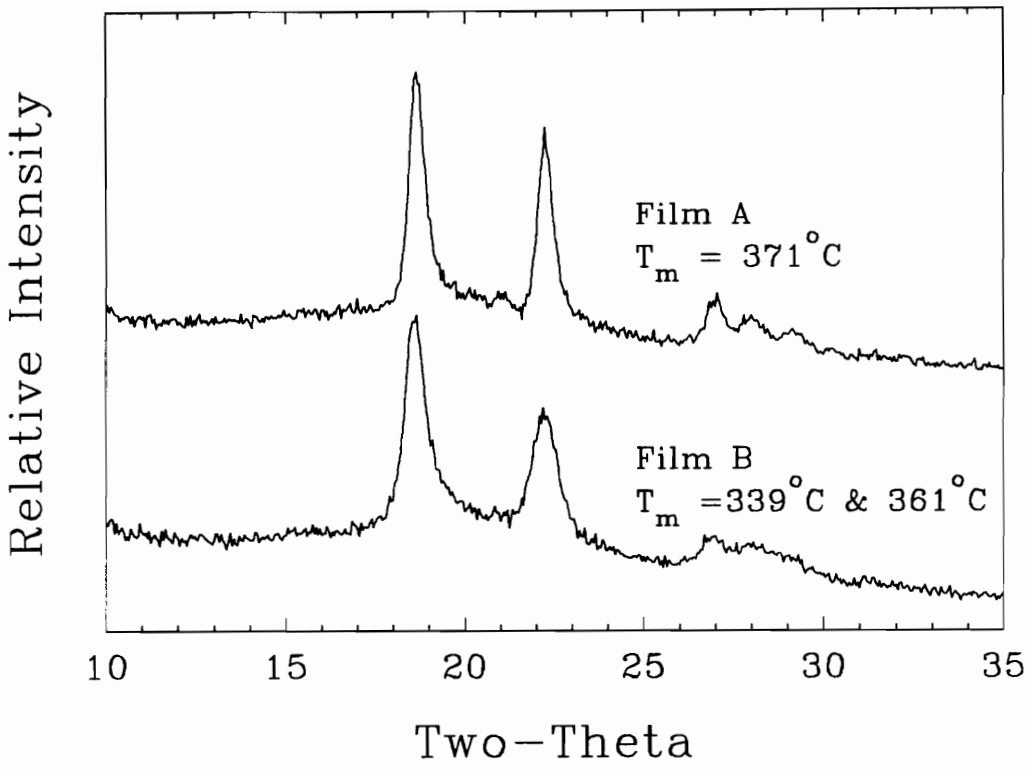

Figure 4.5 Wide angle X-ray diffraction scans for the dual melting film **B** and the single (higher) melting film **A**.

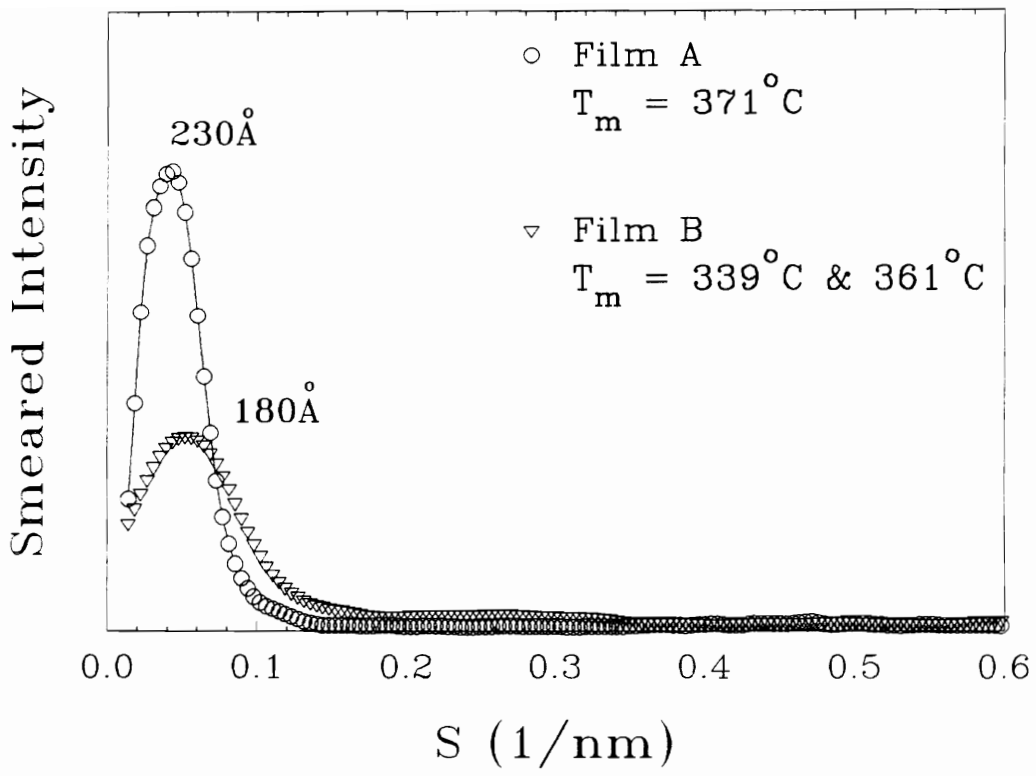

Figure 4.6 Smeared small angle X-ray scattering profiles for the dual melting film **B** and the single (higher) melting film **A**.

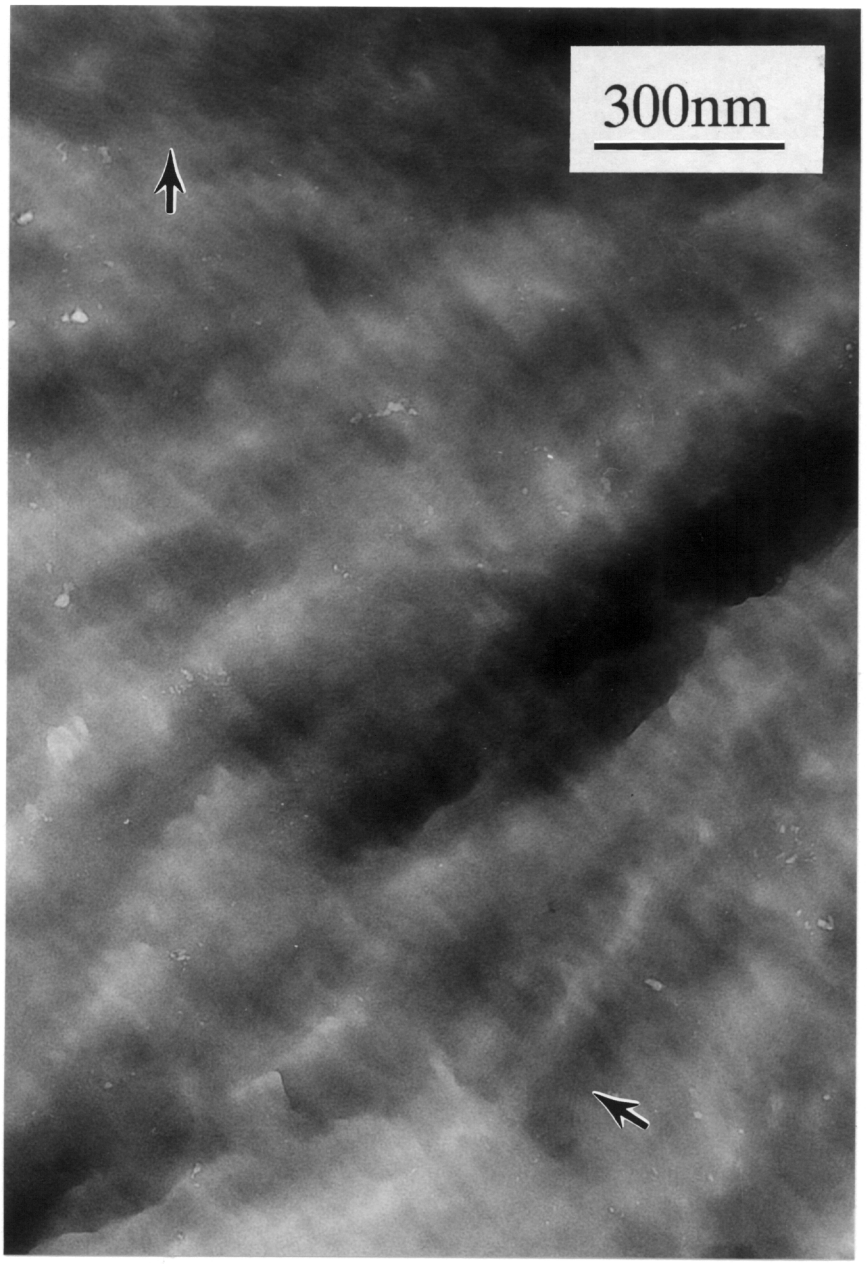

Figure 4.7 TEM of the 10.0/f/d film annealed to possess a high population of the lower melting structures (film **C**).

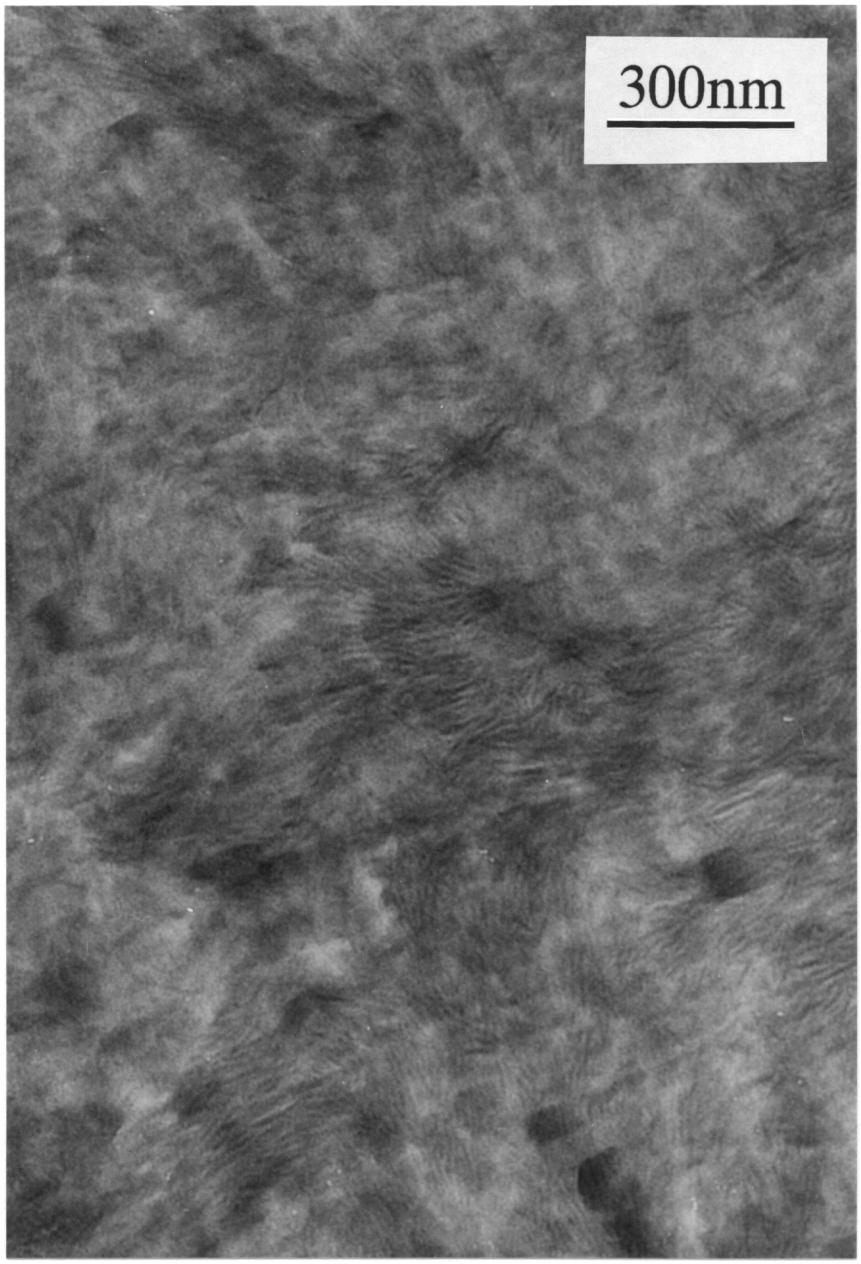

Figure 4.8 TEM at the same magnification of another sample of the same film annealed to possess a single endotherm at 371°C (film A).

Analysis of the evidence presented thus far leads to the conclusion that the lower endothermic transition seen in the DSC trace is due to the melting of relatively thin lamellae whereas the higher melting transition originates from melting of thicker lamellae. This is entirely consistent with the thermodynamics of polymer crystals. The melting point of polymer lamellae, where the lateral dimension is very much greater than its thickness, is directly related to their thickness through the fundamental thermodynamic relationship known as the Gibbs-Thomson equation (Eqn. **2–9**, reproduced here) [87]:

$$T_m = T_m^o \left(1 - \frac{2\sigma_e}{(\Delta h_f)\ell}\right) \qquad \textbf{(2–9)}$$

where T_m is the observed melt temperature, T_m^o is the thermodynamic (equilibrium) melting temperature, σ_e is the chain fold surface energy, ΔH_f is the heat of fusion per mole of crystalline repeat unit, and ℓ is the lamellar thickness. As Eqn. 1 shows, as ℓ becomes larger the observed melt temperature approaches the equilibrium value.

At this point, then, it has been established that the dual melt response is a result of melting of 'thin' and 'thick' lamellae. The question remains, however, as to whether or not any 'thick' lamellae are already present in the films prior to DSC analysis. And, if no thick lamellae are initially present, how rapid is their

creation? These issues are addressed in the next section.

4.8 Kinetics of Melt Reorganization

4.8.1 DSC Data

As noted earlier, the existence of an exotherm between the two endotherms indicates that some melt/recrystallization process is occurring. Because of the time dependent nature of a recrystallization process, one would expect to see the magnitude of the second endotherm decrease, relative to the first, with higher heating rates on the DSC due to a shorter available recrystallization time. With this in mind a series of heating rate scans was conducted in the DSC for the films presenting the dual melt response (5.0%, 7.5% and 10.0%). Heating rates of 5, 10, 20, 30 50 and 70°C/min were used. Endotherm areas for the lower (ΔH_1) and upper (ΔH_2) transitions were determined and the ratio of the first to second endotherm area was then calculated, $\Delta H_1 : \Delta H_2$. Because of the dynamic nature of the peak shapes, i.e., the exotherm 'peak' not being located in the same exact relative position for each scan, a reliable area analysis technique had to be determined. The most consistent method for peak area integration was found to be the following: The first endotherm area integration limits were taken from the point at which the DSC signal began to deviate from the baseline for the first endotherm to the signal minima between the first and second endotherms. The second endotherm

area integration limits were taken from the signal minima to the point where the DSC signal again returned to the baseline. This integration method is not meant to provide an exact measure of the true heat of melting. Rather, the objective is to uncover trends regarding the relative changes in the magnitude of the transitions.

Figure 4.9 displays a plot of the results of this analysis. The first to second endotherm ratio, ΔH_1:ΔH_2, for the 5.0%, 7.5% and 10.0% stoichiometric offset films is plotted as a function of heating rate. Focusing first on the curve for 10% offset film, we note that at heating rates up to 30°C/min the magnitude of the second endotherm is seen to decrease relative to the first. This is consistent with a decrease in conversion of the lower to higher melting material due shorter recrystallization times. However, at the faster heating rates of 50°C/min and 70°C/min the first to second endotherm ratio levels out at about 1.1. At the highest [reasonably achievable] heating rate of 70°C/minute, the elapsed time between the two endotherm peaks is approximately 25 seconds. Yet the second transition remains in magnitude approximately equal to the first. Thus, the primary question regarding the pre-existence of 'thick' lamellae is unanswered by this data alone. Two possible scenarios present themselves. Either there is a small, but finite, population of thicker lamellae already present in the film, or the rate of transformation from the thinner to thicker lamellae is sufficiently rapid that it cannot be detected by DSC, i.e., considerably faster than 25 seconds. Due

to the chain rigidity and stiffness of this polyimide, evidenced by its high glass transition temperature, the latter possibility seems unlikely. However, the endotherm ratio analysis of the higher molecular weight 7.5% and 5.0% offset CPI-2 films as a function heating rate shown in Fig. 4.9 clearly show that this is, indeed, the case. In both of these films the decrease in the second endotherm magnitude with increasing heating rate is much more pronounced and neither display asymptotic behavior. In fact, at the heating rate of 70°C/min, the magnitude of the second endotherm is virtually non-existent in the 5% film (about a 50:1 ratio). We may conclude that, for the higher molecular weight samples, insufficient time was available for lamellar melt recrystallization during the DSC scan at high heating rates. By implication, then, there *was* sufficient time for transformation in the low molecular weight 10.0% offset film -- ca. 25 seconds was long enough.

If we re-examine the DSC traces displayed in Fig. 4.2, it is apparent that the development of the dual endotherm response with decreasing molecular weight is a kinetic manifestation. That is, the lower molecular weight samples, with their lower melt viscosity and shorter reptation time, can recrystallize faster, thereby allowing for the presence of a second (higher) melt transition.
A logical consequence of this line of reasoning would be that the complete lack of a second endotherm in the 2.5% offset (high Mw) film is also a kinetic result. A slow heating rate scan at 5°C/min of this film confirms this -- see Fig. 4.10. Here

it can be seen that a second endotherm, otherwise masked by the 'fast' heating rate of 20°C/minute, is present. Thus, the conclusion to be drawn from the data thus far is that there are no 'thick' lamellae present in the films prior to DSC analysis and the second melting transition is wholly the result of a melt-reorganization process occurring during heating in the DSC.

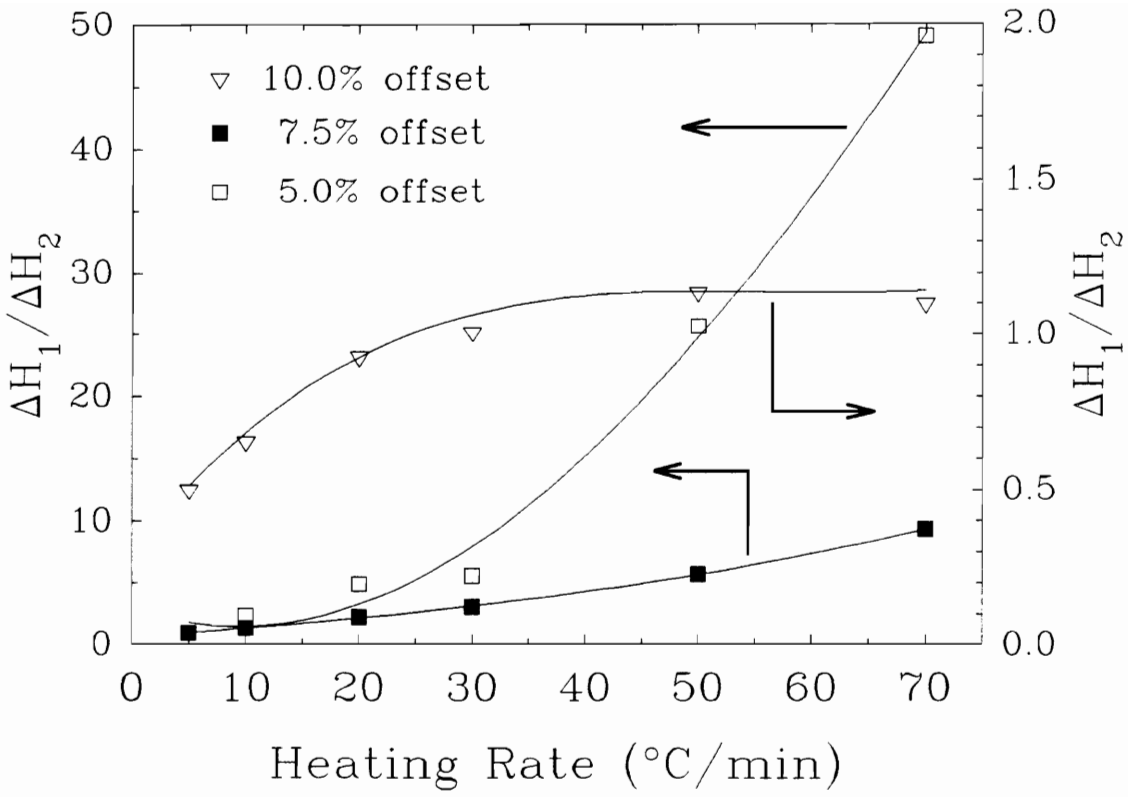

Figure 4.9 The ratio of the first to second melt endotherm areas as a function of heating rate for the 5.0%, 7.5% and 10.0% stoichiometric offset LaRC CPI-2 films.

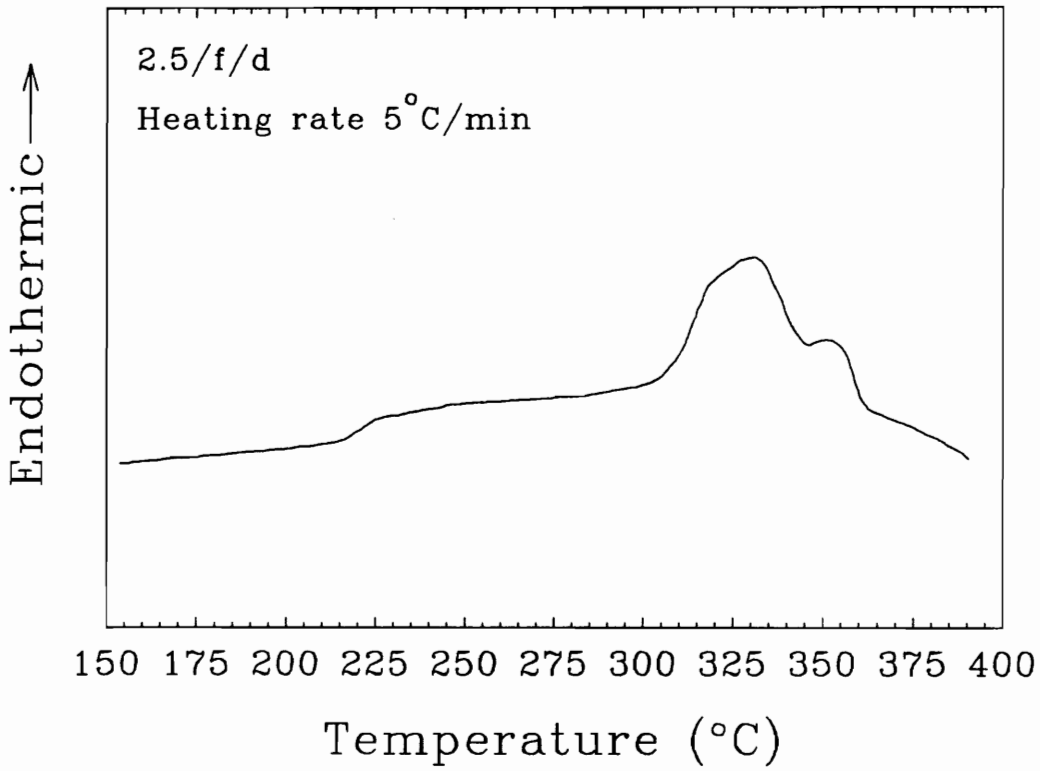

Figure 4.10 DSC thermogram of a 2.5/f/d film heated at 5°C/min clearly showing the presence of a second endotherm..

4.8.2 Synchrotron SAXS Analysis

As indicated above, the rate of transformation of 'thin' to 'thick' lamellae in the 10.0% offset film occurred, with some surprise, very rapidly. In order to gain a real-time perspective of the rapid changes in lamellar dimensions as a result of thermal treatment of this sample, SAXS analysis of pinhole collimated data from the National Synchrotron Light Source (NSLS) at Brookhaven was employed. Both a temperature ramp and temperature jump experiment were run with this material. In the ramping experiment the sample was heated from 300°C to 370°C at 5°C/min. Figure 4.11 shows a sample of the data collected during this run. The absolute intensity is plotted as a function of the angular variable s. The shift in the peak position to smaller s values (greater long spacings) is evident between 320°C and 350°C. Thus, we are provided a measured 'view' of the changes occurring during heating wherein thinner lamellae are melt-reorganized into thicker lamellae which are then, themselves, melted completely. As the film is taken through higher temperatures the lamellae melt and the SAXS peak disappears.

The temperature jump experiment reveals the rapid development of the thicker lamellae under isothermal conditions. Here the sample was equilibrated at 300°C and then rapidly heated to 331°C and held for 15 minutes. The initial equilibration time at 331°C was approximately 20 seconds. From the peak

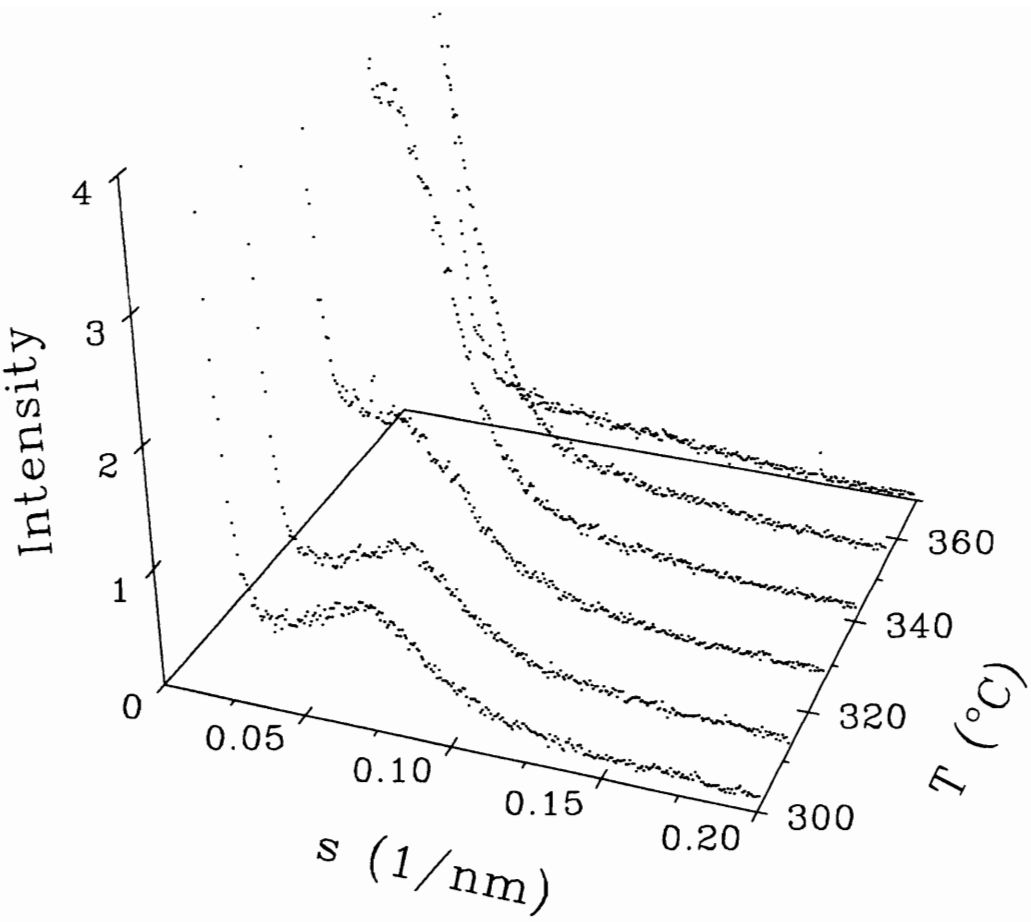

Figure 4.11 Synchrotron SAXS scans of the 10.0/f/d film as a function of temperature at a heating rate of 5°C/min. The upturn in intensity at low s values was removed for the sake of clarity.

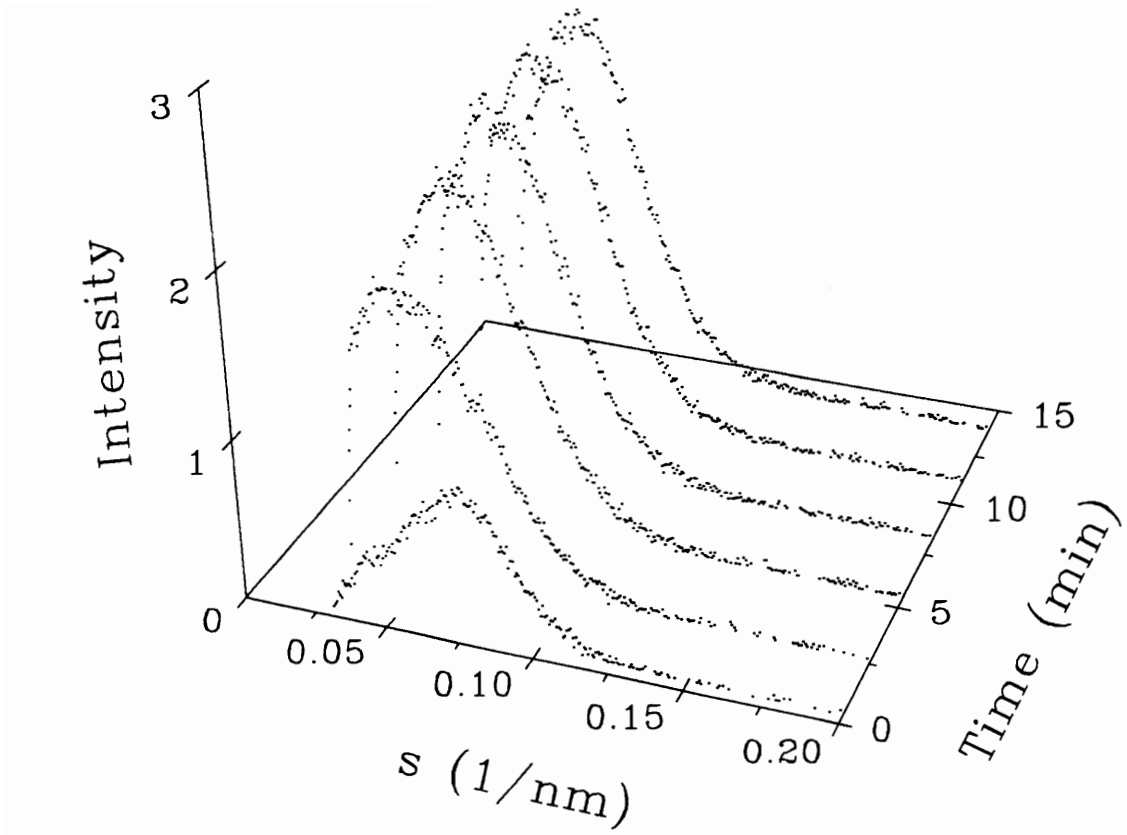

Figure 4.12 Synchrotron SAXS isothermal scans (331°C) of a different sample of the 10.0/f/d film. The upturn in intensity at low **s** values was removed for the sake of clarity.

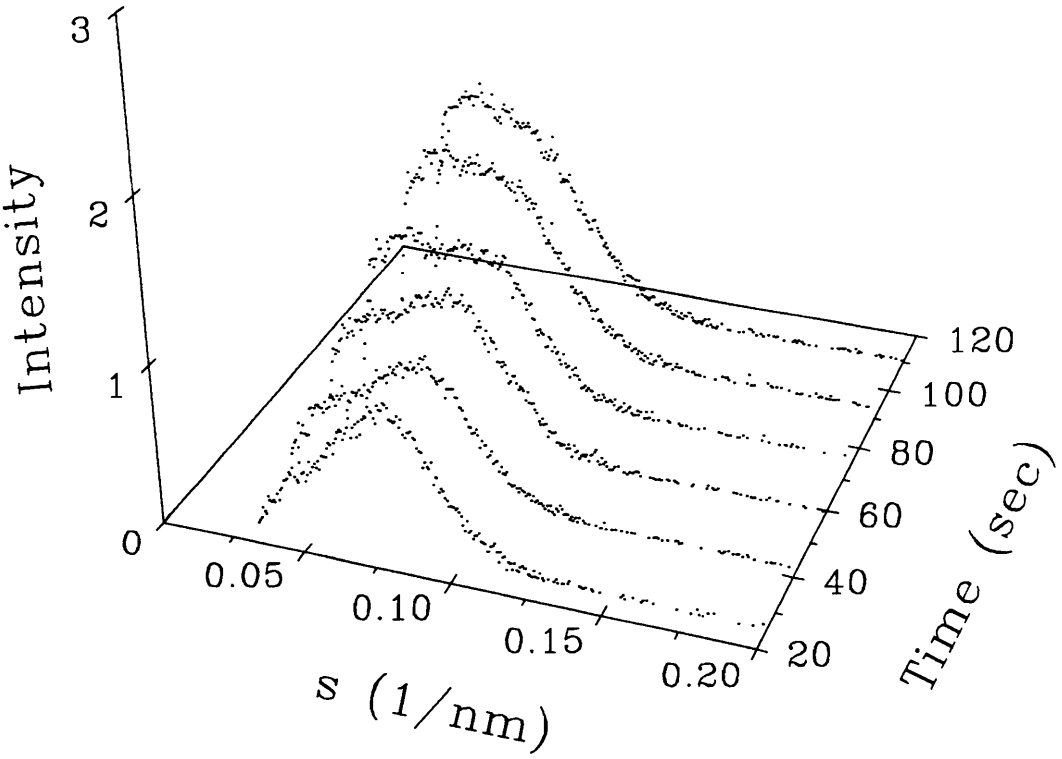

Figure 4.13 The first 2 minutes of the isothermal Synchrotron SAXS scans shown in Fig. 12.

positions shown in Fig. 4.12 it is clear that nearly all of the changes have already occurred within the first two and a half minutes. Figure 4.13 presents an expanded view of the changes occurring within the first two minutes. The development of the thicker lamellae is clearly seen to occur at the expense of the thinner lamellae within this short time frame. It should be noted here that this 'annealing' temperature is about 10°C below that of the maximum in the exotherm between the two melt transitions. Hence, the rate of transformation is expected to be very much slower at this lower temperature. Given the time resolution restrictions (minimum of 17 second scans) of this experimental setup, it is doubtful that the melt recrystallization phenomenon could be captured as clearly at 341°C.

4.9 Conclusions and Summary

Evidence presented in this chapter regarding the dual melt transition observed in LaRC CPI-2 polyimide films clearly points to a lamellar melt recrystallization process occurring during heating. A film sample annealed at the exotherm temperature between the two melting transitions displayed a higher melting transition with greater long spacing from SAXS and visibly thicker lamellae seen through transmission electron microscopy. This is entirely consistent with fundamental thermodynamic relationships regarding crystal melting in polymeric systems. DSC analysis indicates that the melt recrystallization

process is a kinetic phenomenon dependent upon molecular weight. Furthermore, DSC evidence suggests that only the lower melting [thinner] lamellae are present in the films initially. Despite the chain rigidity in this polyimide, DSC and synchrotron SAXS analysis clearly show that the melt recrystallization process is very rapid for the 10% stoichiometric offset (lowest molecular weight) film. An explanation for the exact mechanism of the melt reorganization process is not presently available. It is possible that a kinetic barrier exists to prevent a continuous lamellar thickening as has been suggested by Blundell et al. [115] for the poly(aryl ether ketone) in their study.

CHAPTER 5

DEPENDENCE OF MELT AND CRYSTALLIZATION BEHAVIOR UPON BOTH SYNTHESIS AND PROCESS VARIABLES

5.1 Introduction

This chapter focuses upon the processing of LaRC CPI-2. Three main areas are presented. Section **5.2** introduces the DSC response of LaRC CPI-2 films and powders. In particular, differences in glass and melting transitions are compared and contrasted. In section **5.3** a previously published study [116] of the changes in LaRC CPI-2 films during thermal imidization is presented. Here the development of crystallinity was followed during the imidization process. Lastly this chapter presents the unusually strong dependence of melting temperature of LaRC CPI-2 powders upon processing conditions. In section **5.4** the processing of powders in DMAc and m-cresol is discussed and the greatly differing melting behavior is presented. The results of several analytical techniques used in an attempt to explain the differences in melting behavior are also presented.

5.2 General Differential scanning Calorimetry (DSC) Analysis of LaRC CPI-2

5.2.1 Protocol for DSC Analysis

In order to compare thermal behavior of polymer samples from DSC analysis, it is important to have consistent and reproducible conditions. The

magnitude and temperature of a melting transition in polymers is dependent upon the heating rate employed. Equally important is the thermal history of the samples being compared. Thus, second-heat scans, following a standard heat cycle, are used to compare the inherent thermal properties of polymer samples. The first-heat, with the subsequent cooling cycle, acts to remove thermal history received during processing and impart a uniform thermal history for all samples. For this reason standard DSC protocols, as described in chapter 3, were set forth for the LaRC CPI-2 polymers.

As will be shown in this chapter LaRC CPI-2 polymers have dramatically differing melting transitions depending upon the particular synthetic method employed. LaRC CPI-2 polymers, powders and films, synthesized in either NMP or DMAc have melting transitions on the range of 333°C to 364°C, while CPI-2 powders synthesized in m-cresol have melting transitions in the range of 408°C. Each of these 'types' of polymer have their own specific DSC protocol. The standard protocol, for the polyimides produced in NMP and DMAc, and the modified protocol, for the higher melting powders produced in m-cresol, as shown earlier in chapter 3, are reproduced below:

Standard protocol:

Used for:	CPI-2 synthesized in DMAc or NMP
Nitrogen Flow:	20cc/min
First heating:	150°C to 395°C @ 20°C/min
Isothermal Hold:	395°C for 1 minute
Cooling:	395°C to 150°C @ -10°C/min

Second heating:	150°C to 450°C @20°C/min

Modified protocol:

Used for:	CPI-2 synthesized in m-cresol
Nitrogen Flow:	20cc/min
First heating:	150°C to 435°C @ 20°C/min
Isothermal Hold:	435°C for 1 minute
Cooling:	435°C to 150°C @ -10°C/min
Second heating	150°C to 475°C @20°C/min

As will be discussed thoroughly in chapter 6, LaRC CPI-2 polymers produced in DMAc are very sensitive to time in and temperature of the melt. This sensitivity manifests itself in the second-heat thermograms for these polymers. The second-heat scans from the standard protocol reveal a very much reduced second (dual) melting transition for the films and powders synthesized in DMAc. This is a direct result of the "extended" time at the "high" temperature of 395°C. A shorter time at a lower temperature will produce a second melting transition much greater in magnitude. An example of this can be seen in Fig. 5.1. Here the second-heat scans of a 7.5/p/d cpi-2 polymer which has been subjected to two different heat cycles is displayed. The scan for sample (**a**) was only heated to 375°C (just above the original second-heat transition) immediately followed by the standard -10°C/min cooling to 150°C. This scan displays a very large second endotherm transition, in marked contrast with the second-heat scan from sample (**b**) which was subjected to the standard protocol (395°C X 1 minute). This result should be kept in mind when noting the lack of second

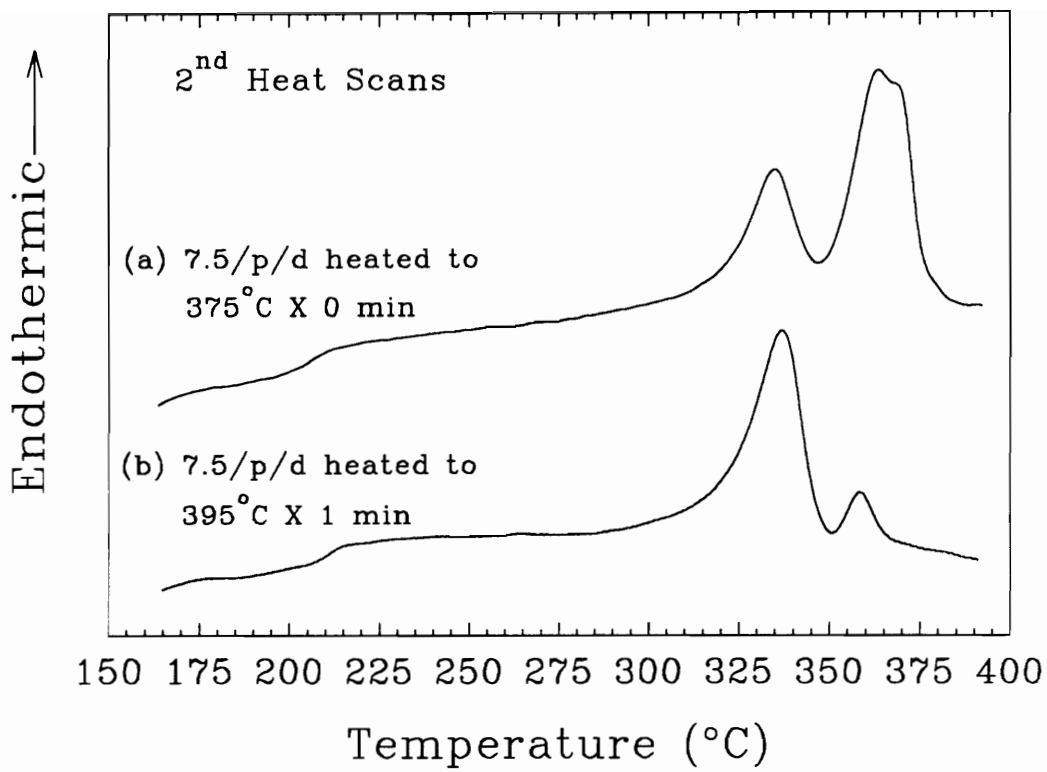

Figure 5.1 Second-heat scans of a 7.5/p/d cpi-2 polymer which has been subjected to two different heat cycles. Sample (**a**) was only heated to 375°C before cooling at -10°C/m. Sample (**b**) was heated according to the standard protocol (395°C X 1 minute).

endothermic transitions displayed in some of the second-heat DSC scans presented in this chapter.

Some explanation is in order regarding the specific choice of the isothermal hold at 395°C in the standard protocol. Though this temperature is well above the end of the second melting transitions in the lowest stoichiometric offset polymers it is just sufficient to fully include the second melting transition in the highest (10%) stoichiometric offset CPI-2. The one minute hold at this temperature simply allows the samples to fully stabilize thermally before the -10°C cooling step.

5.2.2 LaRC CPI-2 Films

As was shown in chapter 4, the level of crystallinity and glass transition temperatures reflected in the DSC thermograms for the LaRC CPI-2 films are highly dependent upon the molecular weight of the sample. In order to make comparisons of the glass transition temperatures it is necessary to view second heat thermograms wherein process history has been removed. The first and second-heat scans of a series of films, in increments of 2.5% stoichiometric offset from 0% to 10%, are shown in Fig. 5.2 (a&b). As might be expected, second-heat thermograms of the series reveal a dependence of the T_g upon stoichiometric offset. As seen in Fig. 5.2(b) the T_g increases from 209°C for the 10/f/d film to 233°C for the 1:1 stoichiometric film. This trend in T_g indicates that the

stoichiometric offset films are of sufficiently low molecular weight to be considered oligomeric. Indeed, looking back on Table 4−1, the 10%, 7.5% and 5% offset films all have very low calculated number average molecular weights of 15k, 9.8k and 7.2k, respectively. The fact that the 2.5/f/d film has a lower T_g than the 1:1 film (226°C vs 232°C) is unexpected, however. The calculated molecular weight for this film is 30k, well beyond the oligomeric range. The lower T_g in this film leads one to suspect that the achieved molecular weight was somewhat lower than the calculated value. As will be discussed in section **5.2.3**, this same trend of decreasing T_g with increasing stoichiometric offset is seen in the powders samples as well.

A simple method for determining the T_g for an infinitely high molecular weight LaRC CPI-2 polyimide is to plot the low molecular weight glass transition temperatures as a function of inverse molecular weight. The zero intercept of this plot yields the T_g of the infinite molecular weight polymer, $T_g(\infty)$, as seen in Fig. 5.3. The molecular weight values used for the abscissa were calculated from the Carothers relationship [27] as discussed in chapter 2. The relationship for the film samples is very linear and gives a $T_g(\infty)$ of 234°C. This compares well with the observed T_g of 233°C for the 1:1 stoichiometric offset film. Clearly the relationship for the powder samples is much less linear. In particular, the lowest molecular weight powder has a greater T_g than is expected. With this exception, the T_g's of the powders are uniformly lower than their film counterparts. This is

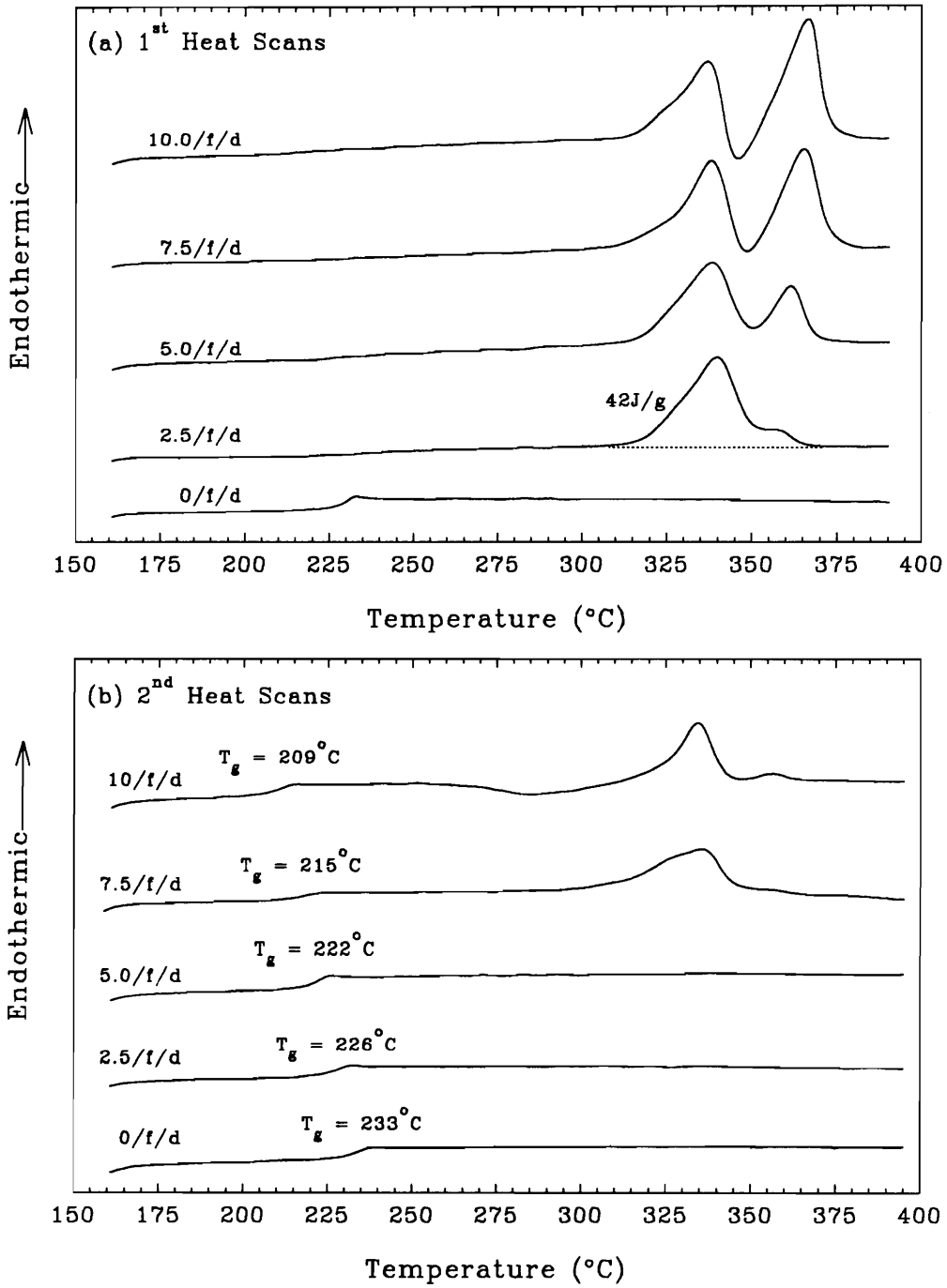

Figure 5.2 The first (**a**) and second-heat (**b**) scans of a series of films, in increments of 2.5% stoichiometric offset from 0% to 10%.

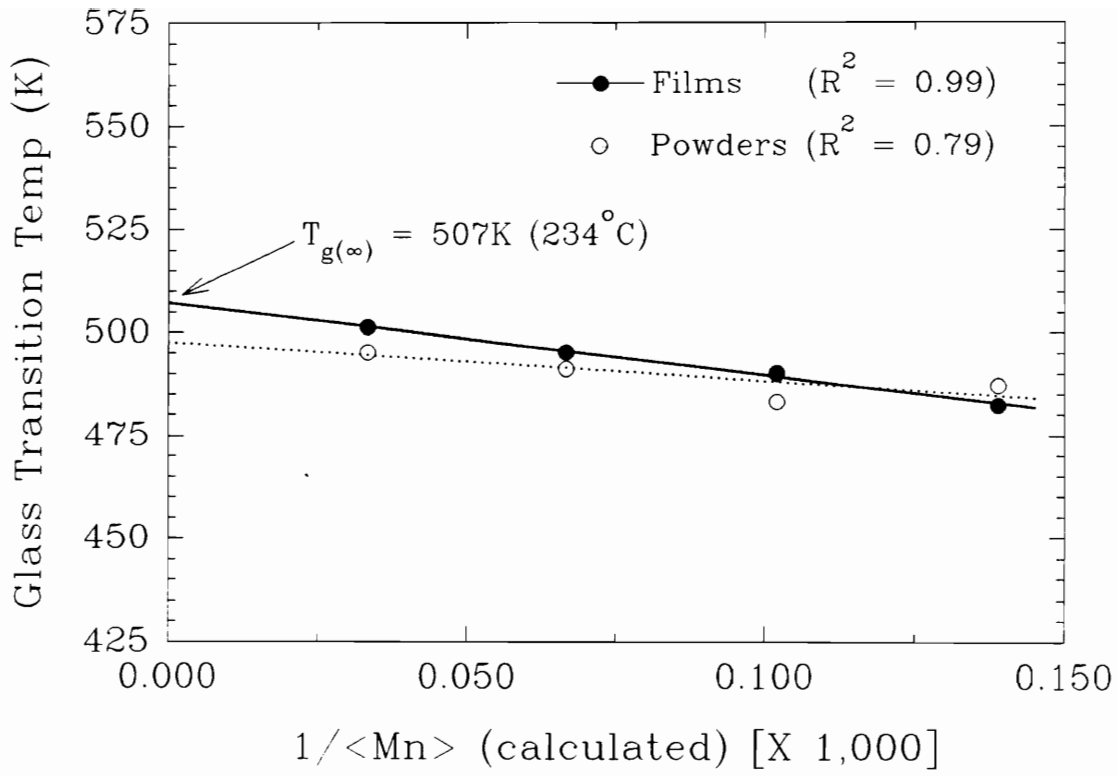

Figure 5.3 Plot of observed T_g as a function of inverse calculated molecular weight.

discussed in greater detail in section **5.2.4**.

It should be noted that the magnitude of the ordinate scales in both (a) and (b) of Fig. 5.2 is the same (4mW). Thus, the reduced magnitude of the second heat endotherms of the 7.5/f/d and 10.0/f/d can be visually compared to their first heat counterparts. It may be noted that the second heat scan of the 10.0/f/d film shown in Fig. 5.2 (b) reveals a slight recrystallization before melting. This reproducible feature is most likely the result of the elimination of crystal nucleation during the isothermal hold at 395°C. Upon the second heat from the glass the higher nucleation density initiates crystallization at a temperature above the T_g where chain flexibility is sufficiently high. A possible explanation for why this happens only in the 10.0/f/d material may be that the lower M_n of this material allows for a more rapid relaxation of the chains thereby allowing for the nucleation sites to be eliminated at the elevated temperature. The integrated area for the melting transition in the 2.5% offset film is shown (42J/g) to give the reader a visual reference of the magnitude of these transitions. Due to the non-uniform nature of these transitions, the integrated values are not shown for all peaks: no further meaningful information would be gained.

It is revealing that the conditions of the standard protocol were sufficiently intense to remove any trace of crystallinity in the 0 to 5% offset films. This indicates that the polymers are quite sensitive to time in the melt. An in depth analysis of the response of LaRC CPI-2 polymers to melt time and temperature is

presented in chapter 6.

Another point which deserves comment is that the shape of the first-heat curves shown in Fig. 5.2 (a) are slightly different than the thermograms of the same samples, excepting the 7.5/f/d, shown in Fig. 4−2. This is due to minor differences in the sample character due to variations in the film thickness and does not indicate any great difference in samples. The effect of film thickness on melting behavior is discussed in the next section.

5.2.2.1 Effect of film thickness

The thickness of the fully processed LaRC CPI-2 films varies from film to film. The average film thickness generally increases with increasing stoichiometric offset (0% to 10%) from 2.5 to 5.5 mils. This seems counter intuitive, considering that each film was cast at the same solids concentration of 15% (w/w) and that the higher molecular weight poly(amic acid)s have a greater solution viscosity. The lower viscosity poly(amic acid)s spread out to a thinner initial thickness: Though each film's initial thickness was controlled by spreading it out with a doctor blade set at a 30mil gap, the low molecular weight materials (7.5% and 10.0% offset) were of such low viscosity that their poly(amic acid)s did not remain within the confines established by the doctor blade. Thus, one would expect the low molecular weight films to be thinner than their higher molecular weight counterparts.

An explanation for the greater thickness in the higher stoichiometric offset films may be offered in terms of lateral shrinkage of the film. In addition to the solvent loss during thermal imidization crystallization also occurs with a consequent thickening effect. This is evidenced by the appearance of the films on their glass (or Pyrex®) substrates immediately after the thermal imidization procedure. Coincident with increasing stoichiometric offset (and nominal level of crystallinity) there is an increasing level of shrinkage and fracturing of the film and detachment from the substrate. So much so that, for the 10.0/f/d material, for example, a detached film boundary existed outside the perimeters of the imidized film -- at the original periphery of poly(amic acid). The film had apparently broken up and retracted away from its initial outline as solvent was lost and crystallization occurred[a]. In areas where shrinkage was great the film was broken up into curved platelets similar in appearance to sections of mud in a dry lake bed. The film's concave face was on the side of the substrate. As discussed in detail in section 5.3, this is a result of crystallization beginning at this surface and proceeding toward the air surface during the thermal imidization process. In fact, an amorphous layer remains at the air surface of each of the films after the full imidization procedure. The film curvature, then, is undoubtedly associated with

---

[a] *As the film shrank, pieces of glass (or Pyrex®) were pulled away from the rest of the substrate leaving a pock-marked surface on the substrate. The degree of pock-marking is directly related to the stoichiometric offset of the film being made: For the 7.5% and 10.0% offset films the effect is so great that glass (or Pyrex®) can only be used once per side.*

the uneven crystallization.

Though great care was taken to ensure that the substrates were kept level at all times during processing, the general character of the film is not consistent throughout: In addition to the generally uniform thickness over the majority of the film's area there are thin and thick regions of each film. The thicker regions are very much darker, opaque, brittle and curved than the thin sections. This appears to be the result of thickness only. That is, the darkness is not of sufficient magnitude to indicate that any decomposition has occurred. In order to provide a semi-quantitative perspective on the variance in thickness within the films three categories have been established: thin areas; most of film; and thick areas. The thickness values for these areas, in mils, is shown in Table 5.1 for each film. As can be seen from the third and fourth columns the thickness of the films generally becomes greater with increasing stoichiometric offset. We know that, as seen in Fig. 5.2 (a), the level of crystallinity also increases with increasing stoichiometric offset. Thus, the thickness increase parallels increases in crystallinity.

Table 5.1. Thickness of LaRC CPI-2 films (in mils).

Film	Thin areas	Most of film	Thick areas of film
0/f/d	Uniform thickness throughout at 2.5mils		
2.5/f/d	3.0	3.0	4.5 - 6.0
5.0/f/d	3.0	3.0	4.5 - 5.5
7.5/f/d	3.0	4.5 - 5.0	7.0 - 8.0
10.0/f/d	3.5	5.0 - 5.5	7.0 - 8.0

Thick and thin portions of the same film will provide a different thermal response in the DSC. For example, the DSC thermograms shown in Fig. 5.4 reveal a considerable difference in melting profiles between thin (3.0 mil) and thick (7.0-8.0 mil) portions of the 7.5/f/d film. In the DSC trace corresponding to the thin portion of the film the T_g can be clearly seen, followed by an exothermic crystallization prior to the characteristic multiple melting transition. Though the first melting transition is greatly reduced in magnitude the second is comparable to that seen in the thick portion of the film.

The apparent general correspondence between film thickness and level of crystallinity may be understood best in terms of chain mobility. In the low molecular weight poly(amic acid)s chain mobility is much greater than their high molecular weight counterparts. As imidization proceeds crystallization can occur to a much greater degree in these films with a concomitant increase in film thickness.

Differences in thickness/crystallinity *within* a particular film cannot be explained by differences in molecular weight [chain length]. However, chain mobility may still be the cause of the differences. Portions of the individual films which are greater in thickness quite possibly had a greater solvent fraction present which would have enhanced chain mobility. This, then, would have facilitated crystallization in a pseudo-'solvent induced crystallinity' effect. It is also possible that a greater nucleation density in these areas promoted more crystallization

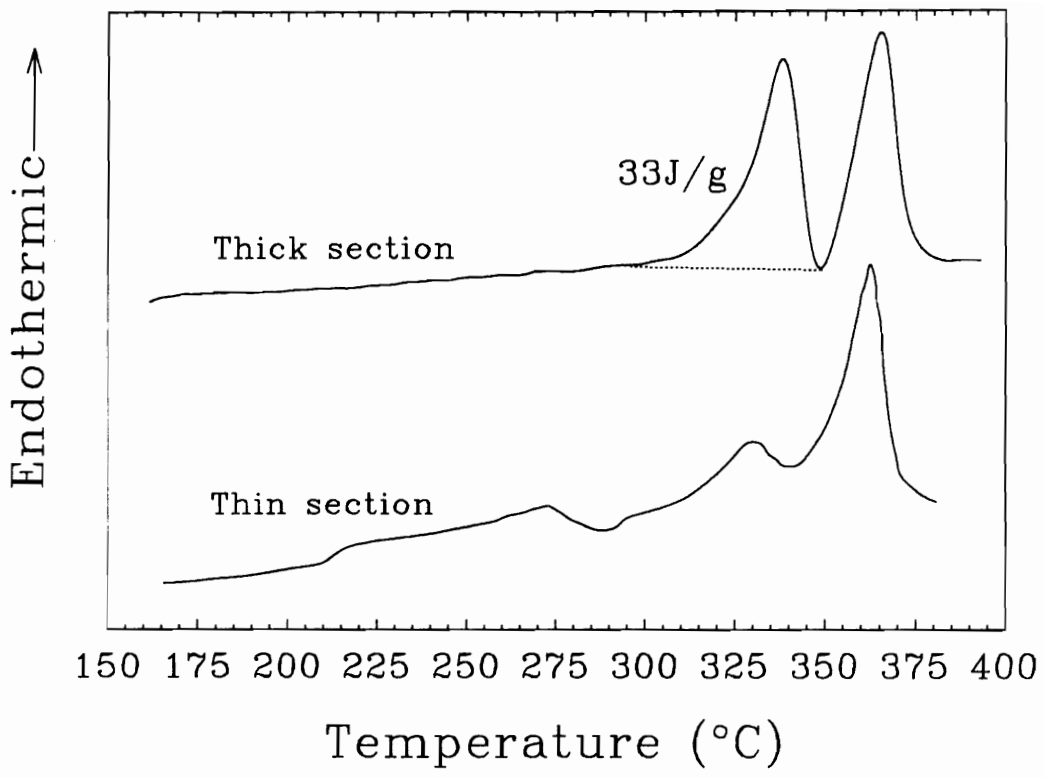

Figure 5.4 DSC thermograms of thick (7.0-8.0 mil) and thin (3.0 mil) portions of a 7.5/f/d film.

which, in turn, would have slowed solvent evaporation during thermal imidization.

Further complicating the understanding of the relationship between film thickness and properties is the fact that the level of imidization (degree of completion) may be dependent upon the thickness of the film. It is known that the rate of imidization is dependent upon the presence of solvent [38]; as solvent is lost the imidization rate slows. It is logical, then, to find that thicker films imidize to higher degrees than thinner ones as a result of a higher retention of entrapped solvent, as Ginsburg et al. found [54]. It should be remembered, however, that the differences in imidization level were primarily kinetic in origin. That is, with sufficient time at elevated temperatures the differences due to thickness were resolved [54]. Presumably differences in imidization levels would present different thermal responses in the DSC. Unfortunately, as discussed in section **5.3.3**, it is not possible to clearly quantify levels of imidization in LaRC CPI-2 films, so further speculation in this matter would be fruitless.

Regardless of the exact nature of the differences within individual films, it is important to note that they exist. Because the thermal response in the DSC is dependent upon the thickness of the particular sample being analyzed, some variations in thermal profile are present from sample to sample. In order to minimize these variations, and to provide comparable data for comparison between film types, specimens for all types of analysis (DSC, TGA, TEM etc...) were taken from the thicker sections of the films, where the levels of crystallinity

are greatest.

5.2.3 LaRC CPI-2 Powders Synthesized in DMAc

As in the case of the films it is useful to look at both the first and second heat scans of the powders -- see Fig. 5.5(a&b). Here the integrated value (62J/g) for the melting transition in the first heat scan of the 0/p/d material is shown to provide the reader with a qualitative reference of the magnitude of these transitions. As in the case of the films, the development of the dual endothermic response is dependent upon the stoichiometric offset. Here also, under the standard protocol conditions, only the two lowest molecular weight materials possess second heat melting transitions. As noted earlier (and shown in Fig. 5.3), the T_g values decrease with decreasing molecular weight. It should be noted that the magnitude of the ordinate scales in both (a) and (b) of Fig. 5.5 is the same, but larger than that used for Fig. 5.2 (a&b), 9mW versus 4mW.

Several interesting features are presented by the DSC analysis of the powder samples. The discussion of these is most profitable in terms of a comparison with the films and is thereby presented in the next section.

5.2.4 Comparison of LaRC CPI-2 Films and Powders Synthesized in DMAc

Looking at the juxtaposition of the LaRC CPI-2 films and powders provides some interesting insight into the effect of processing on this polymer. As

can be seen in Fig. 5.5(a), the first heat thermograms of the powders are very different than their film counterparts shown in Fig. 5.2(a). Immediately apparent is the presence of a melting transition in the 0% offset powder while there is a lack of one in the corresponding film. This would indicate that there is a very strong solvent effect. The reader is reminded that both the film and the powder for these 0% LaRC CPI-2 polymers were derived from the same poly(amic acid) batch. It is unlikely that the 0% offset powder was of dramatically lower molecular weight. Furthermore, the T_m for this powder is *higher* than the successively lower molecular weight powders -- see Fig. 5.5(a). Thus, it appears that there is likely a solution-induced crystallization process occurring in the powders during processing. This is, undoubtedly, a fairly complicated process in that the development of crystallinity is occurring during the imidization process 'in' solution. The reader is here reminded of the fact that the LaRC CPI-2 powders precipitate from solution during the thermal imidization process, as described in chapter 3. It is quite possible that the development of crystallinity is the *reason* that the powders precipitate from solution during processing. The concept of simultaneous imidization and crystallization is certainly not an unreasonable possibility. As described in the next section (**5.3**) this appears to be what is occurring during processing of the films: Crystallinity develops very early in the stepwise thermal imidization process.

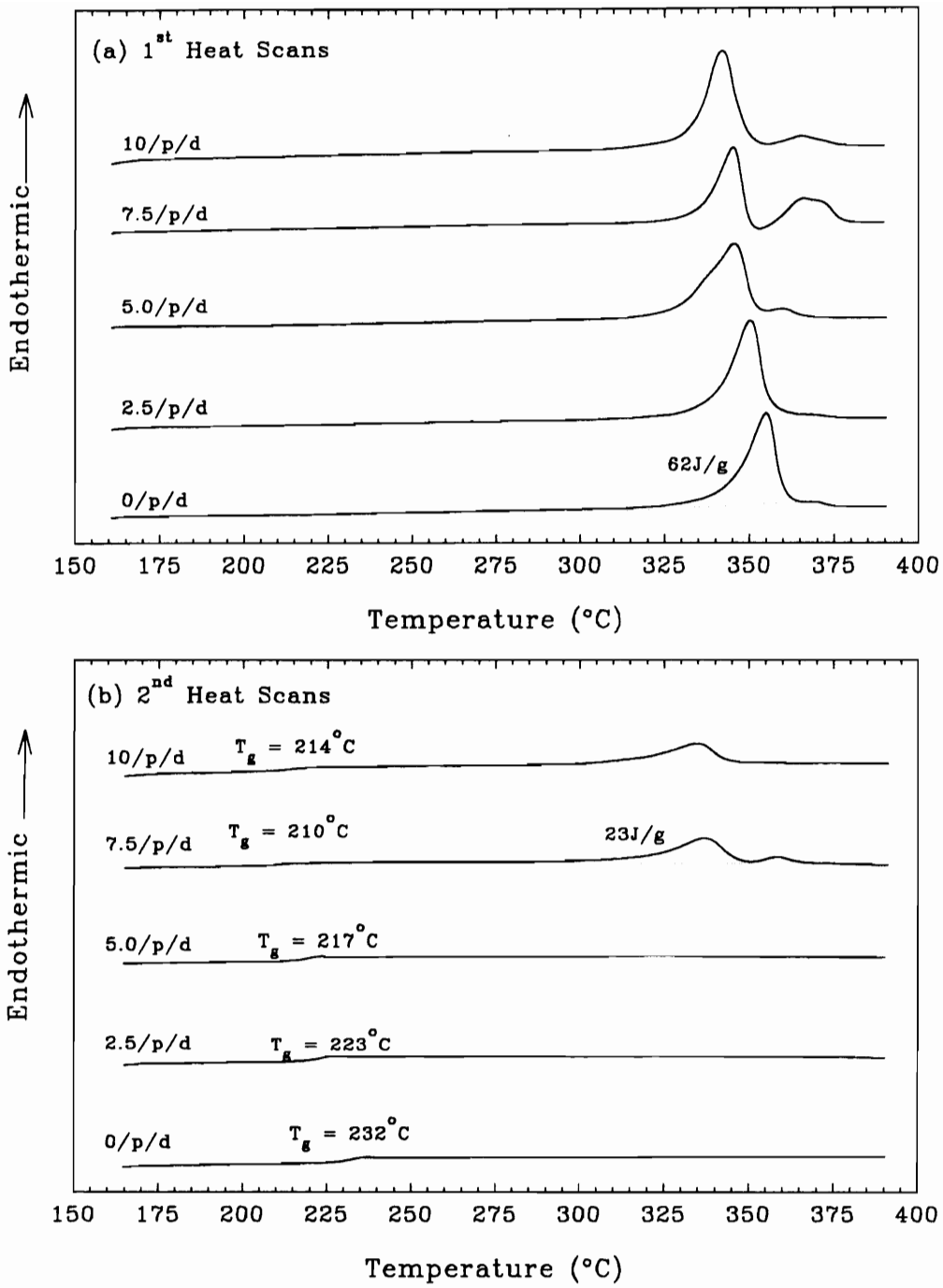

Figure 5.5 First (**a**) and second-heat (**b**) scans of a series of powders, in increments of 2.5% stoichiometric offset from 0% to 10%.

Comparing the first melting T_m values for the powders shown in Fig. 5.5(**a**) to those of the films in Fig. 5.2(**a**) it can be seen that both series follow a trend of decreasing T_m with decreasing molecular weight. Likewise the development of the second melting transition is developed at the lowest molecular weights in the powders, though its presence is not as pronounced. It is also notable that the first melting T_m values for the powders appear to be generally higher than the corresponding values for the films. A comparison of these values is presented in Table 5.2. In each case the powder value is higher. One might be tempted to conclude from this that the powders may have a slightly higher molecular weight. A comparison of the T_g values from the second heat scans, however, does not support this -- see Table 5.3. The powder T_g's are generally lower, which is inconsistent with them being of a higher molecular weight. The apparent deviation of the 10.0/f/d having a lower T_g may be the result of its more amorphous character as indicated by the crystallization exotherm during the second heat as seen in Fig. 5.2(b).

In order to better compare the thermograms of the films and powders which display crystallinity in the second heat scans (7.5% and 10.0% offset), they have been re-plotted as shown in Fig. 5.6. The T_m's of the respective stoichiometric offset polymers match up well: ca. 336°C for the 7.5% offset materials and 335°C for the 10% polymers. The relative magnitudes of the transitions also match well. This supports the proposition that a solution

Table 5.2. Comparison of first-heat peak melting transition temperatures of the lower endotherms (T_{m1}) in LaRC CPI-2 powders and films.

% Stoichiometric Offset	1st Heat T_{m1} Film (°C)	1st Heat T_{m1} Powder (°C)	Difference in 1st Heat T_{m1} (°C)
0	none	335	---
2.5	340	350	+10
5.0	339	345	+ 6
7.5	338	345	+ 7
10.0	337	342	+ 5

Table 5.3. Comparison of the glass transition temperatures, T_g (taken from the second heat scans), in LaRC CPI-2 powders and films.

% Stoichiometric Offset	T_g Film (°C)	T_g Powder (°C)	Difference in T_g (°C)
0	233	231	-2
2.5	228	222	-6
5.0	222	218	-4
7.5	217	210	-7
10.0	209	214	+5

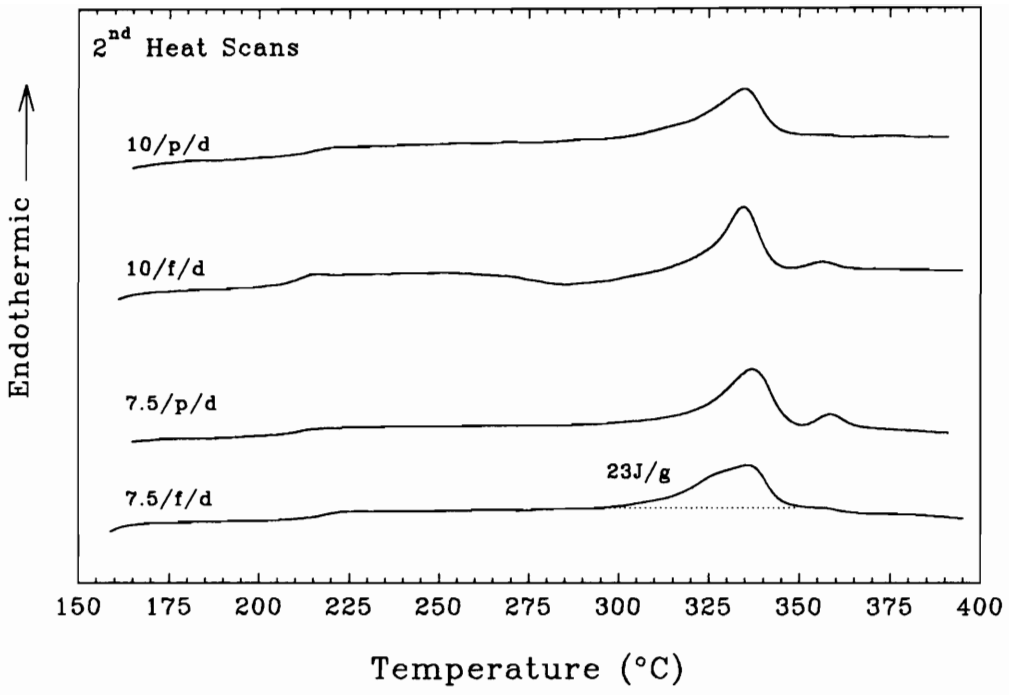

Figure 5.6 Second heat scans of 7.5% and 10.0% offset films and powders.

crystallization effect has played a role in the initially higher T_m's and heats of fusion for the powders.

5.2.5 Summary of DSC Analysis

Several interesting observations have now been presented and discussed with regard to DSC analysis of LaRC CPI-2 powders and films. Firstly, it was shown that the presence of the dual melting transition in the second-heat scan is very much dependent upon the conditions of the heat cycle. This provides a glimpse into the melt sensitivity of these materials which will be discussed in much greater detail in chapter 6. It was also shown that, in addition to the obvious differences in crystallinity with changing molecular weight, there are differences between, and within, film samples. Furthermore, these thickness differences effect the thermal response of the films. Dramatic differences in melting behavior between films and powders were also presented and discussed. Powders generally melt at a higher temperature than films of the same molecular weight. An explanation for these differences was given in terms of a solution induced crystallinity effect in the powders. The glass transition temperature, T_g, of both the powders and films are found to be dependent upon molecular weight. An extrapolated value of T_g for the infinite molecular weight LaRC CPI−2 is ca. 234°C.

5.3 Thermal Imidization of LaRC CPI-2 Films

5.3.1 Thermal Imidization of LaRC CPI-2 and other Polyimides

The synthetic method for the production of LaRC CPI-2 polyimide films involves stepwise thermal imidization of a poly(amic acid) cast from dimethyl acetamide (DMAc) or n-methyl pyrrolidinone (NMP), wherein the film undergoes isothermal staging for one hour each at 100°C, 200°C and 300°C. This stepwise thermal imidization cycle, originally developed by researchers at NASA [46], has been adopted by many others in the production of a variety of polyimide films [47 - 51].

Many studies have been conducted to study the mechanisms and side reactions involved during thermal imidization of poly(amic acid)s [14, 44, 117, 118]. In the study of the thermal imidization of poly(amic acid) films derived from oxydianiline (ODA) and pyromellitic dianhydride (PMDA), Feger et al. [14, 15] showed that a complex formed between the poly(amic acid) and the solvent medium, 1-methyl-2-pyrrolidinone (NMP). This interferes with imidization until decomplexation occurs at higher temperatures (ca 350°C), at which point the newly freed NMP acts as a plasticizer and facilitates imidization. This conclusion is supported through FTIR studies by Snyder et al. [118]. Here a significant presence of side reactions resulted from imidization (of the same polymer-solvent system) at lower temperatures, whereas closed ring imide formation predominated

at higher temperatures (>400°C). Young et al. [44] analyzed the process of thermal imidization of soluble polyimide films. Here the researchers were able to accurately track molecular weight with degree of imidization in N,N-dimethylacetamide (DMAc). They found a dramatic reduction in molecular weight during thermal imidization which reached a minimum at temperatures between 150°C-200°C. As the imidization temperature increased beyond this range, the molecular weight values increased. The final polyimide reached <Mn> values of about 60% that of the original poly(amic acid) value of 106,000 g/mole. In a study which investigated many aspects of crystallinity in a semicrystalline polyimide similar in structure to LaRC CPI-2, Pratt et al. [119] observed the development of crystallinity during thermal imidization using a procedure similar to the one currently under study. The development of crystallinity, as calculated from WAXD, appeared to follow a somewhat convoluted non-linear course with the level of imidization. The objective here was to study the crystalline changes occurring in an aromatic polyimide during a standard stepwise thermal imidization cycle used in the processing of LaRC CPI-2, as well as by many others in the processing of polyimides.

5.3.2 Experimental Approach

For the stepwise thermal imidization study, the polymerization through the amic acid stage followed the standard format as described in chapter 3. Some

deviation was necessary in order to obtain samples for subsequent analysis. The specific synthetic process was as follows: 1,4-bis(4-aminophenoxy-4'-benzoyl)benzene (1,4-BABB) (0.01318 mole) was reacted with oxydiphthalic dianhydride (ODPA) (0.01219 mole) and phthalic anhydride (PA) (0.00198 mole) to form a phthalic anhydride endcapped poly(amic acid) with a calculated number average molecular weight of ca. 9,700 g/mole as per the Carother's relationship [27]. The solids content was 15% (w/w) in dimethyl acetamide (DMAc). The reaction proceeded under a dry nitrogen blanket, at room temperature with stirring, for 27 hours. The poly(amic acid) was then removed and centrifuged for approximately 1 hour and then cast onto clean, dry Pyrex plates and spread out with a doctor blade set at a 30mil gap. The average thickness of the fully cycled films was approximately 7 mils[b]. The films were dried under forced dry air for 18 hours at room temperature. Imidization proceeded by placing the films in a Fisher IsoTemp programmable forced air oven for 2 hours at 50°C before the oven was heated at 5°C/minute to 300°C with one hour isothermal holds at 100°C, 200°C and 300°C. The oven was then allowed to cool at -5°C/min to ca. 50°C.

A schematic representing this thermal profile is shown in Fig. 5.7. Film samples labeled as **'a'-'i'** were removed at specific stages during the imidization process, as shown in Fig. 5.7 and Table 5.4. It is a necessary consequence of the removal of film samples during the imidization process that the oven

---

[b] *This value represents the thicker portions of the film which were used in this study.*

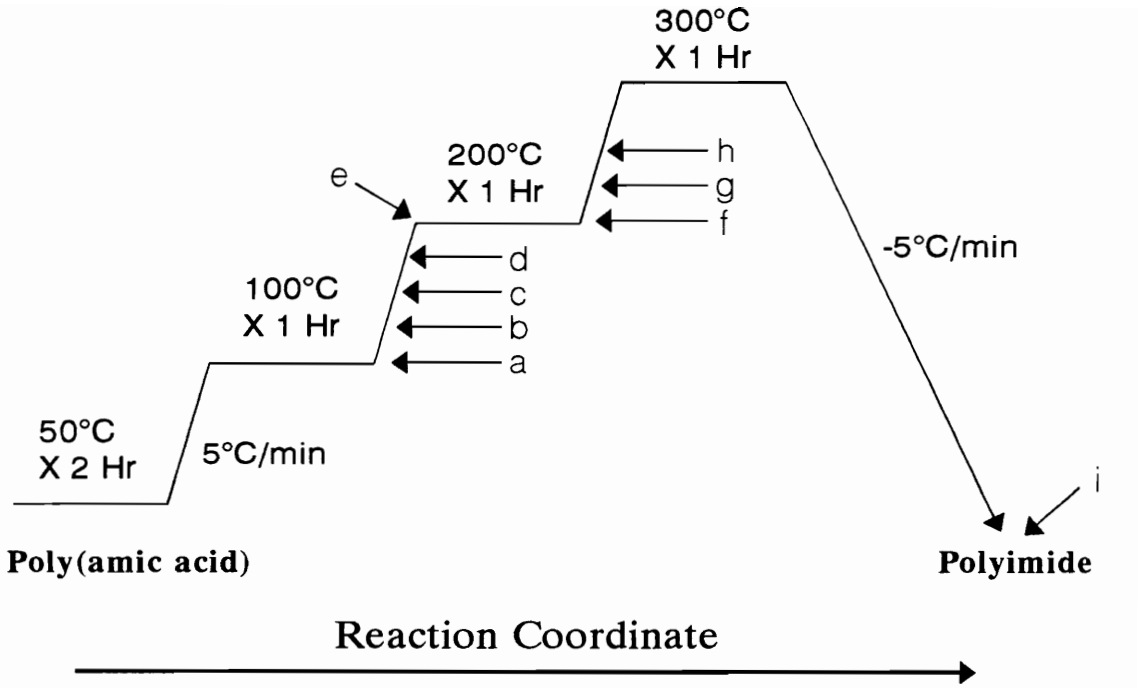

Figure 5.7. Stepwise thermal imidization profile.

Table 5.4. Sample identification for stepwise thermally imidized films, 'a' through 'i'.

Film Sample ID	Temperature (°C)	Time at Temperature (Hr)
a	100	1
b	125	0
c	150	0
d	175	0
e	200	0
f	200	1
g	225	0
h	250	0
i	300	1*

*Film sample 'i' held at 300°C for one hour plus the −5°C/minutes cool down to ca. 50°C.

environment is temporarily disturbed. This disturbance was minimized through rapid sample removal and minimal ambient air exposure to the chamber. At temperatures higher than 250°C the oven could not recover quickly from the heat lost during sample removal. Hence, no samples were taken beyond 250°C until the cycle was complete and the final sample 'i' was removed at room temperature. The films were removed from the Pyrex plates by soaking in ca. 50°C water for approximately one hour. The films were then allowed to air dry.

5.3.3 Infrared Spectral Analysis

Ideally, the degree of imidization would be quantified for all stages of this stepwise process. Fourier Transform Infrared Spectroscopy (FTIR) analysis is typically employed to achieve this objective by tracking the development of the characteristic imide band ca. 1777cm^{-1}. For quantitative results the FTIR spectra must be normalized to some peak that is unaffected by the chemical changes occurring during imidization. In a study following thermal and microwave imidization in an aromatic polyimide containing ketone and ether connecting groups, Kishanprasad and Gedham [120] normalized the spectra intensity using an aromatic absorption band at 1500cm^{-1}. In the present study it was found that the reaction solvent, DMAc, presented a peak which greatly overlapped this aromatic band. No other available IR bands, common to both the imide and amic acid, were left unaffected by the imidization process. Hence, quantification of the degree of imidization was not possible in the LaRC CPI-2 system. It was noted,

however, that the presence of an anhydride band, at ca. 1850cm^{-1}, was not found in any of the film samples. This indicates that there was no significant amount of chain scission occurring during the imidization process, as has been noted by some researchers [44, 68].

5.3.4 Wide Angle X-Ray (WAXD) Analysis

Wide angle X-Ray diffraction (WAXD) was employed in order to quantify the changes in the amount of crystallinity during imidization. A common procedure for the determination of the degree of crystallinity in polymers is known as the method of Hermans and Weidinger [121, 122]. Here several WAXD scans of a polymer with differing amounts of crystallinity are normalized with regard to their X-Ray optical density and the incoming beam intensity. Then the areas corresponding to the crystalline and amorphous halo regions are then determined by forming a demarcation line between the amorphous and crystalline regions. These areas are used to solve a set of linear equations in which the areas for the 100% crystalline and 100% amorphous material can be determined. The linearity of the relationship between the crystalline and amorphous areas is used to confirm the validity of the technique and accuracy of the results. Further confirmation is presented in terms of the match between the mathematically determined 100% amorphous area and the area from a completely amorphous sample. In the present study the optical densities of the film samples were very

low and small fluctuations in beam intensity greatly disrupted the normalization values for the scans. Consequently, the desired linear relationship was not achievable. Lacking this internal validation, great care was taken to use a consistent method for the demarcation between the crystalline and amorphous regions. A single amorphous halo profile that best fit all diffractograms (when scaled to the proper intensity) was chosen in order to eliminate errors introduced by changing curve shapes. All integrations were taken from 11° to 35° two-theta. The reproducibility of this method to estimate the level of crystallinity was found to be plus or minus 2%. It should be noted that the crystal percent values presented here do not represent absolute values but, rather, provides an index of the crystallinity. The self consistent method, however, allows for the determination of trends in crystallinity.

Figure 5.8 shows the WAXD patterns for the thermally staged films. The first evidence of crystallinity appears in the 150°C imidized film, sample 'c', whereby the analysis just described provided 18% crystallinity. The crystalline content increases significantly along the reaction coordinate to about 39% at stage 'f' (200°C for 1 hour). Thereafter, only gradual changes occur until the final stage is reached and the crystalline fraction increases by a modest jump of 4% to 46% crystallinity for sample 'i'. It is notable that a considerable increase in crystallinity occurs during the 1 hour staging at 200°C.

5.3.5 Thermal Analysis

DSC of the series of films reveals complex changes occurring in the films in the sub-melting temperature range of the least imidized films-- Fig. 5.9. In the 150°C to 200°C temperature range the thermograms of films **'a'** and **'b'** display large multiple transitions, while at higher temperatures the dual melting transitions characteristic of this polyimide are evident. Since these films were completely amorphous before DSC analysis, it is clear that a crystallization process occurred during heating in the DSC. TGA scans of the series of films, shown in Fig. 5.10 reveals a mass loss beginning in the 150°C region for the least imidized films which shifts to progressively higher temperatures with increasing imidization. The significant weight loss of approximately 20% for films **'a'** and **'b'** in the 150°C to 200°C region correlates well with the multiple transitions seen for these films in the DSC traces. Thus, these transitions are believed to be caused by a combination of several overlapping endothermic and exothermic events. Most assuredly, solvent loss and crystallization are occurring, which may be accompanied by imidization, as well. It is noteworthy that there is a dramatic difference in the TGA loss profiles for the two 200°C film samples. Sample **'e'**, taken at the beginning of the 200°C isotherm, loses considerable mass below 200°C. Sample **'f'**, held at 200°C for one hour, begins to loose significant mass in the 225°C region. This parallels a considerable increase in the crystallinity from 32% to 39%. Thus, during this isothermal hold at 200°C, solvent is lost with a

concurrent increase in the crystallinity .

In general, it is apparent that the magnitude of the changes in crystallinity at each stage paralleled the weight loss profiles for the film samples. The crystallization process that began between 125°C and 150°C steadily increased the crystal fraction until the film had been held for one hour at 200°C (sample **'f'**). Here a plateau was reached, at about 40% crystallinity, where only modest changes in crystallinity occurred by processing to 250°C (sample **'h'**). The TGA thermograms clearly show a significant weight loss for the samples leading up to sample **'f'**, corresponding to the region where the greatest increases in crystallinity occurred. Similarly, a plateau in the weight loss curves is noted for samples **'f'-'h'**, see Fig. 5.10. The modest difference in the TGA loss profiles between sample **'h'** and the fully imidized sample **'i'**, parallels the modest increase in crystallinity of about 4%. Since the total weight loss due to the water of imidization is only on the order of 5%, it is safe to relate the TGA profiles to primarily solvent loss. The correspondence between weight loss and crystalline development can be attributed to the mobility of the polymer chains. In the stages that show dramatic changes in crystallinity, residual solvent caused a plasticization effect which provided greater chain mobility thereby allowing crystallization to proceed. Concurrent with this effect, the glass transition temperature of the polymer undoubtedly increased as imidization proceeded. Thus, a combination of a low glass transition temperature and plastization promoted dramatic crystallization

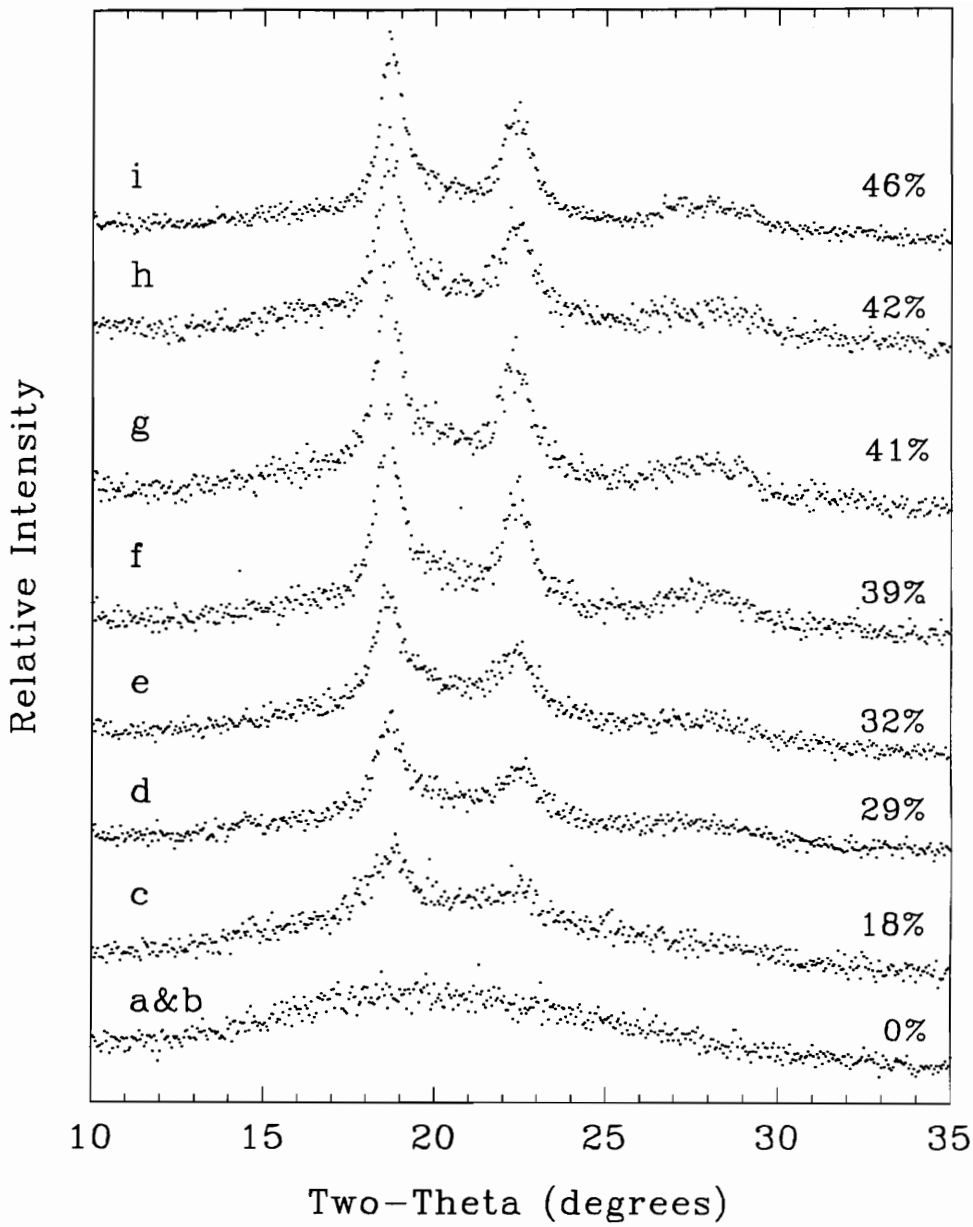

Figure 5.8. Wide angle X-ray diffraction (WAXD) scans of thermally staged films, **'a'** through **'i'**.

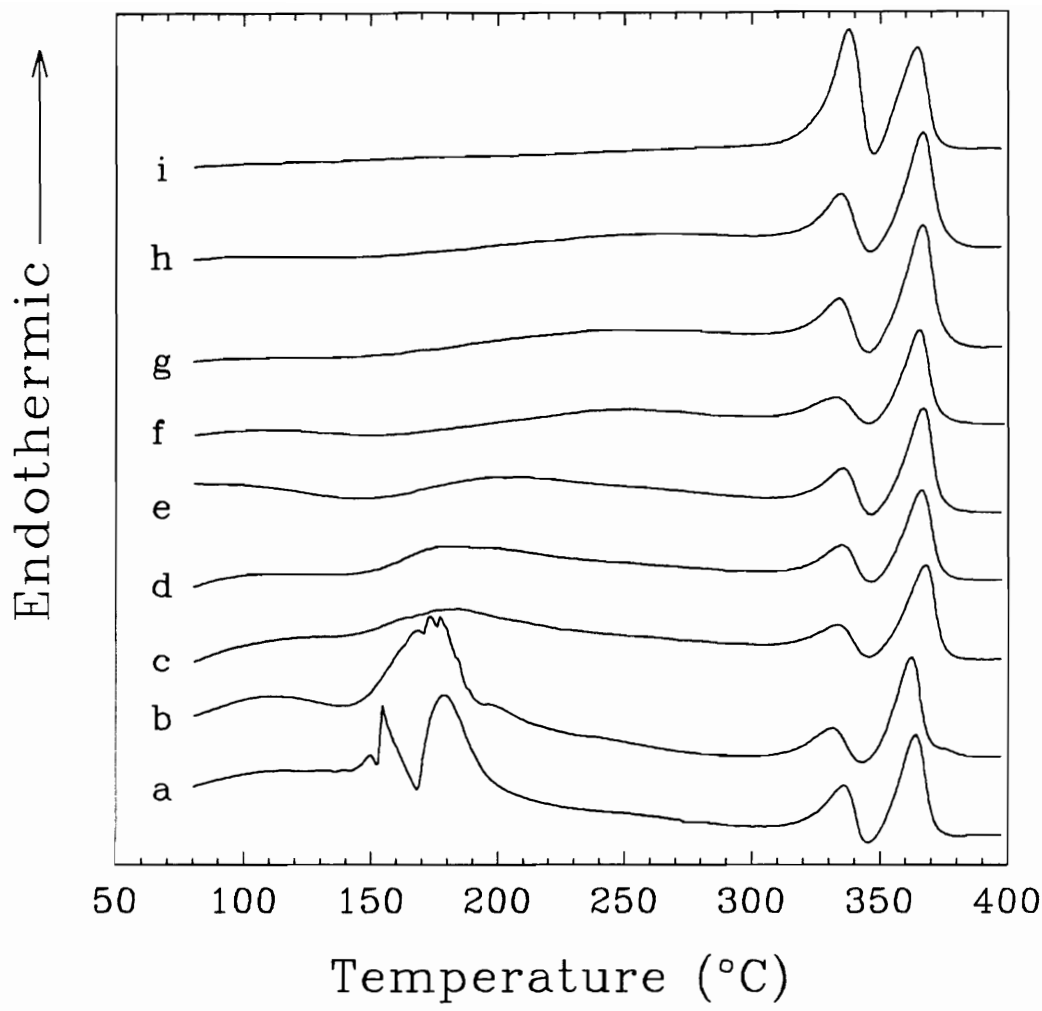

Figure 5.9. Differential scanning calorimetry (DSC) thermograms for the thermally staged films, 'a' through 'i'.

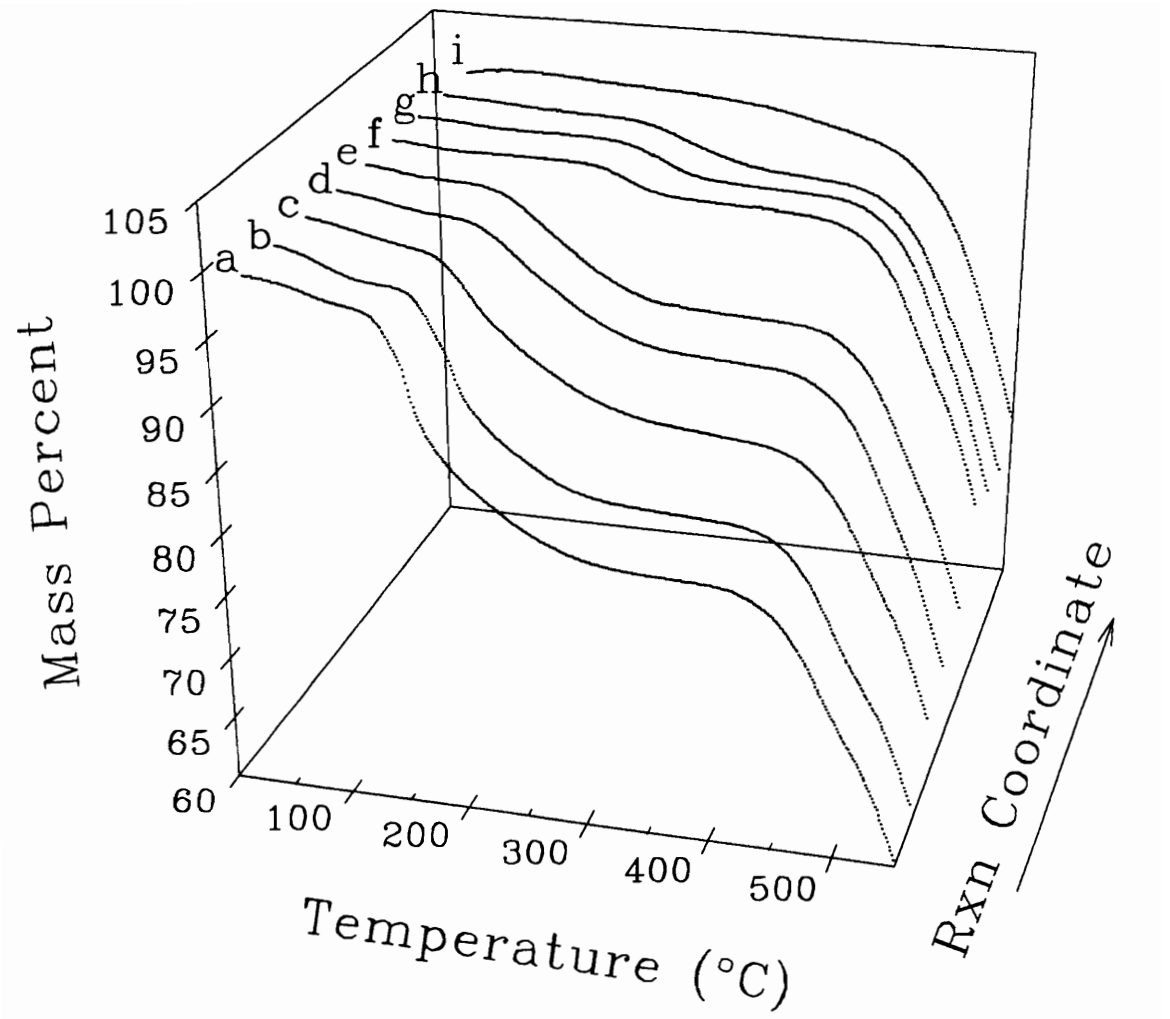

Figure 5.10. Thermogravimetric analysis thermograms of the thermally staged films, **'a'** through **'i'**.

changes in the early stages of the thermal treatment. As solvent was lost and imidization proceeded, chain mobility was restricted and crystalline changes were less dramatic.

5.3.6 Small Angle X-Ray (SAXS) Analysis

SAXS analysis provides an interesting insight into the development of the crystalline superstructure during the imidization process. Figure 5.11 shows SAXS profiles of the stepwise imidized films plotted as the smeared intensity as a function of **s**, where $\mathbf{s} = (2/\lambda)\sin(\Theta/2)$, λ is the wavelength and Θ is the radial scattering angle. As samples **'a'** and **'b'** are completely amorphous there are no scattering centers. As expected the curves for these samples display a monotonically decaying curve at low **s** values. Samples **'e'** through **'i'** all show a scattering profile where the peaks are well defined. The 'peak' positions for films **'c'** and **'d'** are not easily resolved, however. Thus, no clear information may be gained from these curves as presented.

Given that the scattering centers for these curves are lamellar in texture with the lateral length very much greater than the thickness (at least 2 orders of magnitude), it is appropriate to apply the Lorentz' correction for platelike structures. This operation corrects the scattered intensity for the random orientation of the lamellar plates (with respect to the X-ray beam) and the amount of actual radiation observed as a result of an intersection of the scattered

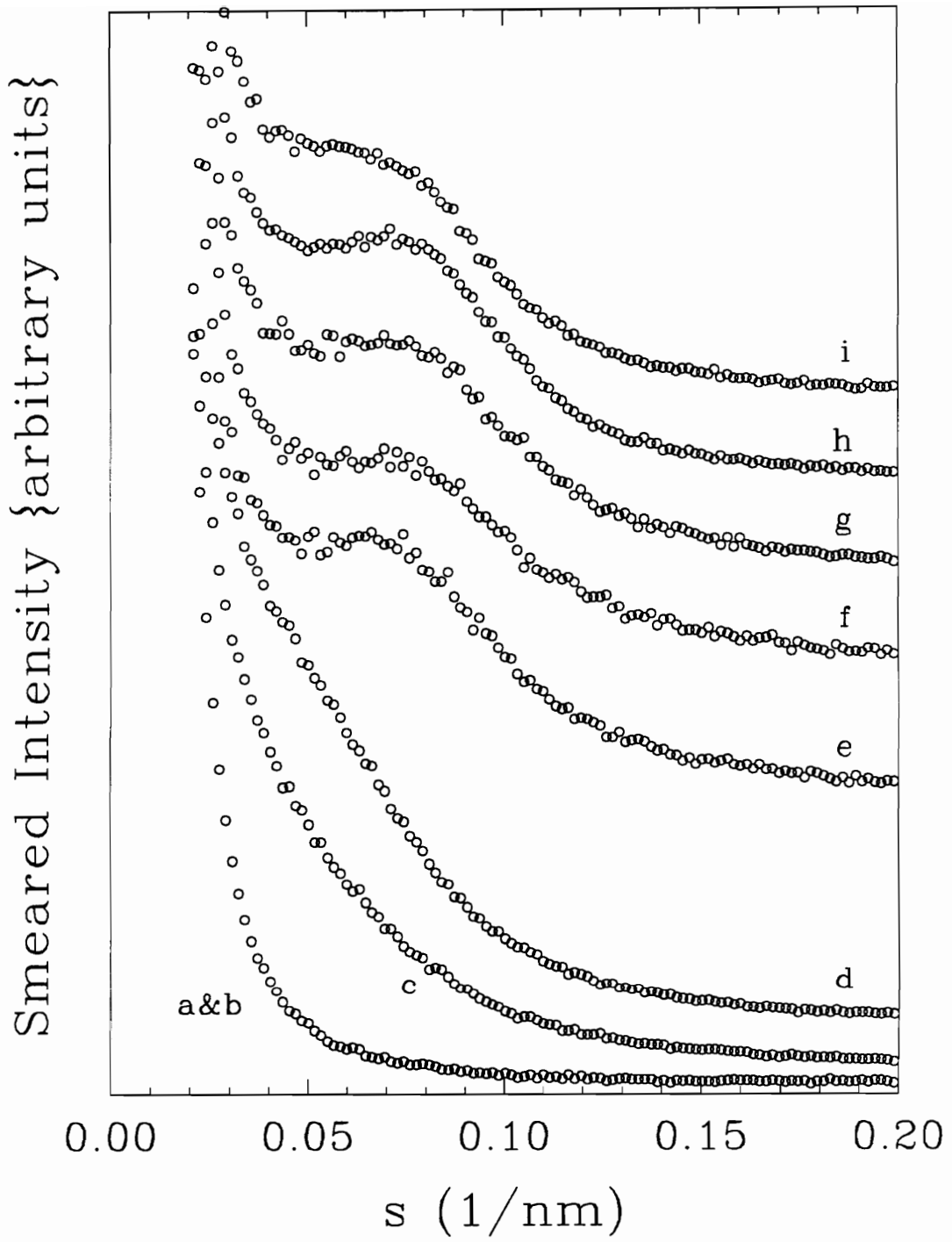

Figure 5.11 Small angle X-ray scattering (SAXS) scans for the thermally staged films, **'a'** through **'i'**.

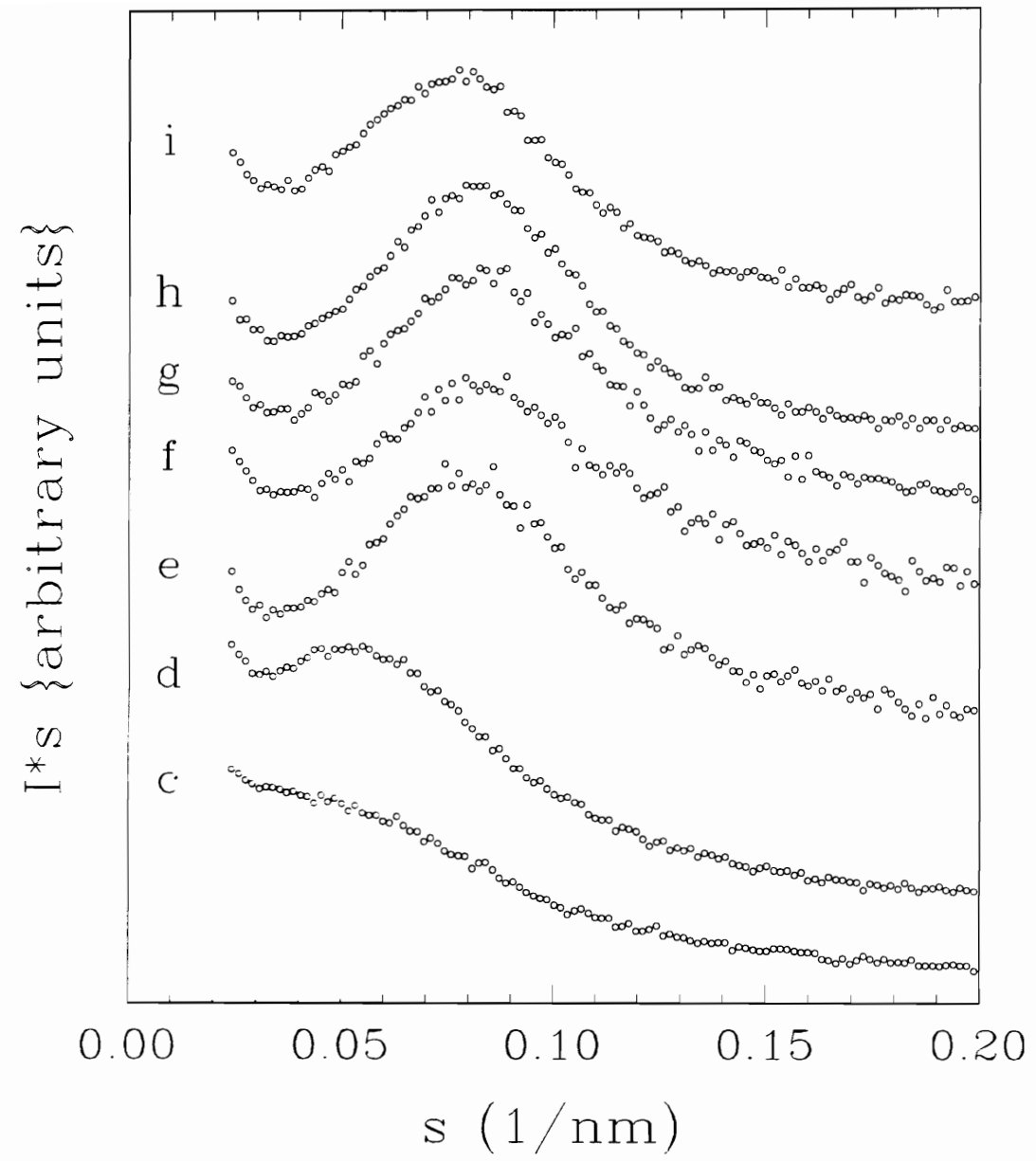

Figure 5.12 Lorentz plot of the small angle X-ray scattering (SAXS) scans for the thermally staged films, 'a' through 'i'.

radiation (in reciprocal space) with the Ewald sphere [123 - 125]. In this case of lamellar plate scattering from slit smeared SAXS data, the Lorentz' correction is a multiplier of **s**. That is, I(corr) = I(obs)*s. A consequent effect of this correction is an enhanced peak resolution which allows for a more quantitative comparison of the long spacings discussed above. Analyzing the peak positions, thus created and shown in Fig. 5.12, one finds that the long spacing is quite large for the low crystallinity samples '**c**' and '**d**' (200Å and 180Å, respectively). The long spacing drops dramatically for sample '**e**' to about 130Å. Samples '**f**' through '**h**' all exhibit long spacings on the order of 120Å. As a result of the final staging of the films the long spacing increases slightly to a value of about 130Å for sample '**i**'. Figure 5.13 shows these trends in the long spacing along with the changes in bulk crystallinity. A possible explanation for the dramatic drop in long spacing may be found in terms of a lamellar in-filling (insertion) process and/or a contraction of the amorphous phase. In the earliest stages of crystalline development, below 29%, widely spaced lamellae are formed at about 200Å apart in sample '**c**' and 180Å in sample '**d**'. As the degree of crystallinity increases, lamellae are inserted between the previously formed lamellae dramatically lowering the long spacing to about 130Å for sample '**e**' and 120Å for samples '**f**' through '**h**'. A lamellar insertion mechanism of this kind was first proposed by Keller [126] to explain a drop in SAXS long spacing during isothermal crystallization of isotactic polystyrene. A similar drop in long spacing was found by Hsiao et al. [127] during

the isothermal crystallization of poly(aryl ether ether ketone). Here also a lamellar insertion mechanism was used to explain the results. In the present case a contraction of the amorphous phase between adjacent lamellae during imidization and crystallization may also be occurring, which could help account for these results. The increase in long spacing in the final stage may be the result of an isothermal lamellar thickening process, wherein the distance between the scattering centers is increased slightly. As will be shown in the next section, new crystalline superstructures are developed late in the imidization process. It is possible that the formation of inherently thicker, new lamellae, at the higher temperatures is sufficient to cause an increase in the long spacing.

5.3.7 Transmission Electron Microscopy (TEM)

TEM analysis reveals that the crystalline superstructure development is non-uniform. The superstructure appears to develop at the glass surface of the film and progress upward with increasing thermal staging with some spherulites isolated in the amorphous layer above the crystal growth front. This would imply that the glass acts as a nucleating surface and a self-nucleation process occurs as the crystal growth front progresses toward the air surface. In all the film samples, excepting sample 'i', a sizable amorphous layer (ranging from approximately 4 to 25% of the film thickness) exists at the air surface. In sample 'i' the amorphous layer is very thin, on the order of 1 micron which is less than 0.5% of the film

thickness. Figures 5.14 and 5.15 show the TEM cross-sections for samples **h** and **i**, respectively. The crystalline and amorphous regions are near the air surface of the films. The arrows indicate the vertical direction from the glass to air surface.

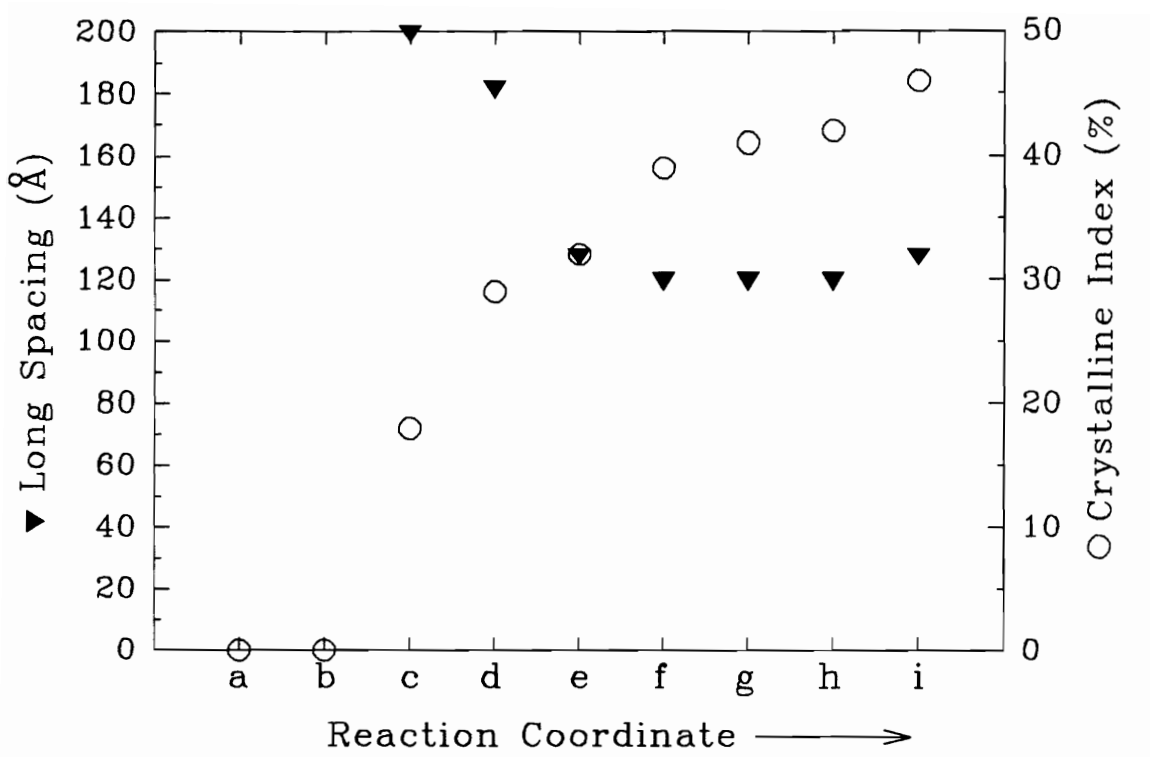

Figure 5.13 Results of SAXS and WAXD analysis showing the long spacing and crystalline index, respectively.

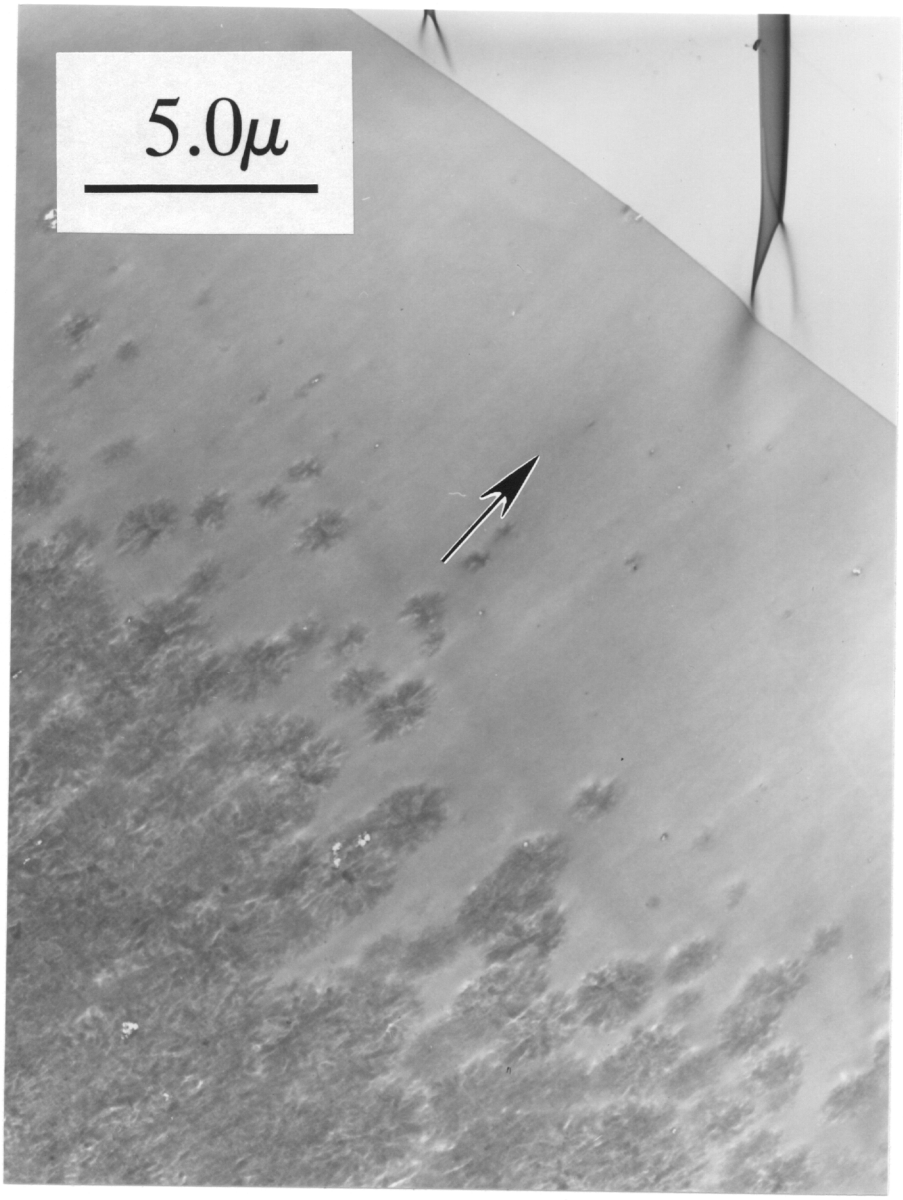

Figure 5.14 TEM micrographs of cross-sections of sample 'h'. The crystalline and amorphous regions are near the air surface of the film. The arrow indicates the vertical direction from the glass to air surface.

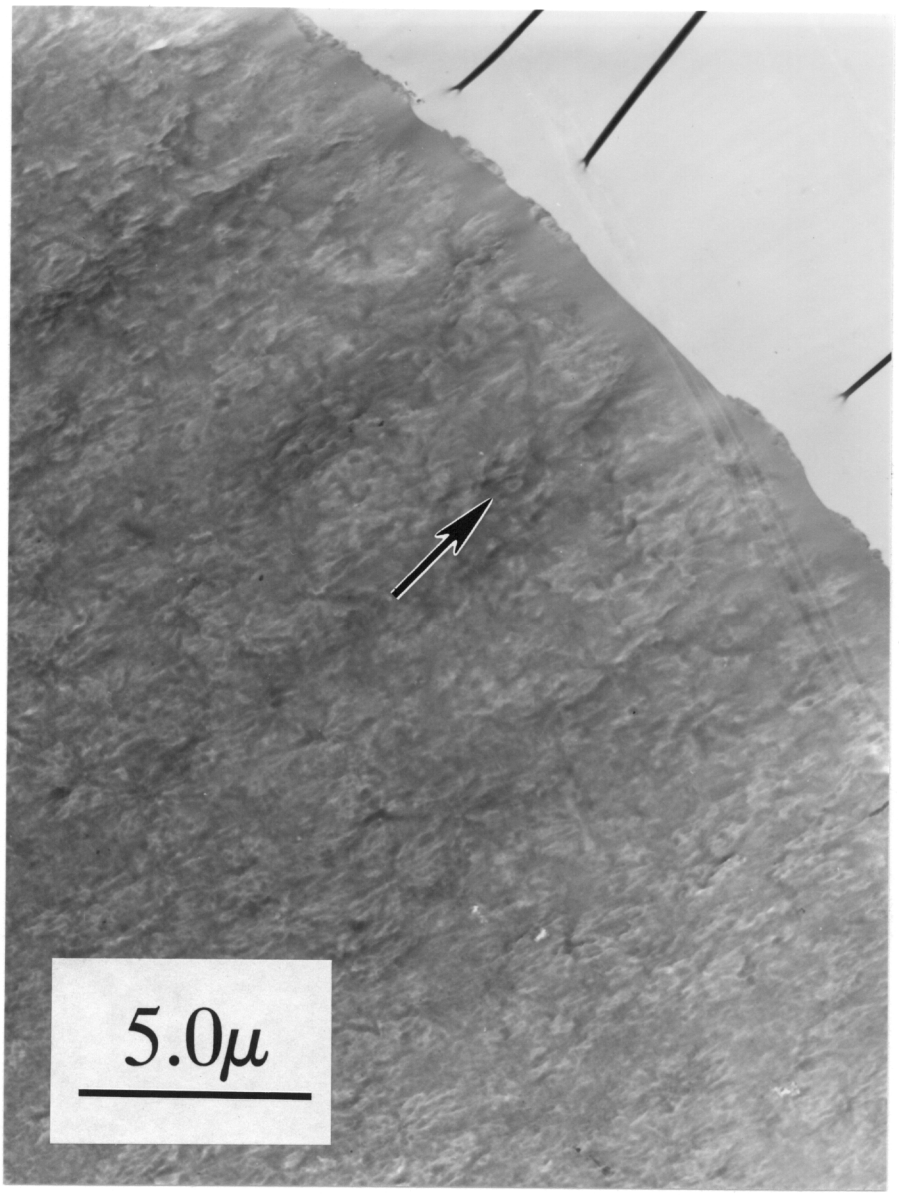

Figure 5.15 TEM micrograph of a cross-section of sample 'i'. The crystalline and amorphous regions are near the air surface of the film. The arrow indicates the vertical direction from the glass to air surface.

The considerably larger amorphous layer in the incompletely staged film **h** is readily apparent (approximately 10-13 microns). The 'filling-in' of the amorphous layer with crystal superstructure in the last thermal stage corresponds well with the final increase in crystallinity for sample 'i'. It is notable that there exists a large amorphous layer in the early staged samples where the crystalline index is low. For example, in sample 'c' approximately 20 to 25% of its thickness is amorphous. Thus, the crystalline index for that part of the possessing crystalline superstructure is actually much higher (on the order of 24%).

As was discussed in section **5.2**, LaRC CPI-2 displays a strong dependence of the level of crystallinity upon the molecular weight of the polymer. Thus, one would expect that the progressive development of crystallinty from the glass to the air surface also to depend upon molecular weight. That is, higher molecular weight samples should have larger amorphous zones at their air surface because of an overall lower rate of crystallization. TEM cross sections of fully imidized films with varying molecular weights, as calculated from the Carothers relationship, showed that the expected trend is present (TEM micrographs not shown). The amorphous layer thickness, along with the percentage of the total film thickness of approximately 4 to 8 mils, for the fully imidized films, ranked along with sample **i** is: 15μm(11%), 4μm(3%), 1μm(0.5%) and 0.5μm(0.3%) for films with calculated molecular weights of 30,000, 15,000, 9,700 and 7,200, respectively. All of these films were produced in the same fashion including the percent solids

concentration at the time of casting the poly(amic acid)s. Presumably differing solvents, solids concentrations and temperature profiles would have an effect on the extent of the amorphous layer. It may be noted here that a necessary consequence of a final film product possessing a thin amorphous layer on the surface would be an inherent susceptibility to chemical attack at that surface.

5.3.8 Scanning Electron Microscopy (SEM)

Scanning Electron Microscopy (SEM) provides another perspective of the amorphous layer that remains at the air surface of the films. SEM images also help to explain macroscopic observations. In the 5%, 7.5% and 10% offset films there is a great deal of cracking through out the thicker regions. In many areas where cracking has occurred the films have not entirely separated -- there appears to be a thin layer of film on the air (convex) surface which keeps the otherwise fragmented pieces together. SEM images reveal that this is the amorphous layer which has not fractured like the bulk (semicrystalline portion) of the film. Figure 5.16 is an SEM micrograph, nearly edge-on, of a broken 5.0/f/d [fully imidized] film fragment showing a crack through the bulk of the film which has been blunted by the amorphous layer. In an image of another fractured film fragment (7.5/f/d) where complete separation has occurred, one can see a contrast in how the film separated -- see Fig. 5.17. Throughout the bulk of the film a 'clean' separation has occurred indicating brittle failure. The amorphous layer (arrow),

however, appears to have undergone ductile failure.

5.3.9 Summary of the Thermal Imidization of LaRC CPI-2 Films

The development of crystallinity during thermal imidization of a LaRC CPI-2 film was shown to progress through stages that depended upon the time and temperature of the process. The magnitude of the changes in crystallinity paralleled the weight loss profiles for the film samples. This relationship was explained in terms of chain mobility. Crystalline development began between 125°C and 150°C with a final increase in crystallinity to 46% noted in the last stage of the process. There appears to be only gradual increases in crystallinity during imidization at 200°C X 1Hr, 225°C and 250°C. This is consistent with less chain mobility due to less available solvent at these stages, along with the fact that significant conversion has already taken place. At no stage during thermal imidization was the 1850cm^{-1} anhydride peak found, indicating that no significant chain scission occurred. SAXS analysis suggests that a two stage process may exist

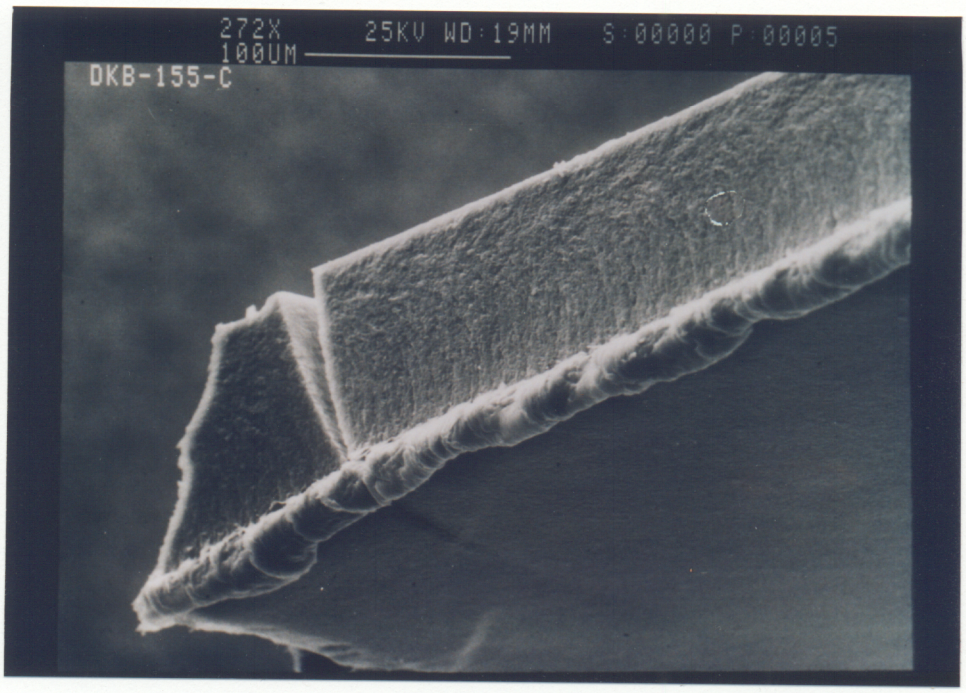

Figure 5.16 SEM micrograph, nearly edge-on, of a broken 5.0/f/d [fully imidized] film fragment showing a crack through the bulk of the film which has been blunted by the amorphous layer.

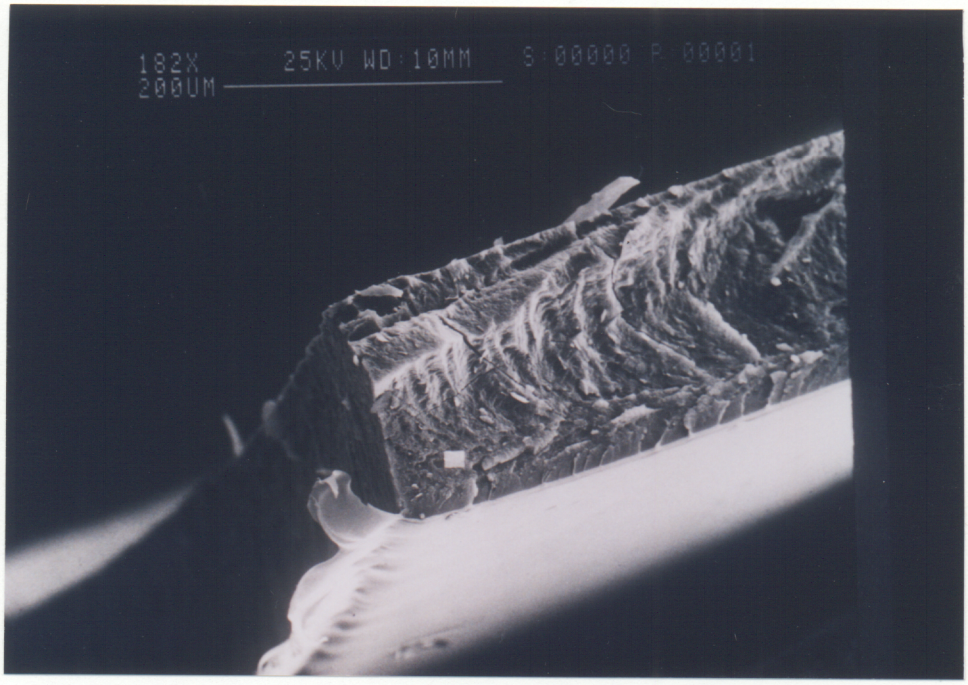

Figure 5.17 SEM micrograph of a fractured fragment of a 7.5/f/d [fully imidized] film where complete separation has occurred showing the difference in fracture character between the amorphous layer and the bulk (semicrystalline phase).

for the development of the crystalline superstructure. In the first stage, occurring below 200°C, widely spaced lamellae are formed. Crystallization then proceeds by inserting lamellae between previously formed lamellae and/or incorporation of amorphous material between lamellae into the crystalline phase. Subsequently, a thickening of the lamellae may occur in the final stage. The development of crystalline superstructure begins at the glass surface of the films and progresses upward towards the air surface. The glass surface appears to act as a heterogeneous nucleation site with subsequent self-nucleation of new superstructures. An amorphous layer remains on the air surface of LaRC CPI-2 films. The extent of this layer is dependent upon the molecular weight of the polymer. Inherently thicker lamellae formed in the latter stages of the thermal treatment may help to explain the increase in long spacing noted in the final stage of the process.

5.4 Comparison of 7.5% Offset LaRC CPI-2 Powders Synthesized in DMAc and m-Cresol

5.4.1 Chemistry and Processing

As was described in chapter 3 there a few key differences between the synthetic procedures used in the production of LaRC CPI-2 polyimides in m-cresol versus DMAc. Primarily, the reaction is conducted at 15% (w/w) solids in m-cresol (10% (w/w) in DMAc) at ca. 180 - 185°C overnight without an 18 hour poly(amic acid) equilibration step. Perhaps the greatest single difference, though,

is the solvent itself. It is known that the rate of thermal imidization generally increases with increasing solvent polarity and basicity [10, 11]. Though m-cresol is more polar than DMAc it is certainly less basic. Indeed, it is slightly acidic (pK_a (m-cresol) = 10.0; [128]). The effect of this acidity may be more important after processing than during the imidization procedure. The possible effects of acidity are discussed in detail in chapter 6 (section **6.5**). After thermal imidization 'in' solution the work-up and post thermal treatment of both powders is the same. It should be remembered here that both of the powders under discussion precipitated from solution during thermal imidization.

5.4.2 Differential scanning Calorimetry (DSC) Analysis

The difference in the melting behavior between the 7.5/p/d and the 7.5/p/m powders is dramatic. The first and second heat scans for these two powders, under the protocols discussed in chapter 3 and in section **5.2.1**, are shown in Fig. 5.18(**a&b**)[c]. The peak melting temperature of 409°C for the 7.5/p/m powder greatly exceeds even the second melting transition peak temperature of 366°C in the 7.5/p/d material. The 409°C melting peak is very broad (ca. 80°C) , however, and it begins to melt well within the range of the second transition of the dual melt. This broad transition, coupled with its symmetric nature, indicates that

---

[c] *The first heat scan shown in this figure for the 7.5/p/m material is actually a single run DSC trace wherein the upper temperature is well above the 435°C isothermal hold temperature used in the modified protocol. This allows one to see the stable baseline above the melting transition.*

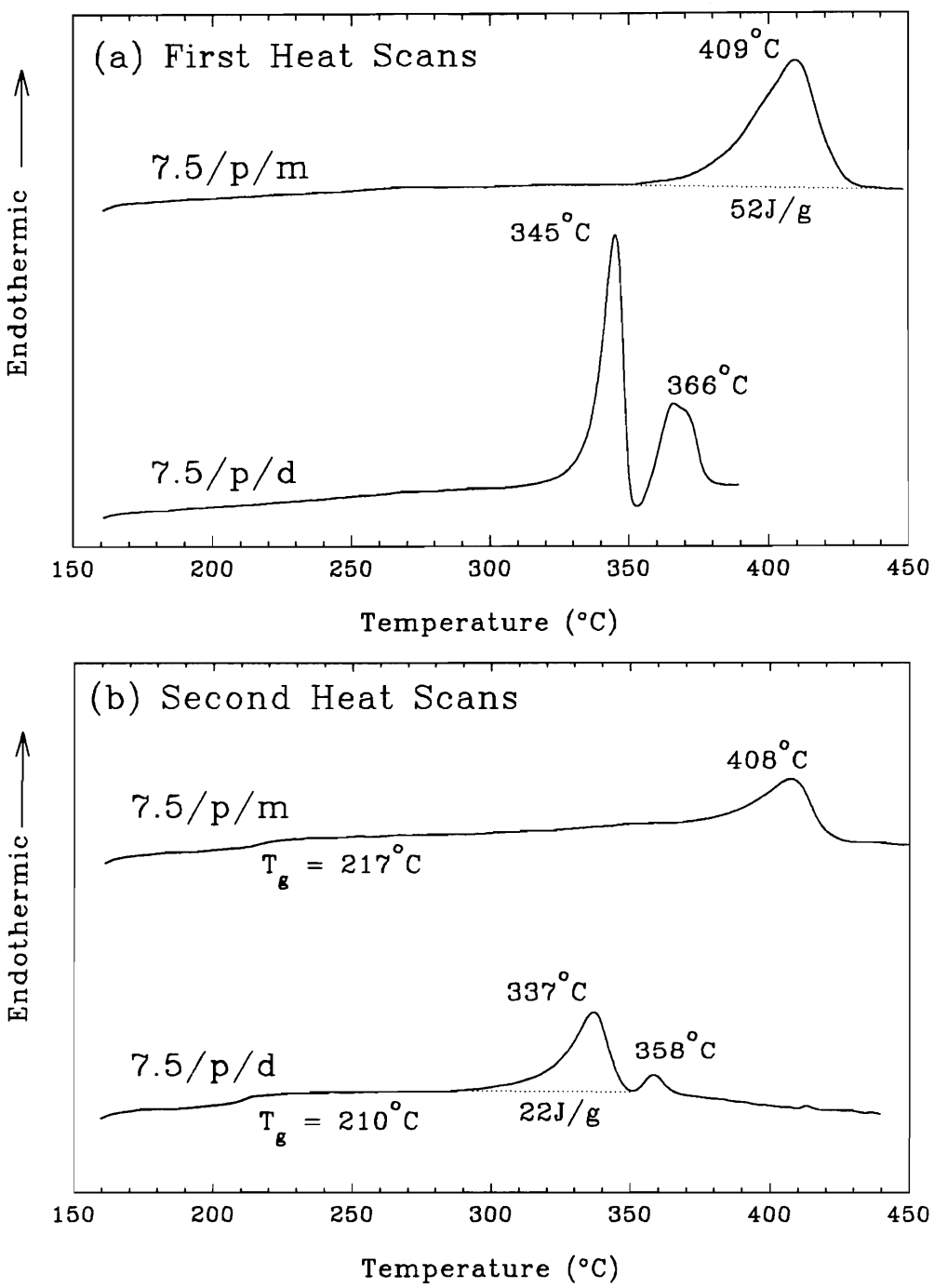

Figure 5.18 First (**a**) and second-heat (**b**) scans for the 7.5/p/d and the 7.5/p/m powders.

there might be a considerably large molecular weight distribution. Any thoughts of a simple solvent effect for explaining the difference in the initial melting temperatures are dispelled by the appearance of the high melting transition in the second heat scan of the 7.5/p/m powder (408°C)-- see Fig. 5.18(**b**). Though the magnitude of the transition is greatly reduced, the peak temperature is still very high relative to the dual melting 7.5/p/d peaks [the magnitude of the ordinate scales are the same in both Fig 5.18 (**a**) and (**b**)]. The glass transition temperatures of these two materials, not detectable in the first heat scans, are readily visible in the second heat traces. The 7°C higher T_g in the 7.5/p/m powder (217°C vs 210°C) might lead one to infer that the molecular weight of this powder is higher and is responsible for the higher melting transition. This is, of course, inconsistent with other observations, namely that the T_m of the 0/p/d powder was only 335°C while its T_g was much higher (231°C). The higher T_g in the 7.5/p/m material may simply be a product of the higher temperature of the melt-hold during thermal analysis (435°C X 1 min). Some cross-linking might be occurring at this elevated temperature resulting in an increase in the T_g. As presented in **6.2.4**. it is known that this material is melt sensitive at this temperature. The T_g is not broad, however, indicating that little if any cross-linking has occurred.

The great disparity between the peak melting temperatures of these two powders is curious and demands some explanation. In order to elucidate the mechanism or characteristic(s) responsible for these differences it is necessary to

apply the suitable analytical tools to further understand these differences.

5.4.3 Thermogravimetric Analysis (TGA)

Thermogravimetric Analysis (TGA) reveals only minimal differences between the two materials. As seen in Fig. 5.19, the weight loss profiles of the two powders are not dramatically different. The 5% weight loss value occurs at 499°C and 506°C for the 7.5/p/d and 7.5/p/m materials, respectively. Though the precipitous weight loss occurs at different temperatures both powders leave a residual char of ca. 5%.

5.4.4 Transmission Electron Microscopy (TEM)

Transmission Electron Microscopy (TEM) reveals dramatically different texture in the two powders. The 7.5/p/d material possesses a sheaflike superstructure as seen in Fig. 5.20. A micrograph of the 7.5/p/m powder, Fig. 5.21, at the same magnification displays a entirely different texture. Here no clear superstructure is present other than what appears to be a chaotic tangle of lamellar bundles. The lamellar structure is much more clearly seen at a higher magnification -- see Fig. 5.22. Here the it is clear that the lamellae are arranged in bundles which are not themselves otherwise associated. In contrast a TEM of the 7.5/p/d powder at the same magnification, as seen in Fig. 5.23, displays no clear lamellar texture.

5.4.5 Small Angle X-Ray Scattering (SAXS)

Small Angle X-Ray Scattering (SAXS) of the two powders reveals a rather surprising result in light of the clearly visible lamellae in Fig. 5.22. No clear scattering peak exists for either the 7.5/p/m or the 7.5/p/d powder. As seen in Fig. 5.24 (**a**), a standard plot of intensity as a function of **s**, the 7.5/p/d powder reveals no scattering peak. There is some scattering from the 7.5/p/m powder, however it is far from the distinct peak one would expect from the well defined lamellae seen in Fig. 5.22. Applying the Lorentz correction to these curves, as discussed before in section **5.3.6**, the scattering from the 7.5/p/m material is more well defined -- see Fig. 5.24 (**b**). The 'peak' for this curve corresponds ca. 170Å. The curve for the 7.5/p/d powder displays no peak whatsoever. It should be noted here that the resolution of the instrument used for this analysis is capable of resolving peaks corresponding to 500Å separation. The reason for this surprising lack of scattering is unclear.

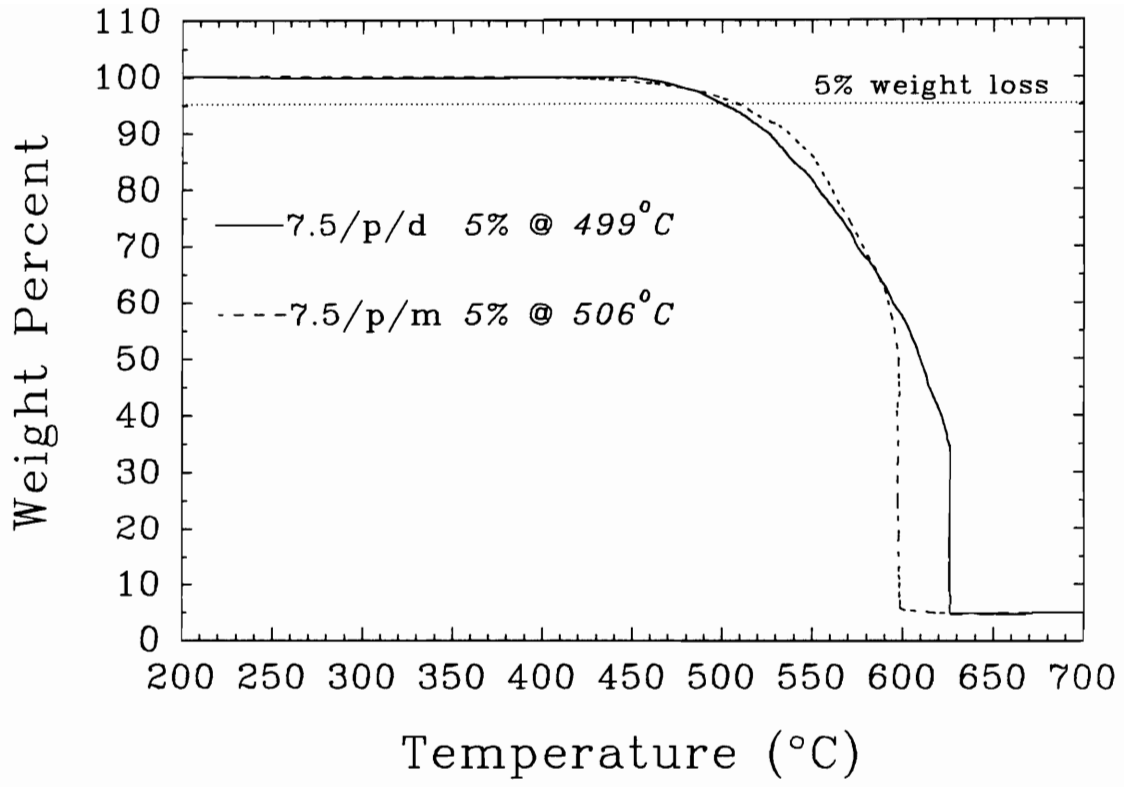

Figure 5.19 TGA thermograms [in air] of the 7.5/p/d and 7.5/p/m powders.

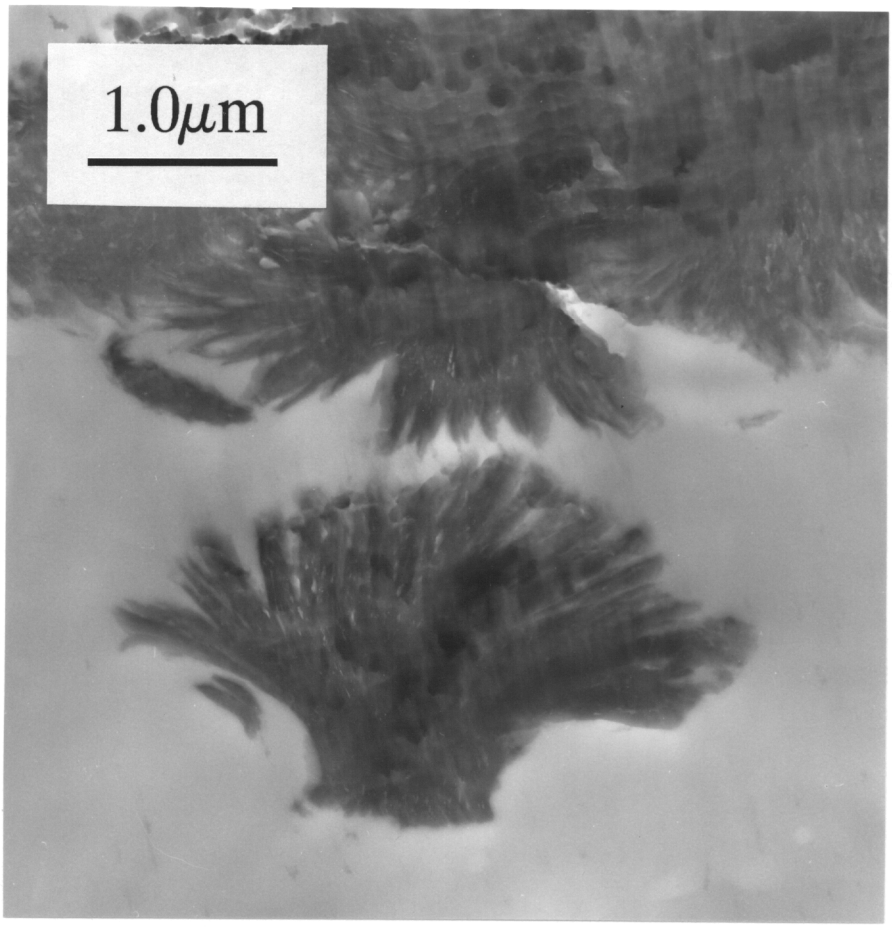

Figure 5.20 TEM of the 7.5/p/d powder displaying sheaf-like superstructure.

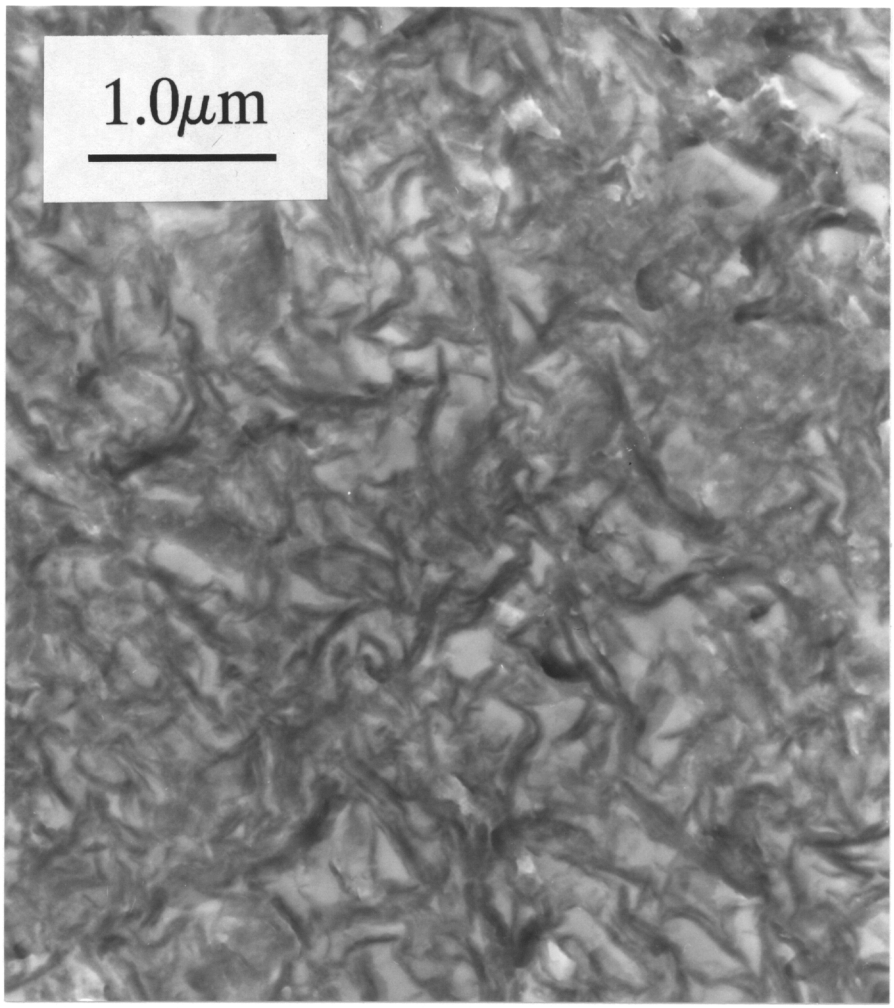

Figure 5.21 TEM of the 7.5/p/m powder displaying chaotic lamellar texture.

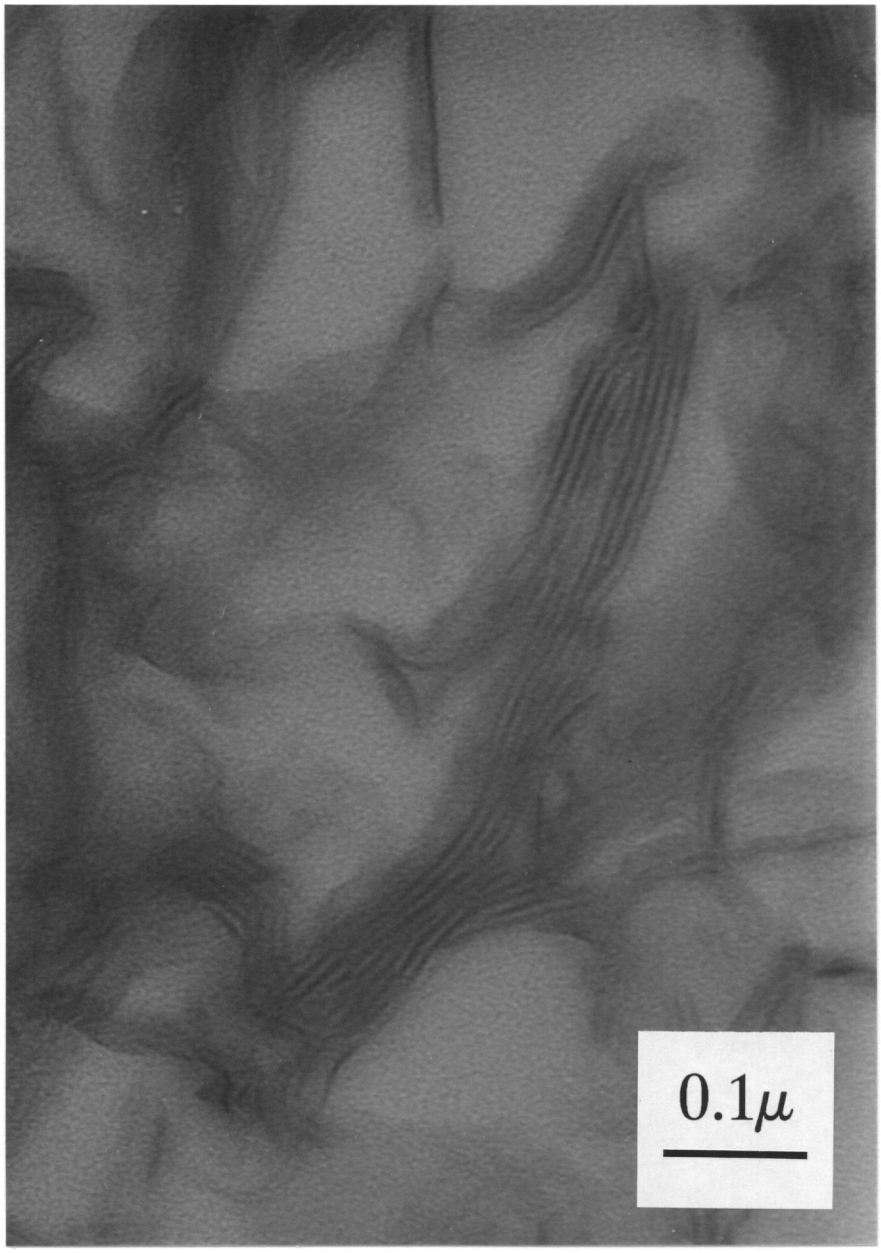

Figure 5.22 TEM of the 7.5/p/m powder shown in Fig. 5.21 but at a higher Magnification. Lamellae are distinctly visible.

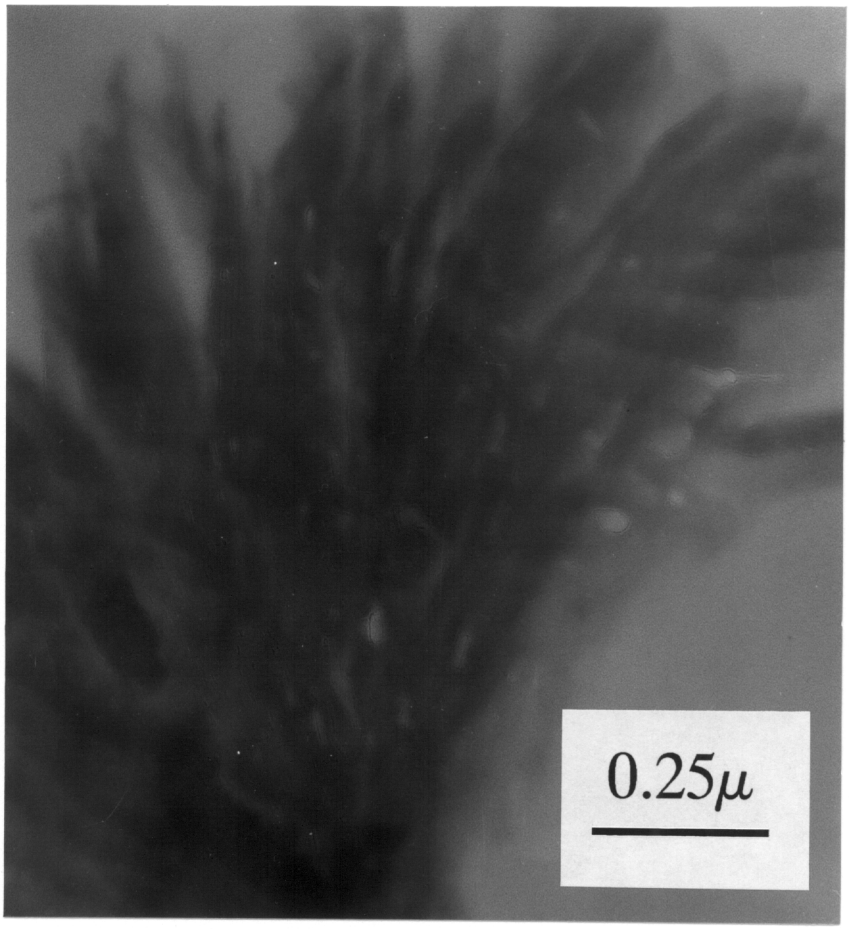

Figure 5.23 TEM of the 7.5/p/d powder shown in Fig. 5.20 but at a higher Magnification. No clear delineation of lamellar structures is evident.

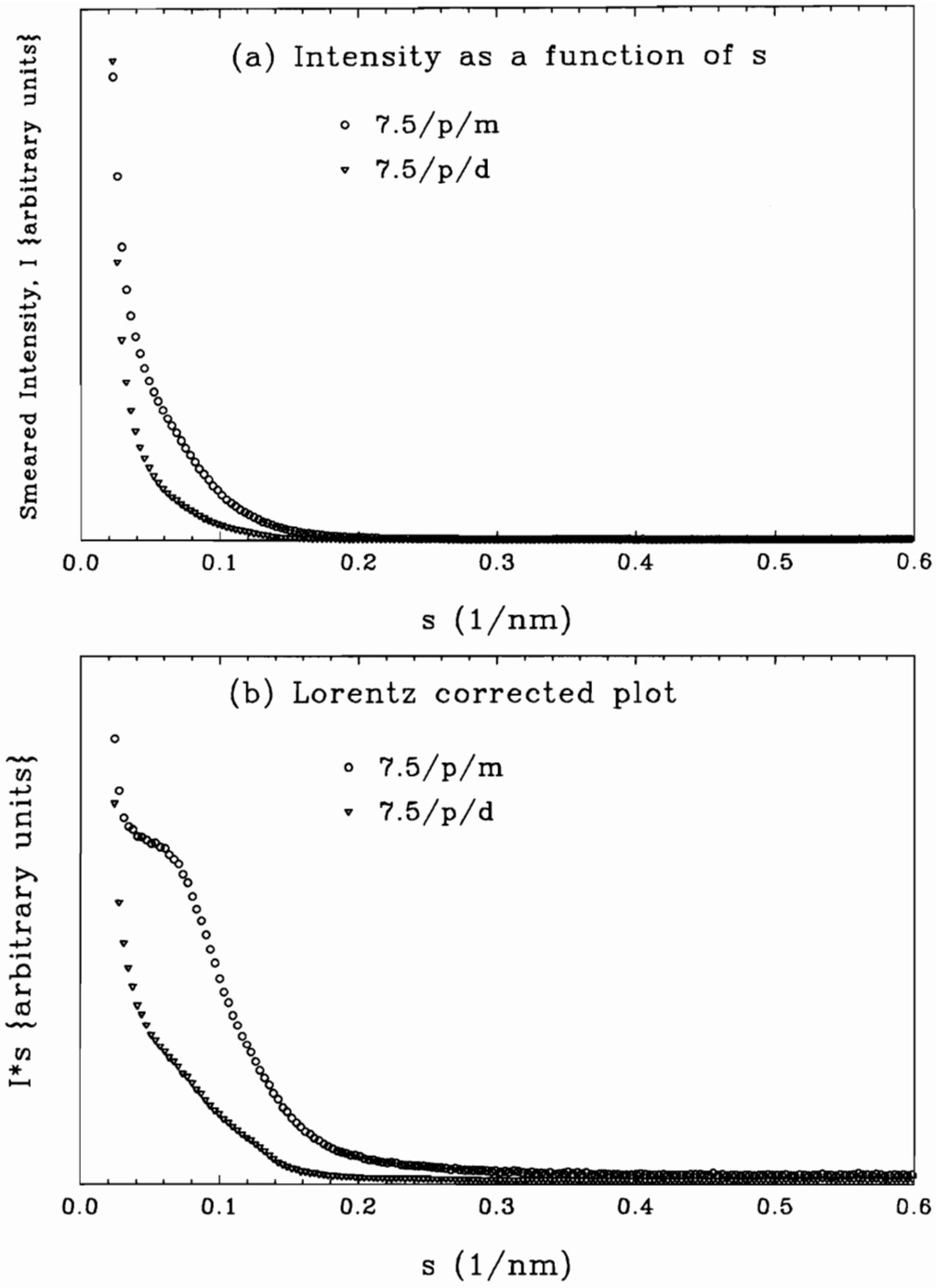

Figure 5.24 SAXS of the 7.5/p/m or the 7.5/p/d powders. Plot (a) is of the smeared intensity as a function of **s**. Plot (b) is the Lorentz corrected graph of I***s** vs **s**.

5.4.6 Wide Angle X-Ray Diffraction (WAXD)

Wide Angle X-Ray Diffraction (WAXD) analysis of the two powders reveals no difference in the crystal lattice structure of the two polymer 'types': The diffraction profiles for both samples are identical with regard to the location of the diffraction peaks-- see Fig. 5.25. The diffraction peaks from the 7.5/p/d powder appear slightly better resolved, but otherwise the differences between the diffraction profiles are negligible. Thus, regardless of the great differences in crystalline superstructure seen in TEM analysis, the fundamental crystalline lattice structure is the same.

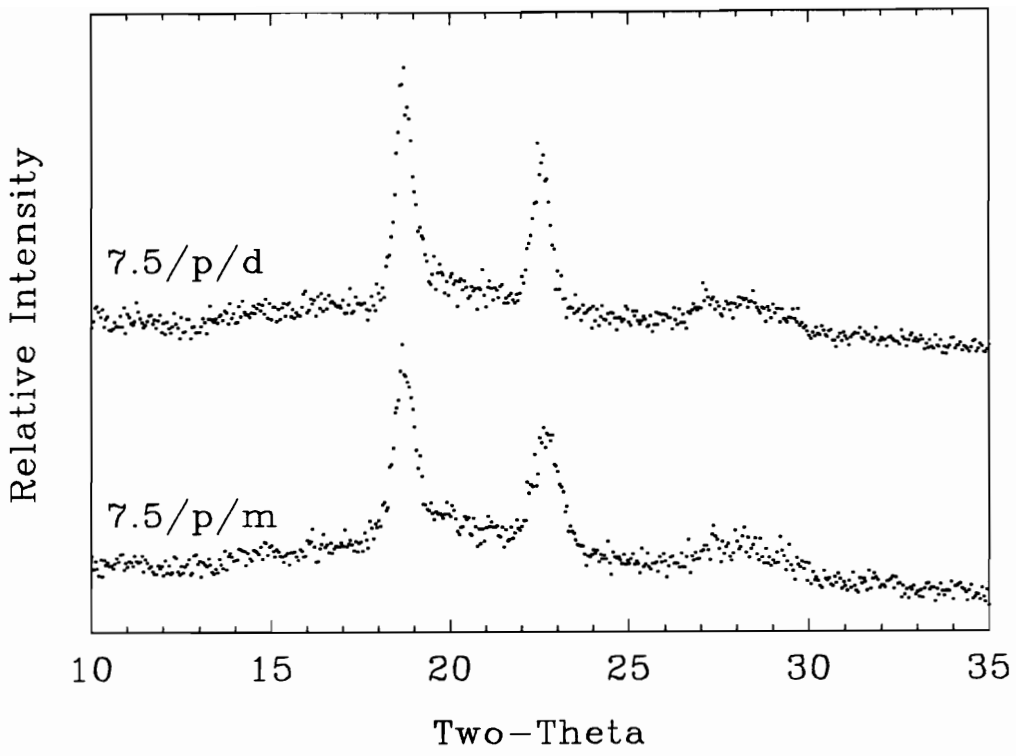

Figure 5.25 WAXD profiles of the 7.5/p/m or the 7.5/p/d powders.

5.4.7 Infrared Spectral Analysis (FTIR)

In the search for an explanation for the disparity in the melting behavior between these two powders it was thought that there might be some key chemical difference between the samples. Fourier Transform Infrared Spectrophotometry (FTIR) analysis was applied in order to investigate this possibility. As can be seen in Fig. 5.26 the FTIR spectra for the two polymer 'types'; are nearly identical. Both possess a hydrogen-bonded $-OH$ stretch at ca. 3400 cm^{-1}. This indicates incomplete polymerization or endcapping since it is most likely that carboxylic acid $-OH$ groups are probably responsible for this peak. The expected primary amine stretch bands in the 3400 cm^{-1} are likely masked by the $-OH$ peak.

In order to more clearly inspect the lower energy end of the spectrum this data has been re-plotted at 2,000cm^{-1} to 400cm^{-1} as seen in Fig. 5.27. A careful review of this spectrum reveals no peaks specific to only one sample. The only substantial differences are the two peaks at ca. 1440cm^{-1} and 1480cm^{-1}. The greater resolution of these peaks, most likely corresponding to primary aromatic amines, in the 7.5/p/m material would seem to indicate a greater proportion of amine chain ends. In the same vein, the greater relative magnitude of the peaks at ca. 1730cm^{-1} and 1250cm^{-1}, most likely corresponding to carboxylic acid functional groups, likewise indicates a greater proportion of amine chain ends in

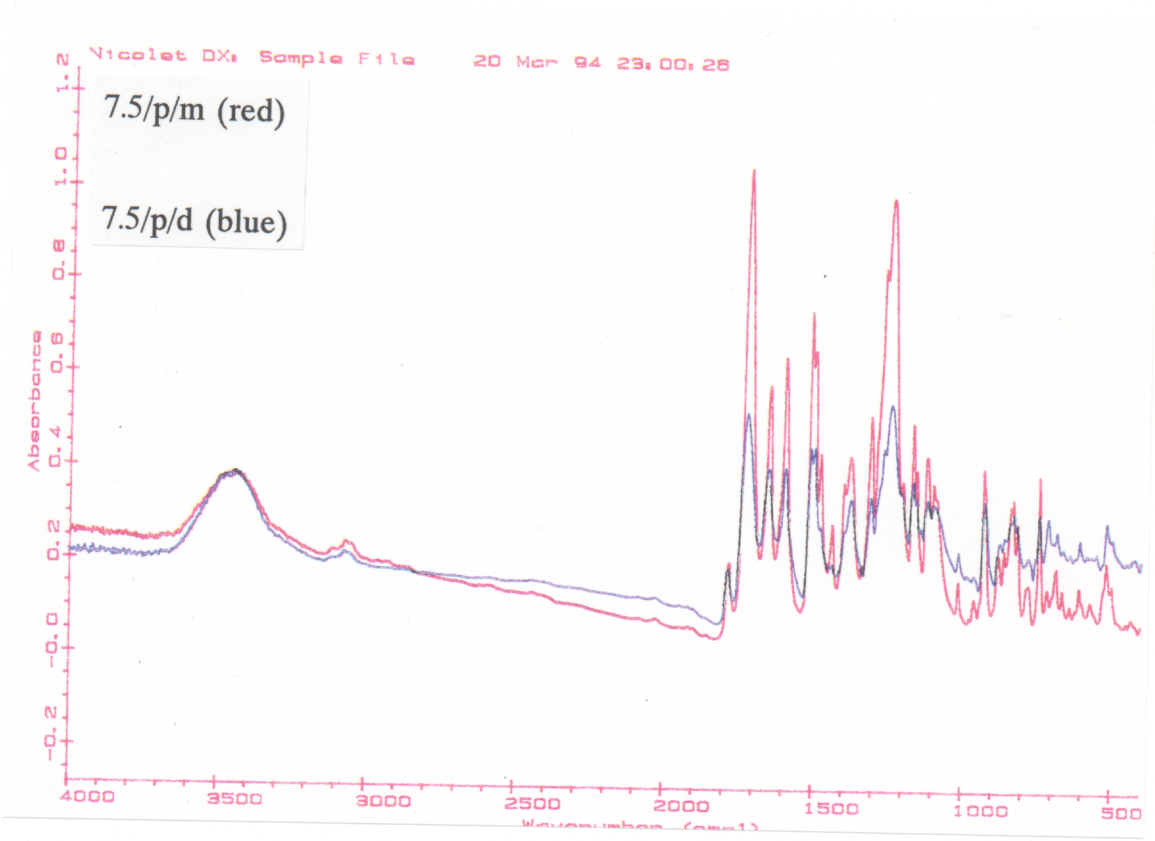

Figure 5.26 FTIR spectra for the 7.5/p/m and the 7.5/p/d powders.

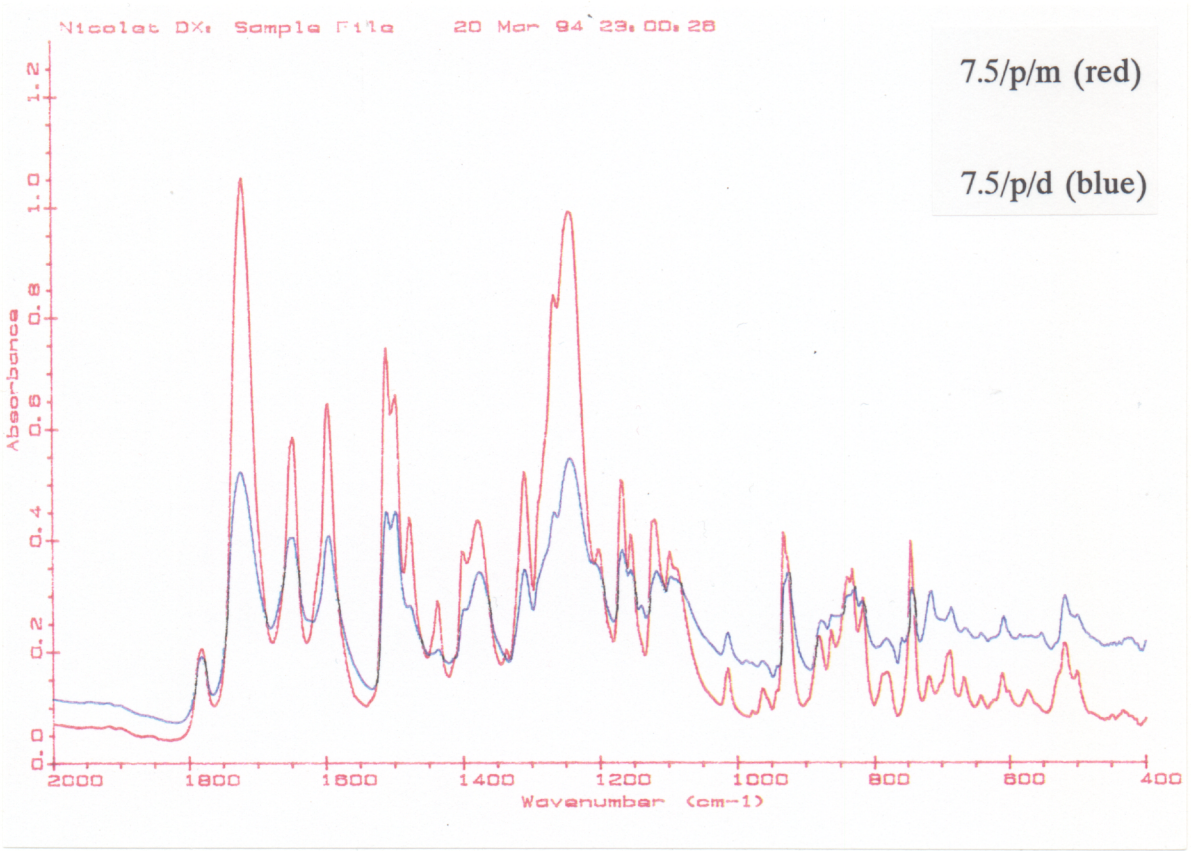

Figure 5.27 FTIR spectra from 2,000cm^{-1} to 400cm^{-1} for the 7.5/p/m and the 7.5/p/d powders.

the 7.5/p/m powder. A lower molecular weight of the 7.5/p/m powder, however, offers no avenue for proposing an explanation for the greatly dissimilar melting behavior of these two polymer 'types'. Thus, FTIR provides no real insight into solving the problem.

5.4.8 Summary of Comparison of Powders

Clearly the melting behavior of these two powders is very different. Three key differences in processing are the solvent (DMAc vs m-cresol), solids concentration (10% vs 15%) and the polymerization imidization sequence (18hr at room temperature vs immediate heat up to ca. 180°C-185°C). Standard analyses show us that there are great differences in melting behavior and crystalline superstructure. However, the fundamental chemical make-up, thermo-oxidative stability and crystalline lattice parameters are the same. None of the analytical methods applied thus far provide clear insight into the mechanism or particular characteristic responsible for the divergent melting behavior of these two powders. In addition to the obvious differences in T_m between these two powders there are other, perhaps more striking, differences with respect to melt sensitivity and maximum achievable T_m's through annealing. For example, the 7.5/p/m powder can be annealed at temperatures up to 420°C yielding melting transitions approaching 490°C. In contrast the 7.5/p/d powders cannot be annealed above 370°C and the maximum observed melting transition is 402°C. These differences,

along with other comparisons, are presented in chapter 6 and therein possible explanations are presented.

5.5 Summary

Several important characteristics of LaRC CPI-2 polyimides were presented in this chapter. The melting behavior of LaRC CPI-2 polymers has been shown to be very dependent upon synthetic and process conditions. Higher molecular weight (0% stoichiometric offset) powders display significant levels of crystallinity while the film counterparts are completely amorphous. Crystalline levels parallel film thickness in a series of stoichiometric offset films and, within individual films, the initial level of crystallinity is related to the thickness. The development of crystallinity in LaRC CPI-2 films has been shown to initiate off the substrate surface very early in the thermal imidization procedure followed by a subsequent growth front progressing toward the air surface as imidization proceeds. Fully processed films display an amorphous layer at their air surface, the thickness of which is inversely proportional to the stoichiometric offset. LaRC CPI-2 powders synthesized in DMAc and m-cresol have been shown to display greatly different crystalline superstructure and melting behavior, while other properties, such as thermo-oxidative stability and crystalline lattice structure, are the same. Analytical investigations presented thus far have not been successful in elucidating the mechanism or characteristics responsible for the differences.

CHAPTER 6

CRYSTALLIZATION AND MELTING BEHAVIOR OF LaRC CPI-2 POWDERS SYNTHESIZED FROM DIMETHYLACETAMIDE AND *m*-CRESOL

6.1 Introduction

As has been previously noted in chapter 5, there are marked differences between the melting behavior of LaRC CPI−2 as synthesized in DMAc versus *m*-cresol. In this chapter a detailed analysis of two 7.5% stoichiometric offset powders (7.5/p/d and 7.5/p/m) synthesized from each of these solvents is presented.

In particular, the response of these materials to various conditions of melt time and melt temperature are investigated, including their unusual ability to 'anneal' at temperatures above their observed melt transition. Though thermodynamic melting temperatures are not calculated, lower limits are determined. Crystallization kinetics information for both powders, as determined through rheological analysis, is also presented. Lastly, a comparison of the two powders is provided with postulated reasons for the divergent behavior of the two powders.

6.2 Effect of Melt Time and Melt Temperature on LaRC CPI−2 Powders

Both melt temperature and time in the melt have the potential to greatly influence the crystallization behavior of a semicrystalline polymer. A simple method to investigate the effect of changing these variables is to observe the crystallization exotherm during cooling in the DSC. Here the peak temperature of the crystallization exotherm during cooling, T_{cc}, provides an indicator of changes occurring in the melt. This value is sensitive to conditions affecting overall crystallization, such as time in the melt, temperature of the melt, molecular weight and nucleating agents [129]. In a study of LaRC CPI, Muellerleile and Wilkes [130] found that with increasing time and temperature in the melt the exotherms were shifted to lower temperatures and decreased significantly in magnitude. The T_{cc} values decreased over 25°C with a 20°C increase in the temperature of the melt from 375°C to 395°C (T_{cc} shifted from 329°C to 302°C). Similarly, the T_{cc} values decreased from 328°C to 316°C with an increase in time in the melt from 2 to 20 minutes at 385°C. These changes were shown to be a consequence of a decrease in the nucleation density caused by physical changes in the polymer.

In the investigations into melt time and temperature effects on LaRC CPI-2 that follow, similar trends in T_{cc} were uncovered. In addition to these logical trends, however, was some very unusual behavior that revealed the complexity of the crystallization and melting of LaRC CPI−2 polymers.

6.2.1 Multiple Crystallization Behavior of 7.5/p/d

Focusing attention on the 7.5% offset powder from DMAc (7.5/p/d), the effect of time in the melt at 375°C on the crystallization exotherm can be seen in Fig. 6.1. The T_{cc} value decreases in a logical progression from 302°C to 294°C to 287°C at 5, 10 and 15 minutes in the melt, respectively. This trend is not unexpected and the obvious question arises regarding the origin of the decrease in T_{cc} and magnitude of the exotherms, i.e., physical, chemical or both? This issue will be addressed in due course. First, it is necessary to investigate more thoroughly the nature of the exothermic response to time in the melt.

As seen in Fig. 6.1, the scan for the sample that experienced the shortest time in the melt (5 minutes) possesses an 'extra' minor dip at about 335°C (arrow). If this baseline deviation is a real exothermic event, then it presents the prospect of a multiple re-crystallization process occurring during cooling. In an attempt to elicit a more intense response at this higher temperature during cooling, DSC experiments with shorter melt times were conducted. Figure 6.2 shows the 5 minute T_{cc} thermogram along with those corresponding to the shorter melt times of 0, 2 and 3 minutes. Clearly, there is a progressive development of a higher temperature exotherm with shorter times in the melt. In fact, the 5 and 0 minute scans form near mirror images of one another, where the dominate transition in the former is found at 302°C, while in the latter the 334°C peak is most prominent. The extremely high value of the dominate T_{cc} peak in the 0

minute scan is surprising. The second heat scan, immediately following this −10°C/min cooling, displays a T_{m1} peak at 335°C, 1 degree above the cooling exotherm. Thus, the primary crystallization event is occurring at nearly the same temperature as the first melting transition during subsequent heating. This can be readily seen in the heat-cool-heat scans shown in Fig. 6.3. It is very difficult for one to accept that, in a polymer, the difference between the crystallization and subsequent melting temperatures could be only 1°C under these conditions. Some explanation for this must be tendered.

In both the first and second heats shown in Fig. 6.3, there is a doublet character to the second melting transition. This appears to be an overlapping of two separate melting transitions which reach their peak value at approximately a 5°C separation. At this point it is logical to suspect some relationship between the very high temperature exotherm (T_{cc} =334°C) and the melting transition that would correspond to the second 'peak' of the doublet.

In order to investigate this possibility and to further understand the nature of the dual exothermic behavior, the effect of cooling rate was investigated. The melt time was chosen to be 2 minutes, since this yields two clear exotherm peaks at 330°C and 311°C as seen in Fig. 6.2. After this 2 minute melt time, the separate samples were cooled at different rates followed by a second heat at 20°C/min. Table 6.1 identifies these samples for future reference.

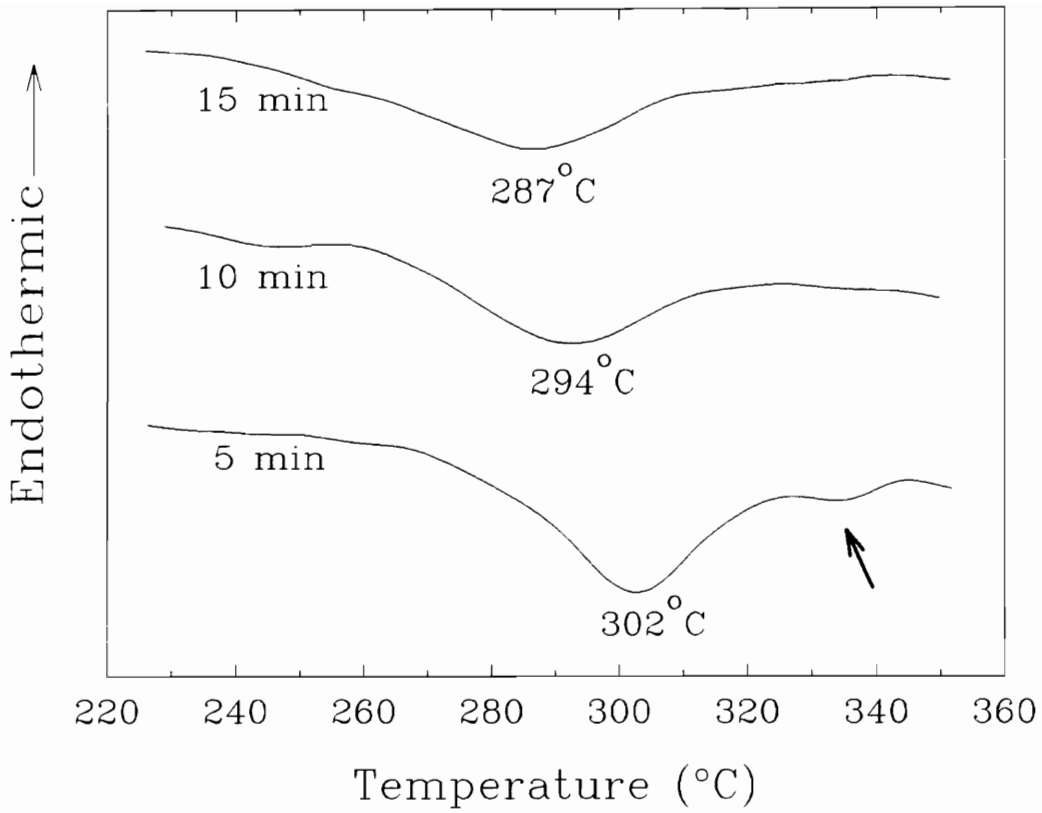

Figure 6.1 T_{cc} scans of 7.5/p/d powder held at 375°C for various times.

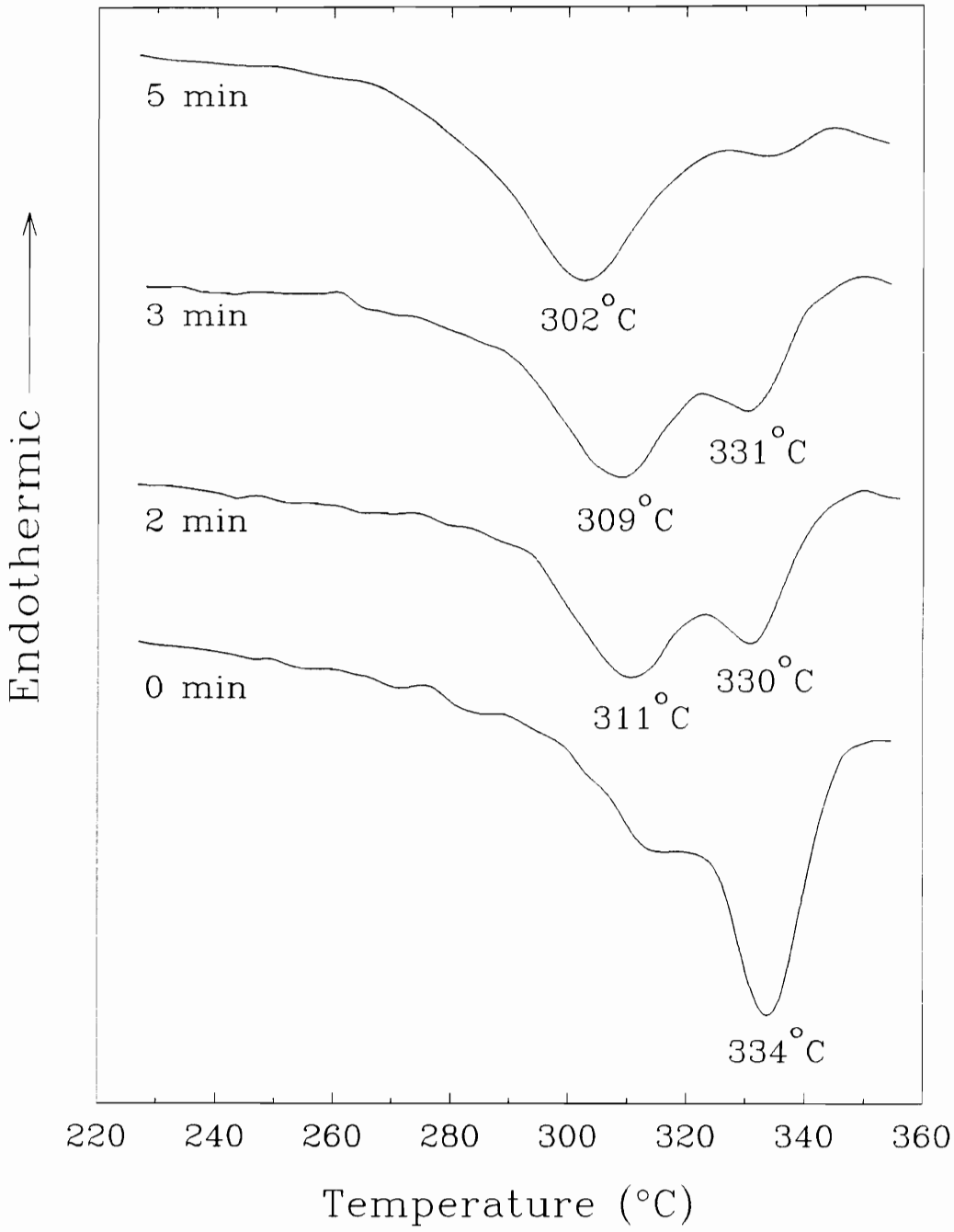

Figure 6.2 T_{cc} scans of 7.5/p/d powder held at 375°C for 5 minutes and less.

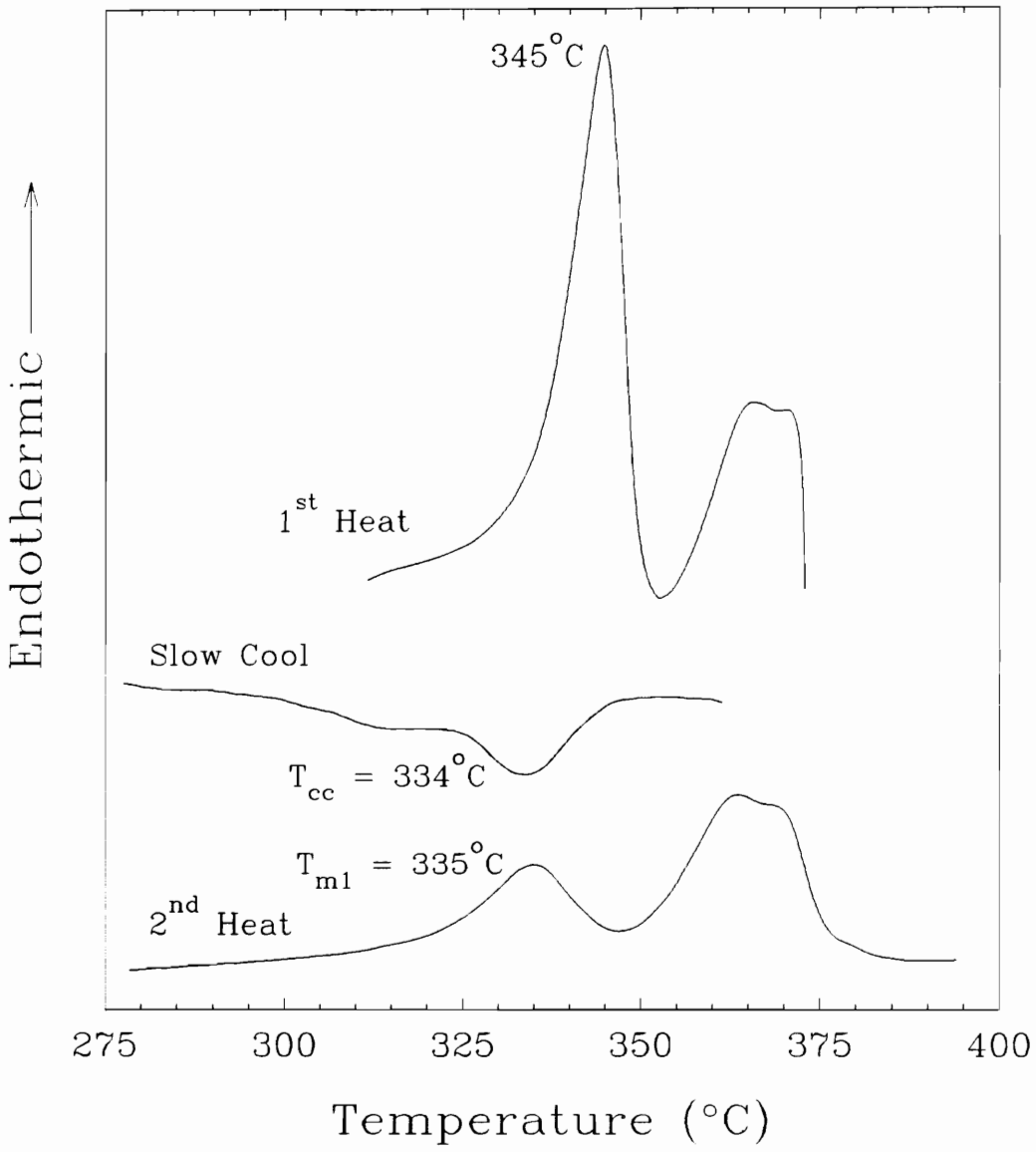

Figure 6.3 Heat-cool-heat scans for 7.5/p/d held at 375°C for 0 minutes.

Table 6.1. Listing of identifiers and cooling rates for samples held in the melt for 2 minutes at 375°C as discussed in section **6.2.1** and as shown in Figs. 6.4 and 6.5.

Sample ID	Cooling Rate
A	−1°C/min
B	−3°C/min
C	−5°C/min
D	−10°C/min
E	−15°C/min
F	−20°C/min

The DSC scans for these samples are shown in Figs. 6.4 and 6.5 for the cooling and heating thermograms, respectively. Using sample **D** as a reference point in Fig. 6.4, we can see that reducing the cooling rate to −5°C/min causes the higher temperature exotherm to become dominate, as seen in sample **C**. This corresponds directly with an increase in the magnitude of the second (upper) peak of the doublet melting transition(s) seen in Fig. 6.5 sample **C**. In addition, the magnitude of the first melting transition is greatly reduced. This is entirely consistent with the idea that a greater fraction of the polymer is in a form corresponding to that which melts at the highest temperature. Referring again to Fig. 6.4, as the cooling rate increases from −5°C/min through −20°C/min (samples **C** through **F**), a clear trend emerges wherein the lower temperature exotherm becomes more prominent at the expense of the upper exotherm. At −20°C/min (sample **F**) the higher temperature exotherm is nearly gone, though it is still evident. The second heat traces for these same samples present a compatible trend. With an increase in cooling rate (with a consequent lower magnitude of the higher temperature exotherm during cooling) there is a marked progressive decrease in the amplitude of the second peak of the doublet endotherm during heating -- seen in Fig. 6.5. In sample **F**, which possessed a very shallow high temperature exotherm, the second melting transition reveals no doublet character whatsoever.

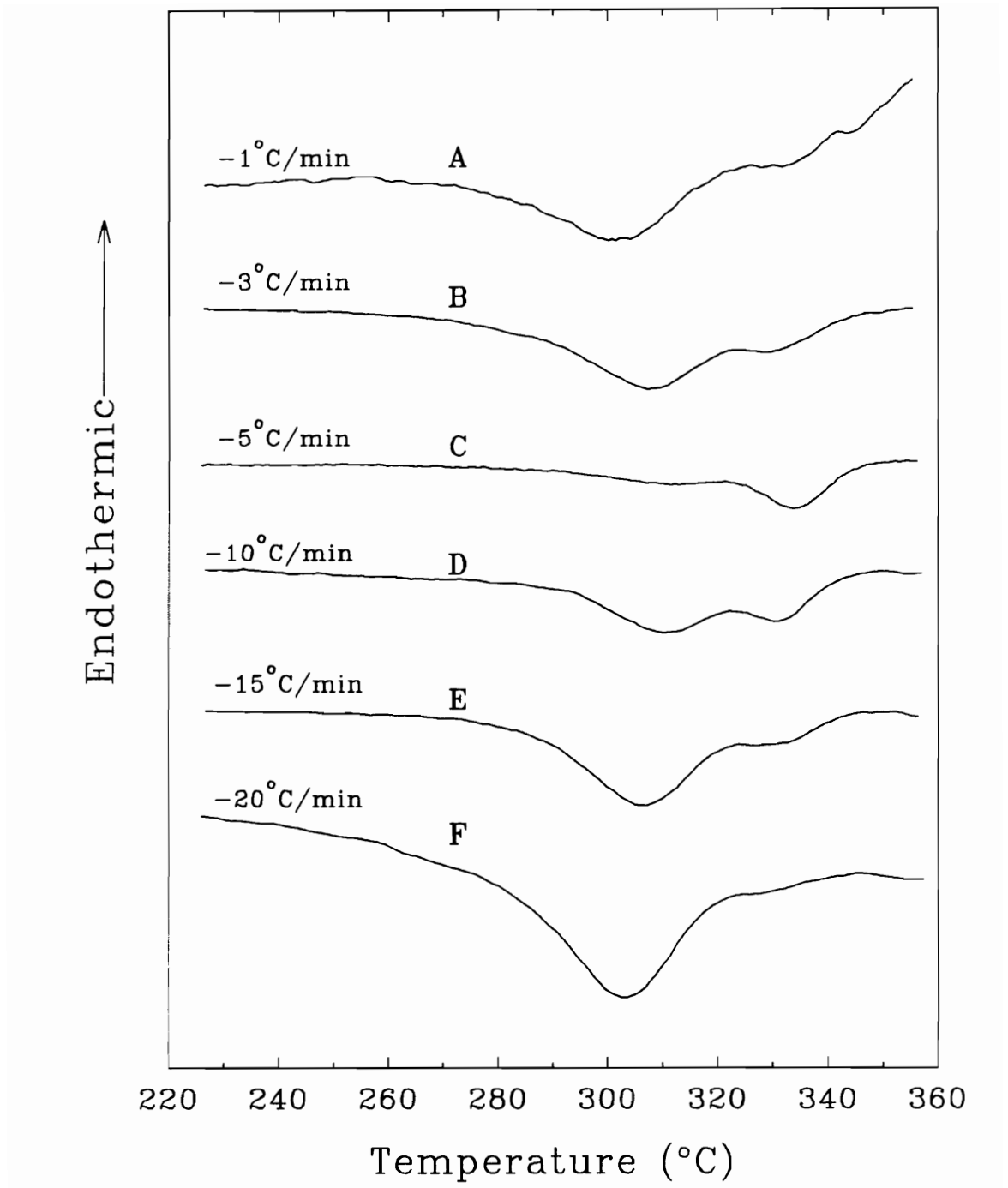

Figure 6.4 T_{cc} scans at -1°C/m to -20°C/m for 7.5/p/d powder samples held at 375°C for 2 minutes. Note -1°C/m and -3°C/m curves amplified by a factor of 20 and 4, respectively.

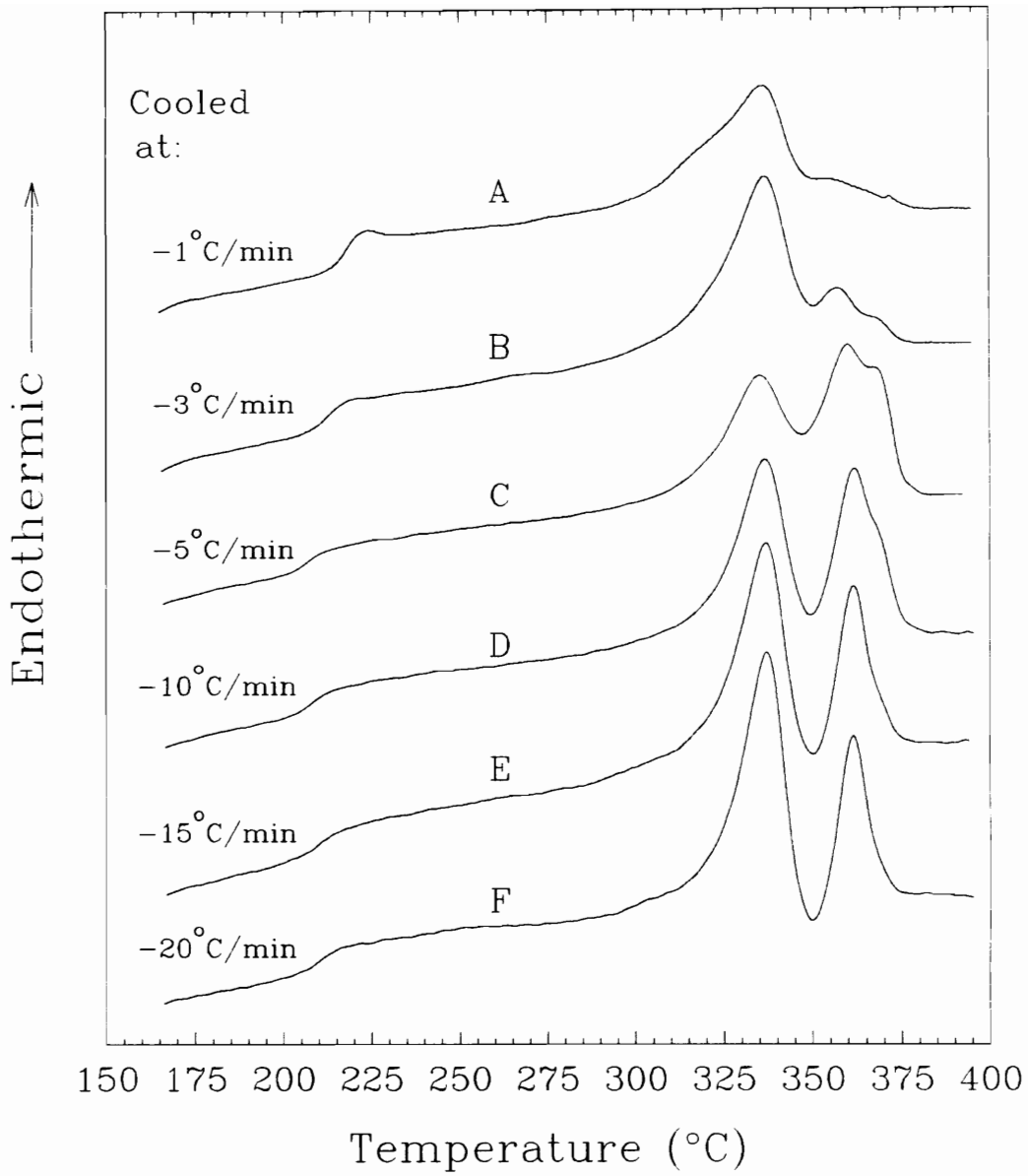

Figure 6.5 Second heat scans of 7.5/p/d samples held at 375°C for 2 minutes.

This trend can be explained in terms of thermodynamic and kinetic influences. The dependence of the higher temperature exotherm on time in the melt indicates that residual nuclei are present initially and are being eliminated with time at elevated temperatures. Furthermore, these nuclei arise from the incomplete melting of the crystals that are responsible for the second, higher temperature, 'peak' of the doublet seen in the first heat DSC thermogram.

With this in mind, the existence of multiple exotherms can easily be explained. Upon cooling, the pre-nucleated polymer, having already overcome the kinetic barrier of nucleation, begins to crystallize at a relatively high temperature. At low cooling rates there is sufficient time at this higher temperature for a great deal of crystallization to occur. But at faster cooling rates, less time is available for crystallization thereby driving it to lower temperatures -- a kinetic effect. Furthermore, supercooling effects become more significant at higher cooling rates which also act to drive the exotherms to lower temperatures. At the lower temperatures (higher undercooling) the bulk free energy of fusion, Δf, shown in Eqn. 2−8 (reproduced here from chapter 2), becomes much greater thereby forcing the crystallization to proceed:

$$\Delta f = \Delta h_f \left(\frac{\Delta T}{T_m^0} \right) k \qquad \textbf{(2−8)}$$

The reader is reminded that Δh_f is the unit heat of fusion, ΔT is the undercooling of the melt below the thermodynamic melt temperature, T_m°, and k is a correction factor which accounts for the temperature dependence of Δf away from T_m° [83, 86].

This does not, however, explain the apparent reversal in the trend for samples **A** and **B**, as seen in Fig. 6.4. In both of these scans the *lower* crystallization exotherm is most prominent. This is the result of an effective increase in time at elevated temperatures (because of the very low cooling rates) with an associated loss of the high-temperature nucleation sites. Thus, the crystallization maximum is shifted to lower temperatures. The striking decrease in the magnitude of the exotherms seen in these scans (in Fig. 6.4 traces **B** and **A** were magnified by a factor 4 and 20, respectively) points to a dramatic decrease in the overall amount of crystallization. One must keep in mind, however, the limited ability of the instrument to detect small changes in heat flow, a natural consequence of lower cooling rates. Thus, the apparent damping of the exotherm curve is due, in part, to the broadening of the period of crystallization and the inability of the instrument to measure this 'spread-out' response. Nevertheless, this does not entirely account for the decreased exothermic response. The second heat scans for samples **A** and **B**, as seen in Fig. 6.5, reveal a considerable drop in the magnitude of the first melting transition. Thus, there was a real decrease in the overall amount of crystallization during cooling for these scans.

It is also noteworthy that the second melting transition, T_{m2}, is greatly reduced for these samples. In fact, the thermogram for sample **A** shows T_{m2} as nearly non-existent. This trace nearly matches that of the second heat for the sample held in the melt for 5 minutes (followed by the standard $-10°C/min$ cooling cycle). Indeed, the second heat scans for samples with melt times of 5 minutes and greater (T_{cc} traces shown in Fig. 6.1) all lack the second melting endotherm. Thus, the disappearance of the second endotherm appears to be directly related to 'extended' times in the melt. With the understanding that the second melt transition is the result of a rapid melt/recrystallization process (as discussed in Chapter **4**), its conspicuous absence here may be explained in terms of a chemical change in the polymer, as opposed to a simple physical reduction in the nucleation density. If the nucleation density alone were affected by the increased time in the melt, then one would expect a decrease in the magnitude of the first endotherm with an associated reduction in the second transition. The presence of the second endotherm is not dependent upon the nucleation density of the polymer. However, if chemical degradation occurred in such a manner as to restrict chain mobility (cross-linking or chain extension), then it would severely reduce the rate of the otherwise rapid re-crystallization which follows the first melting transition. The presence of a chain extension process is, in fact, proposed in this chapter (**6.2.2 Melt Sensitivity**) following evidence presented in its support.

6.2.2 Melt Sensitivity of 7.5/p/d

Rheological analysis of the 7.5/p/d powder in nitrogen reveals an increase in the melt viscosity as a function of time at 375°C— see Fig. 6.6. In a span of 1 hour the melt viscosity, η^*, has increased over a full order of magnitude from ca. 150 Pa·s to nearly 4,000 Pa·s. This rise indicates that some branching, endlinking or cross-linking process is occurring in the melt state. Thus, the general trend of a decrease in the magnitude of the crystallization exotherm(s) with melt time seen in section **6.2.1** may be attributed, at least in part, to a chemical change in the polymer at elevated temperatures.

DSC analysis was further employed as a means of determining the effect of melt time on the ability of the polymer to recrystallize. Here the objective was to determine the recoverability of crystallinity lost at 375°C. The thermal treatment procedure for this analysis involved holding the samples at 375°C for several different times with subsequent quenching to room temperature, well below the T_g. The samples were then annealed at 300°C for 12 hours and allowed to cool to room temperature before DSC analysis. Both the melt and annealing steps were conducted under a nitrogen blanket in a block heating device that allowed for accurate control of the temperature to within 1°C [75].

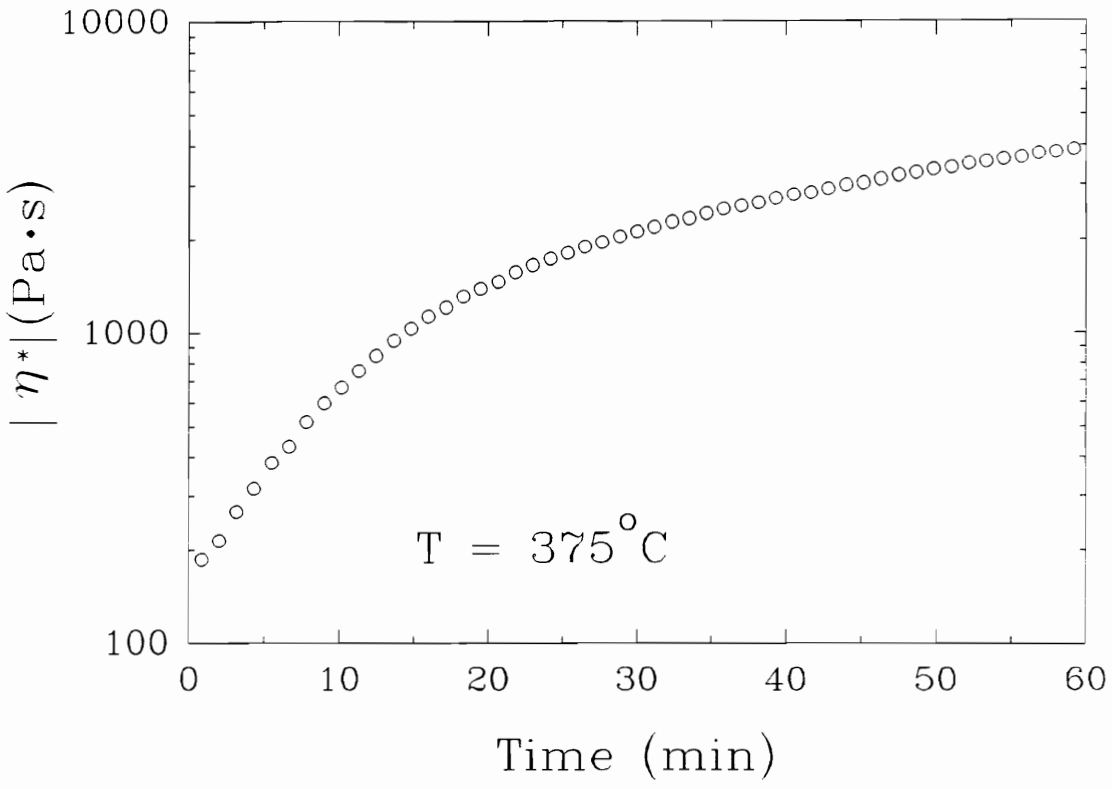

Figure 6.6 Melt viscosity of 7.5/p/d at 375°C in nitrogen.

The long annealing step conducted from the glass, at a temperature well within the crystallization window, provides reasonable conditions for the recovery of crystallinity lost to physical changes in the melt. Thus, enthalpy measured after this process represents a recovered value which serves as an index of the magnitude of the chemical changes occurring in the melt state. If there were no chemical changes during the isothermal hold at 375°C, then the residual heat of fusion would be expected to remain constant. As seen in Fig. 6.7 this is not the case. One hour in the melt at 375°C was nearly sufficient prevent the recovery of any crystallinity. The results from this DSC analysis and the rheological data both point to a striking amount of chemical change occurring at 375°C. This is significant because these changes are occurring at only ca. 10°C above the observed [second] melting temperature.

The exact nature of the chemical reaction occurring at these elevated temperatures is not known. The increase in melt viscosity indicates that a chain extension or cross-linking process is occurring, as opposed to a chain scission process. Two plausible explanations may be immediately proffered.

First, unreacted end-groups on the polymer chains, anhydrides and amines, could combine to form much higher molecular weight chains. This would certainly account for the increase in melt viscosity. Furthermore, if high enough molecular weights were obtained, the loss in the residual heats of fusion could

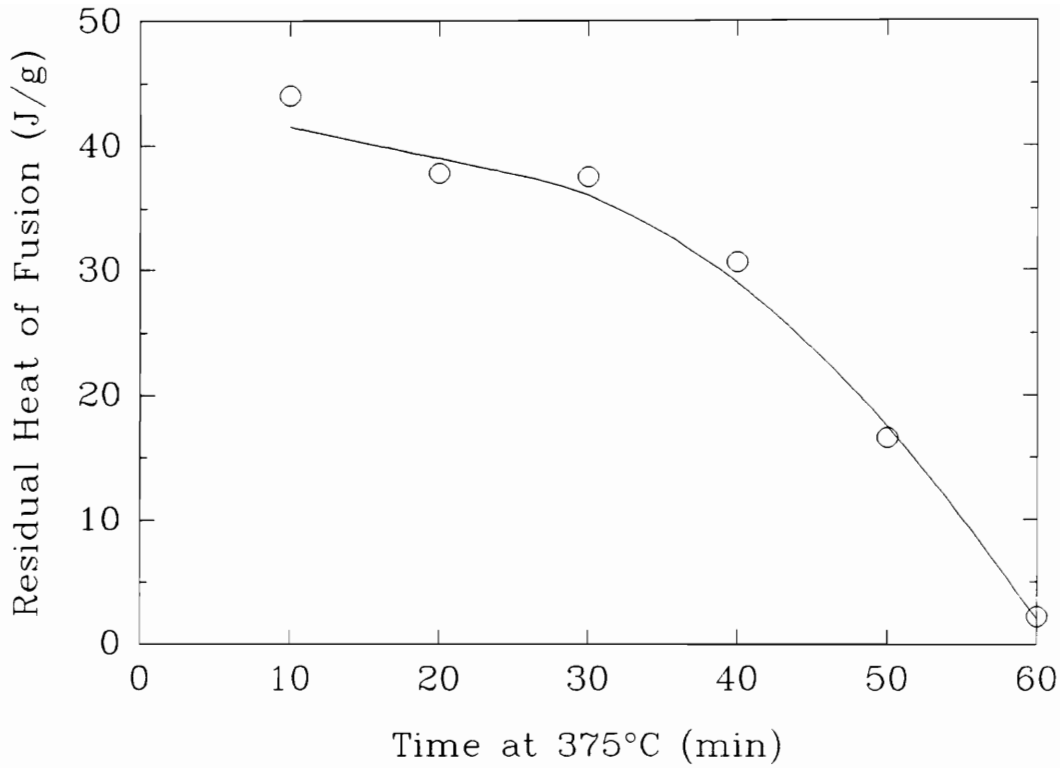

Figure 6.7 Residual heat of fusion for 7.5/p/d samples held at 375°C under nitrogen for times from 10 to 60 minutes.

likewise be explained by this scenario. As has been noted in section **5.2**, very high molecular weight versions of this polymer do not display crystalline character due to the slower kinetics of crystalline formation. However, this scenario is untenable. In order for high enough molecular weights to be obtained the reactions would need to occur in total disproportion to the relative concentrations of the reactive groups present. That is, stoichiometric control is still operative; only a number average molecular weight of ca. 10K will be produced. As will be discussed in section **6.5**, however, there are reasons to suspect that the expected molecular weight is not fully achieved.

A second possibility is that some cross-linking reaction is occurring. Several researchers have studied cross-linking in linear polyimides. In a study of oxidative degradation of poly-N,N'-(4,4'-diphenylether) pyromellitimide (chemical structure of Kapton®) Dine-Hart et al. [131] concluded that a coupling between the diphenylether units was primarily responsible for the cross-linking of films of this polyimide at 400°C. In a review of Russian literature [41] reactions between imide carbonyls and aromatic rings to form aryl-ketone-aryl cross-links, as well as reactions between amine end groups and imide carbonyls to form imine cross-links within the imide ring were reported. Also reported were inter-chain amide links. However, an earlier paper by Dine-Hart and Wright [36] reported that tetraamides expelled their more labile amine component to give the normal cyclized imide. Likewise, attempts to find spectral evidence for amide cross-links

by other researchers was unsuccessful [132]. Although all of these cross-linking pathways are, to some degree, possible, none appear to hold any greater significance over the others.

Another, more likely, reaction presents itself that involves functional groups that are present in the LaRC CPI−2 polyimide. Specifically, un-capped terminal amine end groups polymer may react, at elevated temperatures, with ketone functional groups to form a ketimine molecular link. A schematic of this reaction is shown in Fig. 6.8. Ketimine reactions are not unknown in polymer systems. Ketimine functionalized prepolymers are commonly used in the preparation of polyurethanes [133]. Imine formation reactions have also been used in the formation of poly(aryl ether ketone)s [134 - 137]. Specific, reasons for suspecting that this reaction is occurring in LaRC CPI−2 are discussed in section **6.5**.

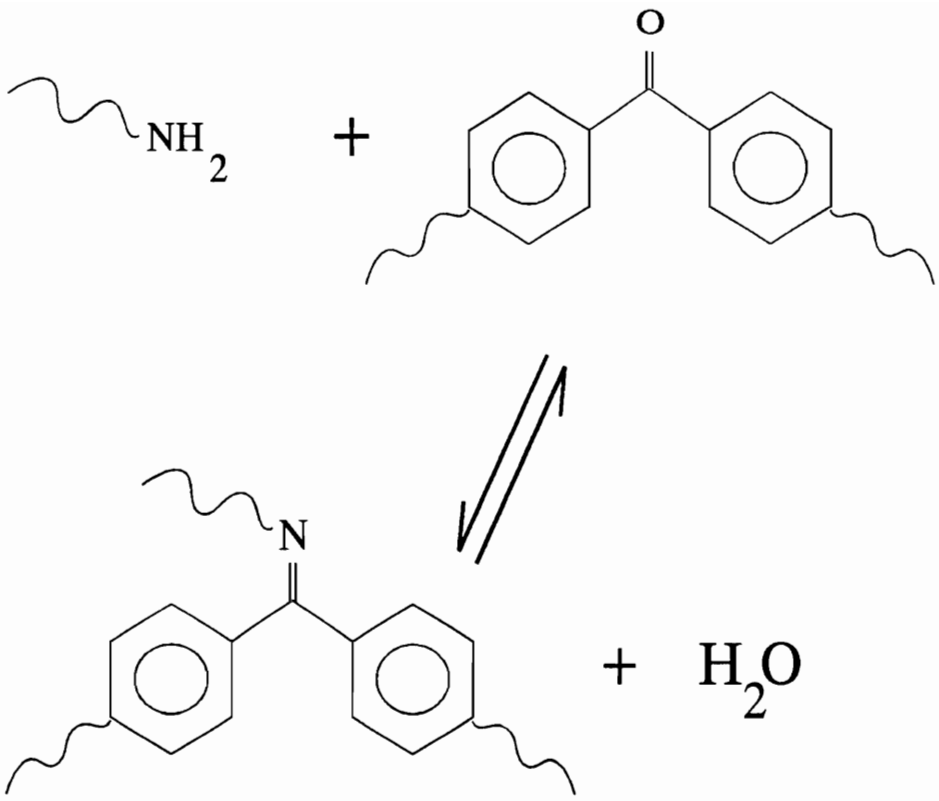

Figure 6.8 Schematic diagram of the reaction between a primary amine end-group and a ketone within a poly(aryl ketone) to form a ketimine link.

6.2.3 Crystallization and Melting Behavior of 7.5/p/m

For the analysis of the powder produced from *m*-cresol, it is again useful to approach the effect of time in the melt by observing the crystallization behavior during cooling. In a fashion similar to that used for the 7.5/p/d material, an initial view of the effect of time in the melt is surveyed at a temperature approximately 10°C above the observed melting transition, 420°C. Figure 6.9 reveals a logical trend of a decrease in the peak transition temperature, T_{cc}, along with a moderate decrease in the crystallization enthalpy, with increasing time in the melt. It is striking that the exothermic peak temperature for the sample held for 5 minutes at 420°C (366°C) is well within the *melting* range of the second melting transition of the 7.5/p/d material. It is also revealing to compare the T_{cc} scans for the 7.5/p/m powder to the those for the 7.5/p/d powder as seen in Figs. 6.9 and 6.1, respectively. The lowest T_{cc} for the 7.5/p/m material, 350°C at the 15 minute hold, is almost 50°C above the highest T_{cc} for the 7.5/p/d powder, 302°C at the 5 minute hold. It should be remembered that the 0 minute T_{cc} scan for the 7.5/p/d powder possessed a T_{cc} of 344°C (see Fig. 6.2), just 6°C below the 350°C for 15 minute T_{cc} scan for the 7.5/p/m material.

Unlike the behavior of the 7.5/p/d material the crystallization exotherms here display only a single peak. This single peak behavior allows for the mapping of the effects of melt time and temperature. That is, trends with the T_{cc} and heat of crystallization values as a function of melt time and temperature are

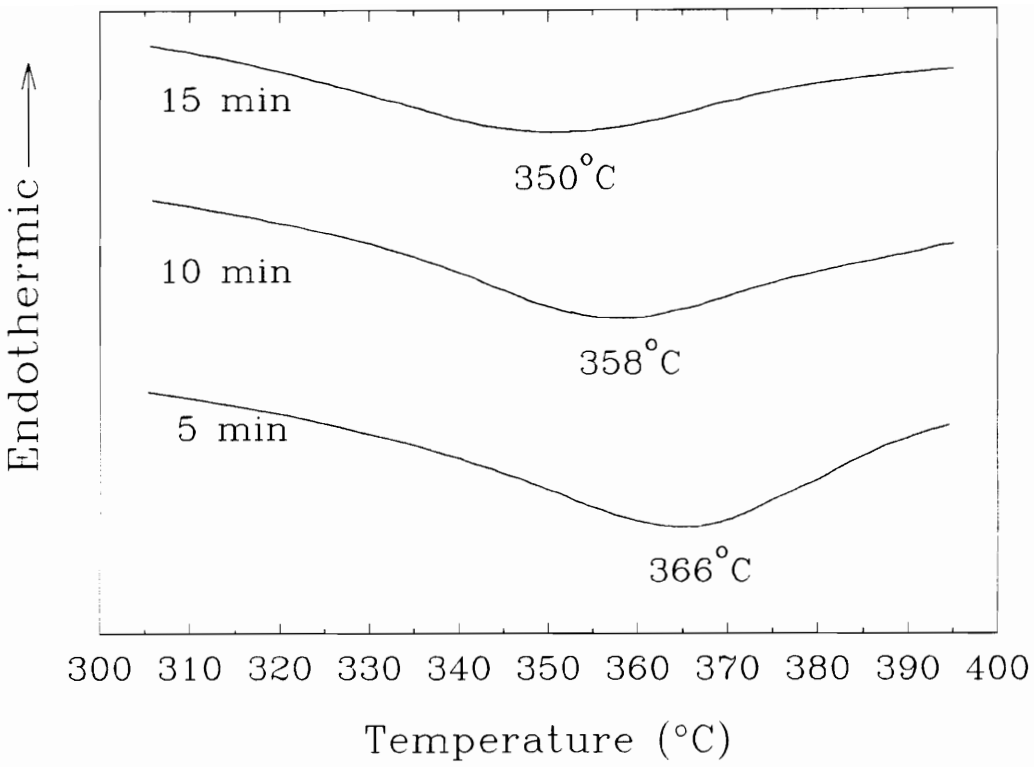

Figure 6.9 T_{cc} scans of 7.5/p/m powder held in the melt at 420°C for 5 to 15 minutes.

determinable. In order to gather this data, DSC scans were performed on a series of samples held for 1, 5, 10 and 15 minutes each in the melt at 5°C intervals between 420°C and 445°C. Figure 6.10 (a & b) displays the results. Focusing first on the effect of melt time and temperature on the peak crystallization temperature, T_{cc}, shown in Fig. 6.10a, it appears that the trend follows an expected profile. For each melt time the peak crystallization temperature decreases as the melt temperature increases. And for each melt temperature the peak crystallization occurs at successively lower temperatures for longer times in the melt. The data points for 10 and 15 minutes at 440°C and 445°C, and 5 minutes at 445°C are "missing" because no crystallization exotherms were detectable under these conditions.

Looking at the effect of melt time and temperature on the heat of crystallization (Fig. 6-10b) reveals an unexpected response: A maximum exists for each melt time at 425°C. From 425°C to higher temperatures a decrease in the crystallization exotherm is found as the melt temperature increases, as expected. Likewise, longer melt times yield lower heats of crystallization. However, for all melt times there is a significant drop in the heat of crystallization as the melt temperature is decreased from 425°C to 420°C. This drop in the magnitude of the crystallization exotherm can be explained in terms of an 'annealing' process which occurs in this polymer above its 'observed' melting transition. That is, even though the polymer is well above its observed melting temperature, it is annealing

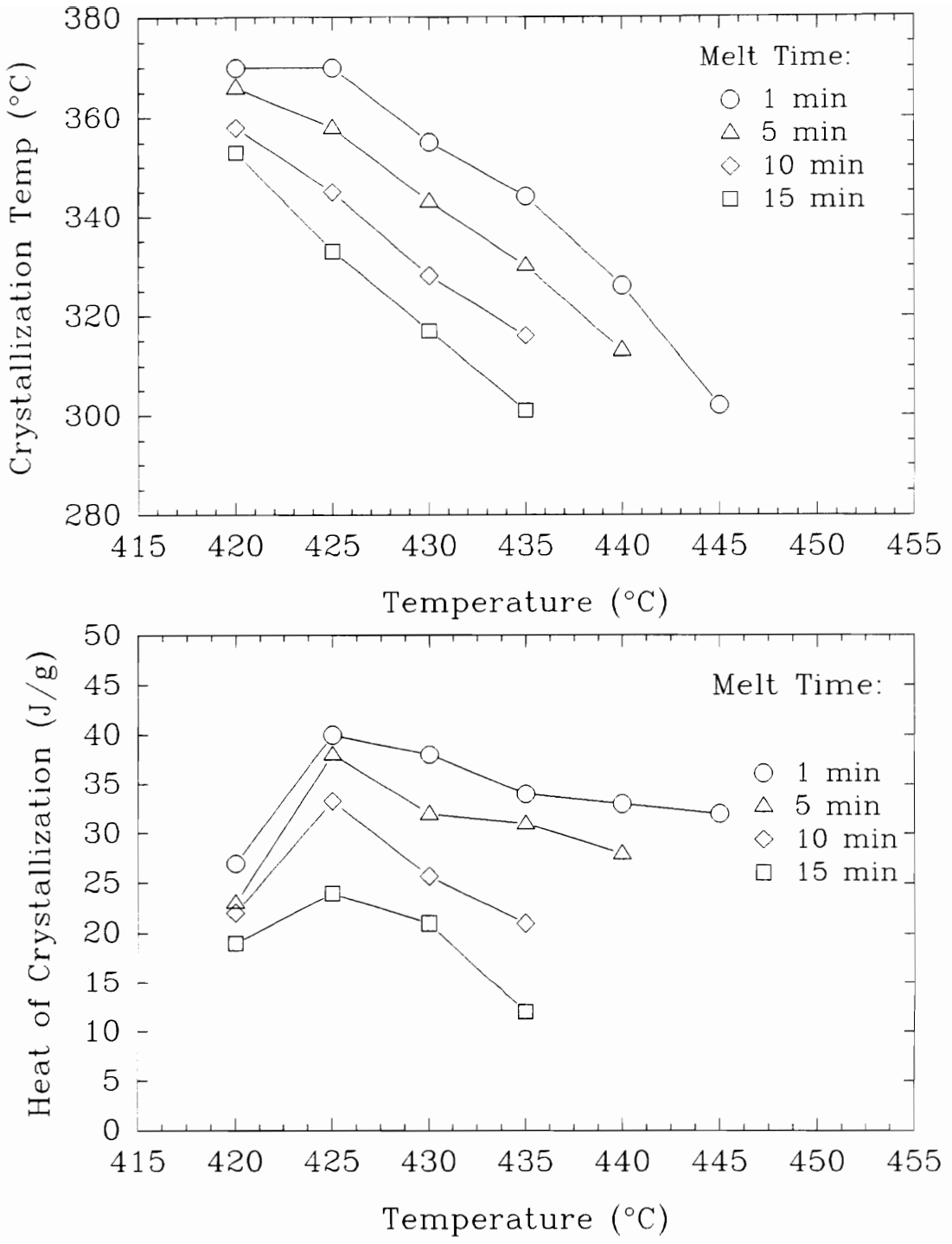

Figure 6.10 Peak crystallization temperature (A) and heat of crystallization (B) as a function of melt time and temperature for 7.5/p/m.

to yield even higher melting crystals. This is made evident in the second heat DSC scans of the powder samples held at 420°C, as shown in Fig. 6.11. In each scan there is a second higher melting transition. The peak temperature for this transition increases from ca. 429°C in the one minute melt time scan to ca. 435°C in the 15 minute melt time scan. Parallel to this increase of the second endotherm with melt time, the lower melting transition decreases from ca. 404°C to ca. 399°C. This is, of course, an expected result of increased melt time. This same effect is seen in the 425°C and higher melt temperature second heat scans, none of which possess a higher melting transition.

The phenomenon of "annealing" above the observed melting transition is not limited to the 7.5/p/m powder. As will be discussed in section **6.3.2,** this same process occurs in the LaRC CPI−2 powder produced in DMAc. Further discussion of the annealing of the 7.5/p/m powder at 420°C is presented in section **6.3.3.**

6.2.4 Melt Sensitivity of 7.5/p/m

Through the T_{cc} analysis it has been made clear that increased time and higher temperatures have had the effect of decreasing the exothermic response during cooling. The reason for this reduction of the amount of polymer crystallized during cooling is unexplained by this data alone. Once again rheological analysis reveals the nature of the change occurring above the melt. In

this case the melt temperature chosen for the measurement of the melt viscosity was 430°C (measurement temperature for the 7.5/p/d material was 375°C). This temperature is well above the zone where annealing can occur.

Similar to the rheological profile for the 7.5/p/d powder, the melt viscosity here has likewise undergone a dramatic increase in the span of one hour -- see Fig. 6.12. The melt viscosity increases from ca. 250 Pa·s to nearly 7,000 Pa·s. As argued before, this rise indicates that some branching, endlinking or cross-linking process is occurring in the melt state. Though this rise in melt viscosity is somewhat greater than that seen in the 7.5/p/d material (η^* increased from ca. 150 Pa·s to ca. 4,000 Pa·s), it is striking that it is occurring at a temperature that is 55°C *higher*. This would indicate that the LaRC CPI-2 powder produced in *m*-cresol possesses, in addition to its higher melting properties, some attribute that inhibits the chemical degradation process occurring at elevated temperatures. This difference between the two powders, along with others already introduced, will be discussed in the comparison section of this chapter (**6.5**).

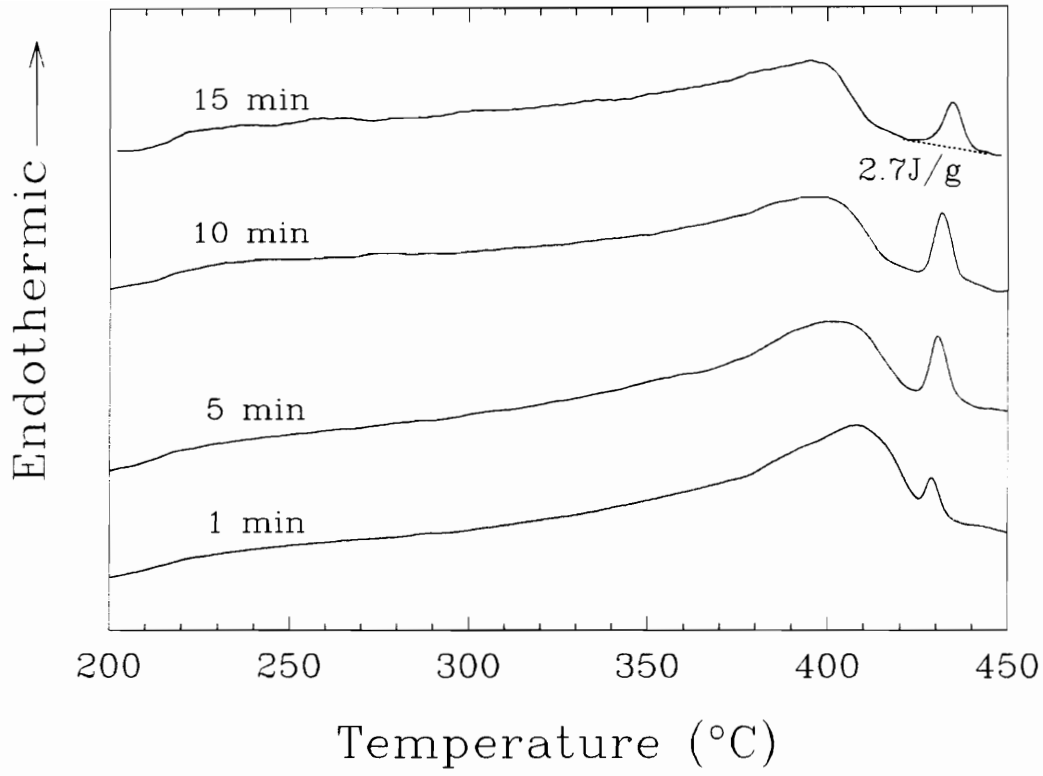

Figure 6.11 Second heat scans for 7.5/p/m samples held at 420°C.

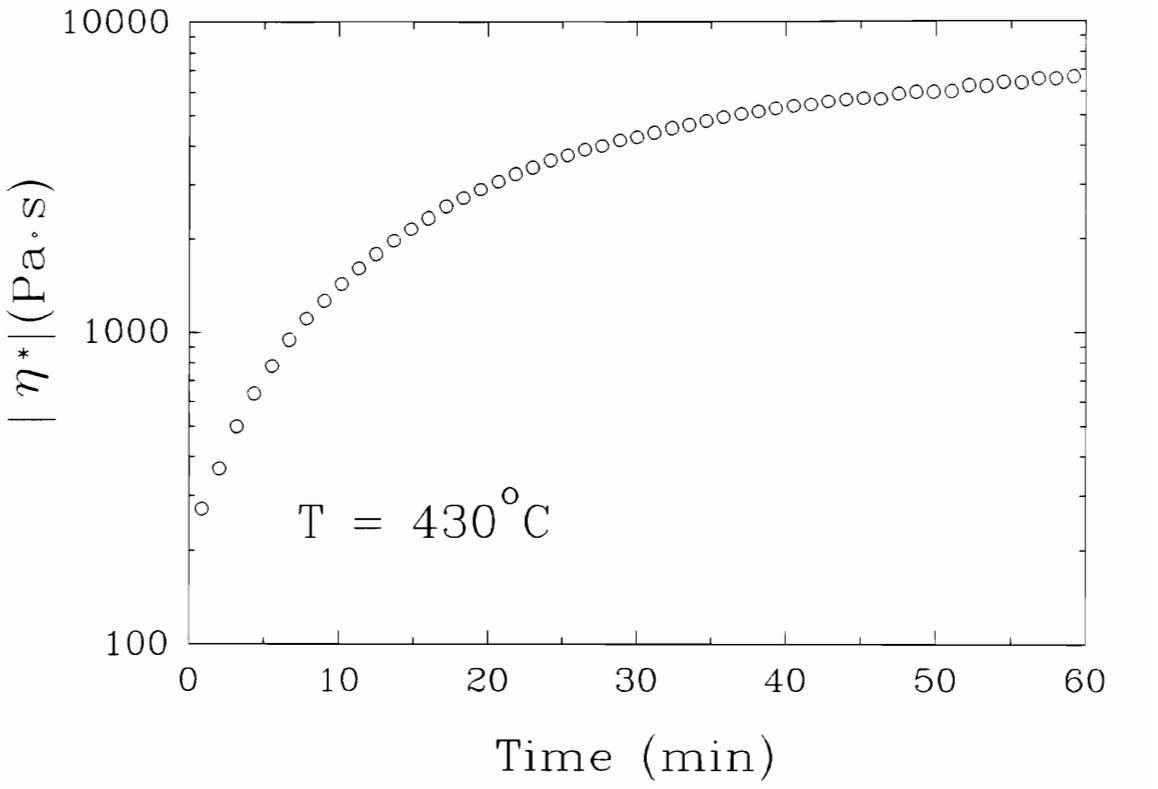

Figure 6.12 Melt viscosity of 7.5/p/m at 430°C in nitrogen.

6.3 Effects of Annealing on LaRC CPI−2 Powders

6.3.1 Methods for Evaluating the Thermodynamic Melting Temperature.

One particular technique often cited for the estimation of the equilibrium thermodynamic melting point of a polymer is the method developed by Hoffman and Weeks [87]. This method uses isothermal crystallization temperatures (T_c) significantly lower than the observed melting transition. The method is based upon the fundamental thermodynamic relationship between the observed melting point of a chain folded polymer crystal and its lamellar thickness as described in the Gibbs-Thomson equation (Eqn. 2.9). In the limit of thickening the 'lamellar' plate is comprised of fully extended polymer chains. This crystalline structure represents the equilibrium thermodynamic form for that molecular weight. The lamellar thickness is inversely proportional to the degree of supercooling used during isothermal crystallization. Thus, a linear relationship exists between the crystallization temperature and the observed melting point. The Hoffman-Weeks method employs an extrapolation of the observed melting temperature - crystallization temperature relationship to a value where $T_m = T_c$.

Attempts at acquiring this data were performed on the 7.5/p/d material at temperatures below the first melting transition, specifically at temperatures of 300°C, 310°C and 320°C. In all cases the thermograms following isothermal crystallization for relatively short periods (less than 30 minutes) revealed multiple endothermic transitions. This, of course, prevents a reasonable application of the

Hoffman-Weeks method. At longer times it was possible to develop a single melting transition. However, this approach yielded continuously increasing melting temperatures as seen, for example, in Fig. 6.13 for the 320°C crystallization. Here it can be seen that the melting temperature increases in a generally logarithmic manner with time, consistent with a lamellar thickening effect. This precludes the employment of the Hoffman-Weeks approach. Hence, another approach for determining the equilibrium thermodynamic melt point was sought.

One ostensibly simple approach comes to mind wherein the observed melt temperature at increasing times is extrapolated to infinite time. This, of course, could be achieved by plotting melt temperature as a function of inverse time and extrapolating to zero. This concept has been proposed by Khanna and Kumar [138]. As discussed by these authors, often these plots are non-linear and extrapolation becomes difficult. Their solution to this problem was to fit their data to an empirically determined equation and solve for T_m^0 -- see Eqn 6-2.

$$[T_m(1 + 1/At^n)] = \frac{T_m^*}{A}(1/t^n) + T_m^0 \qquad \textbf{(6-2)}$$

T_m^* and T_m^0 represent the lowest and highest possible melt points for the polymer in Kelvin. The values 'A' and 'n' are simply constants. An "initial guess" is made for these four terms and the relationship is optimized through a non-

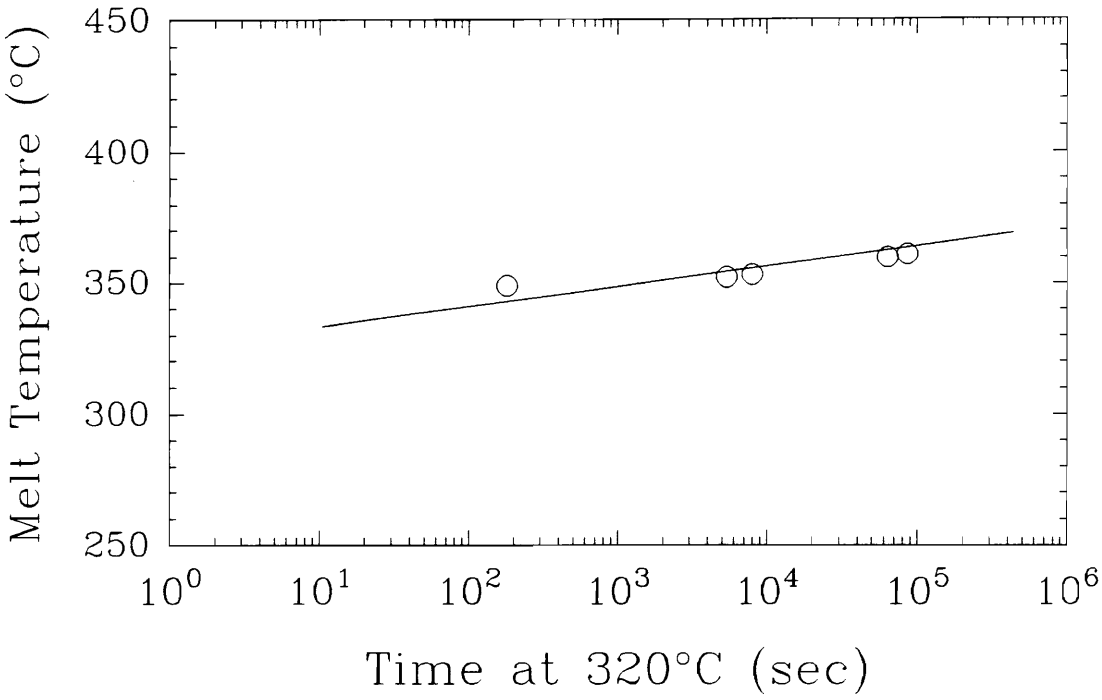

Figure 6.13 Continuously increasing melt temperature for samples of 7.5/p/d held at 320°C.

linear regression analysis. The estimated thermodynamic melt point, T_m^0, is found as the intercept.

With both the 7.5/p/d and 7.5/p/m materials, this analysis was performed and it was found that wildly different thermodynamic melting temperatures could be obtained with only minor variations in the initial 'constants'. Thus, it was determined that this method is inappropriate for this polymer system. However, in the process of gathering this data useful information did surface. Indeed, though the true thermodynamic melt point cannot be determined, a lower limit can be set. That is, the highest observed melting temperature is certainly below the thermodynamic melt point. The determination of these temperatures is presented in the next two sections.

6.3.2 Annealing of 7.5/p/d

In order to maximize the melting temperatures obtained, it was thought that the highest possible isothermal crystallization temperatures should be employed. That is, the lowest possible undercooling should result in the formation of the most perfect crystals obtainable through thermal treatment methods.

With the history of the 7.5/p/d material at 375°C, as discussed in section **6.2.2**, a lower temperature of 370°C was chosen as a beginning temperature for crystallization. Indeed, when the polymer was held in the melt at this temperature

for increasing times, annealing yielded higher melting transitions. This is notable because this "annealing" temperature is approximately in the mid-range of the second melting transition. Annealing times from 10 to 120 minutes yielded higher melting transitions ranging from 381°C to 388°C. Figure 6.14 shows the DSC thermograms for the samples annealed for 20, 45 and 120 minutes. The heats of fusion for these transitions were very small (on the order of 1J/g) for all annealing times from 20 to 120 minutes. The reasons for this can be elucidated from the scans in Fig. 6.14. At short times there is only little conversion of the lower melting material to the higher melting 'third' peak. This is, no doubt, due to the small thermodynamic driving force as a result of the very low supercooling. At longer times there is also low conversion. It is likely that conversion here is restricted by degradation effects. Given that this annealing temperature is only 5°C below 375°C, which has been shown to be detrimental over a period of 60 minutes, it is understandable that there would be very low conversion at longer times. It is worth noting that the T_g increases slightly from ca. 213°C to ca. 218°C in the span of 120 minutes at 370°C. It is probable that there is some degree of competition between processes of crystalline perfection and chain degradation/cross-linking at 370°C. The low magnitude of these higher melting transitions makes their analysis questionable, therefore a lower temperature was employed.

At 365°C the observed melting temperature initially increased significantly,

as seen in Fig. 6.15. However, at annealing times of 110 minutes and beyond, the observed melting temperature stabilized at ca. 387°C. Furthermore, multiple melting transitions were present in all the annealed samples through 120 minutes. This is important in explaining the heats of fusion for the annealed samples as shown in Fig. 6.15. For the annealing times at and below 120 minutes the lower melting crystals have not been reorganized into the higher melting form. At 110 and 120 minutes the transformation is beginning to favor the higher melting form as indicated by the elevated heats of fusion. However, beyond 120 minutes, where only the higher melting transition is present, the heats of fusion have dropped. This, once again indicates a prominent degradation effect. In fact, a sample held for 600 minutes at 365°C possessed no transitions at all. Here degradation was sufficient to override the annealing of the polymer. It is interesting to note that the crystalline phases must have degraded, as well.

Stepping down further in temperature to 360°C long annealing times can be achieved -- see Fig. 6.16. The generally logarithmic nature of the trend in melting temperature with time is clearly present. Very long annealing times were achievable with very high observed melting temperatures. At 1,000 minutes at 360°C the observed melting temperature was nearly 403°C. This event is significant in that the melting temperature of the annealed 7.5/p/d material is now approaching that of the 7.5/p/m powder (T_m = 408°C). The heat of fusion corresponding to this melting transition is only 1.3 J/g, as shown in Fig. 6.17. This

figure reveals the development of reasonably high heats of fusion up until 180 minutes (ca. 51 J/g, T_m = ca. 390°C) with a precipitous drop thereafter. It should be noted that multiple melting transitions were present through the 40 minute sample. Thus, these samples do not have integrated values of the high melting transition shown in the figure. Looking at the change in the glass transition temperature with annealing time it can be seen that its temperature rises dramatically, coincident with the drop in the heat of fusion values. At the highest annealing time the T_g has reached ca. 241°C. This rise is consistent with a cross-linking degradation process. Nevertheless, this annealing temperature has still allowed for a significantly elevated melting transition to be developed.

In conclusion it can be said that, for the 7.5/p/d material, the thermodynamic melting temperature is in excess of 403°C.

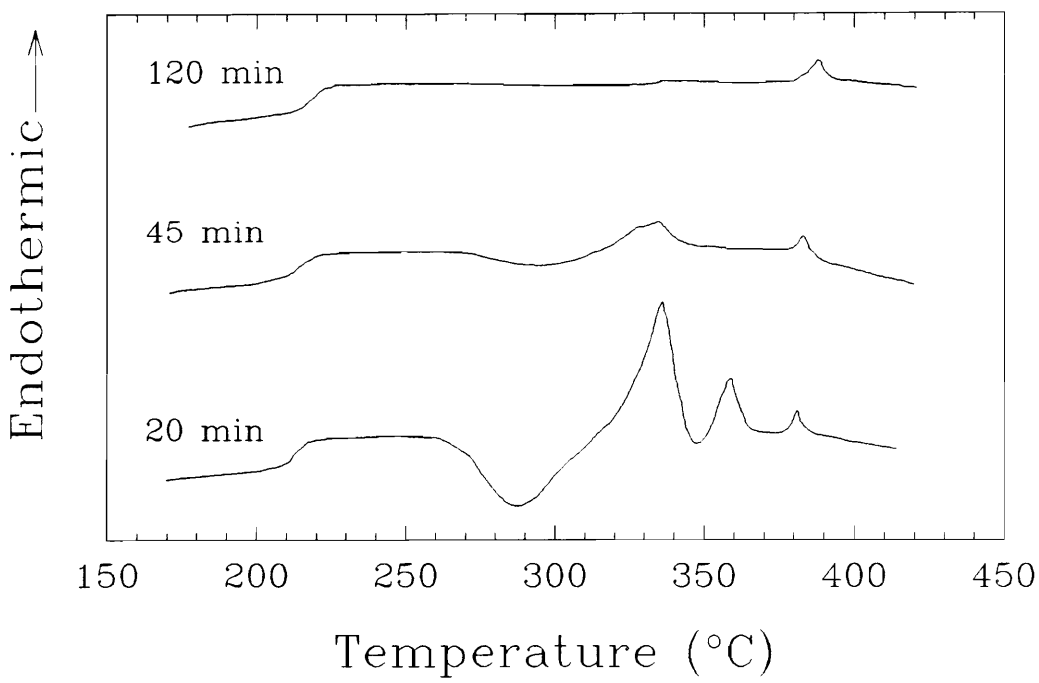

Figure 6.14 DSC thermograms of 7.5/p/d samples held at 370°C for 20, 45 and 120 minutes.

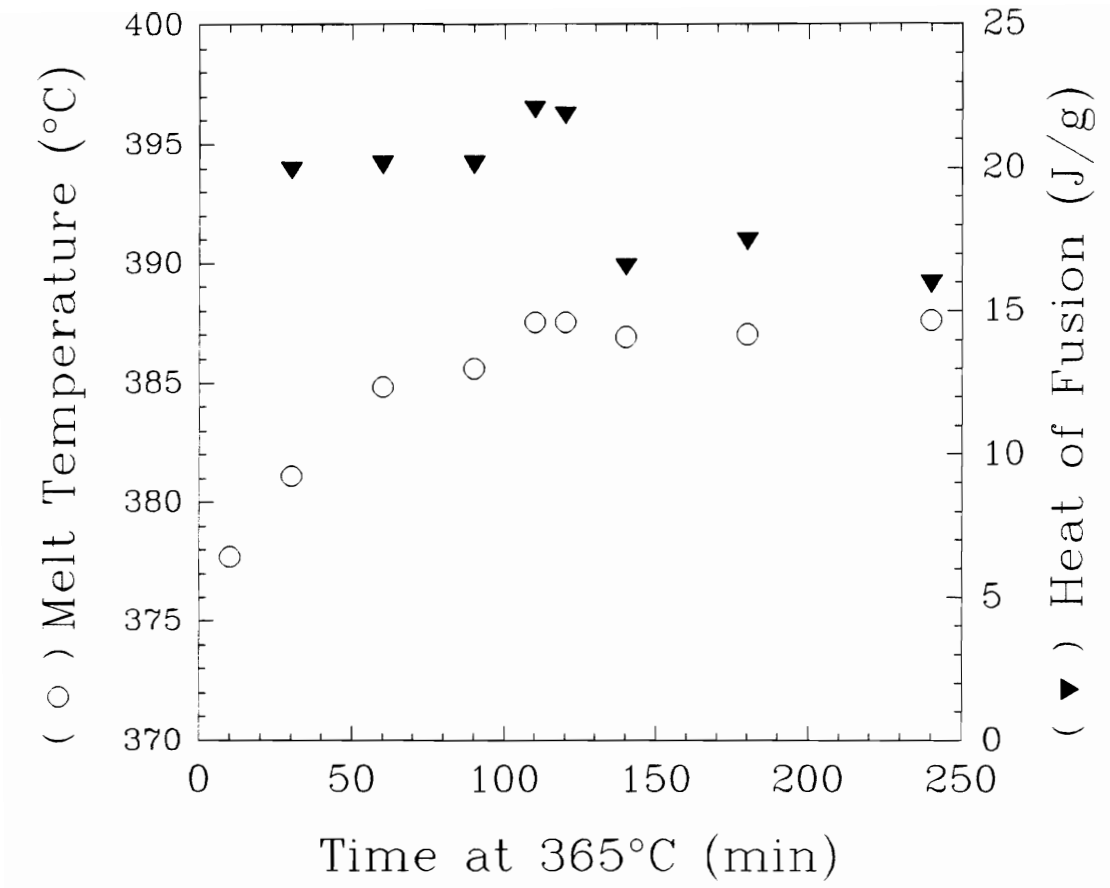

Figure 6.15 Melting temperatures and heats of fusion for 7.5/p/d samples held at 365°C for up to 240 minutes.

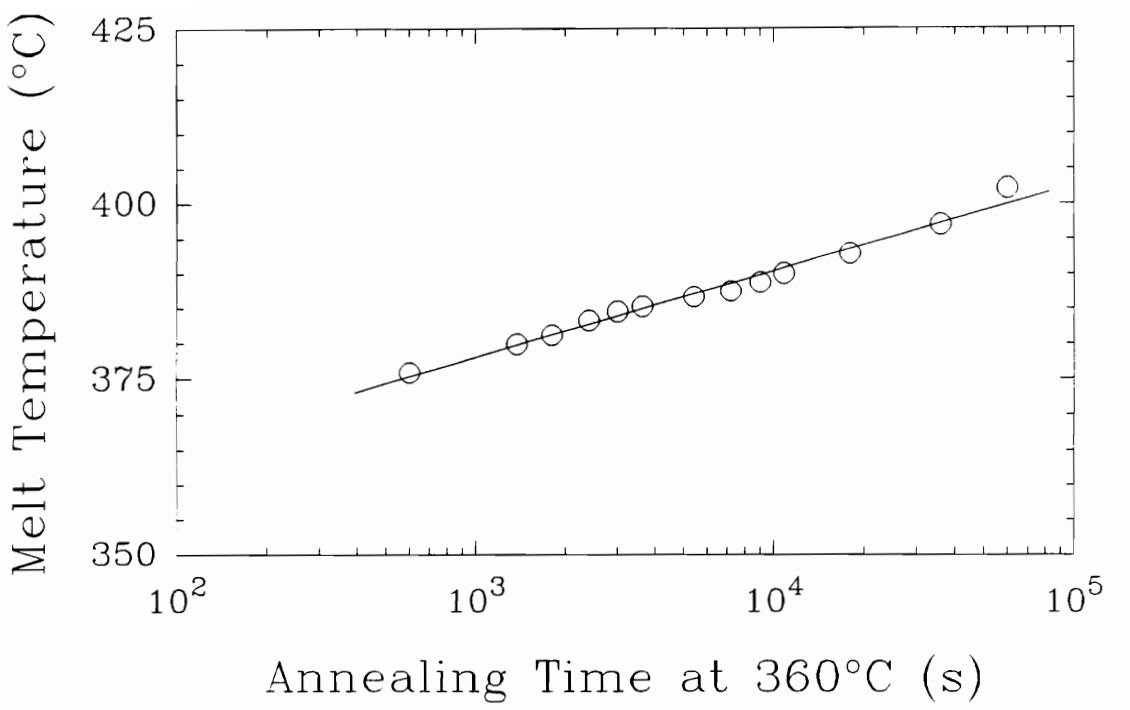

Figure 6.16 Melting temperatures for 7.5/p/d samples held at 360°C.

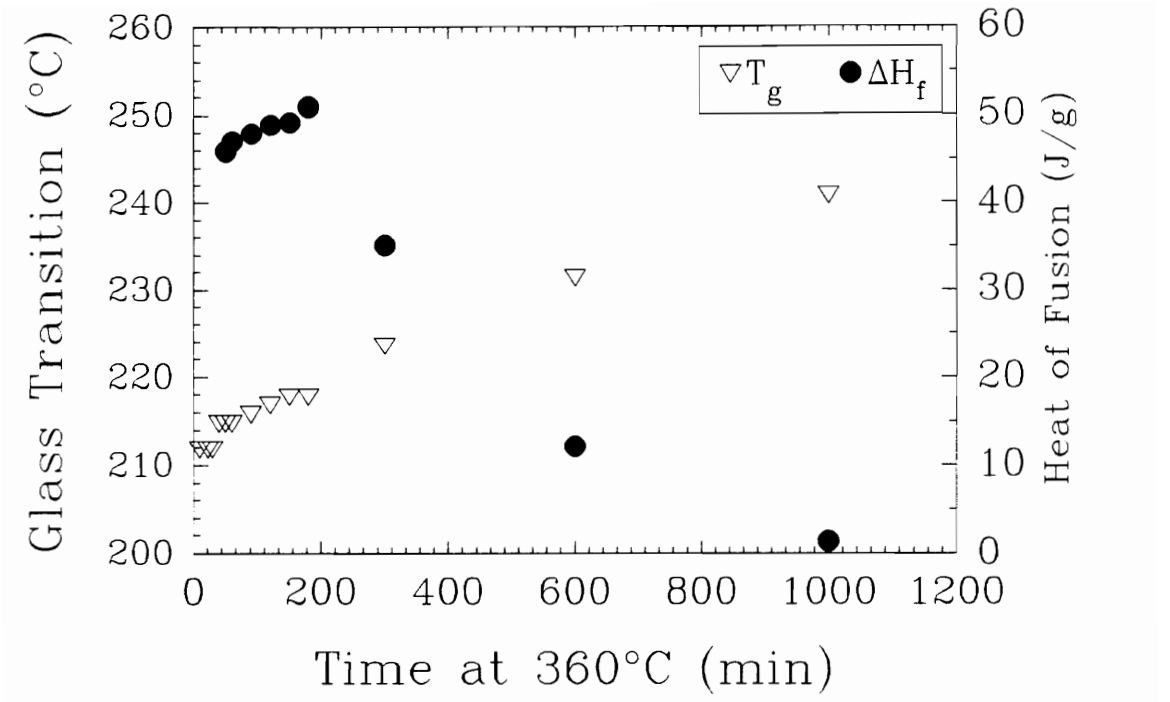

Figure 6.17 Glass transition temperatures and heats of fusion for 7.5/p/d samples held at 360°C.

6.3.3 Annealing of 7.5/p/m

In the case of the 7.5/p/m material the determination of an upper annealing temperature has already been made, as described in section 6.2.3. At 420°C it was shown that an annealing process is occurring -- approximately 12°C above the observed peak melting temperature.

As in the case of the annealing the 7.5/p/d material described above, very long annealing times and high temperatures were achieved in this sample as well. As seen in Fig. 6.18, the observed melting temperatures increase in a nearly logarithmic progression with annealing time. A rather startling result is the extremely high melting temperature of 489°C for the longest annealing time of 800 minutes! Given this high melting temperature, it is useful to inspect the heat of fusion in order to rule out any spurious baseline deviations in the DSC. Figure 6.19 shows both the T_g and heat of fusion values with annealing time. As seen earlier in Fig. 6.17 for the 7.5/p/d powder, T_g increases dramatically with time as the heat of fusion decreases, consistent with a cross-linking degradation process. The heat of fusion goes through a maximum of ca. 4.5 J/g at 180 minutes, thereafter it begins a steady decline. Graphically the changes in crystallinity and T_g can be seen in the DSC traces shown in Fig. 6.20. Here the melting transitions for all of the 420°C

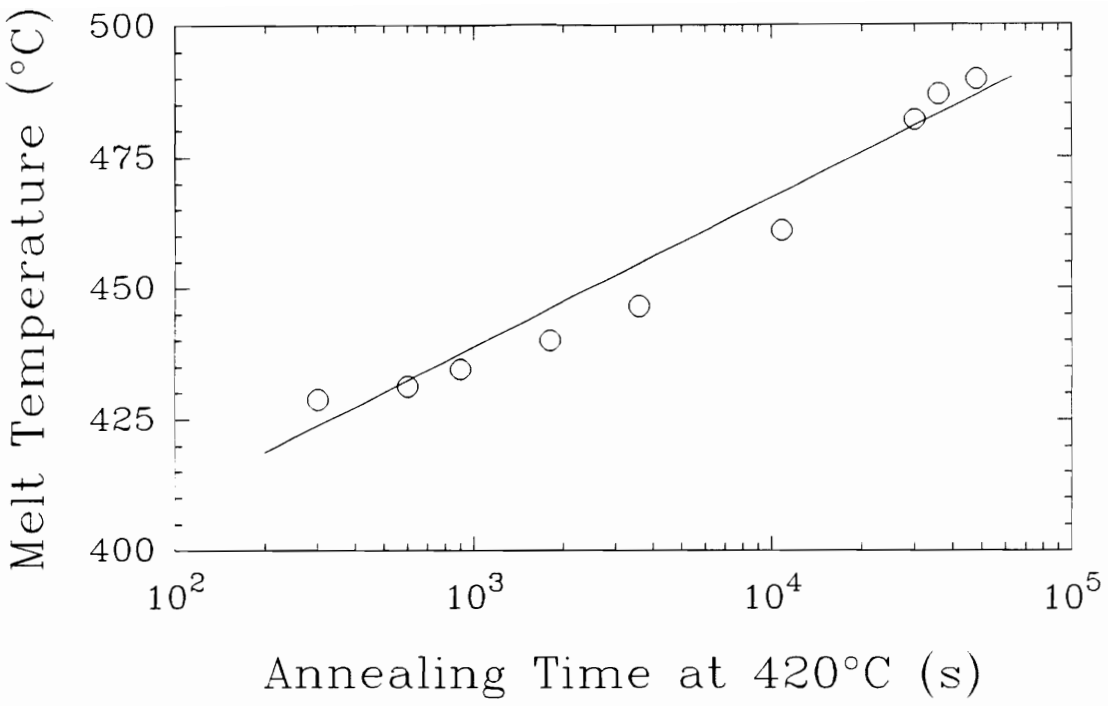

Figure 6.18 Melting temperatures for 7.5/p/m samples held at 420°C.

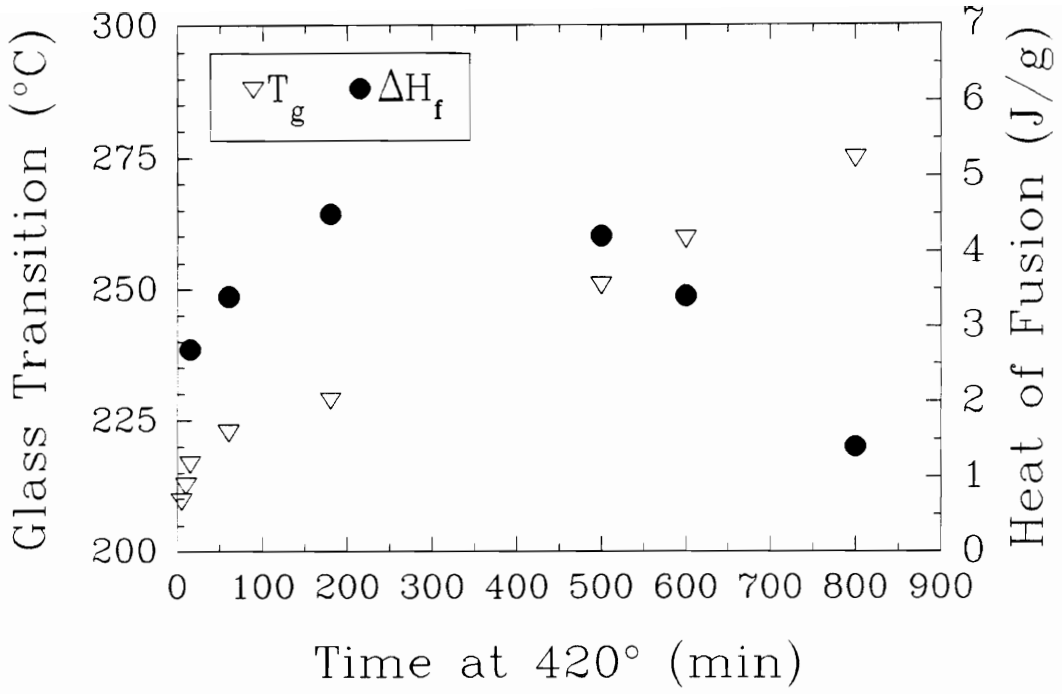

Figure 6.19 Glass transition temperatures and heats of fusion for 7.5/p/m samples held at 420°C.

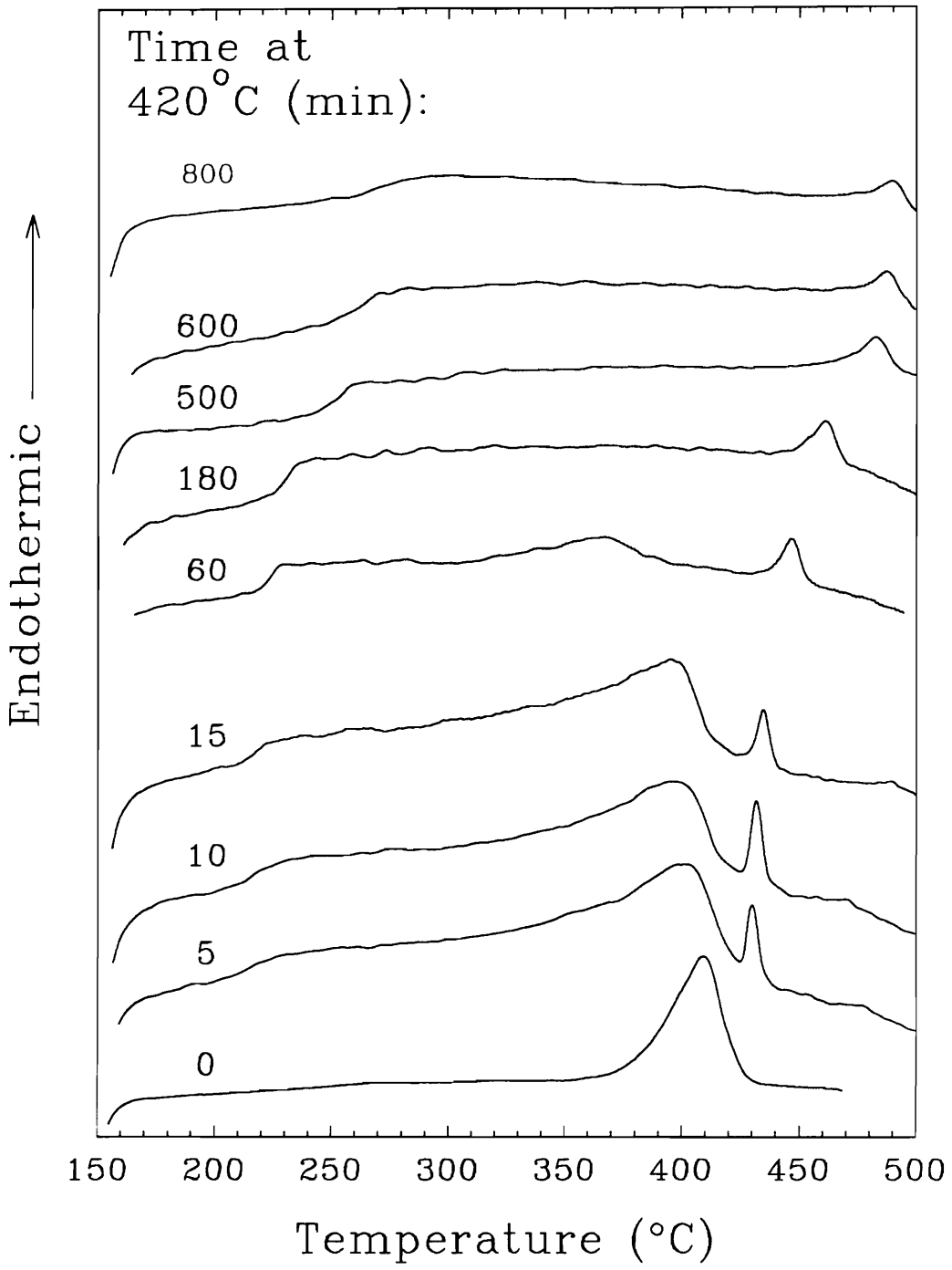

Figure 6.20 DSC traces for the 7.5/p/m samples annealed at 420°C. The magnitude of the 0 minute scan has been reduced by 50%. All times are in minutes.

annealed samples can be seen to increase in temperature coincident with a decrease in magnitude at the highest temperatures. The non-annealed 7.5/p/m DSC trace is shown for comparison (the magnitude of this scan has been reduced by 50% so that the scale for the other scans is reasonable). It is notable that the T_gs only become significantly broad at the 600 and 800 minute times. This would indicate that no significant level of cross-linking has occured up to the 500 minute (ca. 8.3 hour) point.

The nature of the crystals giving rise to the low magnitude transitions at the very high temperatures becomes suspect. It is possible that some other process rather than lamellar thickening and crystal perfection has occurred whereby the crystal structure has changed. Wide angle X-ray diffraction analysis can be employed in order to rule out this possibility. Shown in Fig. 6.21 are the WAXD profiles for the samples with annealing times of 500 and 600 minutes and the unperturbed powder. There is an obvious dramatic decrease in the level of crystallinity at the long annealing times, however, the principle diffraction angles remain the same. It is notable that the diffraction peaks are barely perceptible in the sample annealed for 600 minutes. This sample displayed a melting peak at 487°C with a heat of fusion less than 4 J/g. The 500-minute sample, which displays the easily discernable diffraction peaks, has a melting transition at 482°C with a heat of fusion of 4 J/g. Thus, in order to remain within the realm of certainty, it can be said that the thermodynamic melting temperature is in excess

of 482°C for the 7.5/p/m material.

It should be noted that others have reported on annealing of polymers above their initial melting transition. In a study of the effects of thermal treatment on PEEK, Zhang and Zeng [139] reported achieving melting temperatures of ca. 404°C and 417°C, well in excess of the equilibrium values of 395°C and 389°C reported by Blundell and Osborne [140], and Lee and Porter [141], respectively. This was achieved by annealing at 342°C (2°C above the T_m of 340°C). Zhang and Zeng proposed that the high melting crystals were formed by self-seeding off residual (original) lamellae and cross-linking in the amorphous phase near the crystallizing lamellae.

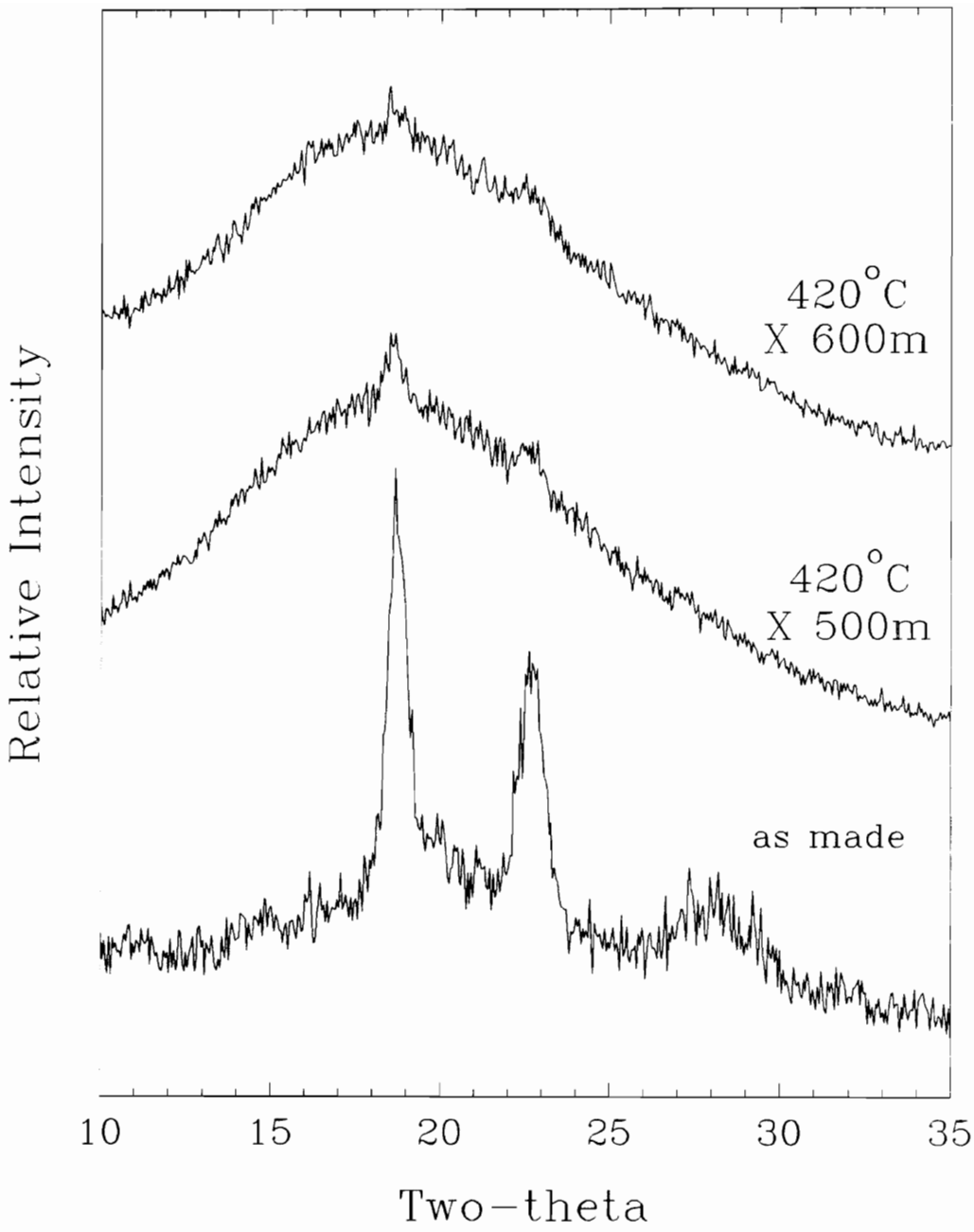

Figure 6.21 WAXD profiles for samples of 7.5/p/m annealed for 500 and 600 minutes at 420°C along with the unperturbed powder.

This is in marked contrast with the lower boundary of 403°C determined for the 7.5/p/d material as discussed in section **6.3.2**. The possible reasons for the dramatic difference are discussed in section **6.5**.

6.4 Crystallization Kinetics via Rheometry Analysis

6.4.1 Crystal Kinetics Analysis of LaRC CPI–2

As discussed in chapter 2, it is desirable to perform an Avrami analysis in order to characterize the crystallization process. A great deal of effort was expended in the attempt to perform this evaluation on LaRC CPI–2 using DSC analysis. Attention was first focused on the 7.5/p/d powder with the express objective of gathering information that would later be used to compare and contrast with data likewise gained from analysis of the 7.5/p/m powder. Ideally, rate constant and Avrami exponent data could be compared thereby allowing for a quantitative comparison of kinetic information.

A myriad of thermal procedures ranging from melt times and temperatures of 0 minutes at 365°C to 15 minutes at 390°C, with isothermal crystallization temperatures ranging from 275°C to 365°C were employed. In every case, one of two circumstances prevailed. Either the beginning of crystallization had already begun before thermal equilibrium was achieved or the exothermic response was too small to reasonably analyze. In the former case the it was clear that the nucleation sites had not been sufficiently eliminated with the result of a very rapid

nucleation initiating bulk crystallization before the DSC could stabilize and capture the event. The obvious counter to this response is to either hold the polymer in the melt longer or at a higher temperature. This approach resulted in the latter condition of a poor exothermic response in which, typically, the amplitude of signal noise was on the order of the amplitude of the exotherm signal.

These results are entirely consistent with the melt time results presented in section **6.2**. At short times, and/or lower melt temperatures, the higher temperature nucleation sites remain allowing the crystallization to begin "prematurely" during cooling while at long times, and/or high temperatures, degradation processes dominate and less of the polymer is able to crystallize.

Thus, it became clear that a method other than DSC analysis would need to be employed in order to gain kinetic information. In a recent study of the effect of nucleating agents in nylon 6, Khanna studied the crystallization process by monitoring the storage modulus, G', over time during isothermal crystallization in a rheological spectrometer [142]. Khanna was able to determine crystallization rates from the slope of the normalized G' curve (min^{-1}) for various nylon samples. A key advantage to this method of analysis is that the response of the instrument is mechanical in nature. None of the signal stabilization factors that plague DSC analysis are operative here: Crystallization will directly cause G' to increase, regardless of the status of the temperature stabilization. Thus, if crystallization

begins before total stabilization of the instrument temperature its initiation will not go undetected. It should be noted here that crystallization in a DSC is quiescent in nature whereas crystallization in a rheometer occurs in a dynamic [shearing] environment.

Though Avrami analysis was not utilized in the work by Khanna it appears that it may be possible to apply it to rheological isothermal crystallization data. With this specific objective in mind, rheological analysis was undertaken on LaRC CPI−2 samples.

As will be discussed in section **6.4.3,** Avrami analysis of the crystallization data does not yield useful results. However, the rheological analysis still offers an excellent view of crystallization rates as discussed in sections **6.4.3** and **6.4.4**. All analysis throughout this section is focused on the two LaRC CPI−2 powders already compared and contrasted throughout this chapter: 7.5/p/d and 7.5/p/m.

6.4.2 Operational Conditions in the Rheometer and Treatment of the Data

In order to acquire acceptable storage modulus data, for subsequent isothermal crystallization analysis, it was necessary to determine optimal operating conditions for each powder type individually. Though strain rates, frequencies and machine constants were the same for both powders, the melt times and temperatures were not (Note that specific instrumental constants and parameters are presented in section **3.3.4.2**). Considerable experimentation was necessary to

find optimal conditions. During this work it was discovered that there was an extreme dependence of the crystallization response upon initial conditions of time and temperature in the melt. Thus, great care was exercised to ensure that each sample, within a class, experienced exactly the same melt history. The 7.5/p/d powder samples were held in the melt at 373°C for 30 seconds while the 7.5/p/m samples were held for 5 minutes at 435°C.

The storage modulus data collected for the crystallization isotherms is sigmoidal in shape as shown in Fig. 6.22. Prior to analytical treatment of the data, all storage modulus curves were normalized thereby allowing for comparative analysis -- see Fig. 6.23. The examples shown in this figure represent isothermal crystallizations ranging from 275°C to 315°C. It is clear that the sample held at 275°C crystallized faster than the others in this example. A full treatment of this and other data is presented in the following sections.

6.4.3 Avrami Analysis

As stated before, it appears that Avrami analysis may be compatible with isothermally collected rheological storage modulus data. There are some obviously distinct differences between crystallizing a polymer within a DSC cell and within a rheometer. Most notably is the perturbation of the polymer that occurs within the rheometer. Crystal nucleation and growth processes are likely to be greatly influenced by the sinusoidal agitation of the polymer melt.

Furthermore, the dimensionality of the growing crystalline superstructure is not likely to have the same degree of freedom as exists in the undisturbed state within the DSC. Nevertheless, Avrami analysis of rheological data is an attractive possibility worth investigating.

Looking at the normalized crystal fractions shown in Fig. 6.23, it can be seen that they are similar to those which may be obtained through standard DSC analysis. It is from this juncture, then, that Avrami analysis was applied. Samples of the 7.5/p/d powder, crystallized from 260°C to 290°C, were initially chosen for examination. Linear regression analysis of the linearized Avrami equation (Eqn. 2−12) for each of these samples was restricted to normalized crystal fractions ranging from ca. 1% to ca. 30%. This range ensures a reasonable representation of the crystallization process while eliminating signal noise at very low crystal fractions and likely avoiding major crystal impingement effects at higher levels of crystallinity.

Table 6.2 displays the results of this analysis. The first item of note is that the regression coefficients for the analysis are all very high. Thus, it is not unreasonable to proceed. The Avrami exponent values do not appear to lend themselves to easy interpretation as they range, unsystematically, from 5.1 to 6.8.

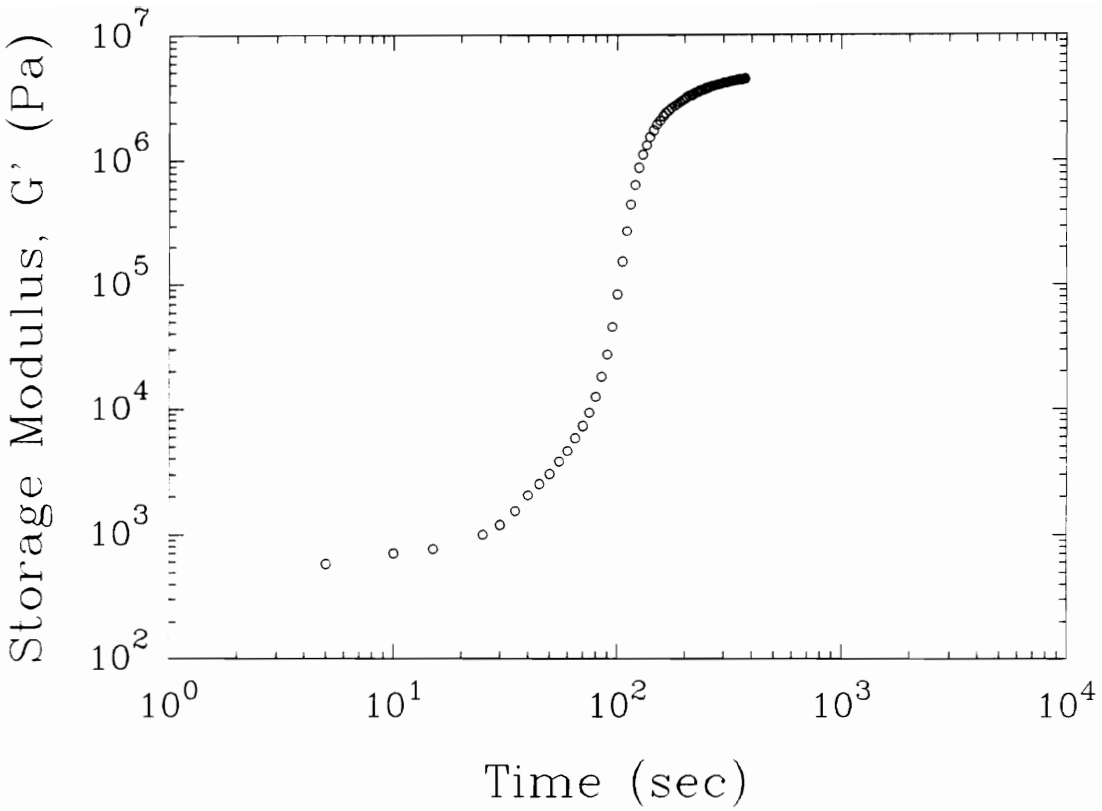

Figure 6.22 Storage modulus as a function of time during isothermal crystallization of a 7.5/p/d powder at 270°C.

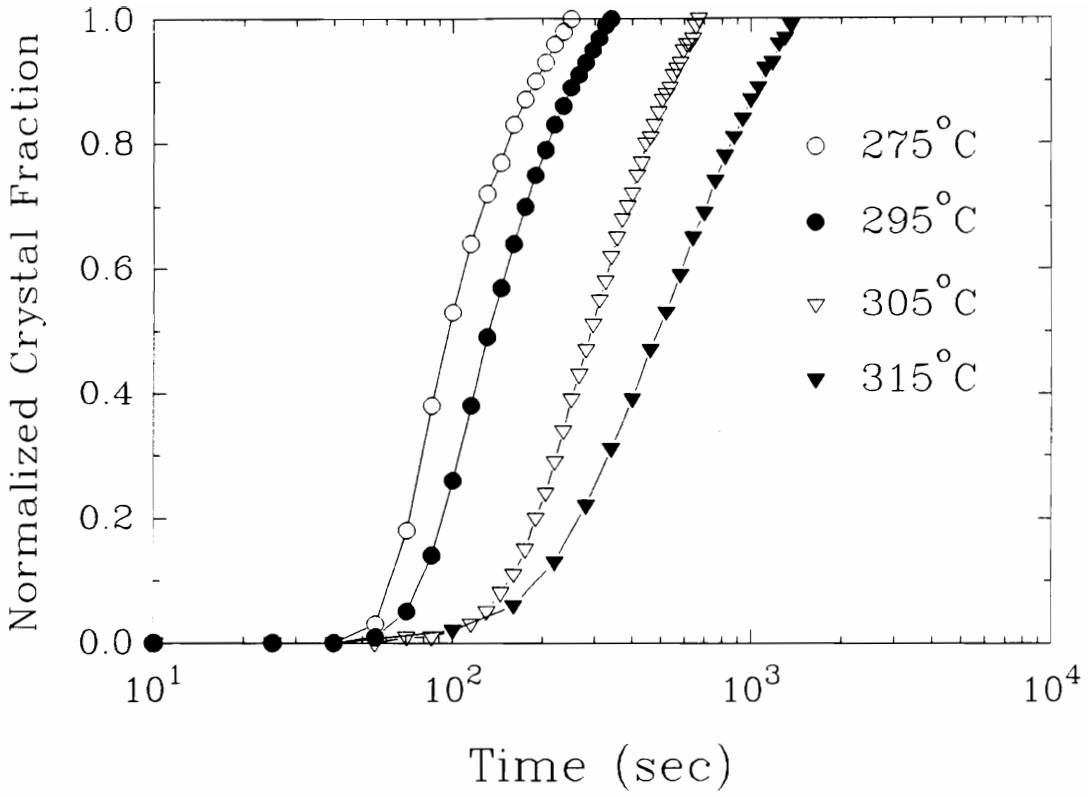

Figure 6.23 Normalized crystal fraction as a function of time for some selected isothermal crystallizations of the 7.5/p/d powder.

Table 6.2. Results from Avrami analysis applied to normalized crystalline data obtained from rheological analysis.

T_x	ln(k)	k(x10^{12})	n	R^2
260°C	-22.54	163	5.1	0.984
265°C	-26.47	3.19	5.5	0.965
270°C	-30.49	0.0573	6.6	0.978
275°C	-30.48	0.0579	6.8	0.979
280°C	-28.80	0.311	5.5	0.997
285°C	-28.40	0.463	6.1	0.980
290°C	-26.59	2.83	5.6	0.974

Most notable, however, is the trend revealed in rate constant values. There is a definite minimum in the range of 270°C to 275°C. This can be seen more clearly in Fig. 6.24. Also included in this figure are the Avrami exponent values. The trend in the rate constants fairly well matches the crystallization half-time data presented in section **6.4.4**. Though this is somewhat interesting, it certainly does not support the application of Avrami analysis to rheological data for LaRC CPI−2 polymers. The rate constant data should, of course, *mirror* the crystallization half-time data, showing a maximum at the temperature of fastest crystallization. As will be seen in the next section, rate constant data derived from the slope of the normalized crystallization curve at 50% crystallinity correlate well with the half-time data, also presented there. Unfortunately both of those analyses contradict the Avrami results.

Given the nonsensical results of the Avrami analysis, and the tenuous justification of its application in this instance, further investigations in this matter were not pursued.

6.4.4 Crystallization Half-time Analysis and Crystallization Rates

Though the Avrami analysis proved useless, the effort of collecting the rheological isothermal crystallization data was not a futile endeavor. In fact, the rheological analysis has allowed for the characterization of the crystallization process for both powder types across a wide range of crystallization temperatures. The two characteristic features of the crystallization process to be discussed in this

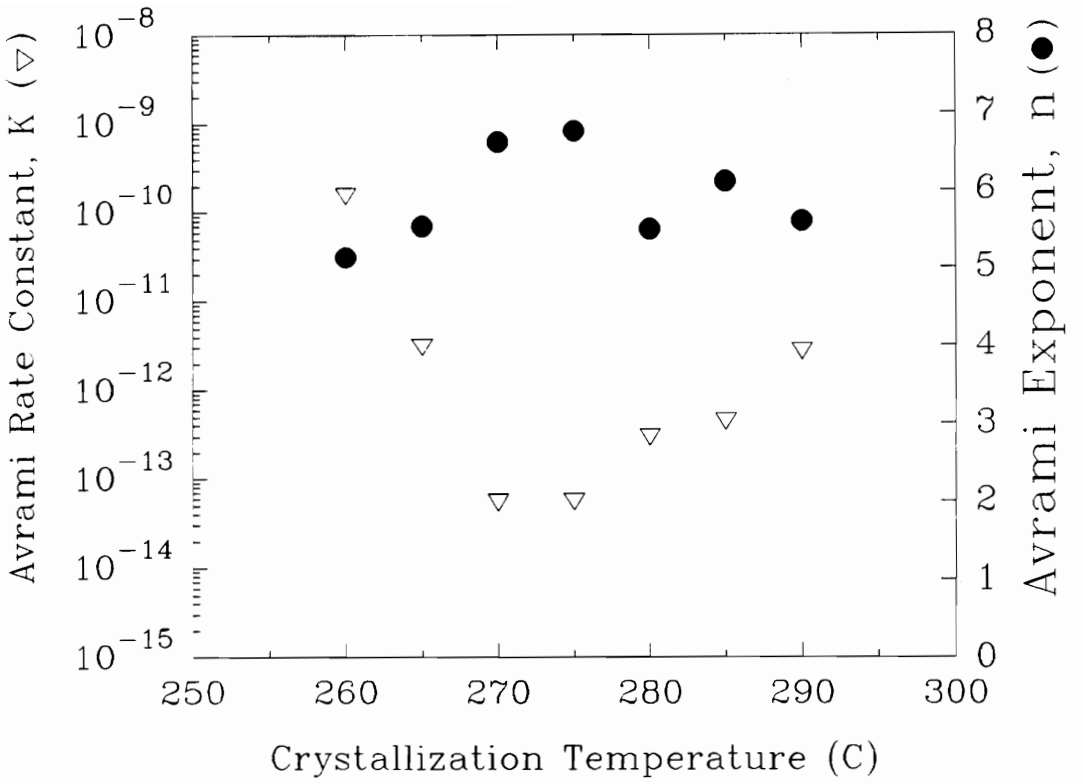

Figure 6.24 Avrami rate constant and Avrami exponent for 7.5/p/d samples isothermally crystallized in the rheometer.

section are the crystallization half time and the rate constant as determined from the slope of the normalized crystallization curve at 50% [normalized] crystallinity.

The crystallization half-time simply represents the time necessary to reach 50% normalized crystallinity. The results of this analysis for both powder types is shown in Fig. 6.25. Though the thermal histories for the two powder types is dramatically different, as described in section **6.4.2**, both sets of data are able to be represented on the same graph. No comparisons, however, should be made between the two powders with regard to the absolute values. What is immediately apparent from the plot is that, in both cases, the crystallization process was characterized through the maximum in crystallization rate. Furthermore, the

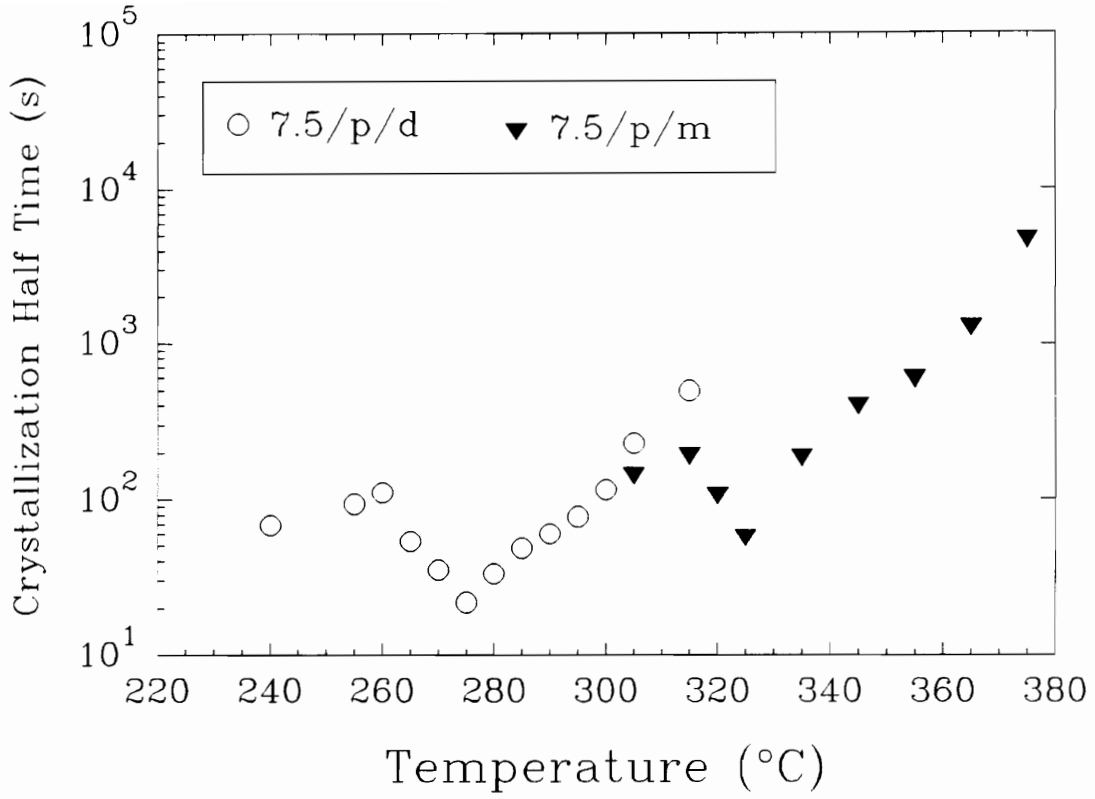

Figure 6.25 Crystallization half–times for both powder types as a function of temperature.

minimum half-times for the two powder types are separated by approximately 50°C: ca. 275°C and ca. 325°C for the 7.5/p/d and 7.5/p/m powders, respectively.

The observation that there are two minima for this 'one' polymer does not, in itself, hold any particular mechanistic significance. It must be remembered that the two powder types experienced greatly different melt times and temperatures. The residual nuclei in the 7.5/p/d powder were not subjected to the higher temperature and longer time that their counterparts in the 7.5/p/m powder experienced (373°C X 30 seconds vs 435°C X 5 minutes). Were it possible to subject both powders to the same thermal history, the two peaks would likely merge.

The lowest temperature data for both curves shows a sharp downward trend indicating a more rapid crystallization process. This is undoubtedly due to the dominating effect of nucleation density at the high degree of supercooling for each powder type.

An analysis of the rate constant, as determined by the slope of the normalized crystallization curve at the exact point of the half-time, provides another view of the crystallization kinetics. It would appear that this analysis simply offers another view of the same data. This is not so. Though the two are interrelated they are not necessarily interdependent. For example, if the polymer sample were to undergo a two-stage process such as a rapid initial crystallization with a subsequently slower final crystallization step, the half-time might

correspond to a point somewhere in the later stage where crystallization was excessively slow. The corresponding slope at this point would indicate slow crystallization whereas, overall, the sample crystallized reasonably quickly. Thus, if the sample experiences a generally single-stage crystallization and the end point was chosen properly, then there will be a reasonable correlation between half-time and the rate constant.

This relationship is what is found for both powder types as shown in Fig. 6.26. Clearly, the rate constant data does not represent a mirror image of the half-time data, but the trends are consistent. Here, as before the data reveal a maximum in crystallization at ca. 275°C and 325°C for the 7.5/p/d and 7.5/p/m powder types, respectively.

6.5 Comparison of LaRC CPI−2 Powders Synthesized in DMAc and *m*-cresol

As has already been shown in chapter 5 and in sections of this chapter, there are great differences in the melting and crystallization behavior between LaRC CPI−2 powders synthesized in DMAc and *m*-cresol. However, the other fundamental crystalline characteristics of the two powders are the same. A brief review of the similarities and differences is provided in Table 6.3.

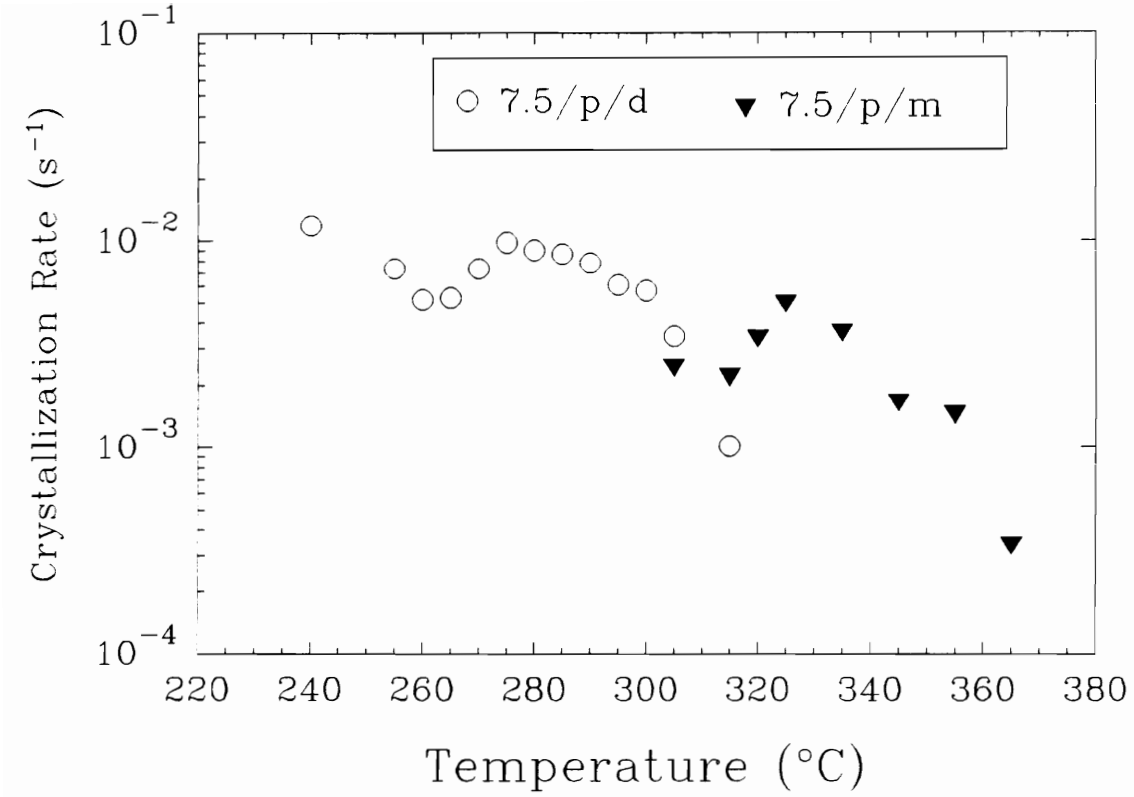

Figure 6.26 Crystallization rates for both powder types as a function of temperature.

Table 6.3. Comparison of LaRC CPI−2 powders synthesized in two different solvents: 7.5/p/d in DMAc; 7.5/p/m in *m*-cresol.

Property	**7.5/p/d**	**7.5/p/m**
T_m	345°C/366°C	408°C
Crystalline Index	48%	46%
WAXD Diffraction Profile	Same	
FTIR Spectra	Same	
TGA (5% loss Temperature)	499°C	506°C
Highest possible crystallization Temperature	370°C	420°C
Highest Clearly Observed Melting Temperature	402°C	489°C

With the knowledge that the mechanism of degradation in both powders involves cross-linking (increase in η^*_{melt}), it is logical to focus attention in this area. It is tempting to simply attribute the differences to a solvent effect. That is, the *m*-cresol acts as a good solvent resulting in the precipitation of a highly/crystalline ordered polymer during synthesis. This highly crystalline polymer then, would have a greater ability to resist the effects of elevated temperatures by possessing a lesser amount of amorphous material available for cross-linking. This scenario, though, is not supported by the WAXD evidence in that there is no great difference in crystalline levels between the two powders, nor in the width of their diffraction peaks. It may be argued that a larger lamellar thickness in the 7.5/p/m powder provides a greater barrier to the cross-linking. It must be remembered, however, that the 7.5/p/m powder showed a greatly enhanced ability to withstand elevated temperatures *above* its melting transition (where these thicker lamellae would be melted out). Thus, another explanation must be sought.

As mentioned in section **6.2.2** the ketimine reaction is a possible route for cross-linking in this polymer. Indeed, there is precedent for the occurrence of this reaction in a similar high performance polymer. A "self cross-linking" phenomenon was reported to occur in an amine terminated linear poly(aryl ether ketone) at temperatures of 220°C by Mohanty et al. [134]. A systematic approach, using oligomers and model compounds for comparison, allowed the authors to

confirm that ketimine formation was responsible for the cross-linking. Looking at the structure of LaRC CPI−2 shown in Fig. 3.1, one could consider it to be a poly(aryl ether ketone) which contains imide functionalities within the backbone chain. The presence of amine groups in LaRC CPI−2 are potentially provided by inefficient end-capping by the phthalic anhydride during synthesis. Additionally, as discussed in section **2.2.2**, a recent study by Kim et al. [55] clearly showed that imine links formed during solution imidization of BTDA-based polyimides. Furthermore, it should be remembered that Hergenrother et al. found that ketone bearing dianhydrides formed gels during polymerization of the poly(amic acid)s [50]. Thus, it is not difficult to envision the ketimine reaction occurring in LaRC CPI−2 polymers.

The possible existence of this reaction by itself, however, does not explain the *difference* in melting and crystallization behavior. In order to explain this, it is necessary to look closer at the ketimine reaction. It is known that the formation of a ketimine in low molecular weight organic compounds, in aqueous environments, is dependant upon pH and the basicity of the amine [143, 144]. A maximum in the rate of formation of the ketimine typically occurs at pH levels of ca. 4.5. No reaction occurs at either very high or very low pH values. Though the reaction conditions in a polymer melt are vastly different from that of low molecular weight organics in solution, it is reasonable to assume that the relative acidity of the environment still plays a role in the reaction. In fact, Mohanty et

al., along with others [134 - 137], used the pH sensitivity of the ketimine reaction to their advantage in synthesizing poly(aryl ether ketone)s. Initially the polymers were synthesized with bulky side groups, attached via a ketimine link, in order to enhance their conformational entropy and thereby remain in soluble for processing and characterization. The final stage of synthesis relied on hydrolysis of the ketimine link with an acid, e.g., triflouromethane sulfonic or hydrochloric acid.

Reflecting on the character of the solvents used in the synthesis of the two powders under consideration we see that the *m*-cresol has the potential to be acidic. In fact, *m*-cresol is not much less acidic than phenol: pK_a (*m*-cresol) = 10.0; pK_a (phenol) = 9.9 [128]. Certainly *m*-cresol is more acidic than DMAc. Thus, it is possible that the *m*-cresol solvent acts to inhibit the ketimine reaction from occurring.

If this were the case, then difference in the initial melting temperatures of the two powders could be explained in terms of a suppression of ketimine branching or cross-linking in the powder as it was being processed in *m*-cresol. The polymer chain produced in *m*-cresol would be more linear in character consequently crystallizing into more ordered, higher melting, structures. The dramatic difference in the ability of the two powders to withstand elevated temperatures would not be explained by this initial state, however. Continued suppression of a ketimine reaction at elevated temperatures would require some

residual amount of *m*-cresol to remain within the powder. As shown in Fig. 5.19, the TGA thermograms of the two powders do not appear to be greatly different, and no dramatic solvent loss at elevated temperatures is apparent. However, it may be possible that only a catalytic amount of *m*-cresol is necessary to suppress the ketimine reaction.

With this in mind a combined gas chromatography mass spectrometry analysis was performed on the 7.5/p/m powder to seek out the presence of *m*-cresol. A 2mg sample of the 7.5/p/m powder was extracted with 250μl of dichloromethane, within which *m*-cresol is soluble. The GC-Mass Spectrometer analysis was then performed on a 5μl injection of the extract. The retention time of 1.83 minutes for the peak on the gas chromatograph matched that of a 5μl injection of a standard solution of *m*-cresol (50ng/2μl). The mass spectrometry analysis of the effluent corresponding to the peak on the gas chromatograph for the extract from the CPI−2 powder matched well with that from the standard solution as seen in Fig. 6.27. The dominate mass fragment peaks at mass 107, 108 and 109 match well in both scans as do most other mass peaks. Both scans match well with the NIST (National Institute of Standards and Technology) standard spectra #2118 for 3-methyl phenol (*m*-cresol). The amount of *m*-cresol in the sample was calculated from the gas chromatograph using a response factor calibrated from the analysis of the standard solution of *m*-cresol. A value of 200ng of *m*-cresol in the 5μl injection sample was found. This translates to

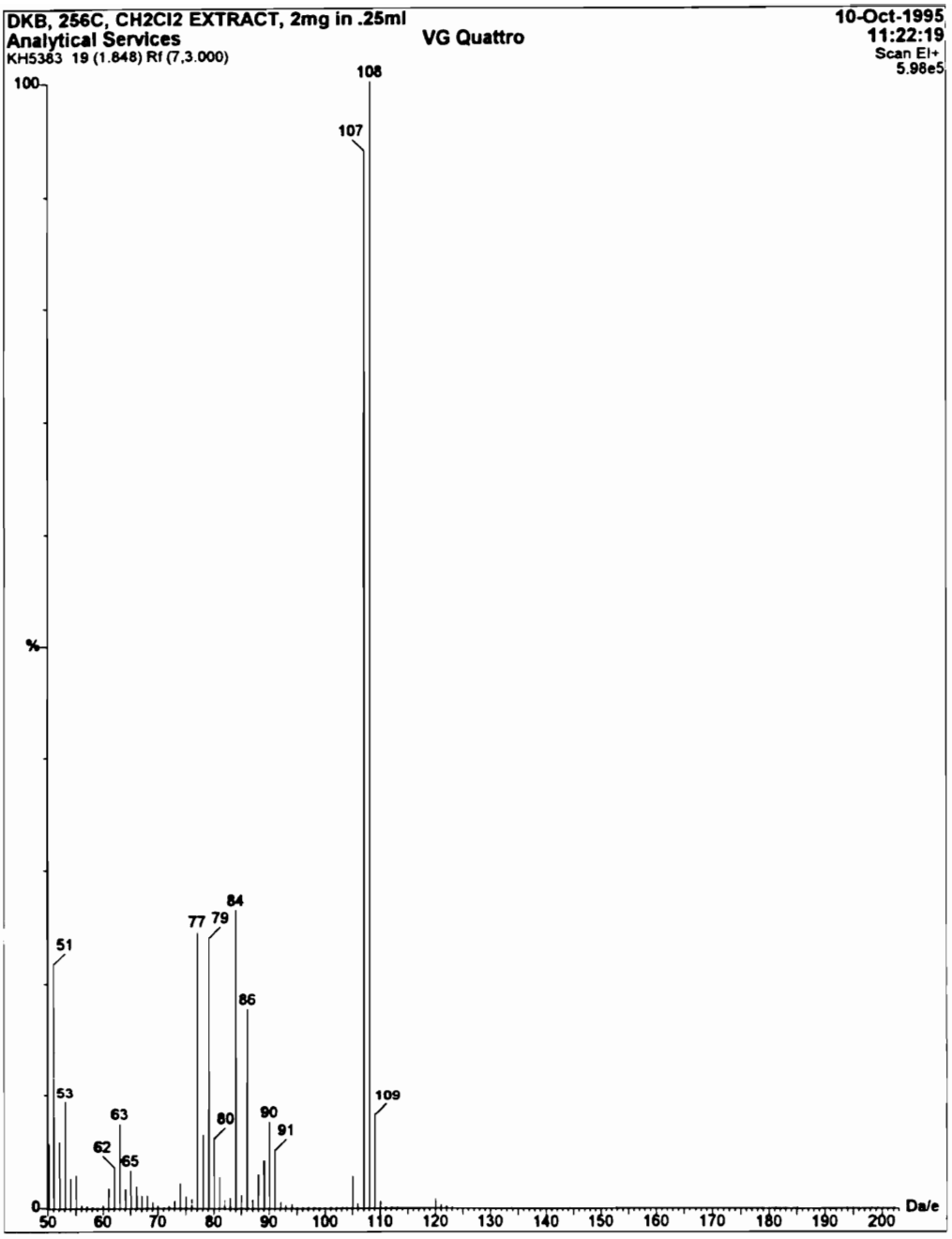

Figure 6.27a The mass spectrograms of the effluent corresponding to the peak on the gas chromatograph for the extract from the 7.5/p/m powder.

Figure 6.27b The mass spectrograms of the effluent corresponding to the peak on the gas chromatograph for the *m*-cresol from the standard solution.

5,000ng *m*-cresol in 1mg of 7.5/p/m, or 0.5% (w/w). Clearly, some residual *m*-cresol remains within the 7.5/p/m powder after synthesis and processing. It should be remembered that the 7.5/p/m powder experienced the same step-wise thermal imidization treatment (through 300°C for 1 hour) after its initial synthesis and work-up, as described in section **3.2.2.2**.

Thus, it is possible that the *m*-cresol might indeed be acting as 'inhibitor' after synthesis and processing in that only a small fraction is necessary to inhibit the imine formation reaction at elevated temperatures. In pursuit of this line of reasoning a 2.5% stoichiometric offset powder and film were produced wherein 2%(w/w) of the standard DMAc solvent was replaced by *m*-cresol. All other synthetic procedures remained unchanged, as described in section **3.2.1**. It was thought that this 'catalytic' amount might be enough to change the chemical dynamics during imidization and thereby yield polymers with the ca. 408°C melting temperature. This was not the case as can be seen in Fig. 6.28. Here, the powder produced with 2% *m*-cresol (2.5/p/d-2m) is shown contrasted to the standard 2.5/p/d powder. As can be seen there is only a slight difference in the melting temperatures and magnitudes of the transitions. Likewise the film version of the 2% *m*-cresol spiked polymer showed no significant change in the melting behavior relative to the standard film produced in DMAc. Though a larger percentage of *m*-cresol in the reaction solvent might cause the melting temperature to rise it would become difficult to differentiate between a 'inhibitor'

versus solvent effect: It is already known that very high levels, i.e., 100%, of *m*-cresol will produce high melting LaRC CPI-2 polyimides. Thus, no other *m*-cresol spiked CPI-2 polymers were produced.

Another possible approach to lend support to the hypothesis that a ketimine reaction is occurring is to compare the melting behavior of an amine versus an anhydride terminated LaRC CPI-2 polymer. An amine terminated LaRC CPI-2 would be expected to have a much higher incidence of ketimine links and thereby present a different melting profile. In order to obtain polymers for comparison two 5.0% stoichiometric offset LaRC CPI-2 films were produced wherein the only difference was the major component. That is, in one film excess anhydride (ODPA) was used while excess amine (1,4-BABB) was used in the other. Neither film was otherwise 'end-capped'.

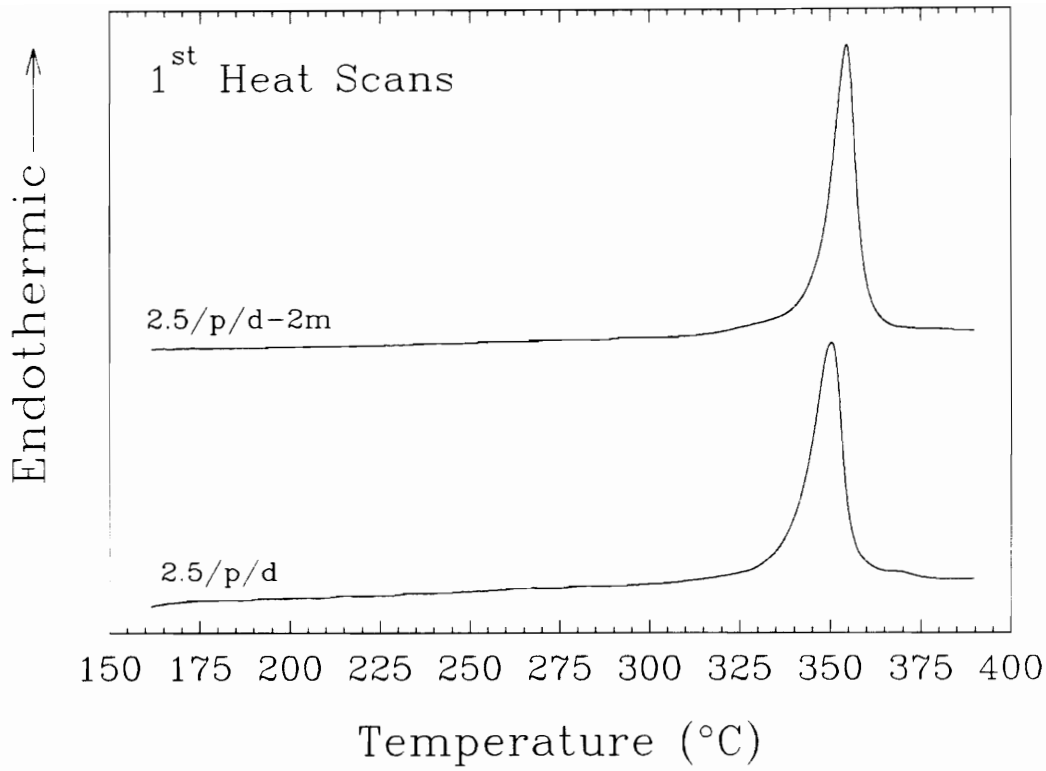

Figure 6.28 First heat DSC thermograms of the standard 2.5/p/d powder and the powder produced with 2% *m*-cresol (2.5/p/d-2m).

As can be seen in Fig. 6.29, the amine-terminal CPI-2 possesses only a single melting transition while the anhydride terminal CPI-2 displays the typical dual melting transition and is comparable to the standard 5.0/f/d sample. As was shown in chapter 4, the presence of the second melting transition is dependent upon the mobility of the polymer chains. The higher molecular weight CPI-2 polymers are less able to undergo the melt-recrystallization process to yield the second melting transition. A polymer with branches would likewise be expected to be inhibited in the melt-recrystallization process and the DSC scan for the amine terminated CPI-2 in Fig. 6.29 is consistent with this concept. Interestingly, the glass transition upon second heating, using the standard protocol described in section **3.3.1.1**, is well above that of the 5.0/f/d reference, 237°C versus 222°C. Indeed, this T_g is even higher than the 233°C displayed by the 1:1 stoichiometric ratio film (0/f/d). The T_g of 227°C for the anhydride terminal CPI-2 is also somewhat elevated relative to the reference film.

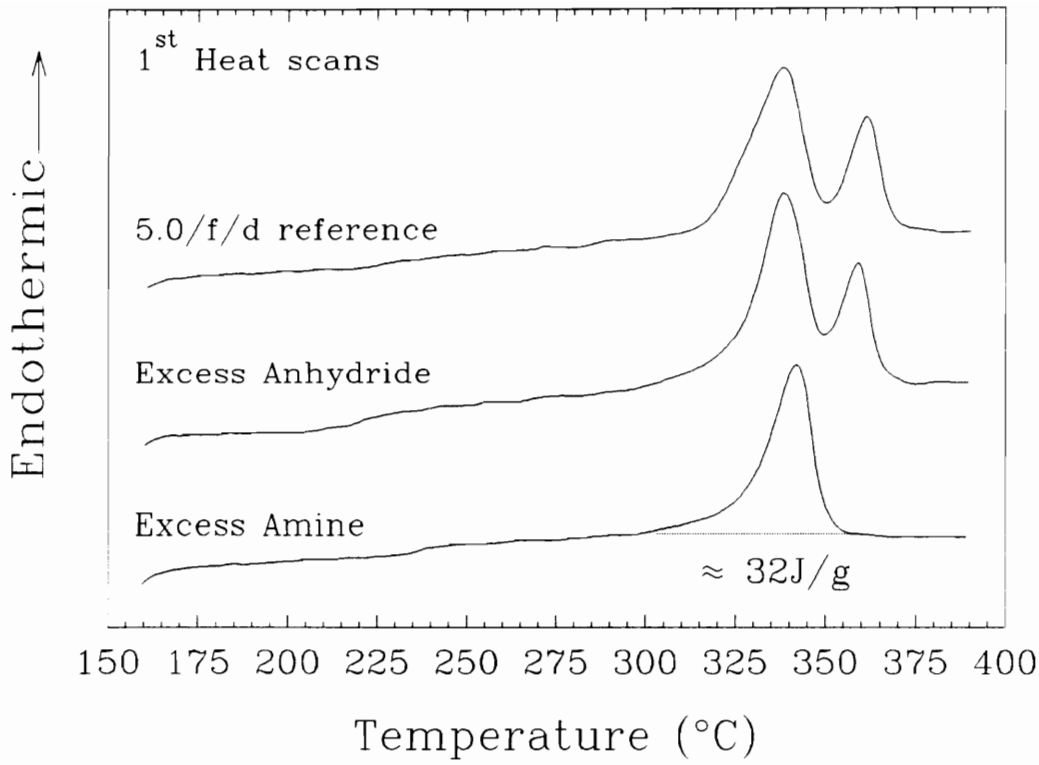

Figure 6.29 First heat DSC thermograms of the amine-terminal, anhydride terminal and standard LaRC CPI-2 powders. All are 5.0% stoichiometric offset.

One qualitative characteristic of these films that is of additional importance here is their flexibility. The anhydride terminal CPI-2, like the reference film, is very brittle and inflexible. In contrast, the amine terminal film is extremely flexible and is fingernail creasable. That is, a very sharp crease can be made in the film without it fracturing. The only other film to display this level of flexibility is the 0/f/d film, which is totally amorphous. This flexibility in the amine terminated CPI-2, along with its single melting behavior, supports the concept that cross-linking/branching has occurred during processing which is dependent upon terminal amine groups. This does not, however, prove that an imine link is responsible for the cross-linking/branching in CPI-2 polyimides.

At this point there is still only circumstantial evidence that a ketimine reaction is operative here. In their work to confirm that the ketimine link was responsible for the "self cross-linking" behavior in their amine terminal poly(aryl ether ketone), Mohanty et al. [134] employed ^{13}C solid state magic-angle NMR spectrometry. The presence of the amine end groups, as indicated by their influence on the benzene ring, was undetectable due to the relatively low population of these groups. However, after thermal treatment at 220°C, they found a peak at a chemical shift of 176.5ppm which was assigned to the -C≡N (imine) link (based on model compound studies). In an attempt to find the ketimine link in the LaRC CPI-2 system a sample of the 7.5/p/d powder was thermally treated at 380°C for 60 minutes under a nitrogen blanket in a controlled

temperature chamber. A spectrogram of this sample, along with an untreated 7.5/p/d powder sample, was obtained from ^{13}C solid state magic-angle NMR. As expected the untreated sample revealed no evidence of terminal amine groups. Unfortunately, the thermally treated sample did not possess a peak that could be assigned to the ketimine function group either. It should be noted that the level of detection for the NMR spectrometer is limited to about 3% (molar) [145]. Thus, this result does not negate the possibility of the presence of ketimine links, it simply indicates that they would be at a very low concentration.

It is necessary to point out that there is some evidence against the concept of the *m*-cresol suppressing imine reaction in the 7.5/p/m powder. Suematsu et al. found *m*-cresol to "facilitate" the [imine] polymerization of hexamethylenediamine with terephthalaldehyde to form a polyimine [146]. The *m*-cresol facilitated the reaction by keeping the polymer in solution, however, not by any catalytic effect.

Yet another possible explanation can be considered in terms of a solvent effect. It will be recalled that both the DMAc and *m*-cresol LaRC CPI-2 powders precipitate out during the thermal imidization 'in' solution (see section **3.2.2**). As discussed in detail in section **2.2.1.2**, it has been well documented that a polyimide undergoes a dramatic drop in molecular weight during thermal imidization, with a subsequent rise in the final stages of thermal processing [36, 43 - 45] (see, for example, Fig. 2.6). It not unlikely that the LaRC CPI-2 powders precipitate from solution at some stage along the reaction coordinate when the molecular weight is

low. This could be due to the development of crystallinity early in the process -- as is known to happen for the films (section **5.3**). Furthermore, it is entirely possible that the *m*-cresol acts as a better solvent thereby keeping the LaRC CPI-2 powder in solution longer, allowing it to reach a much higher molecular weight than its counterpart in DMAc. This same effect could also be achieved due to an acid catalytic effect imparted by the *m*-cresol during polymerization/imidization. As discussed in detail in sections **2.2.1.1** and **2.2.1.3**, both the formation of the amic acid and the imide are known to be acid catalyzed [12, 17, 18, 55]. In fact, it has been shown that the second order rate constant for the acylation reaction (reaction between anhydride and amine) is an order of magnitude greater in *m*-cresol than in DMAc [18]. Thus, it is not unreasonable to postulate that the 7.5/p/m powder reaches a much greater degree of imidization in the acidic *m*-cresol, due to faster reaction kinetics, before precipitating out of solution. If so, the processing in *m*-cresol might allow much higher molecular weight to be achieved simply because the polymer reaches the solid state so quickly.

Higher molecular weight chains, regardless of how they were obtained, would provide a lower concentration of available amine groups for cross-linking in the *m*-cresol powder. Furthermore, this would explain the unexpectedly high melt viscosity for the *m*-cresol powder shown in section **6.2.4,** and the slightly higher T_g for the m-cresol powder over its DMAc counterpart (217°C vs 210°C), as discussed in section **5.4.2.** As pointed out earlier (section **5.4.2**), however, the T_g

of a 0/p/d powder was much higher (231°C) while its T_m was only 335°C. It could be argued that the 0/p/d powder is of higher molecular weight but in a more branched [imine linked] state. It is possible that the reason that the DMAc powders are of lower melting temperature is because of imine branching which was inhibited in the *m*-cresol powders. That is, the differences may be due to the *linearity* of the polyimide chains. It is tempting to postulate that the dual melting observed in the DMAc and NMP powders and films may be due to a more branched chain. That is, there may be a kinetic barrier [provided by branching] to be overcome in order to form thicker lamellae, as found Blundell, Liggat and Flory [110] in an aromatic polyketone (section **2.3.4**).

Reviewing the melt viscosity plots for the 7.5/p/d and 7.5/p/m powders shown in Figs. 6.6 and 6.12, respectively, it is important to note that in both plots the viscosity curve is concave down. In a polymer wherein there is a significant level of branching, to the point of cross-linking, the melt viscosity curve would be concave up -- exponentially rising as the gel point is reached. Looking back at the T_gs for the 7.5/p/m material held at 420°C (Fig. 6.20) the transitions only become significantly broad at the 600 and 800 minute times. This would indicate that no significant level of cross-linking has occurred up to the 500 minute (ca. 8.3 hour) point. Thus, combining the annealing and rheological evidence it would appear that a great deal of chain extension may be occurring at elevated temperatures. By implication, then, both polymers had not reached their

calculated molecular weight values. This, of course, supports the concept that low molecular weight polymers are formed initially. The fact that the *m*-cresol polymer is able to withstand longer times at higher temperatures may be the result of a suppression of an imine reaction, as discussed earlier, thereby allowing chain extension reactions to dominate.

Thus, the large body of evidence presents a complicated picture and is somewhat contradictory. No simple theory to explain the stark differences in the melting, melt stability, and crystallization behavior between LaRC CPI-2 powders synthesized in DMAc versus *m*-cresol is readily apparent. Considerable evidence has been revealed which indicates that the ketimine reaction might be responsible. Proof or denial of this concept may be obtainable through more extensive studies involving model compounds, but this is beyond the scope of this dissertation and will be left for future work.

6.6 Summary

Clearly there are very great differences between the melting and crystallization behaviors to the two LaRC CPI-2 powder types discussed in this section. Both types display an ability to anneal at very high temperatures, relative to their observed melting transitions. The differences between these annealing and annealed melting temperatures is great, however. Viewing the polymer as a whole, the range of observed crystallization and melting temperatures discussed in

this section is extremely broad. Crystallization events analyzed via rheometric analysis ranged from 255°C to 380°C. In both sample types it is clear that there is a very complex set of processes occurring in the melt-annealing temperature zone: Melt-reorganization, to form higher melting crystals, is occurring simultaneously with chemical degradation which destroys crystallinity.

Perhaps most striking of all is the great difference in the ability of the two powder types to withstand elevated temperatures. As discussed in section **6.5**, this is possibly due to higher initial molecular weight of the 7.5/p/m powder and an inhibitor effect of the *m*-cresol which suppresses an imine reaction.

Specific recommendations for future work, designed to answer some fundamental questions regarding the exact nature of the stabilization effect of the *m*-cresol produced powder, will be offered in chapter 7 of this dissertation.

CHAPTER 7

CONCLUSIONS AND RECOMMENDATIONS

The dual melt transition observed in LaRC CPI-2 polyimides is the result of a lamellar melt recrystallization process which occurs during heating in a DSC. A film sample annealed at the exotherm temperature between the two melting transitions displayed a higher melting transition, a greater long spacing as determined from SAXS and visibly thicker lamellae seen via transmission electron microscopy. This is entirely consistent with fundamental thermodynamic relationships regarding crystal melting in polymeric systems, i.e., thicker lamellae melt at a higher temperature. DSC analysis reveals that the thickening process is a kinetic phenomenon dependent upon molecular weight. The rate of transformation from thin to thick lamellae has been shown to be inversely proportional to the molecular weight, as determined from the stoichiometric offset, of the polymer. Furthermore, DSC evidence suggests that only the lower melting [thinner] lamellae are present in the films initially. Despite the chain rigidity in this polyimide, DSC and synchrotron SAXS analysis clearly show that the melt recrystallization process is very rapid for the 10% stoichiometric offset (lowest molecular weight) film. An explanation for the exact mechanism of the melt reorganization process is not presently available. It is possible that a kinetic barrier exists to prevent a continuous lamellar thickening as has been suggested by Blundell et al. [115] for the poly(aryl ether ketone) in their study. It is possible

that molecular modeling studies could provide some answers in this regard.

Several other important characteristics of LaRC CPI-2 polyimides were presented in this dissertation. The melting behavior of LaRC CPI-2 polymers has been shown to be very dependent upon synthetic and process conditions. Higher molecular weight (0% stoichiometric offset) powders display significant levels of crystallinity while the film counterparts are completely amorphous. Crystalline levels parallel film thickness in a series of stoichiometric offset films and, within individual films, the initial level of crystallinity is related to the thickness. The development of crystallinity in LaRC CPI-2 films has been shown to initiate off the substrate surface very early in the thermal imidization procedure followed by a subsequent growth front progressing toward the air surface as imidization proceeds. Fully processed films display an amorphous layer at their air surface, the thickness of which is inversely proportional to the molecular weight, a function of the stoichiometric offset. It may be possible that different processing conditions would result in a more uniform distribution of the crystalline superstructure. In particular, a final processing step at a temperature well above the current 300°C final temperature might allow for a more full transformation of the amorphous material.

LaRC CPI-2 powders synthesized in DMAc and *m*-cresol have been shown to display greatly different crystalline superstructure and melting behavior, while other properties, such as thermo-oxidative stability and crystalline lattice structure,

are the same. A 7.5% offset DMAc powder 'type' melts at ca. 345°C and 366°C while the 7.5% *m*-cresol 'type' melts singularly at 408°C. Both powder types display an ability to anneal at very high temperatures, relative to their initially observed melting transitions. The differences between these annealing and annealed melting temperatures is great, however. Viewing the polymer as a whole, the range of observed crystallization and melting temperatures discussed in this dissertation is extremely broad. Crystallization events analyzed via rheological analysis ranged from 255°C to 380°C. With the annealing data compiled the very it can be seen that LaRC CPI−2 polyimides display a very broad (155°C) observed melting range: from 334°C for an as-made 10.0/f/d sample (see Fig. 4.1) to 489°C for the greatly annealed 7.5/p/m sample discussed in section **6.3.3**. In both the DMAc and *m*-cresol sample types it is clear that there is a very complex set of processes occurring in the melt-annealing temperature zone: Melt-reorganization, to form higher melting crystals, is occurring simultaneously with chemical degradation which destroys crystallinity.

There is a very great difference in the ability of the two powder types to withstand elevated temperatures. This is possibly due to an effect of the mildly acidic *m*-cresol solvent as it inhibits a ketimine reaction and a higher inital molecular weight in the 7.5/p/m powder. The elucidation of the exact mechanism of the stabilization effect provided by the *m*-cresol produced powder might be determinable through model compound studies.

In particular, it may be possible to conduct reaction studies on low molecular weight analogs of LaRC CPI-2. A phthalic anhydride (PA) endcapped 1,4-BABB could be produced wherein the endcapping would be quantitative (by using a great excess of PA during synthesis). By exposing this analog to elevated temperatures in the presence of the free amine 1,4-BABB monomer it may be possible to clearly show the presence of imine links through FTIR and proton NMR in solution. Rheological changes could also be analyzed as a function of temperature. As a comparison, the endcapped 1,4-BABB could be subjected to the same thermal conditions. It would be expected that no imine links would form. The effect of the *m*-cresol could be determined by introducing catalytic amounts into the system before thermal treatment. Further empirical evidence for the inhibition of an imine reaction in LaRC CPI-2 could be provided by producing powders and films in the presence of a catalytic amount of a strong acid such as methanesulfonic or toluenesulfonic acid. The residue of these acids remaining in the polymer would most likely remain throughout the thermal treatment due to their high boiling points ($b.p._{20}$ = 140°C and $b.p._{10}$ = 167°C for toluenesulfonic and methanesulfonic acid, respectively [147]). Thus, an imine 'inhibitor' may remain in the polymer during processing at elevated temperatures.

In order to investigate the possibility of the polymers precipitating from solution at molecular weights lower than predicted, a series of powders of the same stoichiometric offset (say, 7.5%) could be synthesized at differing solution

concentrations. Presumably, the powders would precipitate at successively higher molecular weight values as the concentration decreases. This would be somewhat complicated in the DMAc solvent since the reversible acylation reaction favors the monomers at low concentrations as noted in section 2.2.1.1. Nonetheless, it is probable that trends in T_g, melt viscosity and melt stability within the series would help to explain the differences between the two powders.

REFERENCES

1. Verbicky, J.W., "Polyimides", in Encyclopedia of Polymer Science and Engineering, 2nd ed., vol 12, John Wiley and Sons, New York, (1988).

2. Feger, C., Khojasteh, M. M., and McGrath, J. E., Editors, Polyimides: Materials, Chemistry, and Characterization, Elsevier Science Publishers, Amsterdam, (1989).

3. Wilson, D., Stenzenberger, H.D. and Hergenrother, P.M., editors, Polyimides, Blackie and Sons, Glasgow, (1990).

4. Mittal, K. L., Editor, in Polyimides: Synthesis, Characterization, and Applications, Volumes 1 and 2 , Plenum Press, New York, (1984).

5. Takekoshi, T., *Adv. Polym. Sci.*, 94, 1, (1990).

6. Sroog, C.E., *Prog. Polym. Sci.*, 16, 561, (1991).

7. Bessonov, M.I., Koton, M.M., Kudryavtsev, V.V., and Laius, L.A., Polyimides-Thermally Stable Polymers, Consultants Bureau (Plenum), New York, (1987).

8. Sroog, C. E., *J. Polym. Sci. Macromol. Rev.*, **11**, 161 (1976).

9. Harris, F.W., in Polyimides, Wilson, D., Stenzenberger, H.D. and Hergenrother, P.M., editors, Blackie and Sons, Glasgow, p. 1, (1990).

10. Ardashnikov, A.Ya., Karddash, I.Ye, and Pravednikov,A.N., *Polym. Sci.* USSR, **13**(8), 2092, (1971). {Vysokomol. Soyed., A13(8), 1863-9, (1971)}

11. Pravednikov,A.N., Karddash, I.Ye, Glukhoyedov, N.P., and Ardashnikov, A.Ya., *Polym. Sci.* USSR, **15**(2), 399, (1973). {Vysokomol. Soyed., A15(2), 349-359, (1973)}

12. Kaas, R.L., *J. Polym. Sci. Polym. Chem. Ed., 19,* 2255, (1981)..

13. Brekner, M. and Feger, C., *J. Polym. Sci.: Part A: Polym. Chem.*, **25**, 2005-20, (1987).

14. Brekner, M. and Feger, C., J. Polym. Sci.: Part A: Polym. Chem., **25**,

2479-91, (1987).

15. Feger, C., *Polym. Engr. Sci.*, **29**(5), 347-51, (1989).

16. Frayer, P. D., in Polyimides: Synthesis, Characterization, and Applications, Vol. 1, ed. Mittal, K. L., Plenum Press, New York, (1984), p. 273.

17. Vygodskii, Ya.S., Spirina, T.N., Nechayev, P.P., Chudina, L.I., Zaikov, Ye.G., Korshak, V.V. and Vinogradova, S.V., *Polym. Sci.* USSR, 19(7), (1977), 1738 {Vysokomol. Soyed., A19(7), 1516-1522, (1971)}

18. Solomin, V.A., Kardash, I.E., Snagovskii, Ya.S., Messerle, P.E., Zhubanov, B.A., and Pravednikov, A.N., *Dokl. Chem.* (Engl. Transl.), 236(1), (1977), p. 510 {Original: *Dokl. Akad. Nauk SSSR*, 236(1), (1977), p. 139}

19. Dielectric constants for THF, ACN, DMAc from ref. 10. Dielectric constant for *m*-cresol from Handbook of Chemistry and Physics, 65th ed., CRC Press, (1984).

20. Kaneda, T., Katsusa, T., Kanji, N. and Makino, H., *J. Appl. Polym. Sci.,* 32, 3133-49 (1986).

21. Dror, M. and Levy, M., *J. Polym. Sci. Polym. Chem. Ed.*, 13, 171 (1975).

22. Feld, W.A., Ramalingham, B. and Harris, F.W., , *J. Polym. Sci., Polym. Chem. Ed.,* **21**, 319, (1983).

23. Bower, G.M. and Frost, L.W., *J. Polym. Sci.*, A1, 3135, (1963).

24. Frost, L.W. and Kesse, *I., J. Appl. Polym. Sci.,* 8, 1039, (1964).

25. Sroog, C. E., Endrey, A. L., Abramo, S.V. Berr, C.E., Edwards, W.M. and Oliver, K.L., *J. Polym. Sci.* Part A3, 1373, (1965).

26. Cotts, P.M., Volksen, W. and Ferline, S., *J. Polym. Sci.: Part B: Polym. Phys. ed.* **30**, 373, (1992).

27. Carothers, W.H., *J. Am. Chem. Soc.* **51**, 2548, (1929).

28. Flory, P. J., Principles of Polymer Chemistry, Cornell University Press, Ithica, (1953).

29. Odian, G., Principles of Polymerization, 2nd ed., Wiley, New York, (1981).

30. Rosen, S.L., Fundamentals Principles of Polymeric Materials, Wiley, New York, (1982).

31. Arnold, C.A., Summers, J.D., Chen, Y.P., Bott, R.H., Chen, D.H., and McGrath, J.E., *Polymer*, **30**(6), 986, (1989).

32. Waldbauer, R.O., Rogers, M.E., Arnold, C.A., York, G.A., C.A., Kim, Y.J. and McGrath, J.E., *Polym. Preprints*, 31(2), 432 (1990).

33. Wilkens, D. L., Arnold, C. A., Jurek, M. J., Rogers, M. E., and McGrath, J. E., *J. Thermoplast. Comp. Mat.*, **3**, 4 (1990).

34. McGrath, J.E., Rogers, M.E., Arnold, C.A., Kim, Y.J., and Hedrick, J.C., *Makromol. Chem., Mocromol. Symp.*, 51, 103 (1991).

35. Rogers, M.E., Brink, M.H., Brennan, A. and McGrath, J.E., *Polymer*, 34(4), 849 (1993).

36. Dine-Hart, R.A., and Wright, W.W., *J. Appl. Polym. Sci.*, 11, 609-627, (1967).

37. Volksen, W. and Cotts, P.M., in Polyimides: Synthesis, Characterization, and Applications, Vol. 1, ed. Mittal, K. L., Plenum Press, New York, (1984), p. 163.

38. Kreuz, J.A., Endrey, A.L., Gay, F.P. and Sroog, C.E., *J. Polym. Sci.*, **A-1** (4), 2607, (1966).

39. Laius, L. A., and Tsapovetsky, M. I., in Polyimides: Synthesis, Characterization, and Applications, Vol. 1, ed. Mittal, K. L., Plenum Press, New York, (1984), p. 295.

40. Minnema, L. and van der Zannde, J.M., in Polyimides: Synthesis, Characterization, and Applications, Vol. 1, ed. Mittal, K. L., Plenum Press, New York, (1984), p. 589.

41. Laius, L. A., and Tsapovetsky, M. I., in Polyamic Acids and Polyimides: Synthesis, Transformations and Structure, Bessonov, M.I. and Zubkov, V.A., CRC Press, Boca Raton, FL., 1993, p. 50

42. Echigo, Y., Iwaya, Y., Tomioka, I., Furukawa, M. and Okamoto, S., *Macromol.*, 28(8), 3000, (1995).

43. Young, P.R. and Chang, A.C., *SAMPE Prepr.*, 889, (1985).

44. Young, P.R., Davis, J.R., Chang, A.C. and Richardson, J.N., *J. Polym. Sci.: Part A: Polym. Chem.*, **28**, 3107-3122, (1990).

45. Chen, K.M., Wang, T.H., King, J.S. and Hung, A., *J. Appl. Polym. Sci,* 48, 291-7 (1993).

46. V.L. Bell, B.L. Stump, and H. Gager, *J. Polym. Sci.*, **14**, 2275 (1976).

47. Progar, D.J., Bell, V.L. and St. Clair, T.L., US Pat. 4,065,345, (1977).

48. Bell, V.L., US Pat. 4,094,862 (1978).

49. Hergenrother, P. M., Wakelyn, N. T., and Havens, S. J., *J. Polym. Sci., Polym. Chem. Ed.*, 25, 1093 (1987).

50. P.M. Hergenrother and S.J. Havens, J. Polym. Sci., Polym. Chem. Ed., **27,** 1161-74, (1989).

51. Hergenrother, P.M., Beltz, M.W. and Havens, S.J.. J. Polym. Sci.: Part A: Polym. Chem., **29**, 1483-9 (1991).

52. Numata, S.-I., Fujisaki, K., and Kinjo, N., in Polyimides: Synthesis, Characterization and Applications, Vol. 1, ed. Mittal, K. L., Plenum Press, New York, p. 259, (1984).

53. Baise, A. I., *J. Appl. Polym. Sci.*, **32**, 4043 (1986).

54. Ginsburg, R., and Susko, J. R., in Polyimides: Synthesis, Characterization, and Applications, Vol. 1, ed. Mittal, K. L., Plenum Press, New York, (1984), p. 237.

55. Kim, Y.J., Glass, T.E., Lyle, G.D. and McGrath, J.E., *Macromol.*, 26(6), 1344-58, (1993).

56. Summers, J.D., and McGrath, J.E., *Polym. Preprints*, **28** (2), 230 (1987).

57. Arnold, C.A., Summers, J.D., York, G.A., Bott, R.H., Taylor, L.T., Ward, T.C., and McGrath, J.E., *Polym. Preprints*, **28** (2), 217 (1987).

58. Arnold, C.A., Chen, Y.P., Chen, D.H., Rogers, M.E., and McGrath, J.E., *Mat. Res. Soc. Symp. Proc.*, **154**, 149, (1989).

59. Vinogradova, S.V., Vygodskii, Ya.S. and Korshak, V.V., *Polym. Sci.* USSR,. **12**(9), 2255-62 (1970) {Vysokomol. Soyed., **A12**(9), 1987-93, (1970)}.

60. Takekoshi, T., Kochanowski, J.E., Manello, J.S. and Webber, M.J., *J. Polym. Sci.: Polym. Symp.*, 74, 93-108 (1986).

61. Moy, T.M., DePorter, C.D. and McGrath, J.E., *Polymer*, **34**(4), 819 (1993).

62. Imai, Y., *Polym. Lett.*, 8, 555 (1990).

63. Takekoshi, T., in Polyimides, Wilson, D., Stenzenberger, H.D. and Hergenrother, P.M., editors, Blackie and Sons, Glasgow, (1990) p. 38

64. Wilson, D., in Polyimides, Wilson, D., Stenzenberger, H.D. and Hergenrother, P.M., editors, Blackie and Sons, Glasgow, (1990) p. 187

65. Fryd, M., in Polyimides: Synthesis, Characterization, and Applications, Vol. 1, ed. Mittal, K. L., Plenum Press, New York, (1984), p. 377.

66. St. Clair, T.L., in Polyimides, Wilson, D., Stenzenberger, H.D. and Hergenrother, P.M., editors, Blackie and Sons, Glasgow, (1990) p. 58

67. Dine-Hart, R.A., and Wright, W.W., *Makromol. Chem,* 143, 189, (1971).

68. Muellerleile, J.T., York, G.A., and Wilkes, G.L., *Polym. Commun.*, **32**(6), 176-9 (1991).

69. Hergenrother, P. M., Wakelyn, N. T., and Havens, S. J., *Polym. Preprints,* 28, 92 (1987).

70. Hergenrother, P. M., and Havens, S. J., *SAMPE J.*, **24**(4), 13 (1988).

71. Hergenrother, P. M., and Havens, S. J., *Polymer Preprints*, **28**(1), 92 (1987).

72. Hergenrother, P. M., Beltz, M. W., and Havens, S. J., *Proc. 34th Int.*

SAMPE Symp. Exhib., **34**, 963, (1989).

73. Hergenrother, P. M. and Havens, S. J., *Proc. 36th Int. SAMPE Symp. Exhib.*, **36**, 56 (1991).

74. Hergenrother, P. M. and Havens, S. J., in Polyimides: Materials, Chemistry, and Characterization, ed. Feger, C., Khojasteh, M. M., and McGrath, J. E., Elsevier Science Publishers, Amsterdam, (1989), p. 453.72

75. Muellerleile, J.T., Ph.D. Dissertation, Virginia Polytechnic Institute and State University, 1991.

76. Hermans, P.H. and Streef, J.W., *Die Makromol. Chemie,* **74**, 133 (1964).

77. Bernier, G.A. and Kline, D.E., *J. Appl. Polym. Sci.*, **12**, 593 (1968).

78. Wunderlich, B., Macromolecular Physics Volume 2: Crystal Nucleation, Growth, Annealing, Academic Press, New York, 1976.

79. Lauritzen, J. I., Jr., and Hoffman, J. D., *J. Res. Nat. Bur. Stand.-A. Phys. Chem.* **64A**, 73 (1960).

80. Mandelkern, L., in Comprehensive Polymer Science: The Synthesis, Characterization, Reactions, and Applications of Polymers, Vol. 2, ed. Booth, C., and Price, C., Pergamon Press, New York, (1989), 363.

81. Hoffman, J. D., and Lauritzen, Jr., J. I., *J. Res. Nat. Bur. Stand.- A. Phys. Chem.*, **65A**, 297 (1961).

82. Phillips, P. J., *Rep. Prog. Phys.*, **53**, 549 (1990).

83. Hoffman, J. D., Davis, G. T., and Lauritzen, J. I., Jr., in Treatise in Solid-State Chemistry, (ed. Hannay, N. B.), Vol. 3, Plenum Press, New York, 1976, p. 497.

84. Fatou, J. G., "Crystallization Kinetics," in Encyclopedia of Polymer Science and Engineering, (Suppl. Vol.), John Wiley and Sons, New York, (1989), p. 231.

85. Magill, J. H., in Polymer Handbook (3rd edition), ed. Brandrup, J., et. al., Wiley and Sons, New York, (1989), p. 279.

86. Bassett, D. C., Principles of Polymer Morphology, Cambridge University Press, London, 1981.

87. Hoffman, J.D. and Weeks, J.J., *J. Res. NBS, part A, Phys. and Chem.*, **66A**(1) (1962).

88. Avrami, M., *J. Chem. Phys.*, **7**, 1103 (1939).

89. Avrami, M., *J. Chem. Phys.*, **8**, 212 (1940).

90. Avrami, M., *J. Chem. Phys.*, **9**, 177 (1941).

91. Hiemenz, P. C., Polymer Chemistry: The Basic Concepts, Marcel Dekker, Inc., New York, (1984).

92. Morgan, L. B., *Phil. Trans. A.*, **247**, 13 (1954).

93. Cebe, P., Hong, S.-D., Chung, S., and Gupta, A., Special Technical Publication 937, ASTM, Philadelphia, 1987, p. 342.

94. Day, M., Suprunchuk, T., Deslandes, Y., and Wiles, D. M., *Proc. 34th Int. SAMPE Symp. Exhib.*, May 8-11, (1989).

95. Carpenter, J. *SAMPE J.*, **24**, 36 (1988).

96. Lee, Y., and Porter, R. S., *Macromol.*, **21**, 2770 (1988).

97. Bassett, D. C., Olley, R. H., and Al Raheil, I. A. M., *Polymer*, **29**, 1745 (1988).

98. Blundell, D. J., Chalmers, J. M., Mackenzie, M. W., and Gaskin, W. F. *SAMPE Q*, **16**, 22 (1985).

99. Lee, Y., and Porter, R. S., *Polym. Eng. Sci.*, **26**, 633 (1986).

100. Popli, R and Mandelkern, L., *J. Polym. Sci.: Part B: Polym. Phys. ed.*, 25, 441 (1987).

101. Kelly, J. E., and Baird, D. G., *Proc. 36th Int. SAMPE Exhib.*, 1535 (1991).

102. Chu, J.-N., and Schultz, J. M., *J. Mat. Sci.*, **25**, 3746 (1990).

103. Wittmann, J. C., and Lotz, B., *J. Polym. Sci.: Polym. Phys. Ed.*, 19, 1837 (1981).

104. Talbott, M. F., Springer, G. S., and Berglund, L. A., *J. Comp. Mat.*, **21**, 1056 (1987).

105. Martinez-Salazar, J., Barham, P.J. and Keller, A., *J. Mater. Sci.* **20**, 1616-24, (1985).

106. Ungar, G. et al, *Science* **229**, 386-9 (1985).

107. Cheng, S.Z.D., Zhang, A., Chen, J. and Heberer. D.P., *J. Polym. Sci.: Part B: Polym. Phys. ed.* **29**, 287-97 (1991).

108. Bell, J.P., Slade, P.E. and Dumbelton, J.H., *J. Polym. Sci. Part A-2,* **6**, 1773-81, (1968).

109. Bell, J.P. and Dumbelton, J.H., *J. Polym. Sci. Part A-2,* **7**, 1033-1057 (1969).

110. Cheng, S.Z.D., Heberer, D.P., Lien, H. and Harris, F.W., *J. Polym. Sci.: Part B: Polym. Phys. ed.* **28**, 655-74, (1990).

111. Heberer, D.P., Cheng, S.Z.D., Barley, J.S., Lien, H., Bryant, R.G. and Harris, F.W., *Macromol.*, **24**(8), 1890-8, (1991).

112. Havens, S.J., Research chemist at NASA Langley, Private Communication, January 1992.

113. Muellerleile, J.T. private communication

114. Brandom, D.K. and Wilkes, G.L., *Polymer*, 35(26), 5672-7 (1994).

115. Blundell, D.J., Liggat, J.J. and Flory, A., *Polymer,* **33**(12), 2475-82, (1992).

116. Brandom, D.K. and Wilkes, G.L., *Polymer*, 36(21), 4083-9 (1995).

117. Cotts, P.M., in Polyimides: Synthesis, Characterization, and Applications, Vol. 1, ed. Mittal, K. L., Plenum Press, New York, (1984), p. 223.

118. Snyder, R.W., Thomson, B., Bartges, B., Czerniawski, and Painter, P.C., *Macromol.*, **22**(11), 4166-72, (1989).

119. Pratt, J.R., St. Clair, T.L., Gerber, M.K., and Gautreaux, C.R., in Polyimides: Materials, Chemistry and Characterization, Feger, C., et al. eds., (1989), Elsevier Science Publishers, New York, p. 193.

120. Kishanprasad, V.S. and Gedham, P.H., *J. Appl. Polym. Sci.*, 50, 419-29 (1991).

121. Hermans, P.H. and Weidinger, A., *Makromol. Chem.*, 44-46(24) (1964).

122. Wiedinger, A. and Hermans, P.H., *Makromol. Chem.*, 50(98) (1961).

123. Alexander, L.E., X-Ray Diffraction Methods In Polymer Science, John Wiley and Sons, New York, (1969).

124 . Balta-Calleja', F.J. and Vonk, C.G., X-Ray Scattering of Synthetic Polymers, Polymer Science Library Vol 8., Elsevier, Amsterdam, (1989).

125. Crist, B. and Morosoff, N., *J. Polym. Sci., Polym. Phys. Ed.*, Vol 11, 1023-1045, (1973)

126. Keller, A., *IUPAC Int. Symp., Macromol. Proc.*, Florence, 131-169, (1980).

127. Hsiao, B.S., Gardener, K.H., Wu, D.Q., and Chu,B., *Polymer*, 34(19), 3986-95, (1993).

128. Wingrove, A.S. and Caret, R.L., Organic Chemistry, p. 697, Harper and Row, New York, (1981).

129. Khanna, Y.P. and Reimschuessel, A.C., *J. Appl. Polym. Sci.*, 35, 2259, (1988).

130. Muellerleile, J.T. and Wilkes, G.L., *Polymer*, 34(1), 789-806 (1993).

131. Dine-Hart, R.A., Parker, D.B.V. and Wright, W.W., *Br. Polym. J.*, 3, 222-5 (1971); Dine-Hart, R.A., Parker, D.B.V. and Wright, W.W., *Br. Polym. J.*, 3, 226-34 (1971).

132. Pryde, C.A., *J. Polym. Sci.*, **A27**, 711, (1989).

133. For example: Bock, M. and Halpap, R., *J. Coatings Technol.*, 59(755), (1987); Ott, G., Heimann, U., Santure, D., Reiter, U., German Pat: DE

3918511 (1990).; Suzuki, M. and Nakagawa, K,, Japanese Pat: JP 02048560 (1990); Ernst, G.D. and Schuweiler, A.R., US Pat: 4772643 (1988).

134. Mohanty, D.K., Lowery, R.C., Lyle, G.D. and McGrath, J.E., *Int. SAMPE Symp.*, 32, 408-419, (1987).

135. Roovers, J., Cooney, J.D. and Torporowski, P.M., *Macromol.*, 23(6)., 1611-18, (1990).

136. Lyon, K.R., Texier, A., Gungor, A., Davis, R.M. and McGrath, J.E., *Int. SAMPE Symp. Exhib.*, V. 37, (1992).

137. Brink, A.E., et al. *Polymer*, 34(4), 825-49, (1993).

138. Khanna, Y.P. and Kumar, R., *J. Polym. Sci: Part B: Polym. Phys.*, 27, 369-379 (1989).

139. Zhang, Z. and Zeng, H., *Polymer*, 34(17), 3468-72, (1993).

140. Blundell, D.J. and Osborne, B.N., *Polymer*, 24, 953, (1983).

141. Lee, Y., and Porter, R. S., *Macromol.*, 20, 1336, (1987).

142. Khanna, Y.P., *Macromol.*, 26(14), 3639-43, (1993).

143. Carey, F.A. and Sundberg, R.J., Advanced Organic Chemistry: Part A: Structure and Mechanisms, p. 330-1, Plenum Press, New York, (1977).

144. McMurry, J., Organic Chemistry, second ed., p. 674-6, Brooks/Cole, Pacific Grove, CA (1988).

145. Glass, T.E., VPI&SU NMR spectroscopist, Private Communication, November 1995.

146. Suematsu, K., Nakamura, K. and Takeda, J., *Polym. J.* 15(1), 71-9, (1983).

147. The Merck Index, ninth edition, Windholz, M, Ed., Merck & Co., Rahway, N.J. (1976).

Vita

Don Brandom was born on July 4, 1959. In June of 1990 he started graduate work under Prof. Garth L. Wilkes. In August of that same year he was recalled to active duty in support of Desert Shield/Storm, and returned to graduate school in March of 1991. In April of 1994, while finishing his graduate work, Don formed the start-up company known as High Foam Technologies, Inc., of which he is currently president.